SMALL MOLECULE MIMICS OF HYDROGENASE ENZYMES: SYNTHESIS, PROTONATION, AND ELECTROCATALYSIS

BY

MARIA ELIZABETH CARROLL

DISSERTATION

Submitted in partial fulfillment of the requirements
for the degree of Doctor of Philosophy in Chemistry
in the Graduate College of the
University of Illinois at Urbana-Champaign, 2013

Urbana, Illinois

Doctoral Committee:

Professor Thomas B. Rauchfuss, Chair
Professor Gregory S. Girolami
Professor Andrew A. Gewirth
Professor Catherine J. Murphy

Abstract

In nature, H_2 is processed by enzymes called hydrogenases, which catalyze the reduction of protons to dihydrogen, as well as the reverse reaction. The active sites of the two most prevalent hydrogenases contain NiFe or FeFe cores, bound to thiolates, cyanide, and carbon monoxide ligands. These enzymes are also rich in Fe-S clusters to allow the necessary redox chemistry of hydrogen oxidation and production. Both enzymes operate at rates and overpotentials comparable with the best synthetic Pt catalysts. Due to growing concern over the climate effects of burning fossil fuels, there is a push to replace these fuels with carbon free alternatives, one option being H_2. However, this would require catalysts for H_2 production that are based on cheap, easily accessible metals. This problem inspired extensive research on the development of functional small molecule mimics of the hydrogenase enzymes. The work presented herein is motivated by the goal of understanding the mechanism of hydrogenase enzymes, in order to design better catalysts for hydrogen production. Chapter 1 presents an overview of current methods for the production of H_2, including methods used in industry, as well as heterogeneous and homogeneous metal catalysts.

The most unique features of the active site of [FeFe]-H_2ases are the amino-dithiolate cofactor that bridges the two Fe centers and the rotated geometry of one Fe center, leaving an open coordination site adjacent to the amine, which is the proposed site of substrate binding. Many active site models have been prepared, many of which undergo protonation to form hydride complexes and catalyze proton reduction. However, in all cases, the thermodynamic product of protonation is a bridging hydride, which is not biologically relevant. A number of phosphine substituted diiron complexes have been found to form terminal hydrides at very low temperatures.

Chapter 2 describes the protonation of complexes of the type $Fe_2(xdt)(CO)_4(dppv)_2$ (xdt= pdt, 1,2-propanedithiolate, or adt^{NH}= azadithiolate; dppv= cis-1,2-bis(diphenylphosphino)ethylene, which form terminal hydrides that are stable at 0 °C for ~ 30 minutes and then isomerize to the corresponding bridging hydrides. $Fe_2(adt^{NH})(CO)_4(dppv)_2$ undergoes protonation with weak acids, whereas, the pdt analogue requires strong acid; the difference being attributed to the presence of a pendant base in $Fe_2(adt^{NH})(CO)_4(dppv)_2$, which is initially protonated and then relays the proton to the Fe center. Additionally, in the presence of

excess acid, $Fe_2(adt^{NH})(CO)_4(dppv)_2$ sustains double protonation to form a terminal hydride ammonium species. The complex, $[t\text{-}HFe_2(adt^{NH2})(CO)_4(dppv)_2](BF_4)_2$, is the first example of a crystallographically characterized terminal hydride produced by protonation. The most significant feature of the structure is the NH--HFe distance of 1.88 Å, which indicates dihydrogen bonding. The molecule is positioned to release H_2, and represents a key intermediate in the mechanism of proton reduction catalysis.

Chapter 3 describes the redox and catalytic properties of the terminal and bridging hydrides of $Fe_2(xdt)(CO)_2(dppv)_2$. For both the adt^{NH} and the pdt derivatives, the terminal hydride species are reduced at ~150 mV more mild potentials than the corresponding bridging hydrides. The voltammetry of $[t\text{-H } Fe_2(adt^{NH})(CO)_2(dppv)_2]^+$ is strongly affected by relatively weak acids and proton reduction catalysis proceeds at 5000 s^{-1} with an overpotential (the deviation from the thermodynamic reduction potential of the acid) of 0.7 V. The ammonium-hydride $[t\text{-H } Fe_2(adt^{NH2})(CO)_2(dppv)_2]^{2+}$ is a faster catalyst, operating at 58,000 s^{-1} and an overpotential of 0.5 V. When the adt^{NH} cofactor is replaced with the less biologically relevant ligand pdt or the terminal hydride species are replaced with isomeric bridging hydrides, catalysis is significantly slower (TOF= 5- 20 s^{-1}) and inefficient (overpotential= 0.9- 1.3 V), indicating that hydrogen evolution by biomimetic diiron dithiolates is accelerated by the amine cofactor, to which the hydride ligand must be adjacent, and inclusion of features found in the enzyme results in fast and efficient catalysis.

Unlike models for [FeFe]-hydrogenase, hydride containing models of [NiFe]-hydrogenase were unknown until, in 2009, our group reported the complex $[(dppe)Ni(pdt)(\mu\text{-}H)Fe(CO)_3]BF_4$ (dppe= 1,2-bis(diphenylphosphino)ethane), which was found to undergo substitution of CO with phosphine ligands. Most importantly, these new NiFe hydrides were found to catalyze proton reduction at mild overpotentials. Chapter 4 describes the development of a new synthesis of complexes of the type $(diphosphine)Ni(xdt)(CO)_3$, in which $Fe(CO)_4I_2$ condensed with Ni(xdt)(diphosphine), forming a $Ni^{II}Fe^{II}$ μ-iodide intermediate, which is then reduced to form the neutral NiFe complex. With this new synthetic method in hand, we synthesized of new derivatives, varying in the identity of the dithiolate, the diphosphine, and the ligands on the Fe center.

Having a range of derivatives, we probed the individual roles of Ni vs Fe in catalysis.

The acidity of the hydride appears to be more strongly affected by changes at the Fe center (ΔpK_a^{MeCN} of 4 for L= PPh_3 vs L= CO) than changes at the Ni center (ΔpK_a^{MeCN} of 2.5 for R = Ph vs Cy). The reduction potential appears to be more strongly affected by changes at Ni (ΔE_{red} of 250 mV for R = Ph vs Cy) than at Fe (ΔE_{red} of 200 mV for L = CO vs PPh_3). Changes in the dithiolate have a minimal effect on the reduction potentials of the hydrides, although the rates of hydrogen evolution are strongly affected by the dithiolate. The catalysts operate at overpotentials of 0.4 V and the rates up to 300 s^{-1}, which are good by the standards of model studies although modest by the standards of the enzymes.

Chapters 5 and 6 focus on the development of new methods for the synthesis of bimetallic dithiolato complexes, as well as the effect of changing the metal centers to metals that are not found in hydrogenases. Chapter 5 describes the synthesis of new ferrous dicarbonyl dithiolato diphosphine complexes containing chelating diphosphine and dithiolate ligands. A new building block method for the synthesis of substituted diiron complexes of the type $Fe_2(xdt)(CO)_4$(diphosphine), by reaction of $Fe(xdt)(CO)_2$(diphosphine) complexes with an Fe(0) tricarbonyl source, is described. Additionally, this building block approach is extended to the synthesis of Mn-Fe analogues of the FeFe complexes. The new bimetallic complexes, $[(CO)_3Mn(xdt)Fe(CO)_2(diphosphine)]BF_4$ are synthesized by the reaction of $Fe(xdt)(CO)_2$(diphosphine) with the manganese tricarbonyl transfer reagent, $[(acenaphthene)Mn(CO)_3]BF_4$. These cationic complexes undergo decarbonylative reduction to form neutral MnFe complexes that are models for the $Fe^{I}Fe^{II}$ H_{ox} state of the enzyme. Synthesis of the bridging hydride complex $Mn(CO)_3(pdt)(\mu\text{-}H)Fe(CO)(dppe)$ is described. The hydride complexes been characterized crystallographically, and can be oxidized reversibly, reactivity that is not seen in NiFe or FeFe models that contain hydride ligands.

Chapter 6 describes the synthesis of bimetallic CpCo complexes of the type, $(C_5H_5)Co(xdt)Co(C_5H_5)$ (xdt= pdt, 1,2-propanedithiolate; edt, 1,2 ethanedithiolate, and tdt= 3,4-toluenedithiolate), in an effort to synthesize more electron rich model complexes, by replacing the $Fe(CO)_3$ unit with CpCo. These complexes undergo protonation to form bridging hydride species, which catalyze the reduction of protons, albeit at modest rates and fairly high overpotentials.

Terms Used Within This Thesis

adt^{NH}	azadithiolate, $[NH(SCH_2)_2]^{2-}$
adt^{NR}	N-R-N'-dithiomethylamine, $[N(R)(CH_2S)_2]^{2-}$
$BAr^F{}_{24}$	tetrakis(3,5-bis(trifluoromethyl)phenyl)borate, $[B(C_6H_3(CF_3)_2)_4]^-$
bda	benzylideneacetone
ClAA	Chloroacetic acid, $H_2ClC_2O_2H$
Cp	cyclopentadienyl, $[C_5H_5]^-$
Cy	cylcohexyl, C_6H_{11}
dcpe	1,2-bis(dicyclohexylphosphino)ethane, $Cy_2PCH_2CH_2PCy_2$
dmg	dimethylglyoxime
dmpe	1,2-bis(dimethylphosphino)ethane, $Me_2C_2H_4Me_2$
dpg	diphenylglyoxime
dppe	1,2-bis(diphenylphosphino)ethane, $Ph_2PC_2H_4PPh_2$
dppv	*cis*-1,2-bis(diphenylphosphino)ethane, *cis*-$PPh_2C_2H_2PPh_2$
edt	1,2-ethanedithiolate, $[S_2C_2H_4]^{2-}$
emi	*N*,*N*-ethylenebis(2-mercaptoisobutyramide
Et	ethyl, C_2H_5
$Fc^{+/0}$	ferrocenium/ ferrocene couple, $[(C_5H_5)_2Co]^{+/0}$
H-Cluster	6-Fe active site of [FeFe]-hydrogenase
HOTs	*p*-toluenesulfonic acid, $CH_3C_6H_4SO_3H$
H_{ox}	active, oxidized form of [FeFe]-hydrogenase
H_{red}	active, reduced form of [FeFe]-hydrogenase
Me	methyl, CH_3
Me_2pdt	2,2,-dimethyl-1,3-propanedithiolate, $[S_2C_2H_4C(CH_3)_2]^{2-}$
pdt	1,3-propanedithiolate, $[S_2C_3H_6]^{2-}$

xmbs	1,2-bis(4-mercapto-3,3-dimethyl-2-thisbutyl)benzene
Ph	phenyl, C_6H_5
tdt	3,4-toluenedithiolate, $[S_2(C_6H_3(CH_3)]^{2-}$

Acknowledgements

I would first like to thank my parents and siblings for their incredible support and encouragement throughout my graduate career. My parents have always encouraged me pursue what interests me, even if it results in me moving to the middle of a cornfield in Illinois, and this encouragement has led me to my current career path. I also must thank my family for putting up with countless stressful phone calls and helping me through the tough times. I would like to specifically thank my father for solving one of my crystal structures and answering numerous questions throughout my graduate research. None of my friends can say that their father co-authored a paper with them.

I am also incredibly grateful to my advisor Tom Rauchfuss, for his high level of dedication. Throughout my graduate studies, Tom pushed me to be a better chemist, always encouraging me to ask more questions and dig deeper into problems. Tom was always available when I needed him, and he truly cares about the success of each of his students. I have acquired many skills while working for Tom that will be invaluable in the future.

During the course of my graduate studies, I had the pleasure of working with many fantastic students and postdocs. I want to thank Matt Olsen and Bryan Barton for training me early on in my days in Tom's lab, as well as Chris Letko, James Camara, Dave Schilter, Todsapon Thananatthanachon, and Amanda Mack for always providing helpful advice when it came to a variety of areas. I'd also like to thank the current members of the Rauchfuss group. The many discussions that we've had concerning our projects have been invaluable. I've made great friendships with all of my co-workers, and I am certain that graduate school would have been pretty awful without them. I'd also like to thank the secretaries in the IMP office, Connie Knight, Beth Myler, Theresa Struss, and Karen Neuman, for making everything run smoothly within the department.

Lastly, I'd like to thank Jenny Steele for being an amazing friend and roommate. We both made it through all of the hard times together, and I really value the support that you have provided. I've also had a lot of fun living and going to school with you. I will miss the parties that we held at our house, even if they were to celebrate Mollycat's birthday. I will also thank Mollycat and cat Brody for always make life at our house interesting. After long days at lab, it was always nice to come home to the unconditional love of our pets.

Table of Contents

Chapter 1.

Overview of Hydrogen Production Technologies.

1.1 Global Energy Considerations and Renewable Energy.

In 2011, humans consumed more than 500 x 10^{18} J of energy, and with a growing population, this number is estimated to increase by at least 2% each year.[1,2] Additionally, 86% of the energy consumed came from fossil fuels; oil, natural gas, and coal, which are non-renewable resources and release high levels of CO_2 into the environment. Fossil fuel reserves are sufficient to sustain our energy use for several hundred years, but the larger concern is the effect of increasing CO_2 emissions on the environment.[3] CO_2 levels are estimated to increase to double preanthropogenic values, and it is unclear how this will affect the environment. Therefore, there is a strong drive to develop alternative, carbon free energy sources.[4,5]

One potential alternative fuel is dihydrogen, the sole combustion product of which is water. Extensive work has focused on the development of fuel cells that operate via the combustion of H_2.[6] However, in order for H_2 to be a viable energy source, efficient methods for H_2 production must be developed, as well as methods for transport and storage of hydrogen. The latter issues could be problematic, owing to the fairly low energy density of hydrogen, especially compared to gasoline.[7] Therefore, it would be most appealing for hydrogen to be produced at or close to the source at which it will be utilized. One potential solution is the use of photochemical cells that split water, forming H_2 and O_2, coupled to a fuel cell.[8] This scenario is particularly appealing because water is the sole byproduct of combustion of H_2.

The biggest challenge associated with the use of hydrogen as a fuel is the development of catalysts that perform the half reactions necessary for photochemical and fuel cell operation. These include water oxidation, oxygen reduction, hydrogen oxidation, and hydrogen production. Heterogeneous catalysts are more practical choices for incorporation into photochemical and fuel cells. However, it is difficult to study the mechanism and activity of heterogeneous catalysts. Therefore, studying homogenous systems may aid in the design of heterogeneous catalysts for H_2 production, by either modeling heterogeneous systems or providing a basis for new motifs for H_2 production. This chapter will describe current technologies for production of hydrogen, with the primary focus on the development of new homogeneous catalysts for hydrogen production.

1.2 Industrial Methods for Production of H_2.

The largest industrial source of hydrogen is the processing of coal and hydrocarbons.[7] In these cases, coke or natural gas is heated with steam in the presence of catalyst, via Scheme 1.1, producing CO and H_2. Additional H_2 may be produced via water-gas shift, by passing the gases over a cobalt or iron oxide catalyst.

Scheme 1.1 Gasification of coal and natural gas steam reforming

$$C(coke) + H_2O \xrightarrow{1100\text{-}1300\ ^oC} CO + H_2$$

$$CH_4 + H_2O \xrightarrow{700\text{-}925\ ^oC} CO + 3H_2$$

Yields of hydrogen via these methods are typically lower than the theoretical values, due to the necessity for using hydrocarbon based energy sources to drive the endothermic production of H_2.[9] Steam reforming is currently the cheapest and most common method used for H_2 production. Other processes include the partial oxidation of hydrocarbons and thermal decomposition of methane. Additionally, hydrogen is recovered from a variety of petroleum refining operations. Major issues associated with these methods for H_2 production include the co-formation of CO_2 in some cases, as well as the necessity of fossil fuels to drive these processes.[7]

An alternative method for hydrogen production is electrolysis of water (Scheme 1.2). The presence of electrolytes, MOH, NaCl, HCl, can result in unwanted side products. Additionally, electrolysis has been improved by addition of catalysts at either electrode, but these catalysts may not be stable to the high temperatures and strong alkali solutions involved. In order to avoid these issues, traditional electrolytes have been replaced with proton conducting exchange membranes.[9] Additionally, the use of solid oxide electrolysis cells (SOEC) has enabled H_2 production by high temperature steam electrolysis, which occurs at very high efficiency (comparable to H_2 production by fossil fuels).[10]

Scheme 1.2 Reactions involved in electrolysis of water.

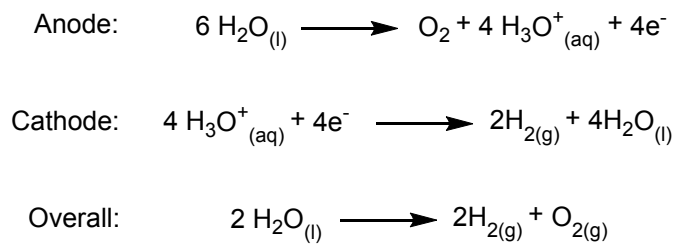

Hydrogen is also a byproduct from a number of industrial syntheses, including electrochemical synthesis of NaOH, chlorine, and chloroalkali compounds, as well as organic syntheses. Lastly, hydrogen forms from the decomposition of ammonia, methanol, and hydrogen sulfide. Liquid ammonia is a somewhat promising medium for the storage and distribution of hydrogen, as it contains ~50% more hydrogen per volume than liquid hydrogen. [9]

1.3 Heterogeneous Catalysts for Proton Reduction.

The best heterogeneous catalysts for proton reduction are precious metal based catalysts, most commonly consisting of Pt black or Pt nanoparticles, but these suffer due to high costs and low abundance.[11,12] The mechanism of proton reduction catalysis at metal surfaces involves initial transfer of an electron from the metal surface to the proton, coupled with transfer of the proton to the surface, forming H_{ads} (Scheme 1.3, step 1). The second, H_2 forming step can either involve combination of two surface adsorbed H atoms (Scheme 1.3, step 2a) or coupling of protonation of H_{ads} with a second electron transfer from the metal (Scheme 1.3, step 2b). The pathway for H_2 formation is primarily determined by the strength of the M-H_{ads} bond.[6]

Scheme 1.3 Mechanism of proton reduction catalysis at a metal surface.

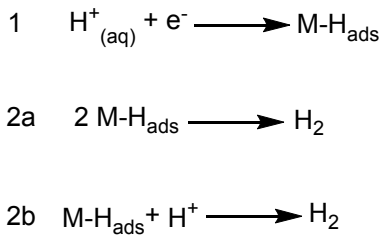

Some research has focused on the use of mixed metal alloys as heterogeneous proton reduction catalysts. For example, Ni_3Ti was found to be a better catalyst than either of the

metals alone. The methodology behind this specific combination of metals was that Ni adsorbs H atoms fairly poorly, but Ti adsorbs them fairly well. Other metal alloys that have been studied include Mo-Ni, Mo-Co, Mo-Pt, Ni-Zr, and Mo-S.[6] When MoS_2 or MoS_3 is adsorbed on a graphite electrode, forming an amorphous MoS_2 film, that is an active catalyst for proton reduction.[13,14] Further studies have shown that the rate determining step in the process is desorption of H_2[15].

A final area of research associated with heterogeneous catalysts for proton reduction is the addition of heteropolyacids to metal surfaces, leading to an interaction that changes the metal d-band position, thus modulating the strength of the M-H_{ads} bond.[6] The best example is a Co electrode electrodeposited with MoO_4^{2-}, which operates at high current densities and low overpotentials, on par with precious metal catalysts.[16] However, the reported heteropolyacid modified metal surfaces only show high efficiencies under alkali conditions, and so under acidic conditions, precious metal catalysts are better catalysts.[6]

1.4 Methods for the Evaluation of Homogeneous Proton Reduction Catalysts.

The activity of an electrocatalyst is typically evaluated based on the following criteria: turnover frequency, overpotential, turnover number, and Faradaic efficiency. Comparison of these properties for different catalysts is complicated by the fact that conditions under which studies are conducted vary widely; different solvents, electrolytes, working and reference electrodes, and acids are employed. Therefore, these differences must be taken into account when comparing the activities of synthetic catalysts.

The activities of electrocatalysts are typically measured by cyclic voltammetry and controlled potential electrolysis experiments. In both cases, an increase in current in the presence of acid is indicative of turnover. The activities of electrocatalysts are therefore determined based on the extent to which current increases in the presence of acid, as well as the potential at which catalytic turnover occurs.

1.4.1 Turnover Frequency

Two methods for evaluating turnover frequency have been reported. In either case, the cyclic voltammograms (CV's) are recorded in the absence and presence of acid, and the reductive current in the absence of acid ($i_{p,}$ Equation 1.1a) and the presence of acid (i_c, Equation 1.1b) are compared.[17] The first measure of activity is the catalytic efficieny (C.E.), and this is a

measure of the extent to which the current increases in the presence of acid. The catalytic efficiency is calculated based on Equation 1.2.

$$i_p = 0.4463FA[cat]\sqrt{\frac{F\nu D}{RT}} \qquad (eq\ 1.1\ a)$$

$$R = ideal\ gas\ constant\ (J/molK)$$

$$F = Faraday\ constant\ (C/mol)$$

$$[cat] = catalyst\ concentration\ (M)$$

$$\nu = scan\ rate\ (V/s)$$

$$D = diffusion\ constant\ of\ catalyst\ (cm^2/s)$$

$$A = area\ of\ electrode\ (cm^2)$$

$$i_c = nFA[cat]\sqrt{Dk[H^+]} \qquad (eq\ 1.1\ b)$$

$$n = \#\ of\ electrons$$

$$[cat] = catalyst\ concentration\ (M)$$

$$[H^+] = concentration\ of\ acid\ (M)$$

$$C.E. = \frac{{}^{i_c}\!/_{i_p}}{{}^{[H^+]}\!/_{[cat]}} \qquad (eq\ 1.2)$$

In many cases, the value of i_c/i_p increases linearly with increasing amounts of acid, and the rate of catalysis is second order in acid. However, at very high acid concentrations, the value of i_c/i_p becomes independent of acid concentration, in other words, it no longer increases with increasing amounts of acid, and the rate of catalysis is zero order in acid. In this regime, the rate of catalysis depends solely on the rate at which H_2 can be released by the catalyst. A value for k_{H2}, or turnover frequency, can be evaluated based on Equation 1.3.[18]

$$i_c/i_p = \frac{n}{0.4463}\sqrt{\frac{RTk_{H2}[H^+]}{Fv}} \qquad (eq\ 1.3)$$

A generalized mechanism for proton reduction by metal catalysts is shown in Scheme 1.4. The order in which the protonation and electron transfer steps occur vary between systems, and it is assumed that the electron transfer steps are fast, and therefore, the rate of electron transfer is negligible. Assuming that a steady state scenario applies, that is, the rate of formation of MH_2 is equal to the rate of consumption of MH_2 (Equation 1.4), the rate can be expressed as shown in Equation 1.5. Based on the definitions of i_c and i_p given in Equation 1.1, i_c/i_p is expressed in terms of the rate equation (Equation 1.6), which simplifies to Equation 1.3, when the concentration of acid is very high.[19]

Scheme 1.4 Generalized mechanism of proton reduction by metal complexes.

$$M + 2H^+ \underset{k_{-prot}}{\overset{k_{prot}}{\rightleftharpoons}} MH_2^{2+}$$

$$MH_2^{2+} \underset{-\ 2\ e^-}{\overset{+\ 2\ e^-}{\rightleftharpoons}} MH_2$$

$$MH_2 \xrightarrow{k_{H2}} M + H_2$$

$$k_{prot}[M][H^+] = k_{-prot}[MH_2] + k_{H_2}[MH_2] \qquad (eq\ 1.4)$$

$$Rate = k_{H_2}[MH_2] = \frac{k_{H_2}[H^+]^2}{\frac{k_{-prot} + k_{H_2}}{k_{prot}} + [H^+]^2}[M] = k_{obs}[M] \qquad (eq\ 1.5)$$

$$i_c/i_p = \frac{n}{0.4463}\sqrt{\frac{k_{obs}RT}{Fv}} = \frac{n}{0.4463}\sqrt{\frac{RT}{Fv}\left(\frac{k_{H_2}[H^+]^2}{\frac{k_{-prot}+k_{H_2}}{k_{prot}}+[H^+]^2}\right)} \qquad (eq\ 1.6)$$

In evaluating the activity of a proton reduction catalyst, direct reduction of protons at the working electrode must also be taken into account.[20] Failing to do so may lead to an overestimation of the turnover frequency. Table 1.1 indicates the potentials at which direct reduction at the working electrode becomes significant for acetic acid at various working electrodes.[20] When acids that are stronger than acetic acid are used, direct reduction by the working electrode will occur at milder potentials. In the studies that are included in later chapters, control experiments were performed in which acid was added in the absence of catalyst, and CV's were collected. The current due to direct reduction at the working electrode was then subtracted from the current measured in the presence of catalyst.

Table 1.1. Potentials for direct reduction of acetic acid at various working electrodes.

Electrode	Potential for Reduction of Acetic Acid (V vs $Fc^{+/0}$)
Pt	-1.6
Glassy Carbon	-2.2
Gold Amalgam	-2.5
Hanging Hg Drop	-2.7

1.4.2 Overpotential

Another measure of the catalyst activity is overpotential, which is defined as the difference between the standard reduction potential of the acid used ($E°_{HA/H2}$) and the potential at which the catalyst reduces the same acid (E_{cat}).[18] Overpotential arises due to the fact that on electrode materials other than Pt, electrochemical reactions tend to be kinetically limited. Overpotential may be viewed as an activation barrier. In order for proton reduction to be catalyzed, higher electron energies than predicted by thermodynamics are required, and so the process occurs at more negative potentials.

In the literature, a number of different methods are used for the determination of E_{cat} and $E°_{HA/H2}$. There are three different ways in which the value of E_{cat} is defined: the onset potential, E_{on}, the potential at half height, $E_{p/2}$, and the potential at maxium current, E_p. Using E_{on} tends to lead to an underestimation of the overpotential, whereas using E_p leads to an overestimation of the overpotential. Using $E_{p/2}$ gives a value that is intermediate between these two values, and therefore, is most commonly used.[18] For experiments that utilize a Rotating Disk Electrode (RDE), the value of $E_{p/2}$ can be read directly from the CV, as the potential at which the current is half of the maximum catalytic current. For experiments that utilize a stationary electrode, the value of $E_{p/2}$ is calculated by subtracting 15 mV from the maximum of the first derivative of the forward scan in the CV. Artero and coworkers have shown that the most accurate value of $E_{p/2}$ is determined in the acid dependent regime.[21]

The value of $E°_{HA/H2}$ is unique to the acid used, as well as the solvent in which the catalysis is performed. The value of $E°_{HA/H2}$ as defined in Equation 1.7 applies to acids that do not exhibit homogonjugation. However, in many solvents, acids and their conjugate bases form stable adducts, which is defined as homoconjugation and is quantified by the association constant K_c (Equation 1.8). Homoconjugation must be taken into account in cases where κ is greater than 1. Formation of the homoconjugate, AHA^-, shifts the acid-base equilibrium in favor of proton release, which effectively increases the acidity. The value of $E°_{HA/H2}$ for the homoconjugate is less negative than for the acid, HA. Therefore, if homoconjugation is not taken into account, the overpotential may be underestimated. Equation 1.9 takes into account the effect of homoconjugation.

$$E^o_{HA/H_2} = E^o_{H^+/H_2} - \frac{2.303RT}{F} - pK_a + \varepsilon_D + \frac{RT}{2F}\ln\frac{C_0}{C^o_{H_2}} \qquad (eq\ 1.7)$$

$$E^o_{H^+/H_2} = standard\ potential\ for\ reduction\ of\ a\ proton\ in\ solvent\ considered\ (V)$$

$$\varepsilon_D = measure\ of\ diffusion\ rate\ of\ products\ vs\ reactants\ (40 \pm 5\ mV)$$

$$C_0 = acid\ concentration\ (mM)$$

$$C^o_{H_2} = concentration\ of\ dissolved\ H_2 (mM)$$

$$AH + A^- \leftrightarrow AHA^- \; K_c \qquad (eq\ 1.8)$$

$$\kappa = C_0 K_c$$

$$E^o_{HA/H_2} = E^o_{H^+/H_2} - \frac{2.303RT}{F} - pK_a + \varepsilon_D + \frac{RT}{2F}\ln(2{K_C}^2 C_0 C^o_{H_2}) \qquad (eq\ 1.9)$$

1.4.3 Faradaic Efficiency and Turnover Number

Both Faradaic efficiency and turnover number are determined based on controlled potential electrolysis experiments. The Faradaic efficiency is a measure of how many electrons are effectively used in the conversion of H^+ to H_2. This value is calculated by measuring the amount of H_2 formed, typically by gas chromatographic headspace analysis, and comparing it to the total amount of charge passed during the formation of H_2. The turnover number is a measure of the amount of H_2 formed per mole of catalyst. Additionally, a turnover frequency can be determined by controlled potential electrolysis methods, but it depends on the constant of the electrolysis cell and not the catalytic steps.[18]

1.5 H_2 Processing in Nature: Hydrogenase Enyzmes

In nature, hydrogen is primarily produced and oxidized by the hydrogenase (H_2ase) enzymes.[22] Two genetically unrelated H_2ases have been identified; they contain Ni and/or Fe thiolate centers, the latter bound to CN^- and CO, and are generally rich in Fe-S clusters, emphasizing the central role of electron-transfer (Figure 1.1).[22,23] In the case of [FeFe]-H_2ases, one 4Fe-4S cluster is directly tethered to the diiron active site, the 6Fe ensemble being called the H-cluster. The [FeFe]-H_2ases also feature an amino-dithiolate cofactor that bridges the two organoiron centers.[24]

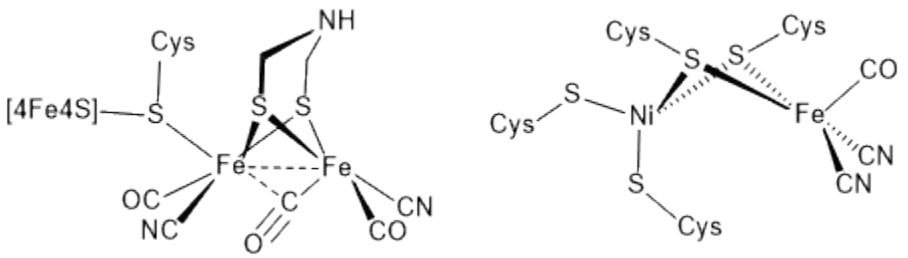

Figure 1.1. Structures of the active sites of hydrogenase enzymes.

The function of hydrogenase enzymes (H_2 uptake vs production) is determined by their location in the cell. When the hydrogenase enzyme is located in the periplasm of the cell, it functions as an H_2 uptake enzyme. Protons and electrons formed in this process cross the membrane into the cytoplasm, where they are used in the formation of ATP and reductants. When hydrogenase enzymes are found in the cytoplasm, they function as H_2 production catalysts. In this case, reduction of protons to H_2 rids the cell of excess reducing equivalents that accumulate during fermentation.[25] The [FeFe]-H_2ases are more active than [NiFe]-H_2ases, and they more commonly function as catalysts for H_2 production (Table 1.2).[26] Additionally, both enzymes operate at overpotentials of ~ 80 mV, which is comparable with Pt catalysts.[27,28] Progress has been made in adsorbing hydrogenase enzymes on electrodes for hydrogen processing, but major drawbacks are associated with the low density of metal sites compared to the size of the protein and general instability under desireable conditions.[29,30]

Table 1.2 Rates of H_2 oxidation and production by hydrogenase enzymes.

Reaction	FeFe	NiFe
H_2 Oxidation	28000	700
H_2 Production	6000-9000	700

Rates quoted in moles of H_2 per mole of enzyme per second measured at 30 °C.

1.6 Homogeneous Transition Metal Proton Reduction Catalysts

There is a large body of literature on transition metal catalysts for proton reduction, and two recent reviews cover this work.[12,18] A subset of this research will be reviewed herein, primarily to compare the mechanisms by which different classes of catalysts operate, as well as their catalytic properties. In many cases, all criteria (overpotential, Faradaic efficiency, TON, and turnover frequency) were not analyzed. Additionally, the methods for evaluating overpotential differed substaintially. Overpotential values were recalculated, such that $E_{cat} = E_{p/2}$ and $E°_{HA/H2}$ values were calculated via the method described by Artero, taking homoconjugation into account when necessary.[21]

The mechanism by which catalysts operate is strongly dependent on a number of factors, including the pK_a and reduction potential of the metal complex, L_nM, as well as the pK_a of the

acid used for catalysis. Catalysis may occur via a monometallic mechanism, as depicted in Scheme 1.5.[31] In this mechanism, a series of two electron and two proton transfers occur to form the species L_nMH_2. When the ligand set is very electron donating or HA is a very strong acid, L_nM will be more prone to protonation and less prone to reduction. Additionally, upon protonation of L_nM, the species that forms, $[L_nMH]^+$, will be reduced at a more positive potential relative to L_nM. Conversely, when the ligand set is not electron donating, L_nM may not be protonatable, but upon reduction, the pK_a of the analogous hydride will shift by ~ 20 units. Therefore, reduction of a species that cannot be protonated will likely enable its protonation. The order of later steps is determined by the same criteria.

Scheme 1.5. Possible pathways for proton reduction catalysis.

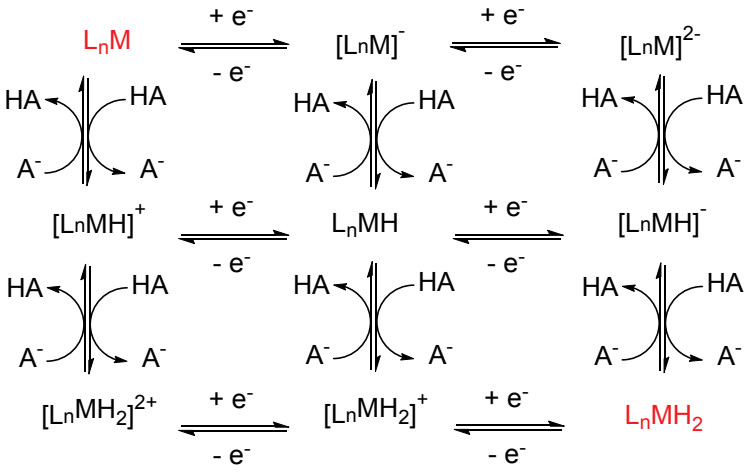

The final species in the catalytic cycle, L_nMH_2, releases H_2 to reform L_nM. The exact nature of L_nMH_2 depends on the system; it can either be a dihydrogen complex or a dihydride. In general, the metal hydride bond is the kinetic site of protonation, so dihydrogen complexes tend to form.[32]

Catalysis may also occur via a bimetallic pathway, as depicted by Scheme 1.6.[33] In this case, a proton and electron transfer occur to form a metal hydride species. Again the order of protonation vs reduction depends on the factors described above. Two L_nMH species couple with each other to form H_2 and L_nM. Typically, the heterometallic mechanism is favored in cases where the complex is not particularly bulky and the concentration of acid is low. Examples of catalysts that operate via the different mechanisms are presented herein.

Scheme 1.6. Possible bimetallic pathways for proton reduction catalysis.

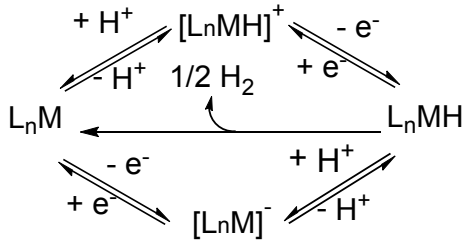

1.6.1 Functional Models of the Active Site of [FeFe]-hydrogenase.

A substantial amount of work has focused on the synthesis of both structural and functional models of [FeFe]-hydrogenase.[34] The first diiron model that functioned as a proton reduction catalyst, $[Fe_2(pdt)(CO)_4(CN)(PMe_3)]^-$, **1**, (pdt= 1,3-propanedithiolate) was reported in 2001 (Scheme 1.7).[35] The complex undergoes protonation with strong acids to form a stable bridging hydride complex, and in the presence of excess acid, undergoes a second protonation at the CN^- ligand. When more than two equivalents of acid are present, it reduces protons at a potential that corresponds to the reduction potential of the doubly protonated species, with a TON of 6 in 15 minutes. The complex operates at fairly high overpotentials (Table 1.3) but is significant in that it is the first example of a functional diiron model complex. The analogous complex, $Fe_2(pdt)(CO)_4(PMe_3)_2$, **2**, in which a CN^- ligand is substituted with PMe_3 also catalyzes proton reduction, but it is significantly slower, to the extent that direct reduction of protons at the glassy carbon electrode is the prominent feature in the CV. The proposed mechanisms for the two complexes are shown in Scheme 1.8. The difference in rates for the two catalysts is attributed to the presence of an internal basic site in **1**; the coupling of the bridging hydride with a proton is facilitated by the CN^- ligand. The lack of an internal base in **2** requires that the bridging hydride be protonated by acid in solution, which may require a structural rearrangement.[36]

Scheme 1.7 Diiron hydrogenase model complexes.

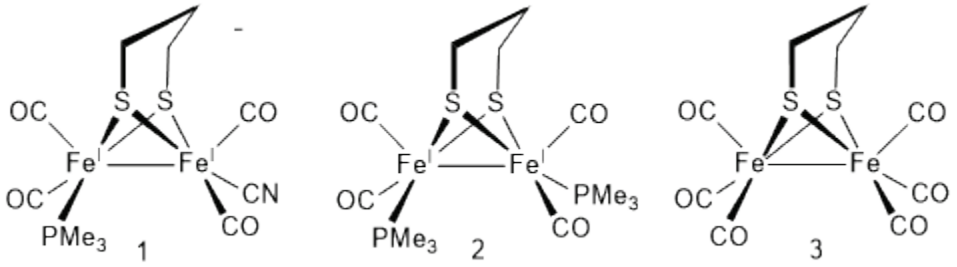

Scheme 1.8. Mechanism of proton reduction catalysis by 1 (a, left) and 2 (b, right) with strong acid.

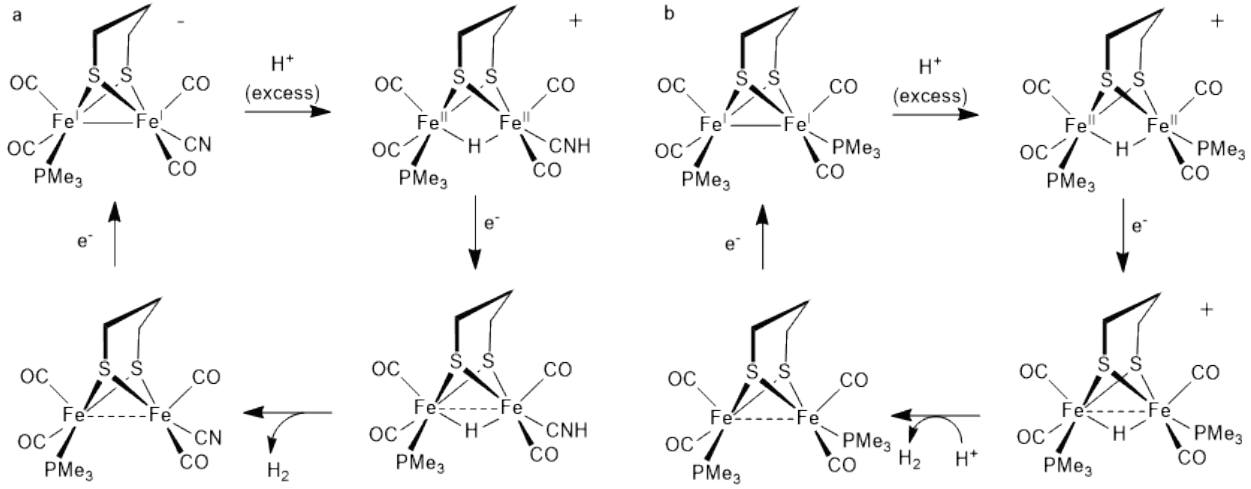

Table 1.3 Electrocatalytic properties of diiron model complexes.

Complex	E_{cat} (V vs $Fc^{+/0}$)	Acid (pK_a) $E°_{HA/H2}$ (V vs $Fc^{+/0}$)	Overpotential (V)
$[Fe_2(pdt)(CO)_4(CN)(PMe_3)]^-$ **1**	-1.45	HOTs (8.3) -0.48	0.97
$Fe_2(pdt)(CO)_4(PMe_3)_2$ **2**	-1.42	HOTs (8.3) -0.48	0.97
$Fe_2(pdt)(CO)_4(PMe_3)_2$ **2**	-2.1	HOAc (22.3) -1.25	0.85
$Fe_2(pdt)(CO)_6$ **3**	-2.15	HOAc (22.3) -1.25	0.90
$Fe_2(pdt)(CO)_6$ **3**	-1.43 (I) -1.65 (II)	HOTs (8.3) -0.48	0.95 1.17

The mechanism by which proton reduction catalysis occurs is highly dependent on the strength of the acid utilized. For example, when weak acid is added to **2**, catalysis occurs at

more negative potentials than those reported with HOTs.[37] Acetic acid is not a strong enough acid to protonate **2** to form a bridging hydride species. Therefore, the first step in the mechanism must involve reduction of the diiron species, which is then basic enough to be protonated by weak acid (Scheme 1.9). Therefore, with weak acid, **2** catalyzes proton reduction at more negative potentials, via an ECCE mechanism, whereas, with strong acid, the reaction occurs via a CECE mechanism. It is relevant to note that despite the fact that in the presence of weak acid catalysis occurs at more negative potentials, the overpotential is actually lower than with stronger acid.

Scheme 1.9. Mechanism of proton reduction catalysis by 2 in the presence of weak acid.

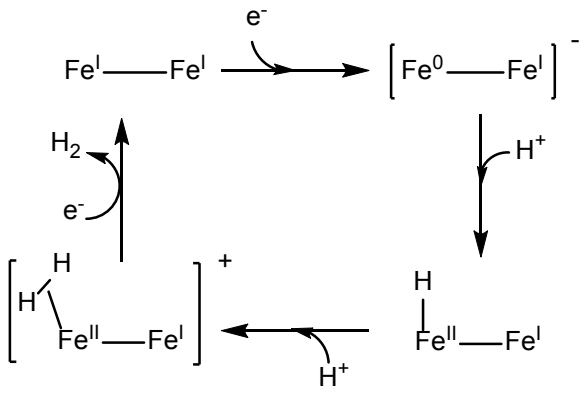

Extensive work has also focused on the characterization of the unsubstituted diiron hexacarbonyl species, such as $Fe_2(pdt)(CO)_6$, **3**. Early work by Darensbourg and co-workers found that in the presence of weak acid (acetic acid), **3** catalyzes the production of H_2. The proposed mechanism is a EECC route (Scheme 1.10). The hexacarbonyl species is not electron rich enough to be protonated by acetic acid, and it must therefore be reduced by two electrons, prior to protonation. Again, the mechanism of proton reduction is strongly dependent on the strength of the acid employed. When stronger acid, HOTs (*p*-toluenesulfonic acid, $CH_3C_6H_4SO_3H$), is utilized, catalysis by **3** occurs at more mild potentials than exhibited with acetic acid.[38] In this case, a single reduction is required prior to protonation by the stronger acid. In this case, two catalytic waves appear, and they are attributed to the two processes depicted in Scheme 1.11. Again, although catalysis occurs at more mild potentials with HOTs than with acetic acid, the overpotential is lower for the weaker acid.

Scheme 1.10. Mechanism of proton reduction catalysis by 3 in the presence of weak acid.

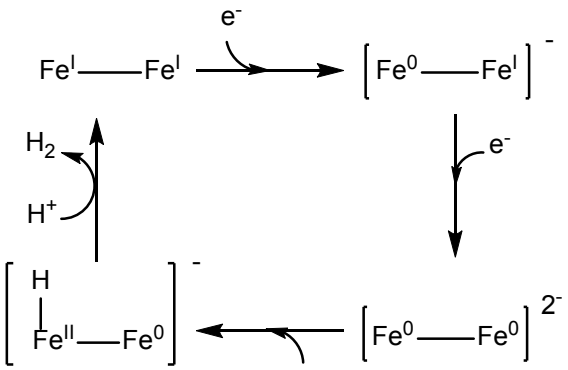

Scheme 1.11. Mechanism of proton reduction catalysis by 3 in the presence of strong acid.

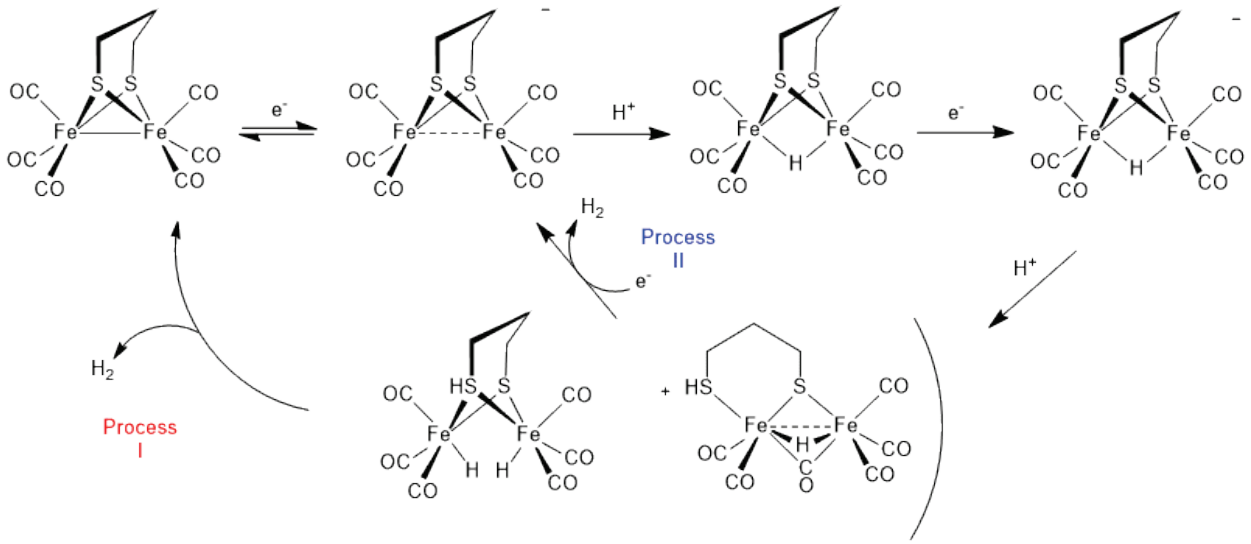

The examples above illustrate the different pathways by which diiron complexes undergo proton reduction catalysis. It is important to note that this is a small subset of the diiron catalysts that have been reported. In general, the complexes reported in the literature are not particularly biomimetic. In many cases, the complexes must be reduced prior to protonation, which is the reverse of the order proposed for the enzyme (the mechanism for the enzyme will be discussed on more detail in Chapter 2). Additionally, all examples of diiron hydrides that catalyze proton reduction do so via bridging hydride species, whereas, the enzyme likely operates via diiron species in which the hydride is terminally bound.[34,39]

1.6.2 Functional Models of the Active Site of [NiFe]-hydrogenase.

In comparison to models for [FeFe]-hydrogenase, there are significantly fewer models for [NiFe]-hydrogenase.[34] Early work focused on the synthesis of complexes that were very structurally similar the active site; however, the majority of these models do not exhibit reactivity that mimic the enzyme. In 2004, Sellman reported that **4**, a Ni_2Fe complex, reacts with $HBF_4{\cdot}Et_2O$ to form H_2.[40] Electrocatalytic studies later found that this complex operates at very low rates (<0.1 TON in 1 h).[41] Another early example of a functional model, a trinuclear $NiFe_2$ complex, **5** (Scheme 1.12), was reported by Schröder and co-workers to be an electrocatalyst for H_2 production (Table 1.4).[42] However, the catalyst is not particularly stable, decomposing after ~1 hour of electrolysis.

Scheme 1.12. Trimetallic [NiFe]-hydrogenase models.

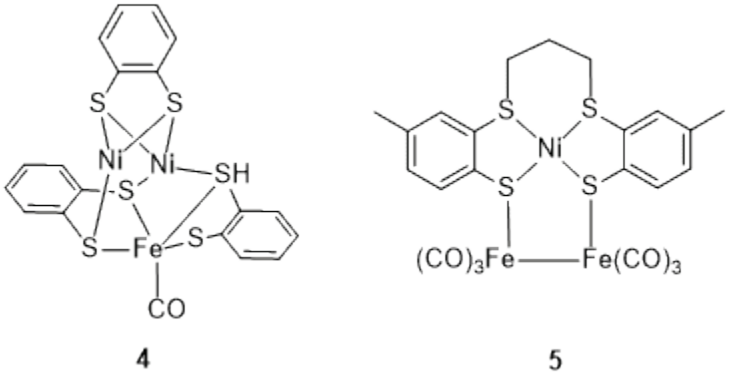

4 **5**

The most significant work on functional NiFe models has come from the group of Fontecave and Areto. Early studies focused on the replacement of the Fe center found in the enzyme with a Ru center, justifying this replacement with the fact that the Fe(II) center in the enzyme is redox inactive.[43] NiRu complexes, **6-11** (Scheme 1.13), containing the N_2S_2 ligand, emi (*N*,*N*-ethylenebis(2-mercaptoisobutyramide), and S_4 ligand, xmbs (1,2-bis(4-mercapto-3,3-dimethyl-2-thisbutyl)benzene) were synthesized and found to catalyze proton reduction at moderate rates and fairly high overpotentials (0.6 -0.77 V) (Table 1.4).[44] Replacement of cymene(Cl) or the $(CO)_2Cl_2$ units in **8** and **9** with Cp (**10a**,**b**) or Cp* (**11a**,**b**), resulted in a slight increase in rate and a decrease in overpotential. The Cp* complexes were found to operate at the highest rates, and the authors attribute this to the bulkiness of the ligand, which protects the metal centers.[45,46] The synthesis of a NiFe complex analogous to **10b** was later reported, and **12**

was also shown to reduce protons at overpotentials similar to the previously reported NiRu catalysts, but it proved to be significantly less stable.[47] The related NiMn complex (**13**) has also been reported, and exhibits similar activity, but operates at a higher overpotential.[48]

Scheme 1.13. Bimetallic [NiFe]-hydrogenase models.

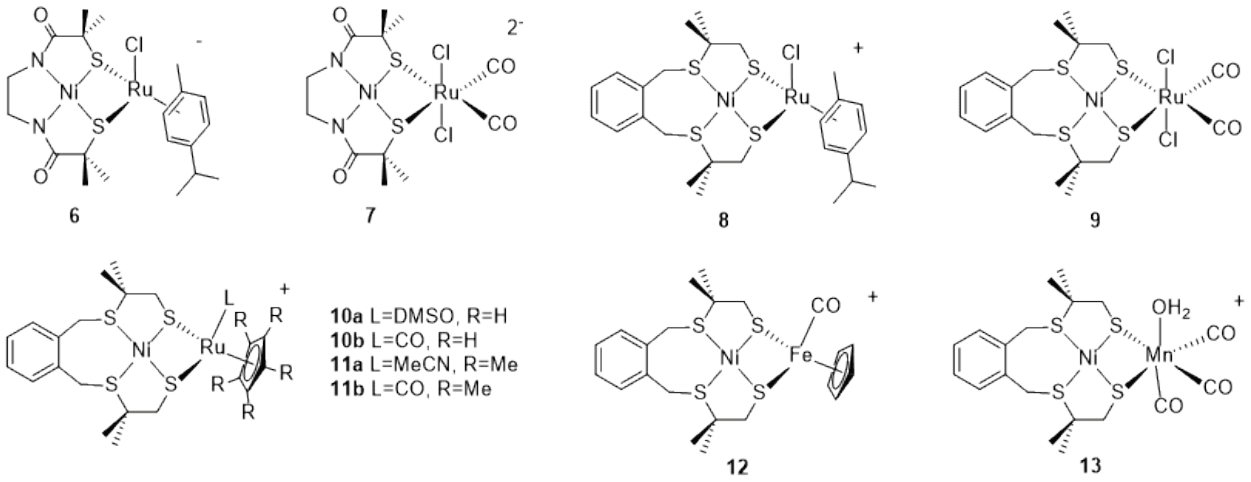

In all complexes, **4-13**, the mechanism of proton reduction is proposed to involve initial reduction of one of the metal centers, followed by protonation of the reduced species. The authors invoke hydride containing intermediates, but hydride containing forms of these NiRu, NiFe, and NiMn complexes have not been isolated.[43]

In 2009, our group reported the synthesis of the first hydride containing NiFe model. **14a**.[49] Complexes **14a-c** (Scheme 1.14), were found to catalyze the reduction of protons. Modifications of the ligands at Fe, replacement of CO with a phosphine or phosphite ligand, were found to give a slight increase in rate but also an increase in overpotentials. Further studies on hydride containing NiFe models will be discussed in Chapter 4.

Table 1.4 Electrocatalytic properties of NiFe models.

Complex	E_{cat} (V vs $Fc^{+/0}$)	Overpotential (V)	TON[c] (mol H_2/mol cat) (Time)	TOF (mol H_2/ molcath)
$[Ni(S_4)Fe_2(CO)_6]$ **5**	-1.28	0.6	6 (1 h)	6
$[Ni(emi)Ru(cym)Cl]^-$ **6** [a]	-1.97	0.77	26.5 (4.5 h)	5.8
$[Ni(emi)Ru(CO)_2(Cl)_2]^{2-}$ **7** [a]	-1.97	0.77	6.8 (4.5 h)	1.5
$[Ni(xmbs)Ru(cym)Cl]^+$ **8** [a]	-1.97	0.77	28.9 (4.5 h)	6.5
$[Ni(xmbs)Ru(CO)_2(Cl)_2]$ **9**[a]	-1.92	0.72	12.4 (4.5 h)	2.75
$[Ni(xmbs)Ru(DMSO)Cp]^+$ **10a** [a]	-1.82	0.62	13 (3 h)	4.3
$[Ni(xmbs)Ru(CO)Cp]^+$ **10b** [a]	-1.92	0.72	15.8 (3 h)	5.25
$[Ni(xmbs)Ru(MeCN)Cp^*]^+$ **11a** [a]	-1.87	0.67	27.8 (3 h)	9.25
$[Ni(xmbs)Ru(CO)Cp^*]^+$ **12b** [a]	-1.97	0.77	6.6 (3 h)	2.2
$[Ni(xmbs)Fe(CO)Cp]^+$ **12** [b]	-1.70	0.75	20 (4 h)	5
$[Ni(xmbs)Mn(CO)_3(H_2O)]^+$ **13** [b]	-1.81	0.86	15.8 (4 h)	3.95

[a] Acid= Et_3NH^+, pK_a^{DMF}= 18.7, $E°_{HA/H2}$= -1.2 V; [b] Acid= CF_3COOH, pK_a^{DMF}= 12.7, $E°_{HA/H2}$= -0.95 V; [c] All catalysts operate at Faradaic efficiencies between 90-100%, except for **7**, which operates at 74%

Scheme 1.14 Structure of hydride containing NiFe models.

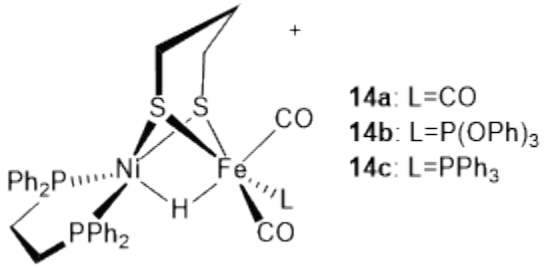

Table 1.5. Electrocatalytic properties of NiFe hydride complexes.

Complex	$E_{p/2}$ (V vs $Fc^{+/0}$)	Overpotential (V)
$[(dppe)Ni(pdt)(\mu\text{-}H)Fe(CO)_3]^+$ **14a**	-1.20	0.5
$[(dppe)Ni(pdt)(\mu\text{-}H)Fe(CO)_2(P(OPh_3)]^+$ **14b**	-1.32	0.63
$[(dppe)Ni(pdt)(\mu\text{-}H)Fe(CO)_2(PPh_3)]^+$ **14c**	-1.30	0.62

1.6.3 Nickel Tetraphosphine Catalysts

DuBois and co-workers have extensively studied a series of Ni tetraphosphine complexes for H_2 oxidation and proton reduction.[50,51] In designing these catalysts, the group sought to mimic certain aspects of the active sites of hydrogenases; specifically, a pendant basic site adjacent to an open coordination site. In order for complexes with such functionality to acts as H_2 processing catalysts, it is necessary for the hydride acceptor ability of the metal center to closely match the proton acceptor ability of the basic site. The overall free energy of the formation of H_2 via a coupling of a metal hydride and a proton is calculated via equations 1.10-1.13. For metal complexes with reversible reductions, the hydride acceptor ability ($\Delta G°_{H-}$) can be calculated, and the pK_a values of many acids (such as protonated amines) are known. Therefore, the appropriate hydride acceptor ability of the metal center and proton acceptor ability of the base can be calculated.[51]

	ΔG^o (kcal/mol)	
$H^+ + H^- \longrightarrow H_2$	-76	(1.10)
$HML_n^+ \longrightarrow ML_n^{2+} + H^-$	ΔG^o_{H-}	(1.11)
$HA \longrightarrow H^+ + A^-$	1.37pK_a	(1.12)
$HML_n^+ + HA \longrightarrow ML_n^{2+} + H_2$	ΔG^o_{H-} -0.76 + 1.37pK_a	(1.13)

Ni tetraphosphine complexes were targeted due to the high hydride acceptor ability of the the metal center in such species. Early studies found that both complexes **15** and **16** are catalytically active for H_2 oxidation but at very slow rates (Scheme 1.13). However, **16** operates

at an overpotential that is 0.6-0.7 V lower than that for **15**. The difference is attributed to the presence of a pendant amine in **16**, which can aid in proton transfer to the metal center. Space filling diagrams of Ni tetraphosphines show that access to the metal center is highly restricted due to steric bulk on the ligand, so in the absence of a pendant base, significant structural rearrangements are necessary for protonation at the metal, leading to a large energy barrier for protonation.[50]

The slow rate for H_2 oxidation by **16** is attributed to the conformation of the PNP ligand relative to the metal center. The more energetically favorable conformation is the chair conformation, but the less favorable boat conformation positions the amine above the metal center. Therefore, the PNP ligand was adapted to include two amines, which forces one of the M-P-CH_2-N-CH_2-P rings into a chair conformation, as in **17a** (Scheme 1.15). In the presence of [(DMF)H]OTf (pK_a^{MeCN}=6.1), **17a** was found to catalyze reduction of protons at a rate of 590 s^{-1} and overpotential of 0.35 V. The effect of the electron donating properties of the P_2N_2 ligand were probed by substituting the para position of the amine phenyl group (**17b-e**). When more electron withdrawing groups are utilized, the rate of catalysis increases, and the overpotential decreases (Table 1.6).[50] Based on controlled potential electrolysis experiments, **17e** operates at a Faradaic efficiency of 94 ± 5 % and a TON of 30.

Scheme 1.15. Ni tetraphopshine catalysts.

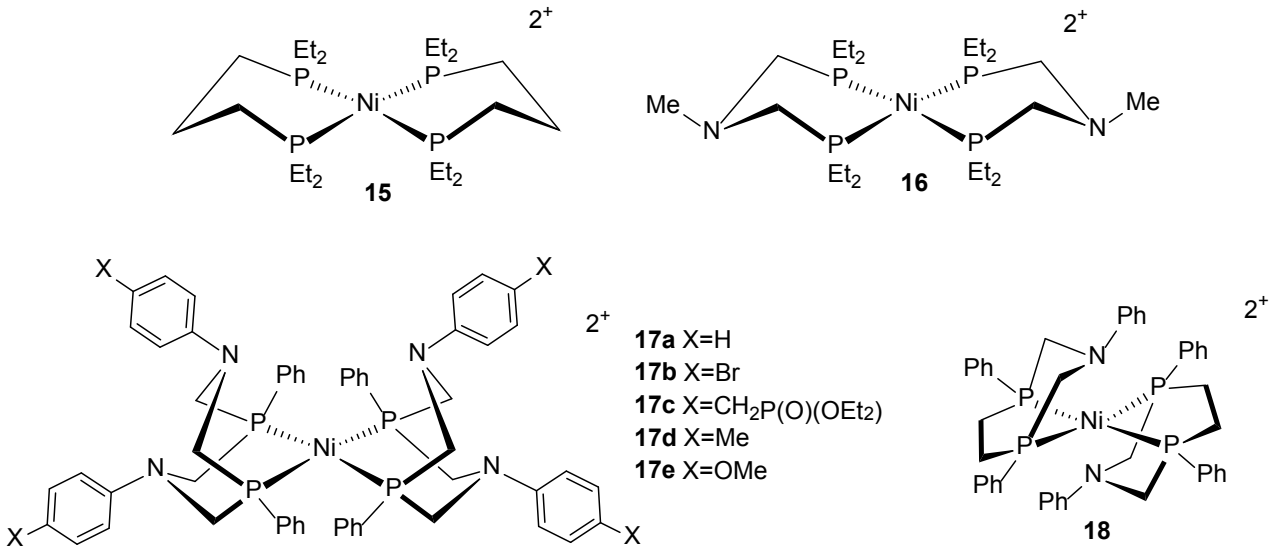

Table 1.6 Electrocatalytic properties of Ni diphosphine catalysts, 3-4, with [(DMF)H]OTf as acid source.

Catalyst	$E_{p/2}$ (V vs $Fc^{+/0}$)	Overpotential[a] (V)	k_{obs} (s^{-1}) (MeCN)	k_{obs} (s^{-1}) (MeCN/ H_2O)[b]
$[Ni(P^{Ph}_2N^{C6H5}_2)_2]^{2+}$, **17a**	-0.80	0.35	590	720
$[Ni(P^{Ph}_2N^{C6H4Br}_2)_2]^{2+}$, **17b**	-0.78	0.33	740	1040
$[Ni(P^{Ph}_2N^{C6H4X}_2)_2]^{2+}$, **17c**[c]	-0.82	0.37	500	1850
$[Ni(P^{Ph}_2N^{C6H4Me}_2)_2]^{2+}$, **17d**	-0.84	0.39	590	770
$[Ni(P^{Ph}_2N^{C6H4OMe}_2)_2]^{2+}$, **17e**	-0.81	0.36	310	480
$[Ni(P^{Ph}_2N)_2]^{2+}$, **18**	-1.13	0.68	3300	100,000

[a] Overpotentials were calculated based on pK_a^{MeCN}= 6.1[52], $E°_{HA/H2}$= -0.45[21]
[b] Water concentrations ranged from 0.02- 24 M
[c] X= $CH_2P(O)(OEt_2)$

A proposed mechanism for the process is shown in Scheme 1.16.[53] The mechanism involves a series of proton and electron transfers, which could be coupled to one another. The rate is independent of acid concentration, so the rate limiting step involves either coupling of a proton and hydride or release of H_2 from the complex (Scheme 1.16, D,E, or F). The rate is likely affected by the formation of inactive species, 5b and 5c, which form by protonation of an exo amine, rather than an endo amine, to form 5 (Scheme 1.17).[53]

In order to avoid formation of such inactive species as 5a and 5b, the disphosphine ligand was adapted to contain a single amine, which is forced into the chair conformation, thus avoiding the possibility of exo protonation.[17] Complex **18** was found to catalyze the reduction of protons at a rate of 3300 s^{-1} and an overpotential of 0.68 V. Bulk electrolysis gives a Faradaic efficiency of 95 ± 5 % and 11 turnovers. The ~6-fold increase in rate compared to **17** is attributed to the fact that inactive exo protonated species cannot form in this system. When water is added to both **17** and **18**, the rate increases, with the increase being most significant for **18**. The increase in rate is attributed to the formation of H_3O^+ (via protonation of water by $[(DMF)H]^+$ (DMF= dimethylformamide), which due to its small size can more easily access the endo amine.[17,53]

Scheme 1.16. Proposed mechanism of proton reduction by $[Ni(P_2N_2)_2]^{2+}$ catalysts. (Substituents on N and P omitted for clarity)

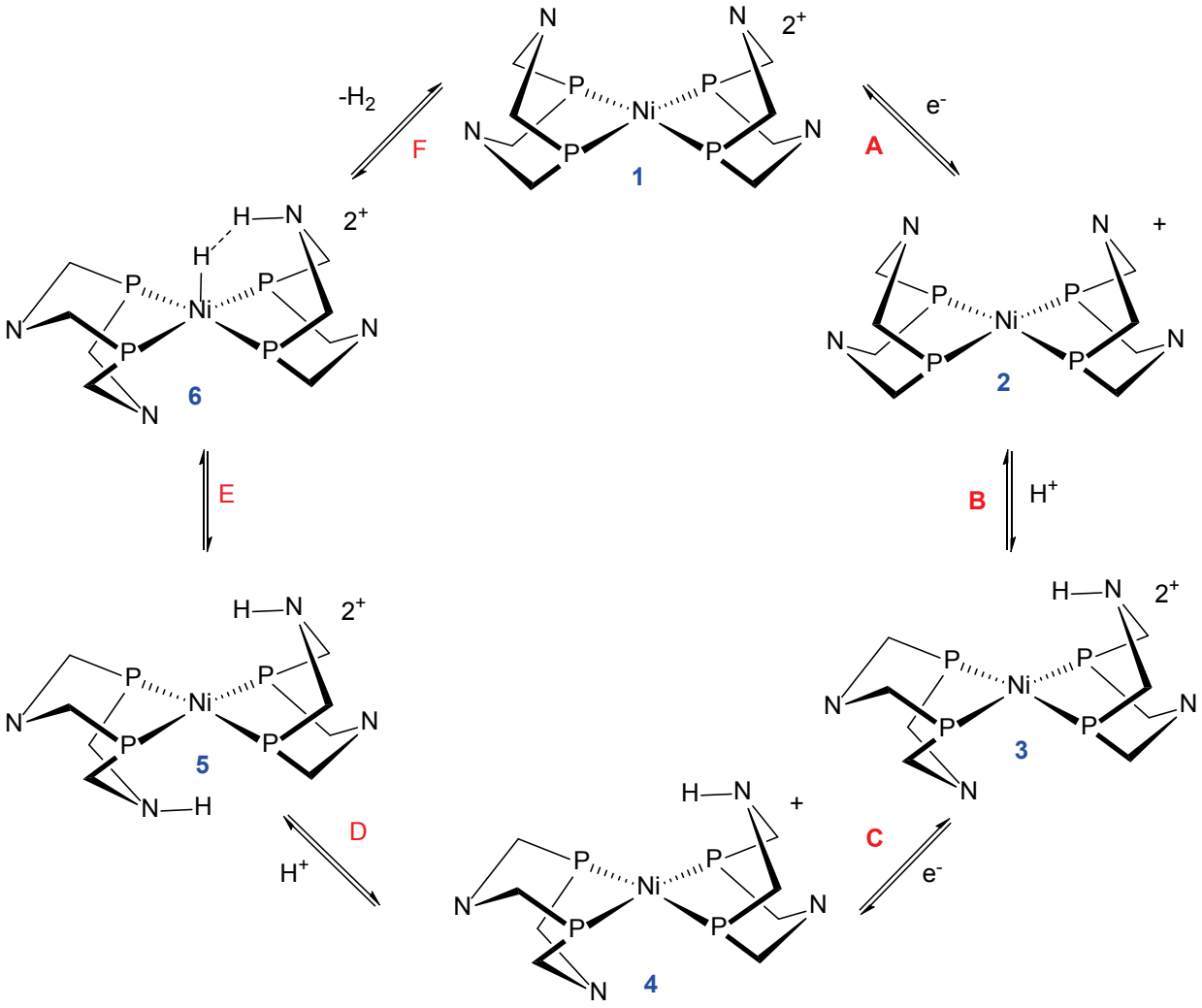

Scheme 1.17. Catalytically inactive exo-protonated forms of Ni catalysts.

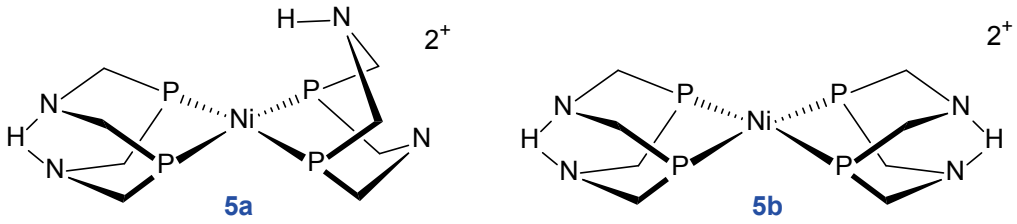

1.6.4 Cobaloxime Catalysts.

Cobaloxime complexes have proven to be efficient proton reduction catalysts, operating at low overpotentials and high turnover frequencies.[33] Connolly and Espenson first reported the cobaloxime complex, $[Co(dmgBF_2)_2(H_2O)_2]^{2+}$, **19a**, as a catalyst for the reduction of protons ($dmgBF_2$= difluoroboryl-dimethylglyoxime) (Scheme 1.18). In this report, hydrogen production was exhibited with the addition of HCl to an aqueous solution of Cr^{2+} and **19a**, and when Cr^{2+} was present in excess, gas evolution continued to occur until it was completely consumed.[54]

Later studies on $[Co(dmgBF_2)_2(MeCN)_2]^{2+}$, **19b**, and $[Co(dpgBF_2)_2(MeCN)_2]^{2+}$, **19c** ($dpgBF_2$= difluoroboryl-diphenylglyoxime) (Scheme 1.16), showed that the cobaloxime complexes are electrocatalysts for the reduction of protons to form H_2, operating at overpotentials of less than 0.2 V (Table 1.7). The related complex, $[Co(dmgH_2)_2(Cl)(py)]^{+}$, **20a**, was also found to be an efficient electrocatalyst. However, the complexes are not particularly stable in the presence of acid, limiting electrolysis time to only ~ 1-2 hours. In an attempt to increase the stability of the catalysts, Artero and co-workers modified the macrocycle, replacing a O-H-O or O-B-O linkage with a $CH_2CH_2CH_2$ linkage. The modified complexes, **21a** and **21b** (Scheme 1.16), exhibit catalytic activities similar to **19a** and **19b**, but proved to be more stable.

Scheme 1.18. Cobaloxime catalysts

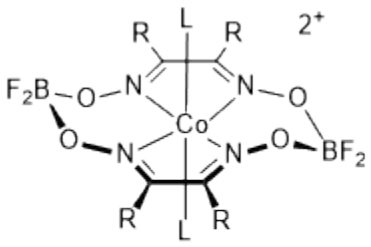

19a R=Me, L= H_2O
19b R=Me, L= MeCN
19c R=Ph, L= MeCN

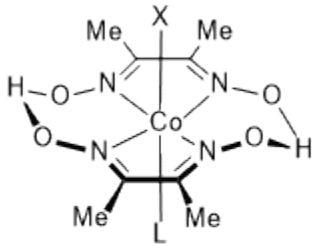

20a L=py, X=Cl^-
20b L=H_2O, X=Br^-

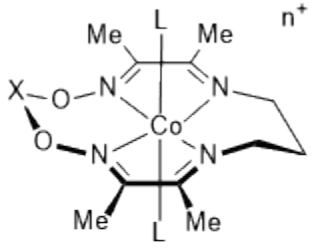

21a L= Br^-, X=BF_2^+, n=0
21b L= Br^-,X=H^+, n=0
21c L= H_2O, X= H^+, n=2

Table 1.7. Electrocatalytic properties of cobaloxime complexes.

Complex	$E_{p/2}$ (V vs $Fc^{+/0}$)	Overpotential (V)	Faradaic Efficiency	TON (mol H_2/mol cat) (Time)
$[Co(dmgBF_2)_2(MeCN)_2]^{2+}$ **19b**[a]	-0.87	0.18	100%	20 (1 h)
$[Co(dpgBF_2)_2(MeCN)_2]^{2+}$ **19c**[b]	-0.67	0.12	90%	11 (1 h)
$[Co(dmgH_2)_2(Cl)(py)]^{+}$ **20a**[c]	-1.32	0.12	85-100%	100 (2.5 h)
$Co(N_4H)Br_2$ **21a**[a]	-0.89	0.19	90%	7 (3 h)
$Co(N_4BF_2)Br_2$ **21b**[a]	-1.10	0.30	91%	20 (3 h)

[a] Acid= CF_3COOH, pK_a^{MeCN}= 12.7, $E°_{HA/H2}$= -0.70 V; [b] Acid= $HCl·Et_2O$, pK_a^{MeCN}= 8.9, $E°_{HA/H2}$= -0.55 V; [c] Acid= Et_3NH^+, pK_a^{DMF}= 18.7, $E°_{HA/H2}$= -1.2 V

Extensive work has focused on the mechanism by which the cobaloxime catalysts operate. There are a number of proposed mechanisms, which are depicted in Scheme 1.19. The first steps of the mechanism involve two electron transfers and a proton transfer to form a Co^{III}-hydride species. From this point, there are four possible pathways. The first mechanism is a heterolytic pathway, in which the $Co^{III}H$ is protonated, releasing H_2 and reforming the Co^{III} complex (Scheme1.19, A). The second mechanism is a homolytic pathway, in which two $Co^{III}H$ species react to form H_2 and the Co^{II} complex (Scheme 1.19, B). The other two mechanisms first involve reduction of the $Co^{III}H$ to $Co^{II}H$; from this point, the mechanism could continue via a heterolytic (Scheme 1.19, C) or homolytic pathway (Scheme 1.19, D). Kinetic and thermodynamic studies have shown that the homolytic pathways have lower barriers and are therefore favored over the heterolytic pathways. However, it is proposed that both mechanisms occur, and the heterolytic pathway dominates when the catalyst concentration is low or the acid concentration is high.

The mechanism is also strongly dependent on the strength of the acid. If the acid is strong enough to protonate both the Co^I and $Co^{III}H$ species, then the reaction follows pathway A. If the acid is strong enough to protonate the Co^I species, but not the Co^{II} species, then the reaction follows either pathway C or D, in which a $Co^{II}H$ species is formed. When a very weak acid is used, which cannot protonate the Co^I species, a fifth mechanism is proposed. In this case,

Co^{I} is reduced to a Co^{0} species, which is then protonated to form a $Co^{II}H$ species. From this point, the mechanism can follow either pathway C or D.[33]

Scheme 1.19. Possible mechanisms of proton reduction by coboloxime complexes.

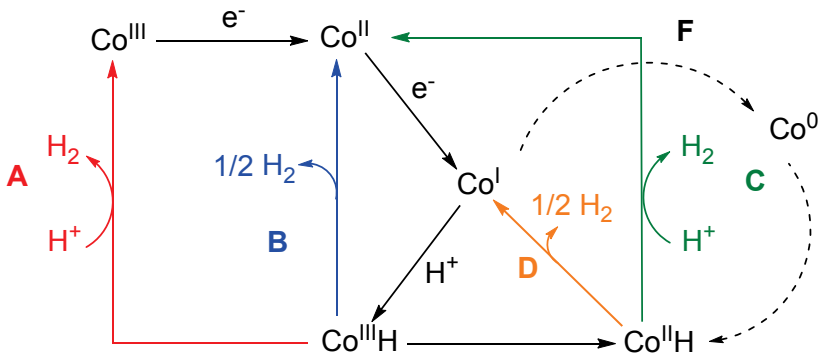

A number of cobaloxime catalysts have been found to operate in acidic aqueous solutions, including complexes **19b**, **20b**, **22**, and **23** (Scheme 1.20). All complexes are stable at pH 2.2 and catalyze proton reduction at high faradaic efficiencies and turnover numbers of 15-20 after a two hour electrolysis.[55]

Scheme 1.20. Water soluble cobaloxime catalysts.

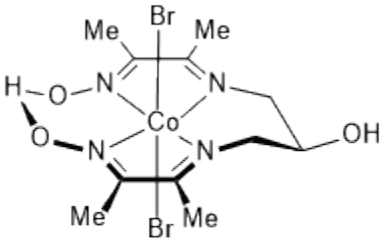

22

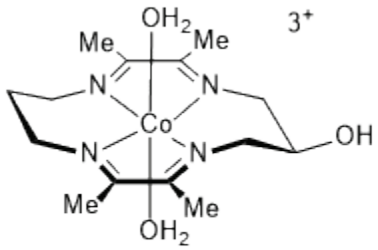

23

In general, the coboloxime catalysts are extremely robust, and they operate at the lowest overpotentials reported for homogeneous catalysts.[12] These characteristics, combined with their stability/ activity in water, make them potential catalysts for use in applications that are relevant to energy production.

1.7 References.

(1) *Annual Energy Outlook* Energy Information Administration, 2012.

(2) *International Energy Statistics*; Energy Information Administration 2012.

(3) *World Energy Report: Energy and the Challenge of Sustainability*; United Nations Development Programme, 2000.

(4) Wigley, T. M. L.; Richels, R.; Edmonds, J. A. "Economic and environmental choices in the stabilization of atmospheric CO2 concentrations." *Nature* **1996**, *379*, 240.

(5) Hoffert, M. I.; Caldeira, K.; Jain, A. K.; Haites, E. F.; Harvey, L. D. D.; Potter, S. D.; Schlesinger, M. E.; Schneider, S. H.; Watts, R. G.; Wigley, T. M. L.; Wuebbles, D. J. "Energy implications of future stabilization of atmospheric CO2 content." *Nature* **1998**, *395*, 881.

(6) Cook, T. R.; Dogutan, D. K.; Reece, S. Y.; Surendranath, Y.; Teets, T. S.; Nocera, D. G. "Solar energy supply and storage for the legacy and nonlegacy worlds." *Chem. Rev.* **2010**, *110*, 6474.

(7) Press, R. J.; Santhanam, K. S. V.; Miri, M. J.; Bailey, A. V.; Tackacs, G. A. *Introduction to Hydrogen Technology*; John Wiley and Sons Inc. : Hoboken, NJ, 2009.

(8) Lewis, N. S.; Nocera, D. G. "Powering the planet: Chemical challenges in solar energy utilization." *Proc. Natl. Acad. Sci. U.S.A.* **2006**, *103*, 15729.

(9) Häussinger, P.; Lohmüller, R.; Watson, A. M. In *Ullmann's Encyclopedia Industrial Chemistry*; Wiley-VCH, Weinheim: Weinheim, 2002.

(10) Hauch, A.; Ebbesen, S. D.; Jensen, S. H.; Mogensen, M. "Highly Efficient high temperature electrolysis." *J. Mater. Chem.* **2008**, *18*, 2331.

(11) Debe, M. K. "Electrocatalyst approaches and challenges for automotive fuel cells." *Nature* **2012**, *486*, 43.

(12) Thoi, V. S.; Sun, Y.; Long, J. R.; Chang, C. J. "Complexes of earth-abundant metals for catalytic electrochemical hydrogen generation under aqueous conditions." *Chem. Soc. Rev.* **2013**, *42*, 2388.

(13) Jaramillo, T. F.; Jorgensen, K. P.; Bonde, J.; Nielsen, J. H.; Horch, S.; Chorkendorff, I. "Identification of active edge sites for electrochemical H2 evolution from MoS2 nanocatalysts." *Science* **2007**, *317*, 100.

(14) Merki, D.; Fierro, S.; Vrubel, H.; Hu, X. "Amorphous molybdenum sulfide films as catalysts for electrochemical hydrogen production in water." *Chem. Sci.* **2011**, *2*, 1262.

(15) Li, Y.; Wang, H.; Xie, L.; Liang, Y.; Hong, G.; Dai, H. "MoS2 Nanoparticles Grown on Graphene: An Advanced Catalyst for the Hydrogen Evolution Reaction." *J. Am. Chem. Soc.* **2011**, *133*, 7296.

(16) Savadogo, O.; Lavoie, H. "Hydrogen evolution reaction in an alkaline medium on cobalt electrodeposited with heteropolyacids." *International Journal of Hydrogen Energy* **1992**, *17*, 473.

(17) Helm, M. L.; Stewart, M. P.; Bullock, R. M.; Rakowski DuBois, M.; DuBois, D. L. "A Synthetic Nickel Electrocatalyst with a Turnover Frequency Above 100,000 s-1 for H2 Production." *Science* **2011**, *333*, 863.

(18) Wang, M.; Chen, L.; Sun, L. "Recent progress in electrochemical hydrogen production with earth-abundant metal complexes as catalysts." *Energy Environ. Sci.* **2012**, *5*, 6763.

(19) Pool, D. H.; Du, B. D. L. "[Ni(PPh2NAr2)2(NCMe)][BF4]2 as an electrocatalyst for H2 production: PPh2NAr2 = 1,5-(di(4-(thiophene-3-yl)phenyl)-3,7-diphenyl-1,5-diaza-3,7-diphosphacyclooctane)." *J. Organomet. Chem.* **2009**, *694*, 2858.

(20) Felton, G. A. N.; Glass, R. S.; Lichtenberger, D. L.; Evans, D. H. "Iron-Only Hydrogenase Mimics. Thermodynamic Aspects of the Use of Electrochemistry to Evaluate Catalytic Efficiency for Hydrogen Generation." *Inorg. Chem.* **2006**, *45*, 9181.

(21) Fourmond, V.; Jacques, P.-A.; Fontecave, M.; Artero, V. "H2 Evolution and Molecular Electrocatalysts: Determination of Overpotentials and Effect of Homoconjugation." *Inorg. Chem.* **2010**, *49*, 10338.

(22) Fontecilla-Camps, J. C.; Volbeda, A.; Cavazza, C.; Nicolet, Y. "Structure/Function Relationships of [NiFe]- and [FeFe]-Hydrogenases." *Chem. Rev.* **2007**, *107*, 4273.

(23) Peters, J. W.; Lanzilotta, W. N.; Lemon, B. J.; Seefeldt, L. C. "X-ray Crystal Structure of the Fe-Only Hydrogenase (*CpI*) from *Clostridium pasteurianum* to 1.8 A Resolution." *Science* **1998**, *282*, 1853.

(24) Silakov, A.; Wenk, B.; Reijerse, E.; Lubitz, W. "^{14}N HYSCORE investigation of the H-cluster of [FeFe] hydrogenase: evidence for a nitrogen in the dithiol bridge." *Phys. Chem. Chem. Phys.* **2009**, *11*, 6592.

(25) Nicolet, Y.; Lemon, B. J.; Fontecilla-Camps, J. C.; Peters, J. W. "A Novel FeS Cluster in Fe-only Hydrogenases." *Trends Biochem. Sci.* **2000**, *25*, 138.

(26) Frey, M. "Hydrogenases: hydrogen-activating enzymes." *ChemBioChem* **2002**, *3*, 153.

(27) Hambourger, M.; Gervaldo, M.; Svedruzic, D.; King, P. W.; Gust, D.; Ghirardi, M.; Moore, A. L.; Moore, T. A. "[FeFe]-Hydrogenase-Catalyzed H2 Production in a Photoelectrochemical Biofuel Cell." *J. Am. Chem. Soc.* **2008**, *130*, 2015.

(28) Jones, A. K.; Sillery, E.; Albracht, S. P. J.; Armstrong, F. A. "Direct Comparison of the Electrocatalytic Oxidation of Hydrogen by an Enzyme and a Platinum Catalyst." *Chem. Commun.* **2002**, 866.

(29) Woolerton, T. W.; Sheard, S.; Chaudhary, Y. S.; Armstrong, F. A. "Enzymes and bio-inspired electrocatalysts in solar fuel devices." *Energy Environ. Sci.* **2012**, *5*, 7470.

(30) Armstrong, F. A. "Recent developments in dynamic electrochemical studies of adsorbed enzymes and their active sites." *Curr. Opin. Chem. Biol.* **2005**, *9*, 110.

(31) Capon, J.-F.; Gloaguen, F.; Petillon, F. Y.; Schollhammer, P.; Talarmin, J. "Electron and proton transfers at diiron dithiolate sites relevant to the catalysis of proton reduction by the [FeFe]-hydrogenases." *Coord. Chem. Rev.* **2009**, *253*, 1476.

(32) Besora, M.; Lledos, A.; Maseras, F. "Protonation of transition-metal hydrides: a not so simple process." *Chem. Soc. Rev.* **2009**, *38*, 957.

(33) Dempsey, J. L.; Brunschwig, B. S.; Winkler, J. R.; Gray, H. B. "Hydrogen Evolution Catalyzed by Cobaloximes." *Acc. Chem. Res.* **2009**, *42*, 1995.

(34) Tard, C.; Pickett, C. J. "Structural and Functional Analogues of the Active Sites of the [Fe]-, [NiFe]-, and [FeFe]-Hydrogenases." *Chem. Rev.* **2009**, *109*, 2245.

(35) Gloaguen, F.; Lawrence, J. D.; Rauchfuss, T. B. "Biomimetic Hydrogen Evolution Catalyzed by an Iron Carbonyl Thiolate." *J. Am. Chem. Soc.* **2001**, *123*, 9476.

(36) Gloaguen, F.; Lawrence, J. D.; Rauchfuss, T. B.; Bénard, M.; Rohmer, M.-M. "Bimetallic Carbonyl Thiolates as Functional Models for Fe-Only Hydrogenases." *Inorg. Chem.* **2002**, *41*, 6573.

(37) Mejia-Rodriguez, R.; Chong, D.; Reibenspies, J. H.; Soriaga, M. P.; Darensbourg, M. Y. "The Hydrophilic Phosphatriazaadamantane Ligand in the Development of H_2 Production Electrocatalysts: Iron Hydrogenase Model Complexes." *J. Am. Chem. Soc.* **2004**, *126*, 12004.

(38) Borg, S. J.; Behrsing, T.; Best, S. P.; Razavet, M.; Liu, X.; Pickett, C. J. "Electron Transfer at a Dithiolate-Bridged Diiron Assembly: Electrocatalytic Hydrogen Evolution." *J. Am. Chem. Soc.* **2004**, *126*, 16988.

(39) Gloaguen, F.; Rauchfuss, T. B. "Small Molecule Mimics of Hydrogenase: Hydrides and Redox." *Chem. Soc. Rev.* **2009**, *38*, 100.

(40) Sellmann, D.; Lauderbach, F.; Geipel, F.; Heinemann, F. W.; Moll, M. "A trinuclear [NiFe] cluster exhibiting structural and functional key features of [NiFe] hydrogenases." *Angew. Chem. Int. Ed.* **2004**, *43*, 3141.

(41) Lauderbach, F.; Prakash, R.; Goetz, A. W.; Munoz, M.; Heinemann, F. W.; Nickel, U.; Hess, B. A.; Sellmann, D. "Alternative synthesis, density functional calculations and proton reactivity study of a trinuclear [NiFe] hydrogenase model compound." *Eur. J. Inorg. Chem.* **2007**, 3385.

(42) Perra, A.; Davies, E. S.; Hyde, J. R.; Wang, Q.; McMaster, J.; Schröder, M. "Electrocatalytic production of hydrogen by a synthetic model of [NiFe] hydrogenases." *Chem. Commun.* **2006**, 1103.

(43) Canaguier, S.; Artero, V.; Fontecave, M. "Modelling NiFe hydrogenases: nickel-based electrocatalysts for hydrogen production." *Dalton Trans.* **2008**, 315.

(44) Oudart, Y.; Artero, V.; Pecaut, J.; Lebrun, C.; Fontecave, M. "Dinuclear nickel-ruthenium complexes as functional bio-inspired models of [NiFe] hydrogenases." *Eur. J. Inorg. Chem.* **2007**, 2613.

(45) Canaguier, S.; Vaccaro, L.; Artero, V.; Ostermann, R.; Pecaut, J.; Field, M. J.; Fontecave, M. "Cyclopentadienyl Ruthenium-Nickel Catalysts for Biomimetic Hydrogen Evolution: Electrocatalytic Properties and Mechanistic DFT Studies." *Chem.--Eur. J.* **2009**, *15*, 9350.

(46) Canaguier, S.; Fontecave, M.; Artero, V. "Cp*--Ruthenium-Nickel-Based H2-Evolving Electrocatalysts as Bio-inspired Models of NiFe Hydrogenases." *Eur. J. Inorg. Chem.* **2011**, 1094.

(47) Canaguier, S.; Field, M.; Oudart, Y.; Pecaut, J.; Fontecave, M.; Artero, V. "A structural and functional mimic of the active site of NiFe hydrogenases." *Chem. Commun.* **2010**, *46*, 5876.

(48) Fourmond, V.; Canaguier, S.; Golly, B.; Field, M. J.; Fontecave, M.; Artero, V. "A nickel-manganese catalyst as a biomimic of the active site of NiFe hydrogenases: a combined electrocatalytical and DFT mechanistic study." *Energy Environ. Sci.* **2011**, *4*, 2417.

(49) Barton, B. E.; Whaley, C. M.; Rauchfuss, T. B.; Gray, D. L. "Nickel-Iron-Dithiolato-Hydrides Relevant to the [NiFe]-Hydrogenase Active Site." *J. Am. Chem. Soc.* **2009**, *131*, 6942.

(50) Yang, J. Y.; Bullock, R. M.; DuBois, M. R.; DuBois, D. L. "Fast and efficient molecular electrocatalysts for H2 production: Using hydrogenase enzymes as guides." *MRS Bulletin* **2011**, *36*, 39.

(51) Rakowski DuBois, M.; DuBois, D. L. "The roles of the first and second coordination spheres in the design of molecular catalysts for H_2 production and oxidation." *Chem. Soc. Rev.* **2009**, *38*, 62.

(52) Izutsu, K. *Acid-Base Dissociation Constants in Dipolar Aprotic Solvents*; Blackwell Scientific Publications: Oxford, U.K., 1990; Vol. 35.

(53) Kilgore, U. J.; Roberts, J. A. S.; Pool, D. H.; Appel, A. M.; Stewart, M. P.; DuBois, M. R.; Dougherty, W. G.; Kassel, W. S.; Bullock, R. M.; DuBois, D. L. "[Ni(PPh2NC6H4X2)2]2+ Complexes as Electrocatalysts for H2 Production: Effect of Substituents, Acids, and Water on Catalytic Rates." *J. Am. Chem. Soc.* **2011**, *133*, 5861.

(54) Connolly, P.; Espenson, J. H. "Cobalt-catalyzed evolution of molecular hydrogen." *Inorg. Chem.* **1986**, *25*, 2684.

(55) McCrory, C. C. L.; Uyeda, C.; Peters, J. C. "Electrocatalytic Hydrogen Evolution in Acidic Water with Molecular Cobalt Tetraazamacrocycles." *J. Am. Chem. Soc.* **2012**, *134*, 3164.

Chapter 2.

Synthesis and Protonation of $Fe_2(xdt)(CO)_2(dppv)_2$ Complexes: Characterization of Terminal and Bridging Hydride Species[†]

2.1 Introduction

As discussed in Chapter 1, [FeFe]-hydrogenases catalyze the reduction of protons at high rates and fairly mild overpotentials. The active site of [FeFe]-hydrogenase features a dithiolate cofactor that bridges two iron centers, both of which are bound to biologically unusual CO and CN^- ligands.[1] Based on X-ray crystallographic studies on the enzyme, the dithiolate bridge contains three light atoms, and the identity of the bridgehead atom could be carbon, nitrogen, or oxygen.[2] These three cannot be distinguished purely by crystallography, but a number of spectroscopic and computational studies support the azadithiolate cofactor shown in Figure 2.1.[3,4] A 4Fe-4S cluster, which functions in electron transfer, is directly tethered to the diiron active site through a cysteine thiolate ligand, and this bond is the only covalent linkage between the active site and the rest of the protein (Figure 2.1). However, hydrogen bonds between the CN^- ligands and nearby residues also connect the active site with the rest of the protein and fix the cluster in the rotated geometry.[5] The 6Fe active site is referred to as the H-cluster.

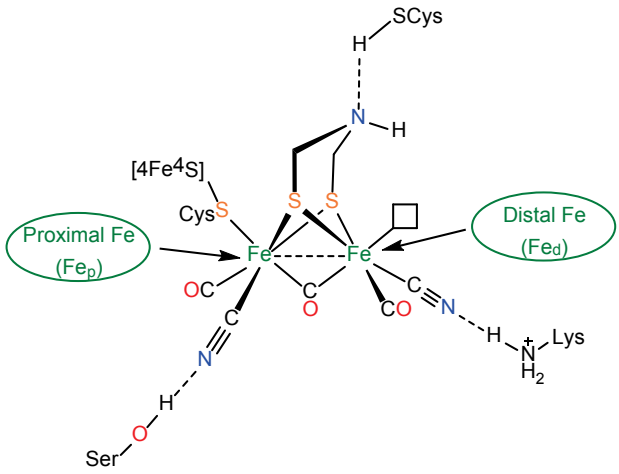

Figure 2.1. Structure of the active site of [FeFe]-hydrogenase.

[†] Portions of this chapter are reproduced from the following publication with permission from the authors. Carroll, M. E.; Barton, B. E.; Rauchfuss, T.B.; Carroll, P.J. *J. Am. Chem. Soc.* **2012**, *134*, 18843–18852.

Two active forms of the enzyme have been thoroughly characterized by spectroscopic, electrochemical, and crystallographic techniques, and these states include H_{ox} and H_{red} (Scheme 2.1). H_{ox} is a paramagnetic, EPR active Fe(II)Fe(I) state, which is converted to the EPR silent H_{red} state by one electron reduction. The exact identity of H_{red} has not been elucidated; it contains either Fe(I)Fe(I) centers or an Fe(II)Fe(II) hydride. In both active forms of the enzyme, the distal Fe is rotated, such that a CO ligand bridges the two Fe centers, and the extent to which is bridges depends on the redox state. This rotated geometry leaves an open binding site on the distal Fe, which is adjacent to the amine cofactor, and this is the proposed site of substrate binding.[1,5]

Scheme 2.1 Active states of [FeFe]-hydrogenase and proposed mechanism of catalytic proton reduction based on DFT calculations by De Gioia *et al*.

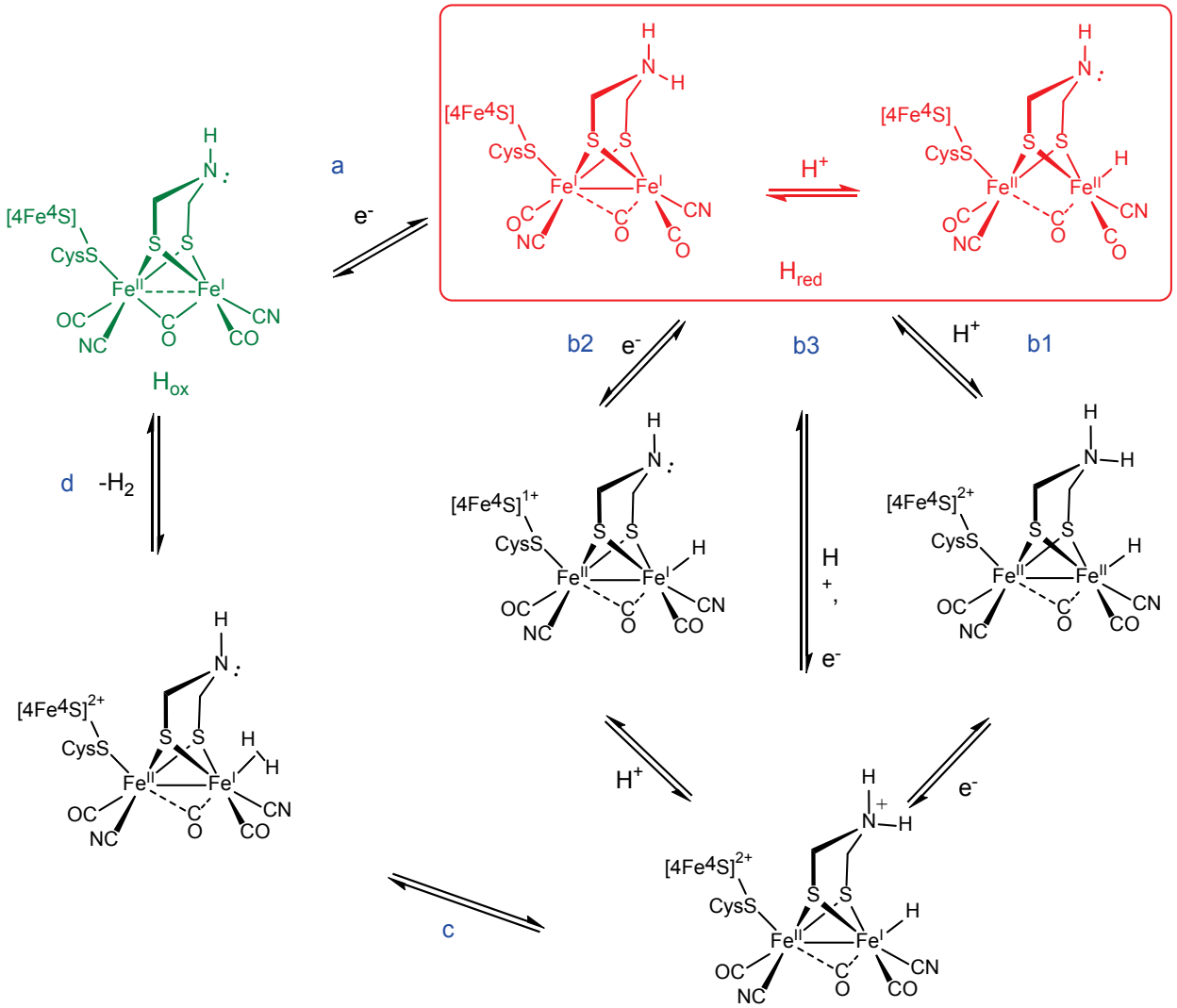

This unique organometallic active site has inspired many synthetic organometallic chemists to synthesize small molecule mimics. One common goal in synthesizing such model complexes is to elucidate the mechanism by which the enzyme operates. Previous research has given some insight into the details of protonation and redox by the enzyme. In a mechanism based on computational studies by De Gioia and coworkers (Scheme 2.1), the first step in the catalytic cycle is conversion of H_{ox} to H_{red} via reduction and protonation (step a). The following steps in the mechanism involve an additional proton and electron transfer. These could occur by three possible paths; protonation followed by electron transfer (b1), electron transfer followed by protonation (b2), or proton coupled electron transfer (PCET) (b3). In any case, a mixed valence ammonium hydride species forms, which then forms a dihydrogen complex (step c) and loses dihydrogen to reform H_{ox} (step d).[6]

There are three main requirements for a successful model of the active site of [FeFe]-hydrogenase:

i. redox activity

ii. reactivity with appropriate substrates (acid or H_2)

iii. mimicry of the structural features of the enzyme

The first requirement of redox activity is typically fulfilled by most diiron dithiolate carbonyl models, and typically, the Fe_4S_4 cluster in not included in models. Instead, the system is simplified by using an electrode as the source of electrons.[7,8] To date, only one synthetic [FeFe]-hydrogenase model reacts with both H_2 and acid; typically models either catalyze H_2 oxidation or proton reduction, as is the case for the complexes discussed herein.[9] The third requirement, that models contain structural features found in the enzyme, has been the most thoroughly investigated.[8]

The synthesis of complexes of the general type $Fe_2(SR)_2(CO)_6$ was reported as early as the 1920's, by treating $Fe(CO)_5$ with a thiol.[10] A more efficient synthesis, which is illustrated in Scheme 2.2, utilizes $Fe_3(CO)_{12}$,[11] and in the 1960's, King applied this method to the synthesis of dithiolate complexes.[12] New methods for synthesizing these complexes, as well as substitution chemistry, have been extensively studied (Scheme 2.2).[8] These methods only apply to dithiolates with simple alkyl bridges, but the enzyme contains an amine cofactor. Because free azadithiols do not exist, a different method for the synthesis of $Fe_2(adt^{NR})(CO)_6$ (adt^{NR}= $[N(R)(CH_2S)_2]^{2-}$) is necessary. The earliest method involved reaction of $[Fe_2(S)_2(CO)_6]^{2-}$ with

bis(chloromethyl)amines (Scheme 2.3a).[13] Later methods involved the condensation of formaldehyde and amines and reaction with $[Fe_2(S)_2(CO)_6]^{2-}$ (Scheme 2.3b), as well as reaction of triazines (Scheme 2.3c) and hexamethylene tetramine (Scheme 2.3d) with $[Fe_2(S)_2(CO)_6]^{2-}$.[14] Recently, we reported a new synthesis of $Fe_2(adt^{NR})(CO)_6$, in which a titanocene azadithiolate transfers the azadithiolate group to an Fe(0) carbonyl source (Scheme 2.3e).[15]

Scheme 2.2. Synthesis of $Fe_2(SR)_2(CO)_6$ complexes.

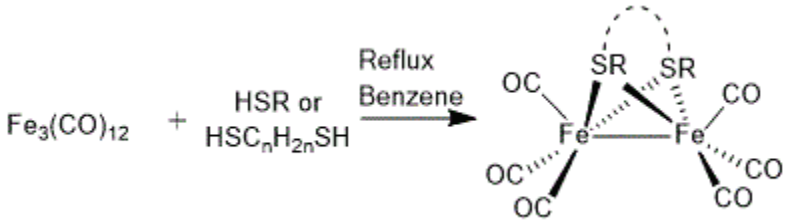

Scheme 2.3. Synthesis of $Fe_2(adt^{NR})(CO)_6$ complexes.

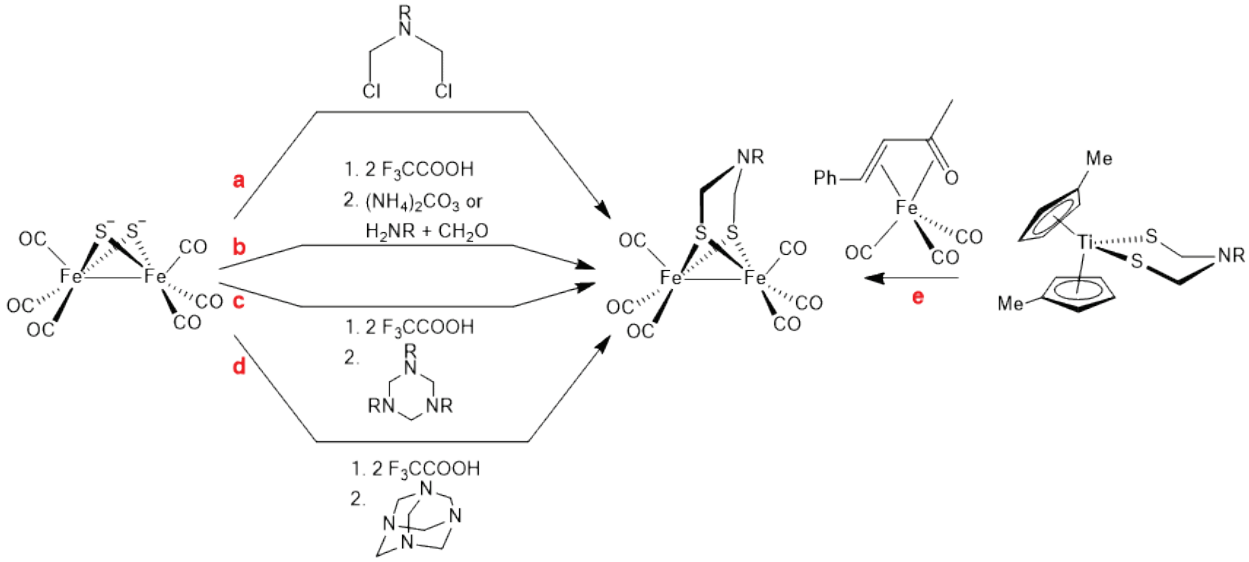

Early work on modeling [FeFe]-hydrogenase focused on hexacarbonyl complexes.[8] However, these complexes are not readily protonated, and the active site contains electron donating ligands, CN^-, in addition to CO. Therefore, complexes of the type $[Fe_2(dithiolate)(CN)_2(CO)_4]^{2-}$ were investigated.[8] Although the IR spectroscopic data for these complexes are similar to those for the enzyme, cyanide containing diiron complexes proved to be poor functional models of the enzyme. For example, oxidation of the dicyanide complexes

results in the formation of insoluble polymers, which likely contain bridging CN^- ligands.[7] Studies of the mixed cyanide- phosphine complex, $[Fe_2(pdt)(CN)(CO)_3(dppv)]^-$ (pdt= 1,2-propanedithiolate, dppv= *cis*-1,2-bis(diphenylphosphino)ethylene) found that, in the presence of an oxidant, Fe_4 derivatives are formed, in which an Fe(I)Fe(I) unit is bridged by a CN^- ligand to an Fe(II)Fe(II) unit (Scheme 2.4).[16] Additional problems arise when the cyanide complexes are protonated; the CN^- ligand is a basic site, and in many cases is the kinetic site of protonation. Additionally, when Fe hydride species form, they are typically unstable.[17] Both of these problems are avoided in the enzyme due to the presence of the protein scaffold, which protects the active site, preventing diiron units from reacting with one another, and forms hydrogen bonds to the CN^- ligands, eliminating them as potential basic sites.

In order to avoid the issues associated with cyanide ligands, our group chose to replace the anionic CN^- ligands with neutral phosphines. Early studies showed that, despite differences in charge, phosphine and CN^- complexes had similar electronic properties, as evidenced by comparison of the redox potentials, pK_a values, and IR spectra for $[Fe_2(pdt)(CN)_n(CO)_4(PMe_3)_{2-n}]^{n-}$ (Tables 2.1, 2.2).[17-21] Therefore, the complexes discussed herein contain phosphine ligands in place of cyanide.

Scheme 2.4 Proposed dimeric product from oxidation of $[Fe_2(edt)(CO)_3(CN)(dppv)]^-$.

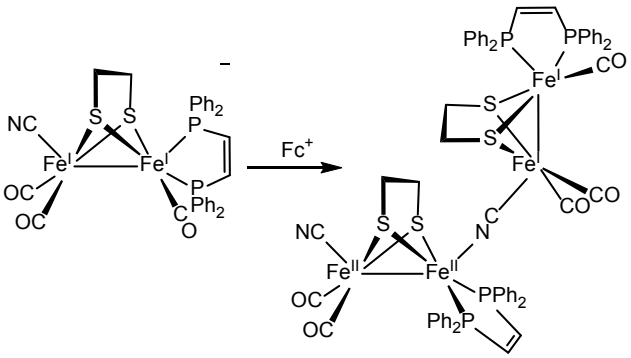

Table 2.1 Acid- base and redox properties of complexes of the type $[Fe_2(pdt)(CN)_n(CO)_4(PMe_3)_{2-n}]^{n-}$ (n=1,2).

Complex	pK_a	E_{ox} (V vs $Fc^{+/0}$)	E_{red} (V vs $Fc^{+/0}$)
$[Fe_2(pdt)(CN)_2(CO)_4]^{2-}$	~14	-0.553	-2.75
$[Fe_2(pdt)(CN)(CO)_4(PMe_3)]^-$	10.4- 11.3	-0.423	-2.61
$Fe_2(pdt)(CO)_4(PMe_3)_2$	10.4- 11.3	-0.233	-2.34
$[Fe_2(pdt)(CN)(CO)_5]^-$	-	0.097	-2.23
$Fe_2(pdt)(CO)_5(PMe_3)$	-	-0.083	-2.33

Table 2.2 IR spectroscopic data for complexes of the type $[Fe_2(pdt)(CN)_n(CO)_4(PMe_3)_{2-n}]^{n-}$.

Complex	ν_{CO} (cm^{-1})	ν_{CN} (cm^{-1})
$[Fe_2(pdt)(CN)_2(CO)_4]^{2-}$	1961, 1917, 1880, 1867	2078, 2029
$[Fe_2(pdt)(CN)(CO)_4(PMe_3)]^-$	1971, 1931, 1895, 1880	2078, 2036
$Fe_2(pdt)(CO)_4(PMe_3)_2$	1979, 1931, 1895, 1880	-
$[Fe_2(pdt)(CN)(CO)_5]^-$	2029, 1974, 1955, 1941, 1917	2094
$Fe_2(pdt)(CO)_5(PMe_3)$	2037, 1980, 1919	-

The synthesis of models that contain the rotated structure present in the enzyme has proven to be the biggest challenge associated with modeling the [FeFe]-hydrogenase active site. In general, the most stable product of protonation of diiron model systems is a bridging hydride species. In the enzyme active site, the H-cluster is fixed in the rotated geometry due to hydrogen bonding between CN^- ligands and adjacent amino acid residues. Therefore, the CN^- ligands play an important role in addition to acting as strong field donor ligands; they aid in holding the active site in the rotated configuration. A number of diiron complexes with terminal hydride ligands have been characterized.[22-26] In all of these examples, phosphine ligands replace CN^-, and the steric bulk of these phosphine ligands inhibits rotation, thus stabilizing the terminal hydride species and slowing isomerization to the corresponding bridging hydrides. [22-26]

Before the work reported herein, there was one example of a crystallographically characterized diiron species containing a terminal hydride. However, this complex was formed by reaction of a cationic diiron species with a hydride source, which is not a biologically relevant path (Scheme 2.5).[22] Other terminal hydride complexes $[HFe_2(pdt)(CO)_4(chel)]^+$ are observable by NMR spectroscopy, but above ca. -30 °C they isomerize to bridging hydride complexes (chel

= chelating ligands) (Scheme 2.6).[23-26] Terminal hydride diiron complexes are characterized by ^{1}H NMR signals at high field (δ -3 to -5), whereas bridging hydrides appear at higher field (δ< -10).

Scheme 2.5 Synthesis of [*t*-HFe$_2$(edt)(CO)$_2$(PMe$_3$)$_4$]$^+$, which has been characterized crystallographically.

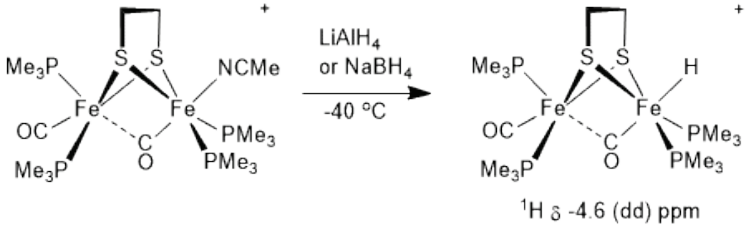

Scheme 2.6 Structures of diiron terminal hydride complexes that have been characterized by NMR spectroscopy, with ^{1}H NMR chemical shift of hydride signal below each complex.

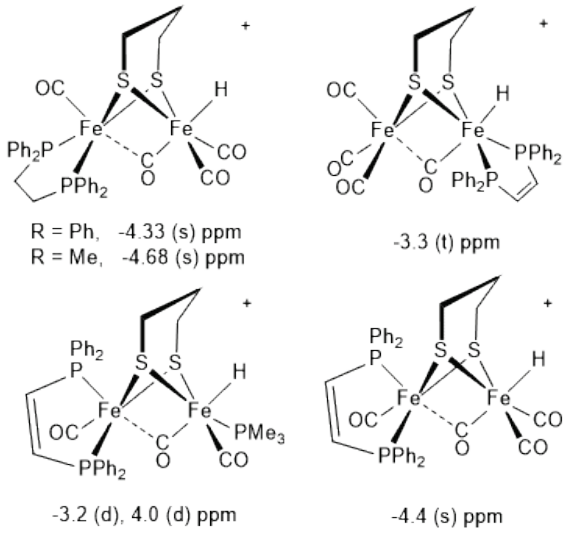

The stability of these terminal hydride complexes is enhanced for sterically crowded or very electron-rich diiron dithiolato carbonyls.[27,28] Thus, Fe$_2$(pdt)(CO)$_2$(dppv)$_2$ (**2**, pdt = 1,3-propanedithiolate) undergoes protonation, albeit only with strong acids, to give a terminal hydride that is stable for several minutes at room temperature (dppv = *cis*-C$_2$H$_2$(PPh$_2$)$_2$). Very recently, Riccardo Zaffaroni found that the complexes Fe$_2$(xdt)(CO)$_2$(PMe$_3$)$_2$ are protonated to form terminal hydride species that are stable for days at room temperature. In this chapter, an extensive investigation of the structural and protonation chemistry of Fe$_2$(adt^{NH})(CO)$_2$(dppv)$_2$ (**1**^{NH}) (adt^{NH} = [NH (SCH$_2$)$_2$]$^{2-}$), with parallel studies on the Fe$_2$(pdt)(CO)$_2$(dppv)$_2$ (**2**), which lacks the amine cofactor is summarized.

2.2 Synthesis and Characterization of $Fe_2(xdt)(CO)_2(dppv)_2$.

The diiron dithiolato dicarbonyl tetraphosphines $\mathbf{1}^{\mathbf{NH}}$ (xdt = adt^{NH}, $[S_2(CH_2)_2NH]^{2-}$) and **2** (xdt = pdt, $[S_2(CH_2)_3]^{2-}$) are prepared by substitution of the corresponding diiron dithiolate hexacarbonyl complexes with dppv. The first dppv ligand is installed by reaction of $Fe_2(xdt)(CO)_6$ with one equivalent of Me_3NO and one equivalent of dppv in refluxing toluene. The second ligand is installed by photolysis of $Fe_2(xdt)(CO)_4(dppv)$ in the presence of dppv (Scheme 2.7). The pdt derivative, **2**, can also be synthesized by this method, or by photolysis of $Fe_2(pdt)(CO)_6$ in the presence of excess dppv. Attempts to apply this method to the synthesis of $\mathbf{1}^{\mathbf{NH}}$ showed that long photolysis times were required, leading to significant decomposition of $\mathbf{1}^{\mathbf{NH}}$.

Scheme 2.7. Synthetic route to $Fe_2(xdt)(CO)_2(dppv)_2$ complexes.

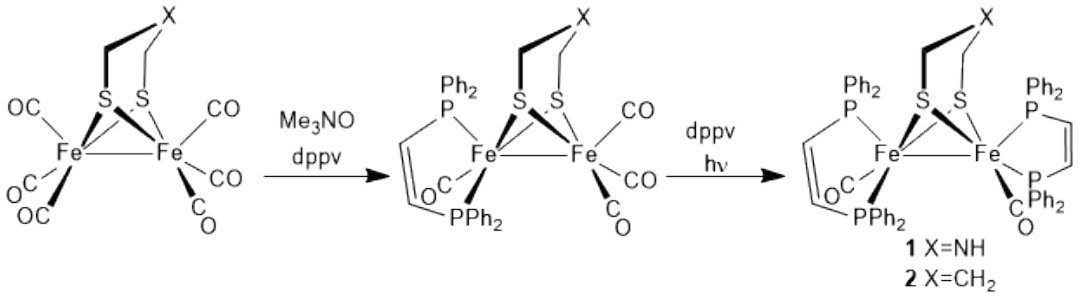

Both complexes $\mathbf{1}^{\mathbf{NH}}$ and **2** are green, air-sensitive solids that are highly soluble in dichloromethane and toluene. The IR spectra for $\mathbf{1}^{\mathbf{NH}}$ and **2** (ν_{CO} = 1888, 1868 cm^{-1}) (Figure 2.2) and related derivatives $Fe_2(edt)(CO)_2(dppv)_2$ and $Fe_2(odt)(CO)_2(dppv)_2$ are similar, indicating that they adopt similar structures and that the donor properties of the dithiolates are comparable.[29]

The room temperature ^{31}P NMR spectra of $\mathbf{1}^{\mathbf{NH}}$ and **2** both display broad signals at ~ δ 90. The spectra suggest that $\mathbf{1}^{\mathbf{NH}}$ and **2** are stereochemically nonrigid in two ways: (i) "turnstile rotation" of the Fe(dppv)(CO) subunits and (ii) "flipping" of the dithiolate bridge (Scheme 2.8). With respect to the latter process, the $X(CH_2S)_2Fe$ rings (X= CH_2, NH, O, etc) are subject to a chair-chair equilibration,[30] as seen in cyclohexane and piperidine derivatives.[31]

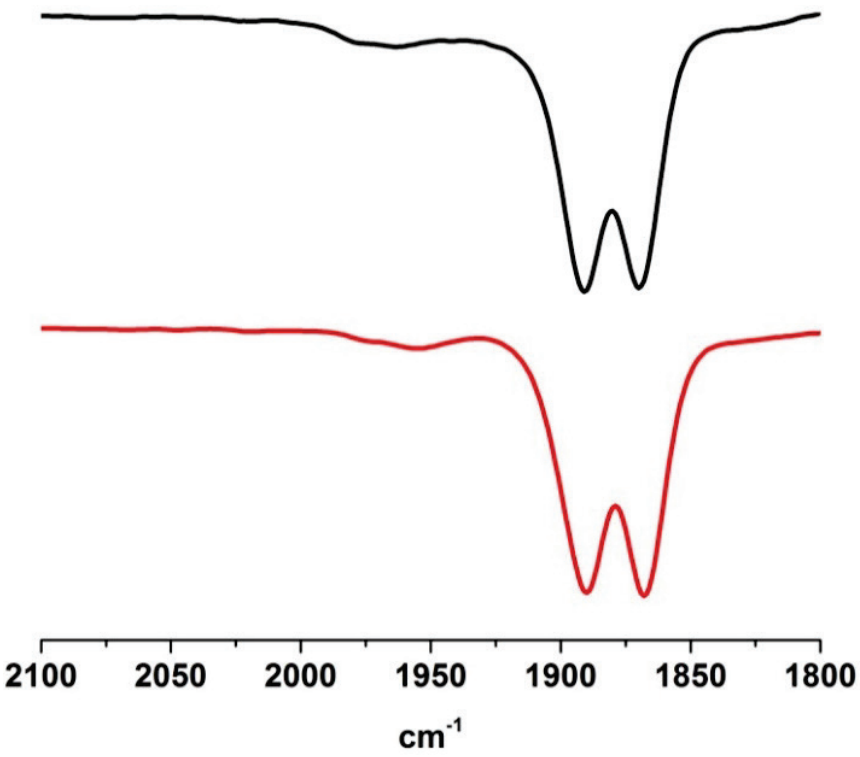

Figure 2.2. IR spectra of $Fe_2(adt^{NH})(CO)_2(dppv)$, 1^{NH} , (black) and $Fe_2(pdt)(CO)_2(dppv)$, 2, (red) in CH_2Cl_2.

Scheme 2.8 Dynamic processes occurring for $Fe_2(xdt)(CO)_2(dppv)_2$.

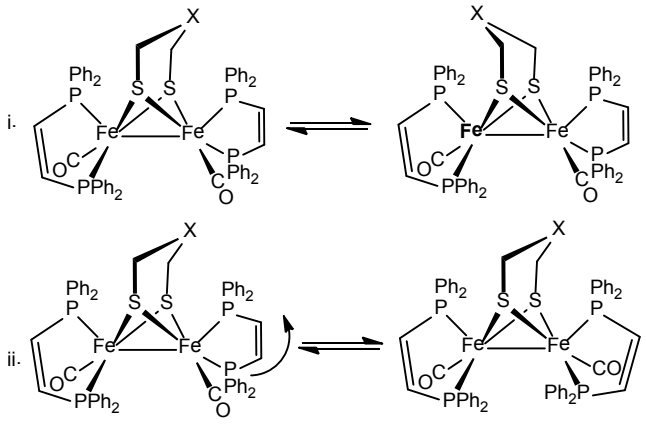

At -80 °C, the ^{31}P NMR spectrum of **1**^{NH} displays four equally intense signals, indicating that the two dppv ligands are chemically inequivalent (Figure 2.3). In contrast, spectra for the related pdt complex **2** show only a pair of signals at low temperatures, an observation that suggests that pdt is a more flexible dithiolate than adt^{NH}.[32] Turnstile rotation at the Fe(dppv)(CO) unit is halted on the NMR timescale at -80 °C, but flipping of the dithiolate continues to be fast. In the adt

derivative, both processes are either slow or cease to occur at low temperatures, which may reflect a higher barrier for the flipping of the adt compared to the structurally related pdt derivative. At -10 °C, this conformational equilibrium becomes rapid on the NMR timescale, and the ^{31}P NMR spectrum simplifies to a broad singlet. The dynamics of the adt^{NH} and the turnstile rotation of the Fe(CO)(dppv) centers appear to be coupled since both processes change from slow to fast exchange regimes at the same temperature range.

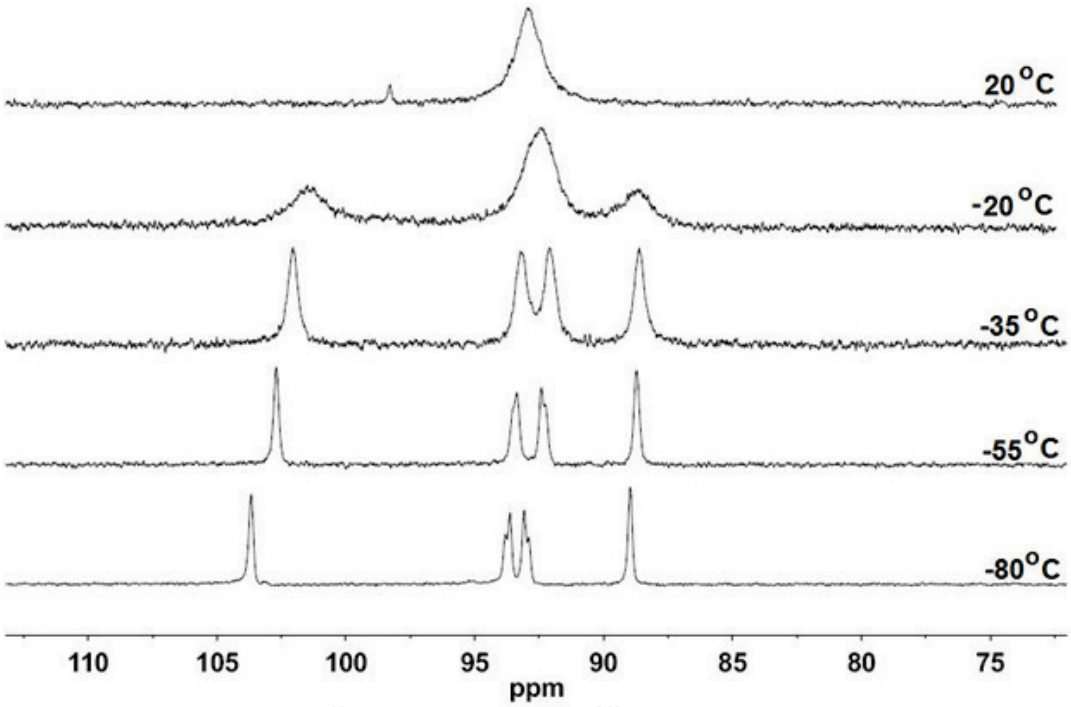

Figure 2.3. Variable temperature ^{31}P NMR spectrum of 1^{NH} in CD_2Cl_2.

The structure of **1**^{NH} was confirmed crystallographically (Figure 2.4), the details being consistent with the NMR results. The phosphorus centers of each dppv ligand occupy axial and basal positions, and the CO ligands occupy basal positions. Space-filling models show that the phenyl groups protect the Fe-Fe bond, which is relevant to the regiochemistry of the protonation of **1**^{NH} and **2**. As will be discussed below, the kinetic site of protonation of both **1**^{NH} and **2** is a single Fe center, not the Fe-Fe bond, which is likely due to the phenyl group blocking this site of protonation. Complex **1**^{NH} adopts a structure that is similar to that for the previously reported complex $Fe_2(edt)(CO)_2(dppv)_2$, edt= ethanedithiolate.[33]

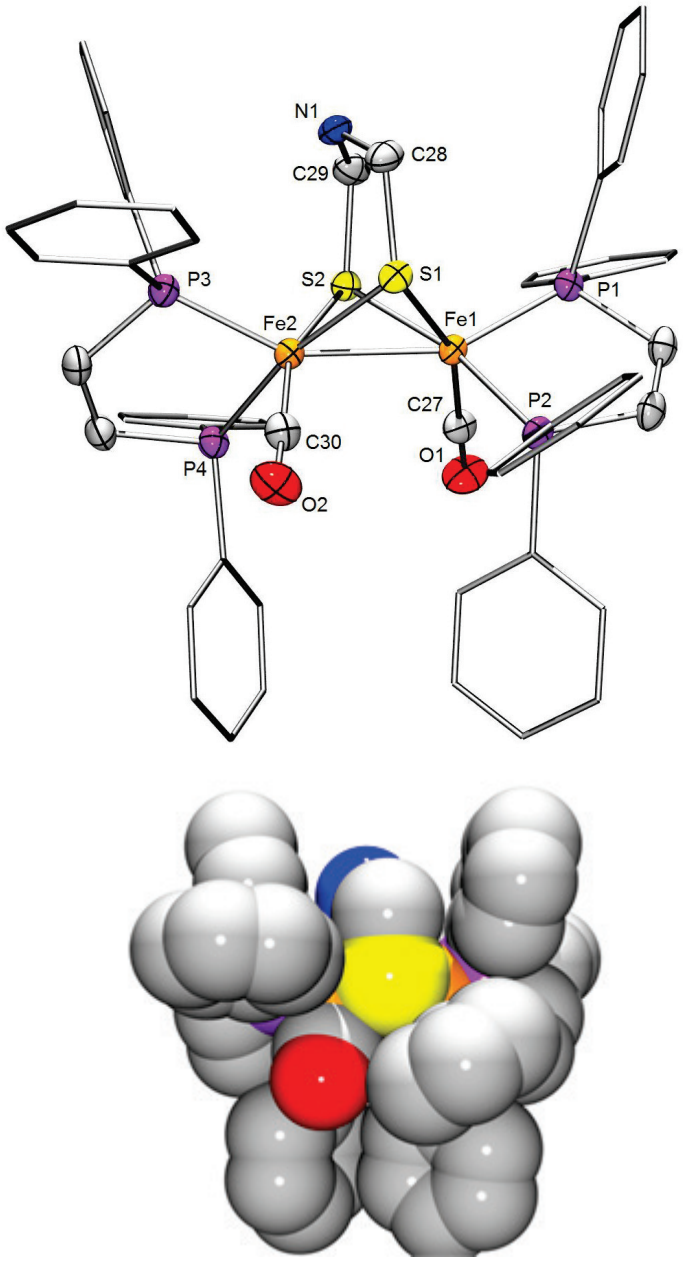

Figure 2.4. Structure of $Fe_2(adt^{NH})(CO)_2(dppv)_2$ (1^{NH}). Left: with thermal ellipsoids drawn at the 50 % Selected distances (Å): Fe1-Fe2, 2.6027(6); Fe1-C27, 1.7381(30); Fe1-P1, 2.1884(8); Fe1-P2, 2.2108(8); Fe1-S1, 2.2108(8); Fe1-S2, 2.2668(8); Fe2-C30, 1.7508(30); Fe2-P3, 2.1937(9); Fe2-P4, 2.2296(8); Fe2-S1, 2.2785(8); Fe2-S2, 2.2668(8). Right: space-filling model showing that the Ph groups block the Fe-Fe bond (red = O, blue = N, yellow = S, orange = Fe, violet = P).

2.3 Redox Properties of $Fe_2(xdt)(CO)_2(dppv)_2$

The cyclic voltammograms of $\mathbf{1}^{NH}$ and **2** are similar. Both compounds exhibit reversible Fe(I)Fe(I)/Fe(II)Fe(I) couples at highly negative potentials (Table 2.3). For **2**, a second quasi-reversible oxidation, corresponding to the Fe(II)Fe(I)/Fe(II)Fe(II) couple, occurs at a potential ~1 V positive of the first oxidation (Figure 2.5).

Table 2.3. Electrochemical Properties of $\mathbf{1}^{NH}$ and 2.

Compound	$E_{1/2}$ in CH_2Cl_2 (V vs $Fc^{+/0}$)	Assignment	i_{pc}/i_{pa}
$Fe_2(adt)(CO)_2(dppv)_2$, $\mathbf{1}^{NH}$	-0.840, -0.616	$[\mathbf{1}^{NH}]^{0/+}$ $[\mathbf{1}^{NH}]^{+/2+}$	0.78, 0.79
$Fe_2(pdt)(CO)_2(dppv)_2$, **2**	-0.940, 0.124	$[\mathbf{2}]^{0/+}$, $[\mathbf{2}]^{+/2+}$	0.98, irrev

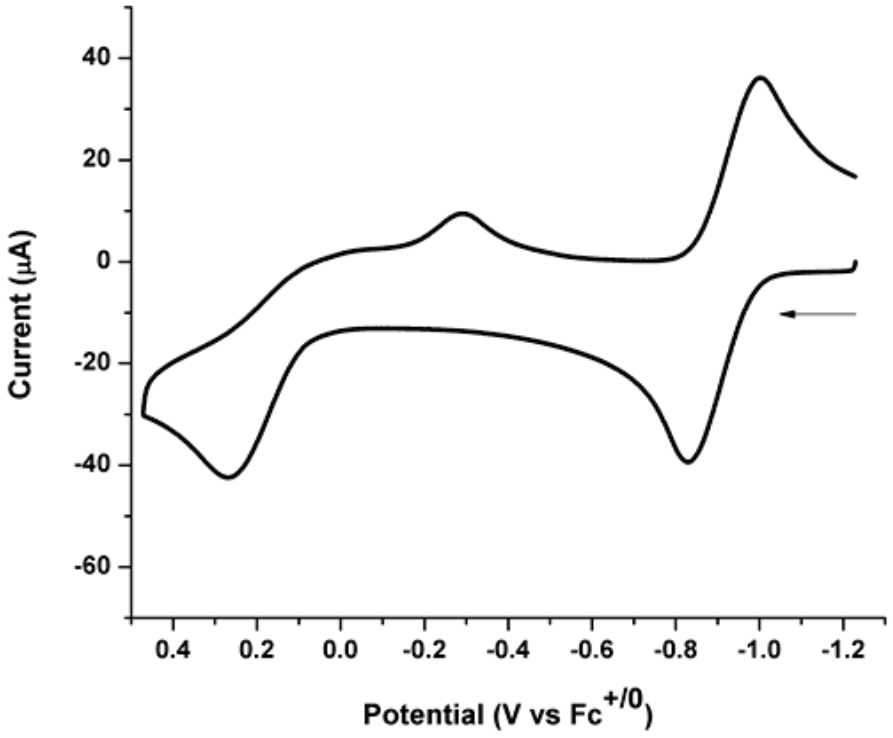

Figure 2.5. Cyclic voltammogram of 2. (Conditions: 0.025 M $[Bu_4N][BArF_{24}]$ in CH_2Cl_2, 1.0 mM 1, GC working electrode, Pt counter electrode, Ag wire pseudo reference electrode, Fc internal standard).

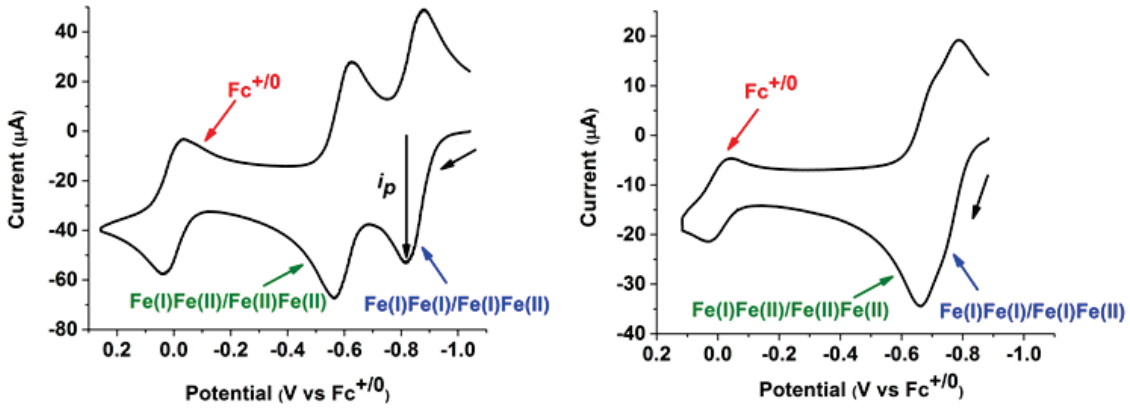

Figure 2.6. Cyclic voltammograms of 1^{NH}. Left: $[Bu_4N]BArF_{24}$ electrolyte, Right: $[Bu_4N]PF_6$ electrolyte (Conditions: 1.0 mM 1 in CH_2Cl_2, GC working electrode, Pt counter electrode, Ag wire pseudo reference electrode, Fc internal standard).

For $\mathbf{1}^{NH}$, a second quasi reversible oxidation occurs at milder potentials than for **2**. The separation and reversibility of the two oxidation events is highly dependent on the identity of the electrolyte employed. When $[Bu_4N]PF_6$ is used as electrolyte, the two waves overlap at a potential of ~ -0.742 V (Figure 2.6). With $[Bu_4N]BAr^F_{24}$ (BAr^F_{24}= tetrakis(3,5-(trifluoromethyl)phenyl)borate) as the electrolyte, the $[\mathbf{1}]^{0/+}$ and $[\mathbf{1}]^{+/2+}$ couples are reversible and well separated, with $E_{1/2}$ of -0.616 and -0.840 V (Table 2.3, Figure 2.6). The effect of electrolyte on the separation of redox couples is well described by Geiger et al.[34] Both oxidation processes are diffusion controlled, with a linear dependence of i_{pa} on (scan rate)$^{1/2}$ (Figure 2.7).

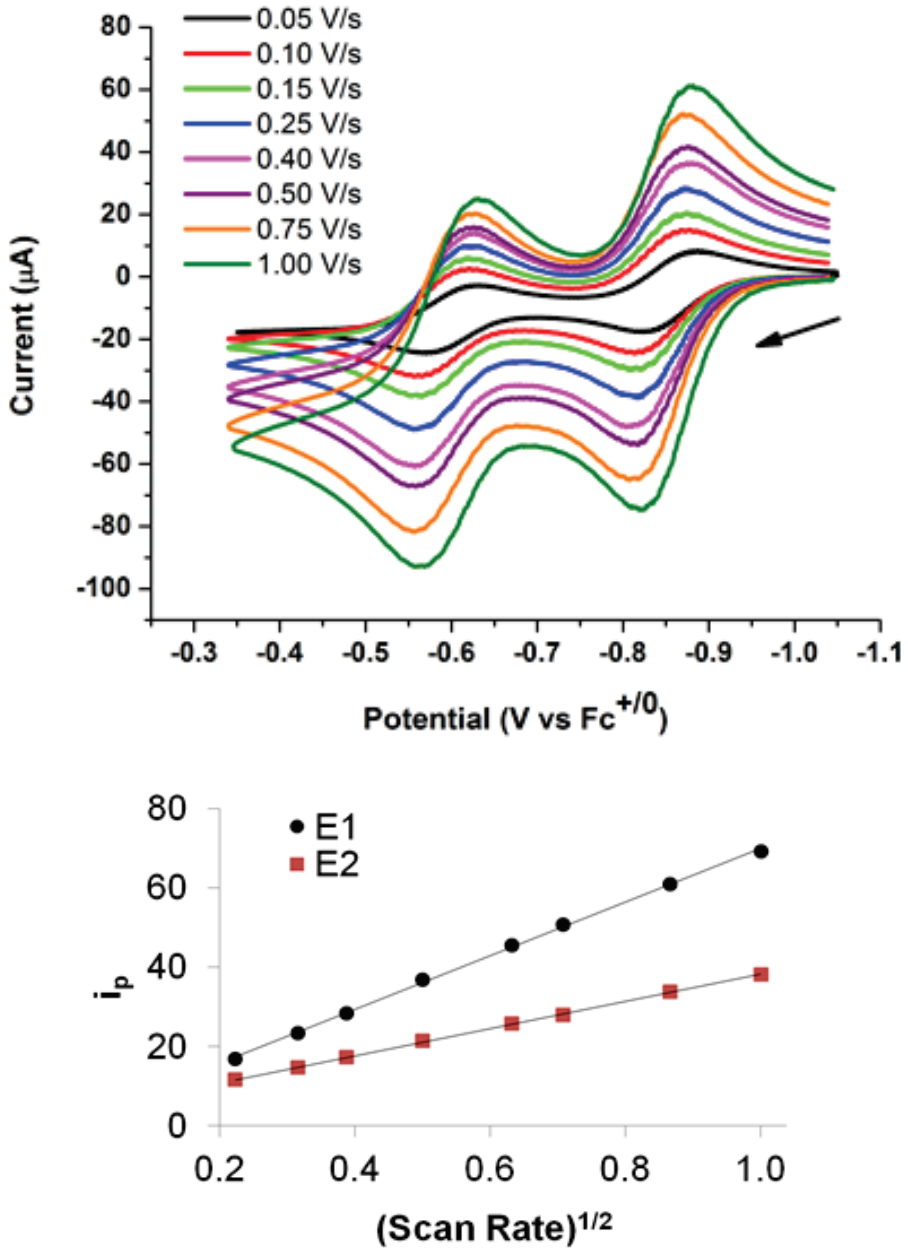

Figure 2.7. Top: Cyclic voltammograms of 1^{NH} at varying scan rates. (Conditions: 0.125 M $[Bu_4N][BArF_{24}]$ in CH_2Cl_2, 1.0 mM 1^{NH}, GC working electrode, Pt counter electrode, Ag wire pseudo reference electrode, Fc internal standard) Bottom: Plot of i_p vs. square root of scan rate for 1^{NH}.

As judged from these data, the Fe(I)Fe(I)/Fe(II)Fe(I) couples for $\mathbf{1}^{NH}$ and **2** occur at similar potentials. However, the second oxidation, the Fe(II)Fe(I)/Fe(II)Fe(II) couple, for $\mathbf{1}^{NH}$ is reversible and only ~200 mV positive of the first oxidation, whereas that for **2** is irreversible and occurs ~ 1V positive of the first oxidation. The difference in redox properties between $\mathbf{1}^{NH}$ and **2**

is likely attributed to the presence of the amine cofactor in $\mathbf{1}^{\mathbf{NH}}$. Previous work on a related complex, $Fe_2(adt^{NBn})(CO)_3(PMe_3)(dppv)$, showed that two electron oxidation causes the amine in the adt to bind to an Fe center, and the formation of this amine bound complex causes the second oxidation to occur at more mild potential than in the analogous pdt complex. Reduction of the amine bound complex causes dissociation of the amine and reformation of the Fe(II)Fe(I) complex.[35] An analogous complex is likely forming upon double oxidation of $\mathbf{1}^{\mathbf{NH}}$ and is the cause of the small $\Delta E_{1/2}$ separating $[\mathbf{1}^{\mathbf{NH}}]^{0/+}$ vs $[\mathbf{1}^{\mathbf{NH}}]^{+/2+}$ (Scheme 2.9). The lack of a pendant base in **2** causes the second oxidation to be irreversible and occur at more positive potentials.

Scheme 2.9. Proposed amine binding upon two electron oxidation of $\mathbf{1}^{\mathbf{NH}}$.

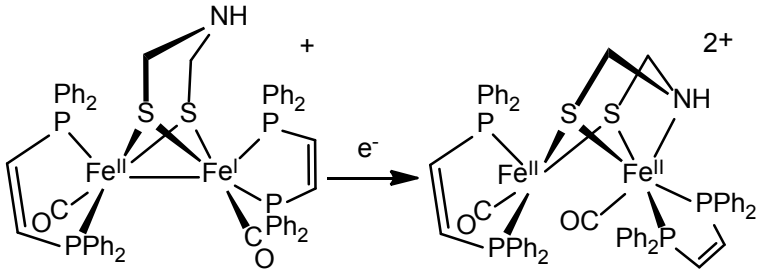

2.4 Protonation of $Fe_2(pdt)(CO)_2(dppv)_2$

Previously, Dr. Bryan Barton showed that, at low temperature, **2** is protonated to form a terminal hydride that is stable at 0 °C for ~30 minutes. Addition of $[H(OEt_2)_2]BAr^F{}_{24}$ ($BAr^F{}_{24}^-$ = $B(3,5\text{-}C_6H_3(CF_3)_2)_4^-$), to a CD_2Cl_2 solution of **2** at -80 °C initially afforded the terminal hydride $[t\text{-}HFe_2(pdt)(CO)_2(dppv)_2]^+$ ($[t\text{-}H\mathbf{2}]^+$)). Its high field ^1H NMR spectrum, a triplet near δ -3.5, indicates a single isomer.[27] This relatively low field chemical shift is often associated with terminal hydrides of related diiron dithiolates. [22-26] The ^{31}P NMR spectrum, which features four equally intense singlets at δ 104, 94, 88, 70 , uniquely defines the structure: the diphosphine on the FeH center is dibasal and the diphosphine on the other ("proximal") Fe center spans apical and basal sites (^{31}P-^{31}P coupling is often weak in such compounds).[36] Selective ^{31}P decoupling of the ^1H NMR spectrum shows that the hydride is coupled to the ^{31}P NMR resonances at δ 94 and 88, indicating that these signals correspond to the two basal phosphorus centers on the Fe-H. The resonances at δ 104 and 70 correspond to phosphorus centers on the non-hydride atom (Figure 2.8). When the sample is warmed to room temperature, the terminal hydride isomerizes

to two isomeric bridging hydrides (μ-H**2**).[32] The pdt complex, **2**, is only protonated by strong acids such as $[H(OEt_2)_2]BAr^F{}_{24}$ or HBF_4Et_2O ($pK_a^{MeCN} = -3$).[37]

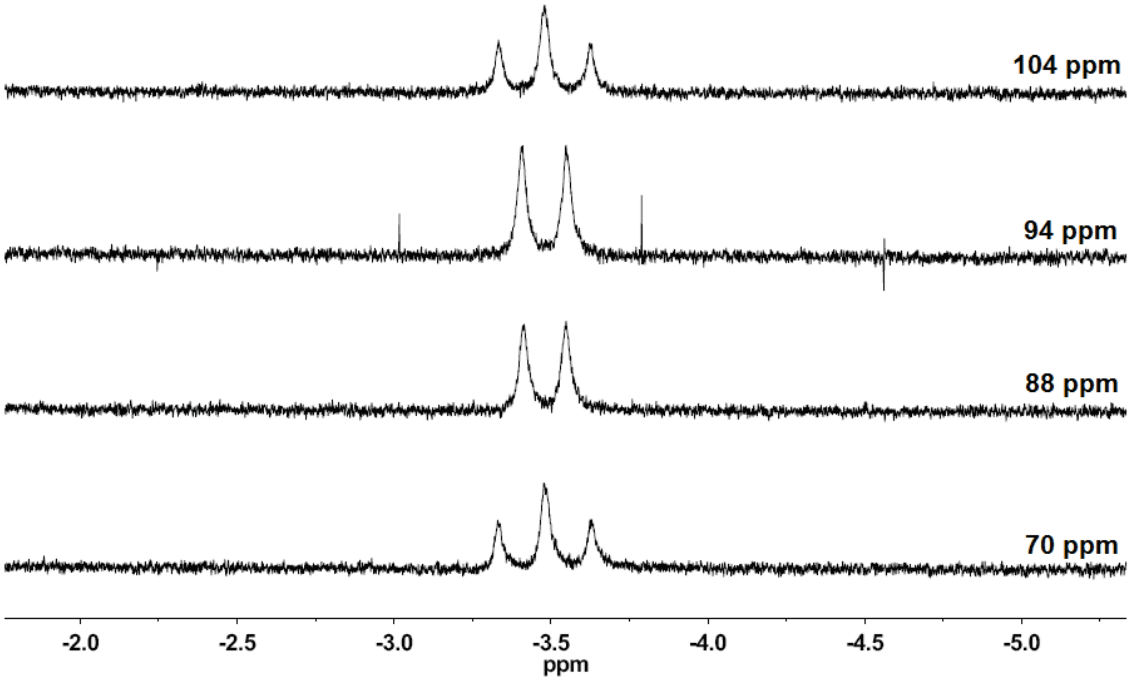

Figure 2.8. High field region of ^{31}P Decoupled ^{1}H NMR spectrum of [*t*-H2]$BAr^F{}_{24}$ (Chemical shift listed corresponds to the ^{31}P NMR shift of the signal that was decoupled).

For similar complexes, $Fe_2(xdt)(CO)_2(PMe_3)_4$ (xdt= pdt, edt), it was found that at -90 °C, protonation occurs at a sulfur of the dithiolate ligand, and there are other examples of S-protonation in diiron dithiolato carbonyl complexes.[28,38-40] Low temperature NMR experiments do not indicate that protonation at sulfur occurs for $\mathbf{1}^{\mathbf{NH}}$ at -90 °C. However, this observation does not rule out the possibility for S-protonation at temperatures below -90 °C.

The IR spectrum of [*t*-H**2**]$^+$ exhibits a strong band at 1965 cm^{-1} (terminal CO), 1905 cm^{-1} (bridging CO), and 1890 cm^{-1}, which we initially assigned as an Fe-H stretch. However, the deuteride, [*t*-D**2**]$^+$ has the same IR spectrum (Figure 2.9). If the band at 1890 cm^{-1} is due to an Fe-H stretch, then it would be expected to shift to lower energy upon deuteration. The ^{31}P NMR spectrum of [*t*-D**2**]$^+$ is identical to that for [*t*-H**2**]$^+$, except that P-D coupling is apparent (Figure 2.10). The IR spectrum of [μ-H**2**]$^+$ only contains ν_{co}= 1951, 1963 cm^{-1}, indicating that the bands at 1890 and 1905 cm^{-1} in the spectrum of [*t*-H**2**]$^+$ are attributed to the terminal hydride species

(Figure 2.11). We propose that two weak bands are present in the IR spectrum due to the presence of two flippamers, and both bands are both due to semi- bridging CO ligands (Scheme 2.10). In the flippamer with the pdt bridgehead CH_2 group adjacent to the hydride, the CO ligand is more bridging, and therefore corresponds to the lower energy band (1890 cm^{-1}). When the CH_2 bridgehead points towards the non-hydride side, the CO is less bridging and therefore corresponds to the higher energy band (1905 cm^{-1}).

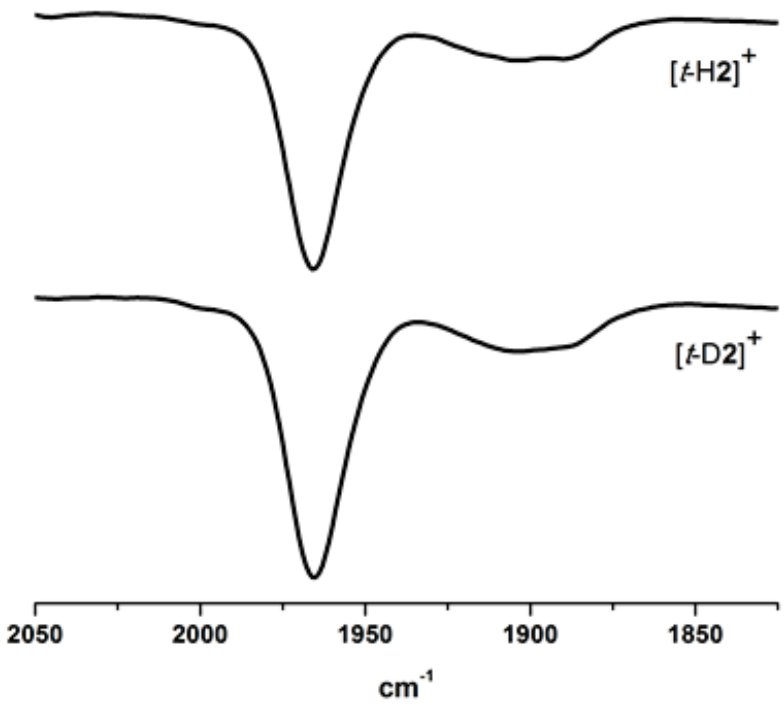

Figure 2.9. IR spectra of $[t\text{-H2}]^+$ and $[t\text{-D2}]^+$ formed by addition of excess $[H(Et_2O)_2]BAr^F{}_{24}$ and $[D(Et_2O)_2]BAr^F{}_{24}$ respectively, to 2, in CH_2Cl_2 at -78 °C.

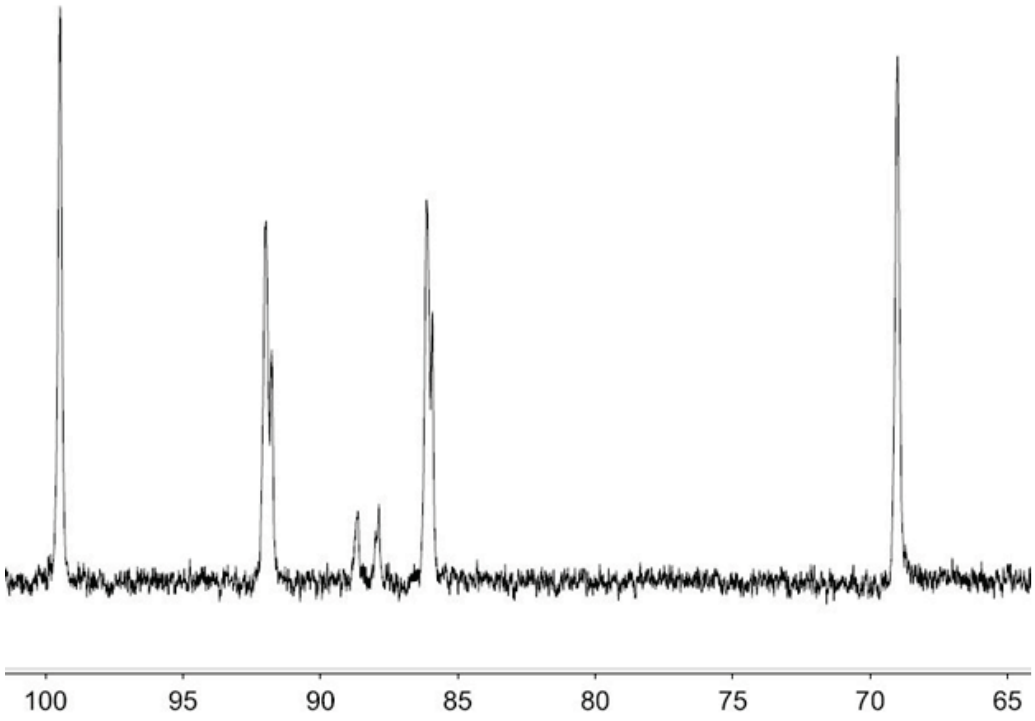

Figure 2.10. ^{31}P NMR spectrum [*t*-D2]$^+$ at -20 °C, formed by addition of excess [D(Et$_2$O)$_2$]BAr$^F_{24}$ to 2 in CH_2Cl_2. Splitting of the signals at δ 86 and 91 is due to coupling of these phosphorus centers with the terminal deuteride. Signals at δ 88 and 89 are due to the presence of small amount of bridging deuteride, [μ-D2]$^+$.

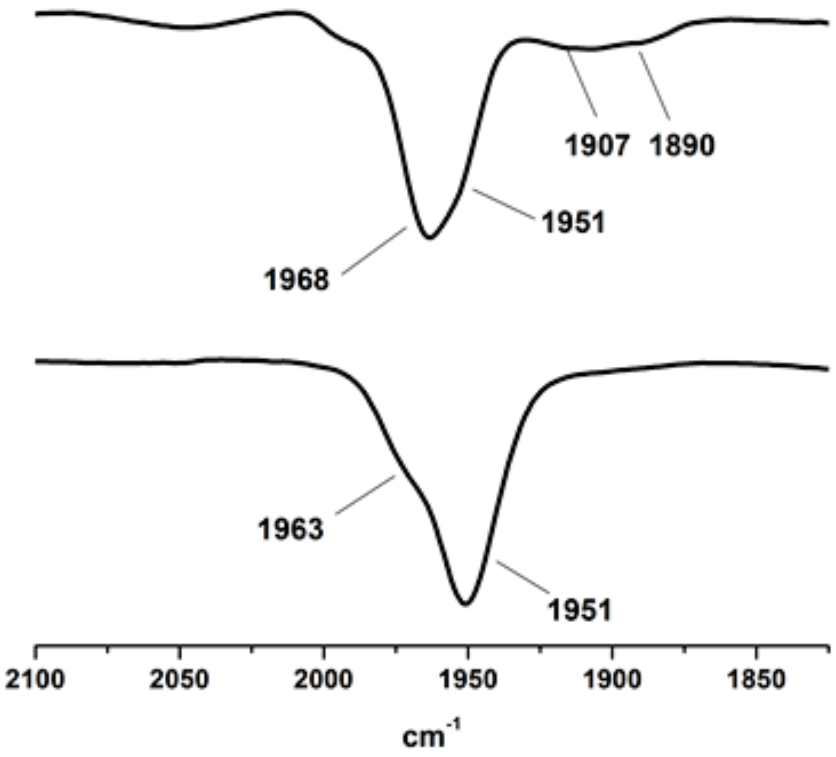

Figure 2.11. Top: IR spectrum of a mixture of $[t\text{-H2}]^+$ (ν_{co}= 1968, 1907, 1890 cm^{-1}) and $[\mu\text{-H2}]^+$ (ν_{co}= 1951 cm^{-1}) formed by protonation of 2 with excess $HBF_4 \cdot Et_2O$ at room temperature in CH_2Cl_2. IR spectrum was acquired immediately after addition of acid. Bottom: IR spectrum of mixture after stirring at room temperature overnight, showing that $[\mu\text{-H2}]^+$ is the only species present.

Scheme 2.10. Proposed structures of $[t\text{-H2}]^+$.

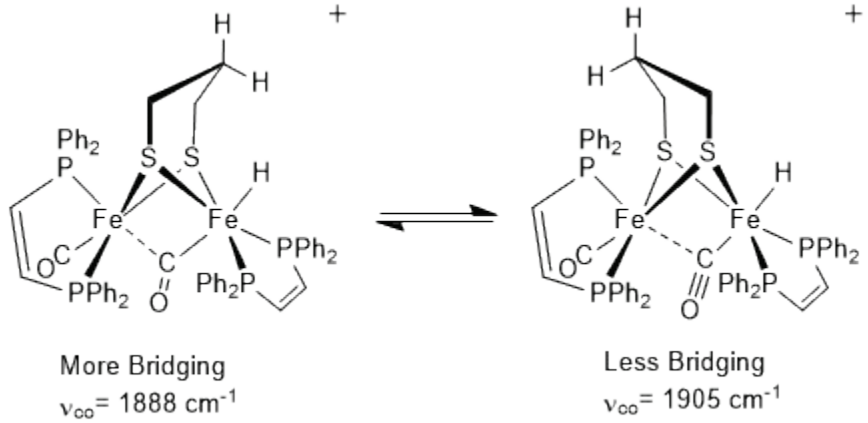

2.5 Singly Protonated Derivatives of $Fe_2(adt^{NH})(CO)_2(dppv)_2$, $\mathbf{1^{NH}}$

Protonation of $\mathbf{1^{NH}}$ with one equivalent of acid gives three isomeric hydrides as well as an ammonium derivative. Addition of $[H(OEt_2)_2]BAr^F{}_{24}$ to a CD_2Cl_2 solution of $\mathbf{1^{NH}}$ at -80 °C initially affords the terminal hydride $[t\text{-}HFe_2(adt^{NH})(CO)_2(dppv)_2]^+$ ($[t\text{-}H\mathbf{1^{NH}}]^+$) (Scheme 2.11). Its high field ^{1}H NMR spectrum, a triplet near δ -4.2, indicates a single terminal hydride isomer (Table 2.4, Figure 2.12a). The ^{31}P NMR spectrum, which features four equally intense singlets (Table 2.4, Figure 2.12a), uniquely defines the structure: the diphosphine on the FeH center is dibasal and the diphosphine on the other ("proximal") Fe center spans apical and basal sites (^{31}P-^{31}P coupling is often weak in such complexes). Selective ^{31}P decoupling of the ^{1}H NMR spectrum shows that the hydride is coupled to the ^{31}P NMR resonances at δ 94 and 83, indicating that these signals correspond to the two basal phosphorus centers on the Fe-H. The resonances at δ 103 and 75 correspond to phosphorus centers on the non-hydride atom (Figure 2.13).

Table 2.4. Spectroscopic data for protonated derivatives of $\mathbf{1^{NH}}$.

Compound	IR: ν_{CO} (cm^{-1})	^{1}H NMR: (δ Hydride)	^{31}P NMR (δ)
$[t\text{-}HFe_2(adt^{NH})(CO)_2(dppv)_2]^+$, $[t\text{-}H\mathbf{1^{NH}}]^+$	1965, 1915	-4.2 (t) J = 73 Hz	103.2, 94.5, 84.0, 75.1
$[t\text{-}HFe_2(adt^{NH2})(CO)_2(dppv)_2]^{2+}$, $[t\text{-}H\mathbf{1^{NH2}}]^{2+}$	1986, 1925	-4.95 (t) J = 72 Hz	98, 89, 76, 74
$[Fe_2(adt^{NH})(\mu\text{-}H)(CO)_2(dppv)_2]^+$, *sym*-$[\mu\text{-}H\mathbf{1^{NH}}]^+$	not obsv'd	-14.8 (tt) J = 25, 5 Hz	91.1, 90.9
$[Fe_2(adt^{NH})(\mu\text{-}H)(CO)_2(dppv)_2]^+$, *unsym*-$[\mu\text{-}H\mathbf{1^{NH}}]^+$	1948, 1969	-13.7 (dtd)	90.1, 87.6, 84.6, 79.2
$[Fe_2(adt^{NH2})(\mu\text{-}H)(CO)_2(dppv)_2]^{2+}$, *sym*-$[\mu\text{-}H\mathbf{1^{NH2}}]^{2+}$	1967, 1985	-15.6 (tt) J = 20, 5 Hz	91.3, 88.7
$[Fe_2(adt^{NH2})(\mu\text{-}H)(CO)_2(dppv)_2]^{2+}$, *unsym*-$[\mu\text{-}H\mathbf{1^{NH2}}]^{2+}$	not obsv'd	-14.5 (dtd)	92.3, 86.0, 82.4, 79.0

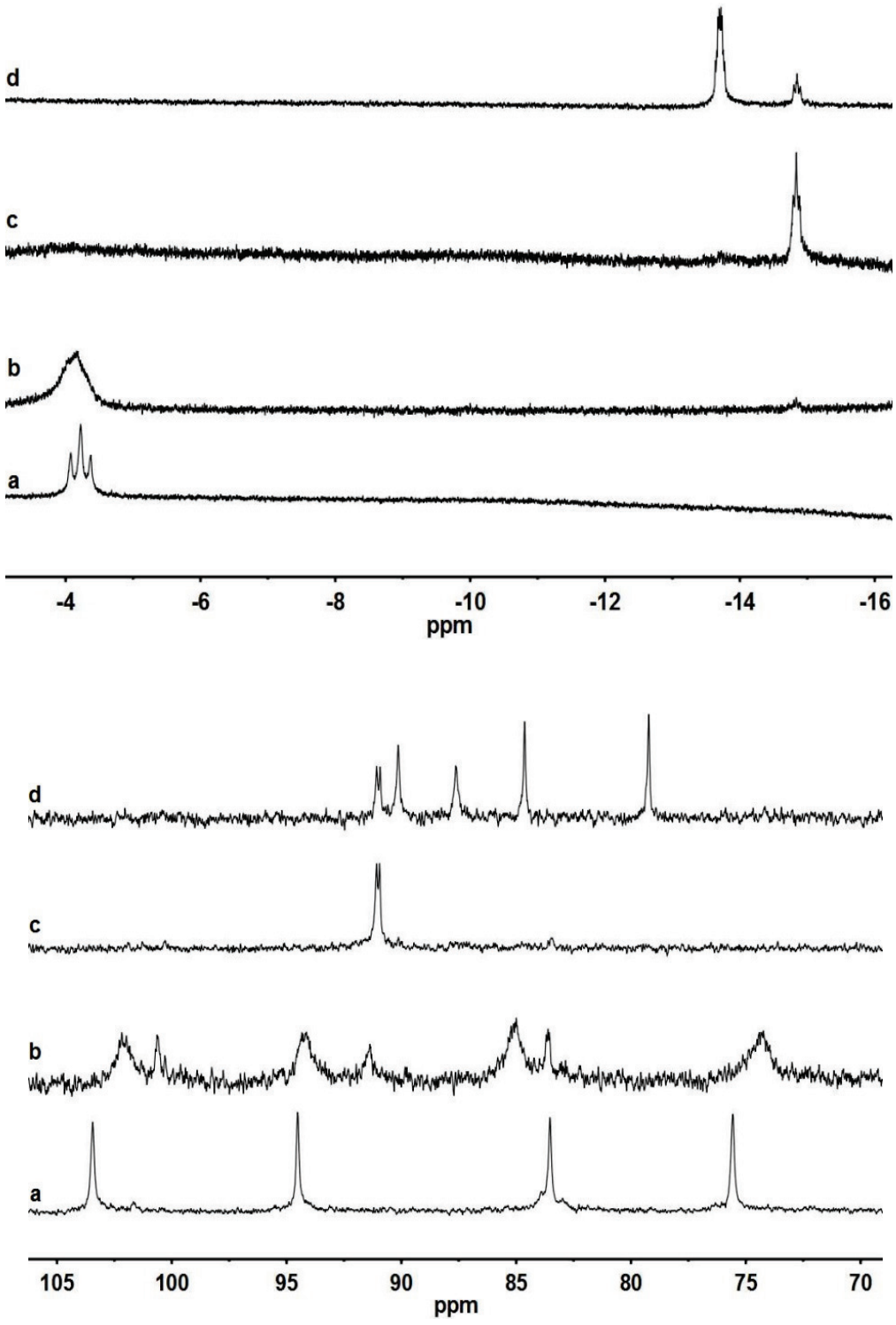

Figure 2.12. ^{1}H and ^{31}P NMR spectra of the products of the protonation of 1^{NH} with $[H(OEt_2)_2]BAr^F{}_4$ in CD_2Cl_2 at various times and temperatures. Spectra a: -80 ºC ($[t\text{-}H1^{NH}]^+$). Spectra b: sample warmed to -10 ºC. Spectra c: sample warmed to 20 ºC (*sym*-$[\mu\text{-}H1^{NH}]^+$, Spectra d: previous sample after standing at 20 °C for 24 h, (mixture of *sym*- and *unsym*-$[\mu\text{-}H1^{NH}]^+$).

Scheme 2.11. Routes of protonation of 1^{NH}.

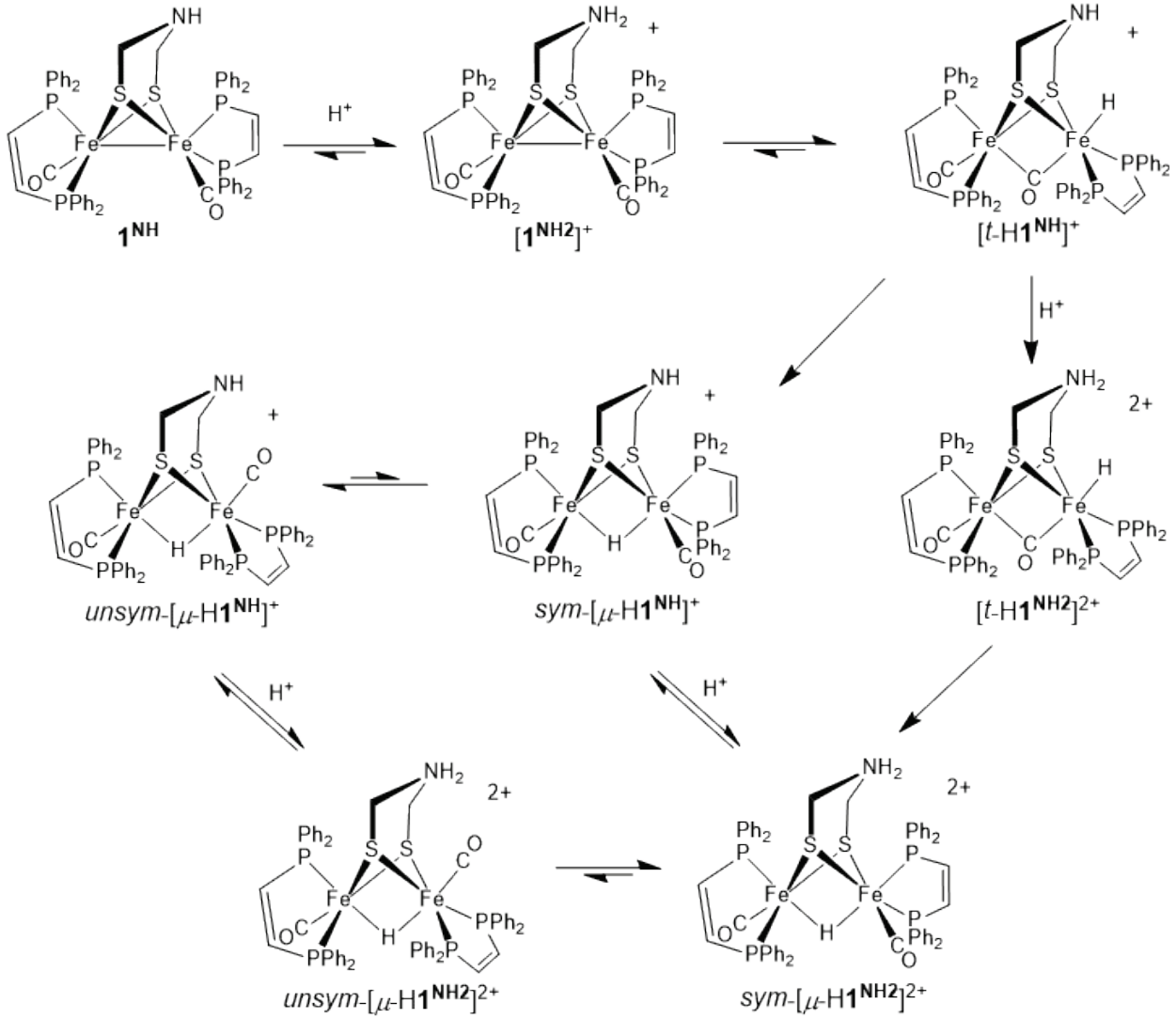

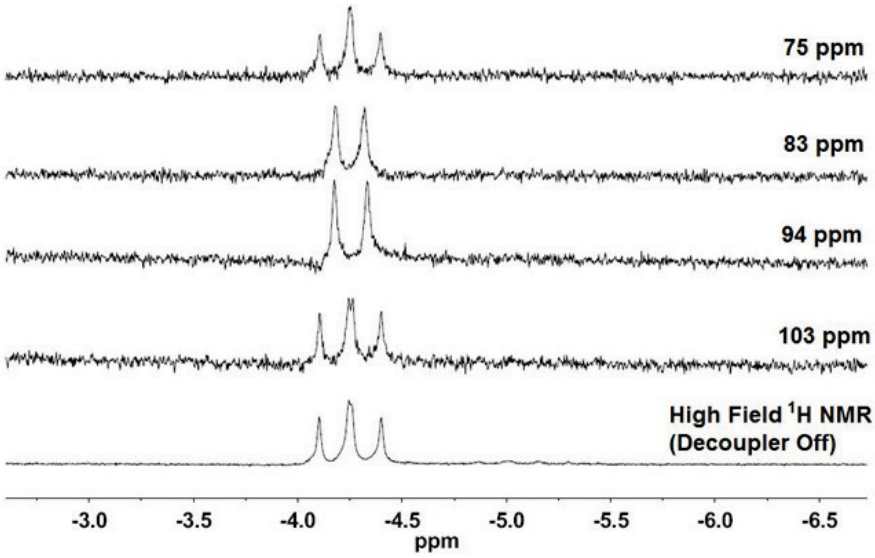

Figure 2.13. High field region of ^{31}P decoupled ^{1}H NMR of [*t*-H1**^{NH}]BAr$^{F}_{24}$ (Chemical shift listed corresponds to the ^{31}P NMR shift of the signal that is decoupled)**

Formation of [*t*-H**1**^{NH}]$^{+}$ is also confirmed by IR spectroscopy. When [H(OEt$_2$)$_2$]BAr$^{F}_{24}$ is added to a CH_2Cl_2 solution of **1**^{NH} at -78 °C, the solution remains green in color. The IR spectrum exhibits a strong band at 1965 cm^{-1}, corresponding to a terminal CO ligand, and a weak band at 1915 cm^{-1}, corresponding to a semi-bridging CO ligand (Table 2.4, Figure 2.14).

Above -20 °C, the triplet at δ -4.2 in the ^{1}H NMR spectrum broadens, as do the ^{31}P NMR signals, and additional signals appear in the ^{31}P NMR spectrum (Figure 2.12b). These changes are consistent with exchange between the Fe-hydride and ammonium tautomer, [**1**^{NH2}]$^{+}$ (Scheme 2.12). Further evidence for the formation of this ammonium species [**1**^{NH2}]$^{+}$ is provided by experiments in which **1**^{NH} was protonated with $HBF_4{\cdot}Et_2O$, rather than [H(OEt$_2$)$_2$]BAr$^{F}_{24}$. Treatment of CH_2Cl_2 solutions with $HBF_4{\cdot}Et_2O$ afforded not only [*t*-H**1**^{NH}]$^{+}$ but also a second species (Figure 2.14). The pattern for the ν_{CO} bands for the other species is identical to that for **1**^{NH}, but the bands are shifted approximately 20 cm^{-1} to higher energy, characteristic of *N*-protonation.[41-43] The new species is thus assigned as the ammonium tautomer [**1**^{NH2}]$^{+}$, (Schemes 2.11, 2.12). The formation of the tautomer is attributed to the ability of BF_4^- to participate in hydrogen-bonding, which has been observed previously in complexes of protonated adt ligands.[44] Upon addition of excess [Bu$_4$N]BF$_4$, the ratio [*t*-H**1**^{NH}]$^{+}$/[**1**^{NH2}]$^{+}$ increased from 2:1 to approximately 1:1, confirming that BF_4^- stabilizes [**1**^{NH2}]$^{+}$ (Figure 2.15).

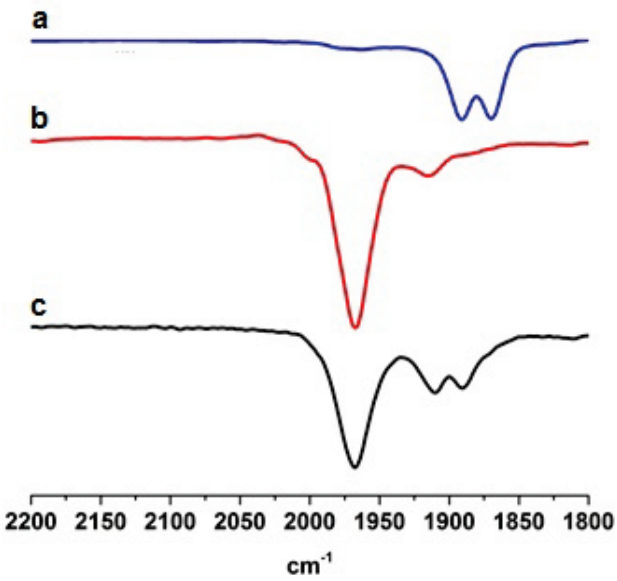

Figure 2.14. IR spectra of (a)1^{NH}, (b) $[t\text{-}H1^{NH}]^+$ formed by protonation of 1^{NH} with $[H(OEt_2)_2]BAr^F{}_{24}$ at -78 °C, and (c) a mixture of $[t\text{-}H1^{NH}]^+$ and $[1^{NH2}]^+$ formed by protonation of 1^{NH} with $HBF_4.Et_2O$ at -78 °C in CH_2Cl_2.

Scheme 2.12 Proposed hydrogen bonding interaction between $[1^{NH2}]^+$ and BF_4^- resulting in stabilization of the ammonium tautomer.

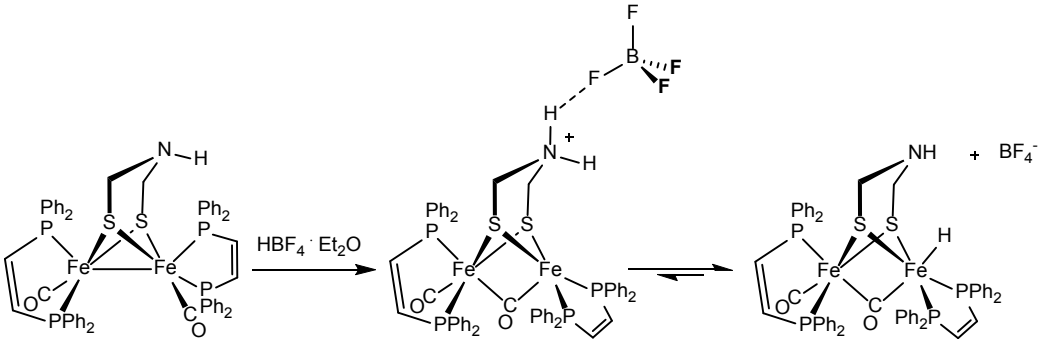

a.

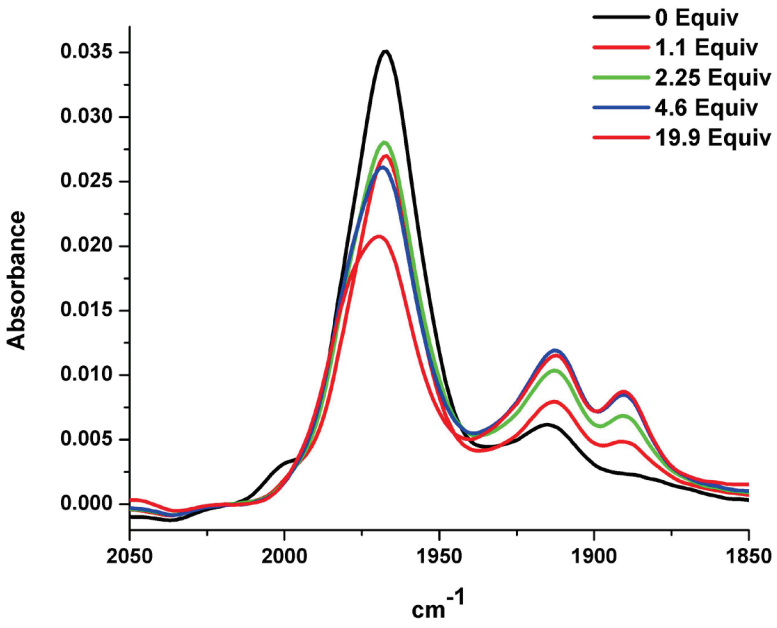

b.

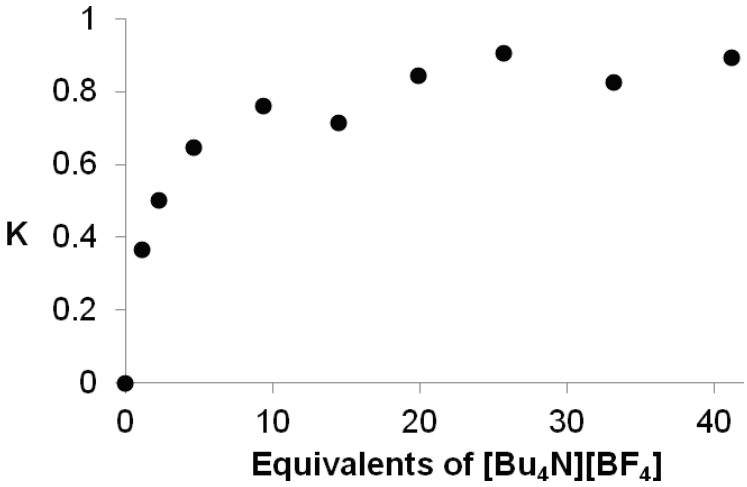

Figure 2.15 a. IR spectra of a solution of [*t*-H1^{NH}]BAr$^{F}_{24}$ with 0, 1, 2, 3, 10 equiv of added [Bu$_4$N]BF$_4$ at -78 °C b. Graph of K (the equilibrium ratio of [*t*-H1^{NH}]$^+$/[H1^{NH}]$^+$) vs. equivalents BF$_4^-$ for a CH$_2$Cl$_2$ solution of [*t*-H1^{NH}]BAr$^{F}_{24}$.

We investigated the reactivity of the ammonium species, $[\mathbf{1}^{\mathbf{NH2}}]^+$, with CO_2. The presence of acidic (NH_2^+) and basic (Fe) sites adjacent to one another could potentially enable the activation of CO_2. However, exposure of a solution of a mixture of $[t\text{-H}\mathbf{1}^{\mathbf{NH}}]^+$ and $[\mathbf{1}^{\mathbf{NH2}}]^+$ to CO_2 resulted in deprotonation of $[\mathbf{1}^{\mathbf{NH2}}]^+$ to form $\mathbf{1}^{\mathbf{NH}}$. No reaction occurred between $[t\text{-H}\mathbf{1}^{\mathbf{NH}}]^+$ and CO_2. (Figure 2.16).

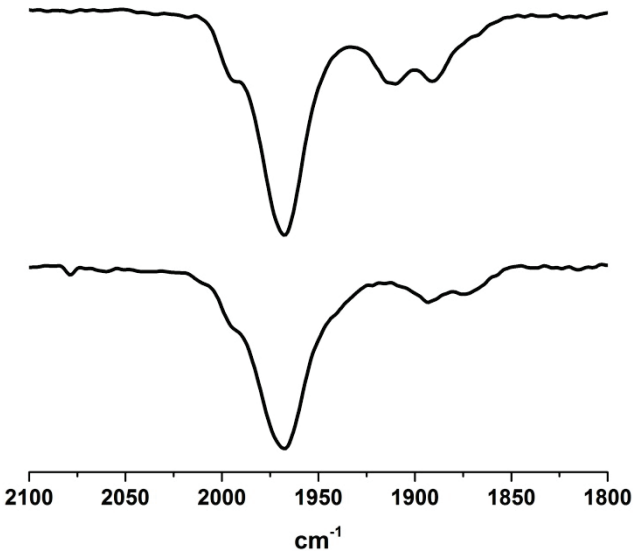

Figure 2.16. IR spectrum of $\mathbf{1}^{\mathbf{NH}}$ + 1.2 equiv $HBF_4{\cdot}Et_2O$ in CH_2Cl_2 at -78 °C (top) and under an atmosphere of CO_2 at 0 °C (bottom).

Near room temperature, $[t\text{-H}\mathbf{1}^{\mathbf{NH}}]^+$ converts sequentially to two isomers that feature bridging hydride ligands ("μ-hydrides", Scheme 2.11). The first μ-hydride isomer, *sym*-$[\mu\text{-H}\mathbf{1}^{\mathbf{NH}}]^+$, has C_2-symmetry (ignoring the adt ligand, which is rapidly flexing and hence effectively planar). In *sym*-$[\mu\text{-H}\mathbf{1}^{\mathbf{NH}}]^+$, each dppv ligand spans one apical and one basal site (Table 2.4, Figure 2.12c). When a solution of *sym*-$[\mu\text{-H}\mathbf{1}^{\mathbf{NH}}]^+$ is recooled to 0 °C, the terminal hydride species does not reform (Figures 2.17). Within minutes at room temperature, *sym*-$[\mu\text{-H}\mathbf{1}^{\mathbf{NH}}]^+$ converts to an unsymmetrical isomer labeled *unsym*-$[\mu\text{-H}\mathbf{1}^{\mathbf{NH}}]^+$. In *unsym*-$[\mu\text{-H}\mathbf{1}^{\mathbf{NH}}]^+$, one diphosphine remains apical-basal and the other is dibasal as indicated by the ^{31}P NMR spectrum, which consists of four singlets (Table 2.4, Figure 2.12d). When the solution is allowed to stand for 12 h at room temperature, a 1:5 equilibrium distribution is reached, favoring *unsym*-$[\mu\text{-H}\mathbf{1}^{\mathbf{NH}}]^+$. The isomerization of $([t\text{-H}\mathbf{1}^{\mathbf{NH}}]^+$ is similar to that observed for the hydrides of **2**.[27] The

formation of the μ-hydrides is also indicated by a change in the IR spectrum. When a solution of [*t*-H**1**$^{\mathbf{NH}}$]$^+$ is warmed to room temperature, the solution changes color from green to orange-brown, and the IR spectrum shows two bands at 1948 and 1969 cm^{-1}, corresponding to *unsym*-[μ-H**1**$^{\mathbf{NH}}$]$^+$ (Table 2.4, Figure 2.18). The IR spectrum of *sym*-[μ-H**1**$^{\mathbf{NH}}$]$^+$ could not be recorded due to its fairly rapid isomerization to the unsymmetrical isomer.

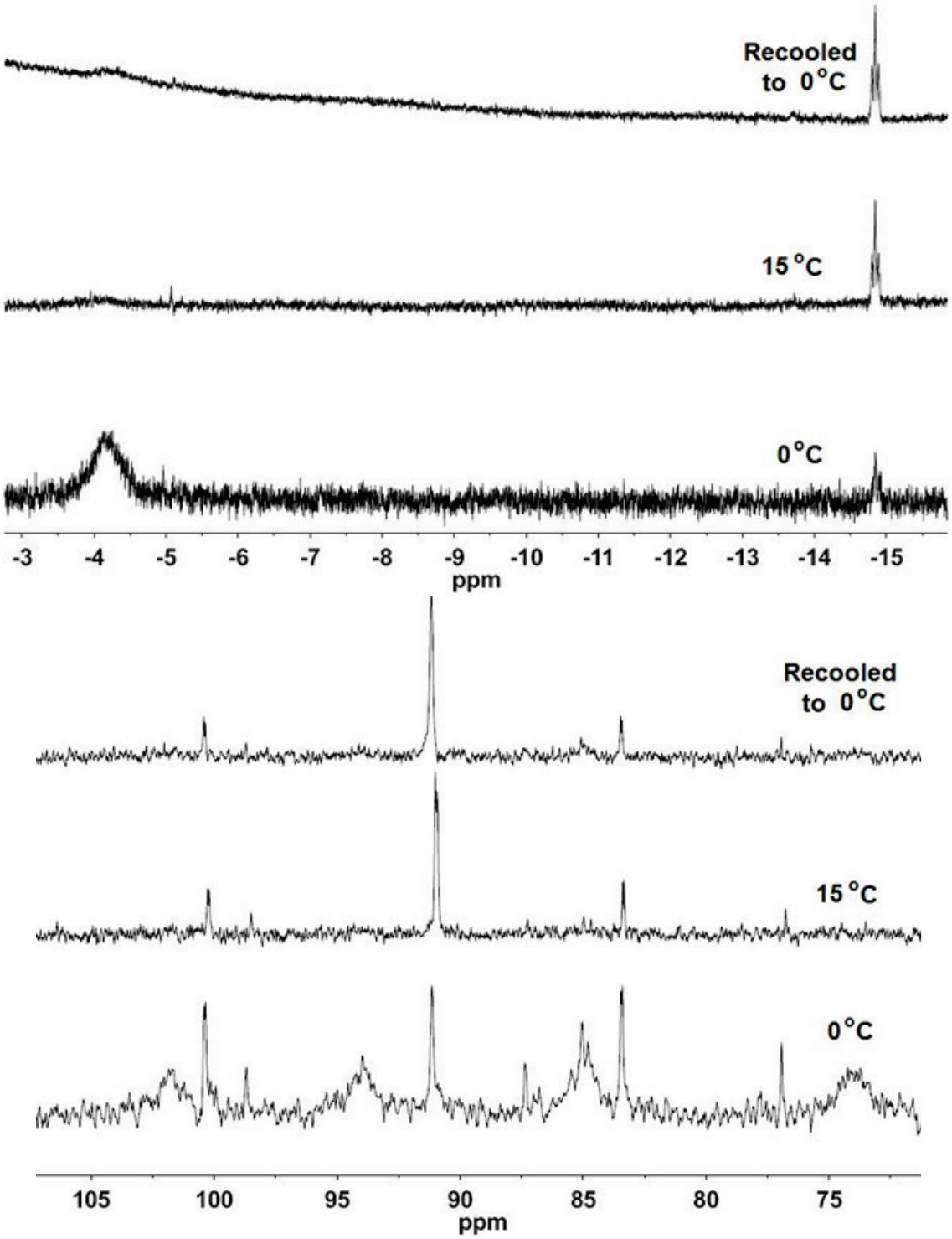

Figure 2.17. High field region of ^{1}H NMR spectrum (top) and ^{31}P NMR spectrum (bottom) of [*t*-H1^{NH}]BAr$^{F}_{24}$ and *sym*-[μ-H1^{NH}]BAr$^{F}_{24}$. At 0 °C [*t*-H1^{NH}]BAr$^{F}_{24}$ is the major species. Upon warming to 15 °C, *sym*-[μ-H1^{NH}]BAr$^{F}_{24}$ is the major species, and this does not change upon recooling to 0 °C.

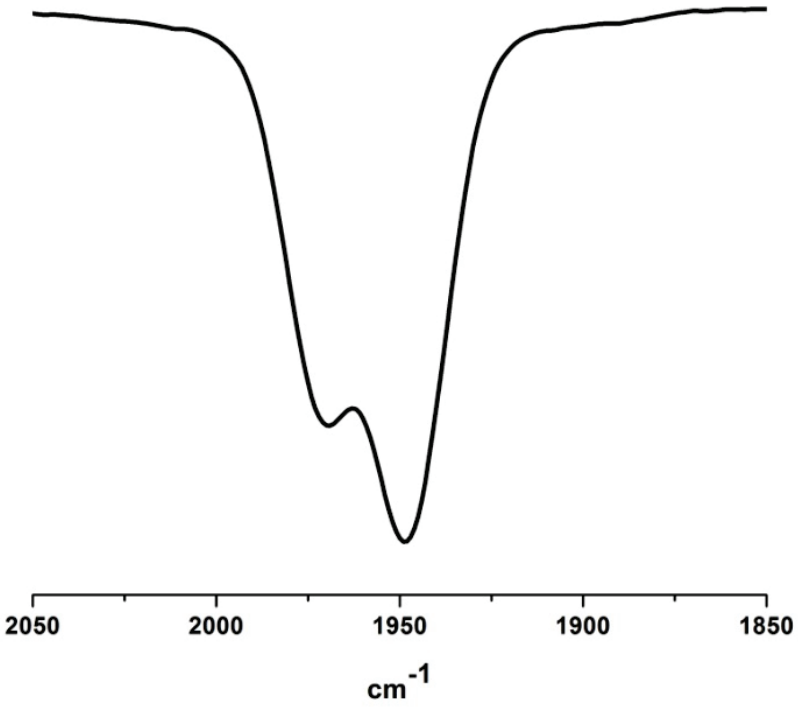

Figure 2.18. IR spectrum of *unsym*-[μ-H1^{NH}]$^+$ in CH_2Cl_2 at room temperature.

2.6 Doubly Protonated Derivatives of $\mathbf{1}^{NH}$

Relevant to the electrocatalysis discussed in Chapter 3, $\mathbf{1}^{NH}$ undergoes double protonation. Addition of *excess* of $[H(OEt_2)_2]BAr^F{}_{24}$, $\mathbf{1}^{NH}$ gave a new species assigned as the ammonium-hydride [*t*-H$\mathbf{1}^{NH2}$]$^{2+}$. According to ^{1}H and ^{31}P NMR spectra, [*t*-H$\mathbf{1}^{NH2}$]$^{2+}$ is structurally similar to [*t*-H$\mathbf{1}^{NH}$]$^+$, i.e. a single isomer with both dibasal (distal to the hydride) and apical-basal (proximal) diphosphine ligands (Table 2.4, Figure 2.19a). The IR spectrum of [*t*-H$\mathbf{1}^{NH2}$]$(BF_4)_2$ exhibits a ν_{CO} pattern identical to [*t*-H$\mathbf{1}^{NH}$]$^+$, but as seen for $\mathbf{1}^{NH}$ vs [$\mathbf{1}^{NH2}$]$^+$, *N*-protonation shifts ν_{CO} bands in the IR spectrum to higher energy by 20 cm^{-1}, compared to that for [*t*-H$\mathbf{1}^{NH}$]$^+$ (Table 2.4, Figure 2.20).

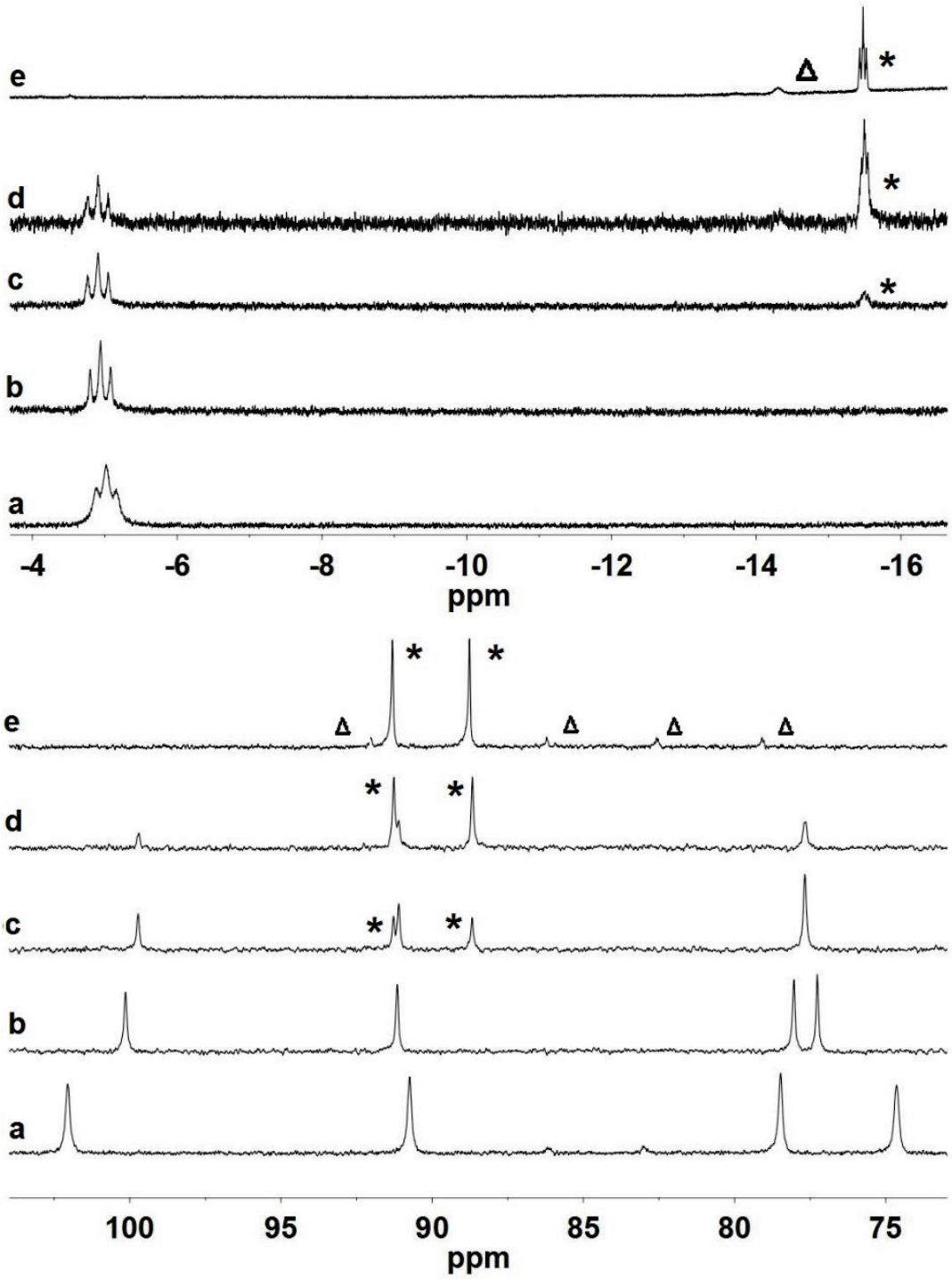

Figure 2.19. ^{1}H and ^{31}P NMR spectra of the protonation of 1^{NH} with 2 equiv of $[H(OEt_2)_2]BAr^F{}_4$ in CD_2Cl_2 at various times and temperatures. Spectra a: -90 ºC ([*t*-$H1^{NH2}$]). Spectra b: sample warmed to 0 ºC. Spectra c: sample warmed to 20 ºC (mixture of [*t*-$H1^{NH2}$] and *sym*-[μ-$H1^{NH}$]$^+$, the latter indicated by asterix), Spectra d: previous sample after standing at 20 °C for 30 min, Spectra e: sample after standing 20 °C for 24 h (mixture of *sym*- and *unsym*-[μ-$H1^{NH}$]$^+$, indicated by asterisk and triangle respectively).

Figure 2.20 IR spectrum of [*t*-H1^{NH2}]$^{2+}$ formed by protonation of 1^{NH} with 2 equivalents of $HBF_4 \cdot Et_2O$ in CH_2Cl_2 at 0 °C.

Single crystals of the ammonium hydride were obtained in the form of the salt [*t*-H**1**^{NH2}]$(BF_4)_2$ (Figure 2.21). In the dication, two Fe(dppv)(CO) centers are linked in the usual way by a dithiolate. One CO ligand is semi-bridging with an Fe-Fe-C and Fe-C-O angles of 66.68(14) and 166.1(4)º, respectively.[45] The dispositions of the dppv groups, being dibasal and apical-basal, conform with the NMR measurements. The crystals are of sufficient quality that the H centers attached to nitrogen and iron were located and refined. Two phenyl groups on the Fe(1)(dppv) center, equivalent to the distal Fe in the active site, form a pocket around the Fe-H and N-H centers. The Fe-H distance of 1.44(4) Å is normal for a ferrous hydride.[46] The ammonium center of the dithiolate cofactor adtH$^+$ is adjacent to the Fe-*H* center. The NH---HFe distance of 1.88(7) Å is shorter than 2.4 Å distance that is twice the van der Waals radius of hydrogen,[47] indicative of dihydrogen bonding.

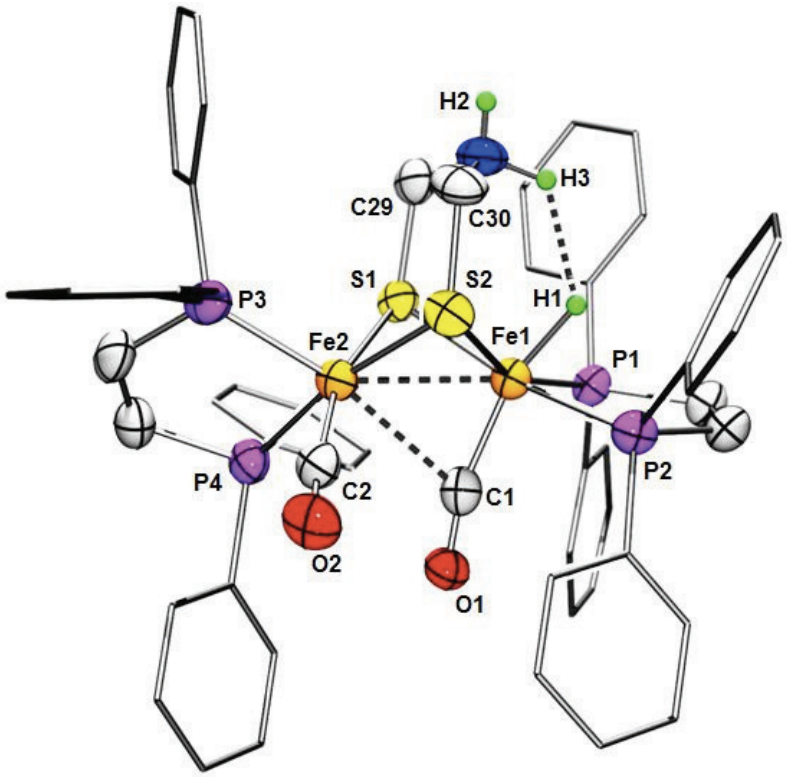

Figure 2.21. Structure of [*t*-HFe$_2$(adt^{NH2})(CO)$_2$(dppv)$_2$](BF$_4$)$_2$, [*t*-H1**^{NH2}](BF$_4$)$_2$. Counter ions and solvent of crystallization are not shown. Selected distances (Å): H1---H2, 1.88(7); Fe1-C1, 1.794(5); Fe1-P2, 2.2141(13); Fe1-P1, 2.2196(12); Fe1-S2, 2.2610(12); Fe1-S1, 2.3009(13); Fe1-Fe2, 2.6155(9); Fe1-H1, 1.44(4); Fe2-C2, 1.769(5); Fe2-P3, 2.2122(14); Fe2-S2, 2.2348(14); Fe2-S1, 2.2564(12); Fe2-P4, 2.2686(14). Angles (º): C1-Fe1-Fe2, 66.68(14); Fe2-Fe1-H1, 130.3(18); S2-Fe1-S1, 83.50(4); S2-Fe2-S1, 85.12(4); O1-C1-Fe1, 166.1(4).**

Warming a CD_2Cl_2 solution of [*t*-H**1**^{NH2}](BAr$^F{}_{24}$)$_2$ does not cause a change in the ^{1}H or ^{31}P NMR spectra until the solution reaches 20 °C (Figure 2.19). At this temperature, the symmetrical μ-hydride, *sym*-[μ-H**1**^{NH2}]$^{2+}$ forms, as indicated by the appearance of a triplet of triplets in the high field region of the ^{1}H NMR spectrum and two singlets in the ^{31}P NMR spectrum. Over time, a multiplet appears in the ^{1}H NMR spectrum, along with four singlets in the ^{31}P NMR spectrum, indicative of formation of the unsymmetrical species, *unsym*-[μ-H**1**^{NH2}]$^{2+}$. However, in this case, the symmetrical isomer is the major species (Table 2.4, Figure 2.19). The ammonium bridging hydide species also forms by addition of [H(OEt$_2$)$_2$]BAr$^F{}_4$ to a CH_2Cl_2 solution of [μ-H**1**^{NH}]$^+$. Again, *N*-protonation shifts the ν_{CO} pattern in the IR spectrum about 15 cm^{-1} to higher energy (Table 2.4, Figure 2.22).

Cooling a CD_2Cl_2 solution of $[\mu\text{-H}\mathbf{1}^{\mathbf{NH2}}]^{2+}$ results in the appearance of four additional signals in the ^{31}P NMR spectrum, indicating that at room temperature, the dithiolate is rapidly flipping, resulting in the appearance of two signals in the ^{31}P NMR spectrum. However, this motion is halted at low temperature, which causes all four phosphorus centers to be inequivalent, and thus the appearance of four new signals (Figure 2.23).

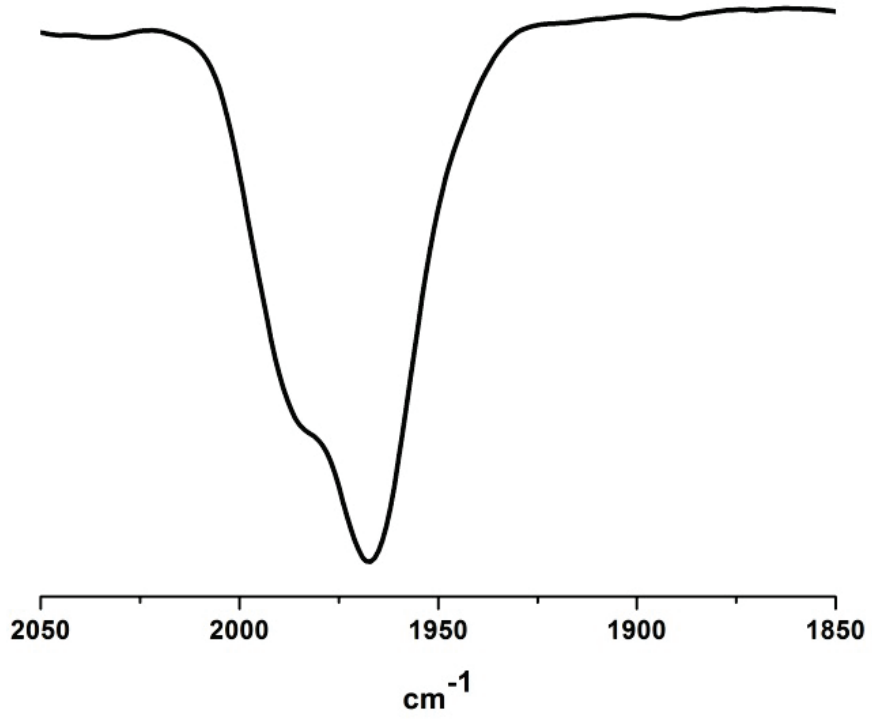

Figure 2.22. IR spectrum of $[\mu\text{-H}\mathbf{1}^{\mathbf{NH2}}]^{2+}$ formed by isomerization of $[t\text{-H}\mathbf{1}^{\mathbf{NH2}}]^{2+}$ at 20 °C in CH_2Cl_2.

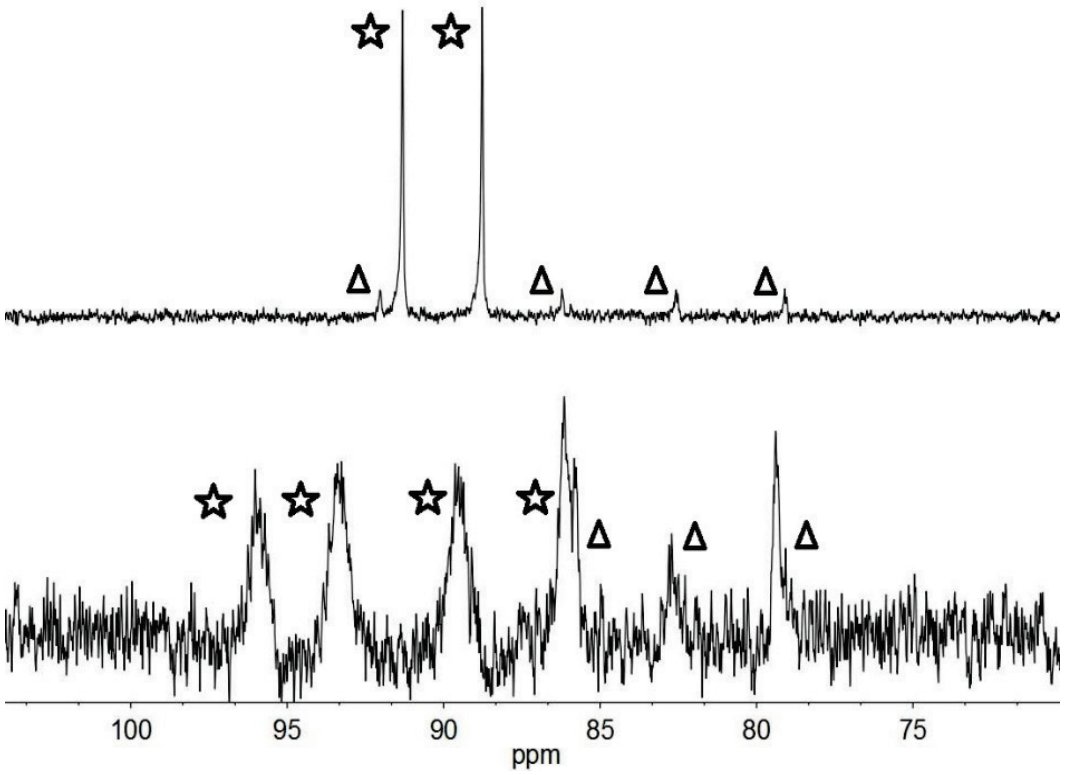

Figure 2.23. ^{31}P NMR spectrum of [μ-H1^{NH2}]$^{2+}$ in CD_2Cl_2 at 20 C (top) and -90 C (bottom). *sym*-[μ-H1^{NH2}]$^{2+}$ indicated by star; *unsym*-[μ-H1^{NH2}]$^{2+}$ indicated by triangle.

2.7 Protonation of $Fe_2(adt^{NH})(CO)_2(dppv)_2$, $\mathbf{1}^{NH}$, with Weak Acids.

Weak acids that do not convert $\mathbf{1}^{NH}$ into detectable levels of [*t*-H$\mathbf{1}^{NH}$]$^+$ at low temperatures quantitatively give [μ-H$\mathbf{1}^{NH}$]$^+$ near room temperature. Qualitatively, the rate of formation of [μ-H$\mathbf{1}^{NH}$]$^+$ correlates with the strength of the acid. Thus, $[HNMe_3]BAr^F{}_4$ ($pK_a^{MeCN} = 17.6$)[37] rapidly converted **1** to [μ-H$\mathbf{1}^{NH}$]$^+$, whereas the same conversion using $[HNEt_3]BF_4$ ($pK_a^{MeCN} = 18.6$)[37] required days for partial conversion (along with decomposition of the diiron species). Addition of H_2ClCCO_2H ($pK_a^{MeCN} = 15.3$)[37] to $\mathbf{1}^{NH}$ results in formation of [*t*-H$\mathbf{1}^{NH}$]$^+$. Based on these results, the pK_a of [*t*-H$\mathbf{1}^{NH}$]$^+$ is estimated to be between 15.3 and 18.6, on the MeCN pK_a scale.

Addition of CF_3CO_2H ($pK_a^{MeCN} = 12.7$)[37] to $\mathbf{1}^{NH}$ at -40 °C gave [*t*-H$\mathbf{1}^{NH2}$]$^{2+}$. The IR spectrum (ν_{CO} = 1986 and 1950 cm^{-1}) of the trifluoroacetate (Figure 2.24) differs from that (ν_{CO} = 1986 and 1925 cm^{-1}) obtained by protonation with $[H(OEt_2)_2]BAr^F{}_4$ and HBF_4•Et_2O, a difference attributed to hydrogen bonding between the trifluoroacetate and the protonated adt ligand. In contrast to the acid-base behavior of $\mathbf{1}^{NH}$, the pdt derivative, **2**, is unaffected by weak acids at low temperature. At room temperature, addition of CF_3COOH to **2** results in partial

formation of [μ-**2**H]$^+$, but the reaction is slow and complete protonated of **2** is not achieved after days.

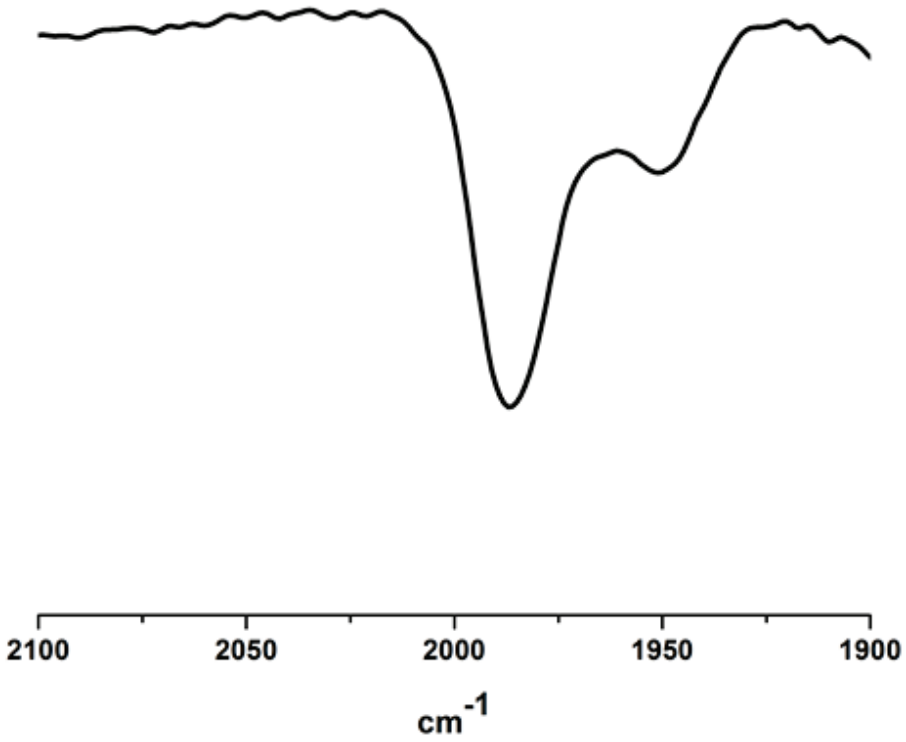

Figure 2.24. IR spectrum of [*t*-H1H]$^{2+}$ formed by protonation of 1^{NH} with 2 equiv of CF_3COOH in CH_2Cl_2 at -78 °C.

2.8 Conclusions

Complexes of the type $Fe_2(xdt)(CO)_2(dppv)_2$ (xdt = adt^{NH}, **1**^{NH}; xdt = pdt, **2**) exhibit very similar spectroscopic properties. These data suggest that the adt^{NH} and pdt ligands have similar inductive effects, and hence similar thermodynamic properties (acidity, hydridicity). Additionally, both complexes are oxidized by one electron at potentials that are within 100 mV of each other (-0.840 V vs -0.940 V), providing further evidence for the similarity of the electronic properties of these two ligands. The presence of the amine functionality in **1**^{NH} enables a more mild second oxidation, compared with **2**.

For both complexes **1**^{NH} and **2**, the kinetic product of protonation is a terminal hydride species, and these are the first examples of diiron terminal hydrides that are stable above -30 °C. In all cases, the terminal hydride species isomerize to corresponding bridging hydrides if

solutions are left at room temperature. Despite the similar electronic properties of these two related complexes, $\mathbf{1}^{\mathbf{NH}}$ can be protonated with weak acids ($pK_a^{MeCN} \sim 15$), whereas **2** can be protonated only by very strong acids, such as $HBF_4 \cdot Et_2O$ (pK_a^{MeCN} -3). This difference is also attributed to the presence of a pendant amine in $\mathbf{1}^{\mathbf{NH}}$, which is initially protonated and relays the proton to the Fe center. Upon protonation of the amine, the effective concentration of protons adjacent to the Fe center is increased, enabling the protonation with weak acids. In the case of **2**, the lack of a pendant amine requires strong acid to protonate the Fe center.

The presence of the amine in $\mathbf{1}^{\mathbf{NH}}$ results in additional differences of these two complexes. A combination of IR and NMR spectroscopic data supports the protonation pathways illustrated in Scheme 2.11. As mentioned above, initial protonation occurs at the amine, resulting in formation of an ammonium species, which then converts to a terminal hydride species. The basicities of two sites - the terminal Fe center and the amine are closely balanced. In CH_2Cl_2 solution, Fe is more basic, and therefore, the terminal Fe-hydride is the major species. However, the equilibrium shifts in the presence of hydrogen-bond acceptors as demonstrated with the influence of $[Bu_4N]BF_4$ on this equilibrium. The lower basicity of a terminal Fe site vs the Fe-Fe bond is indicated by the conversion of mixtures of ammonium cations and $\mathbf{1}^{\mathbf{NH}}$ into $[\mu\text{-H}\mathbf{1}^{\mathbf{NH}}]^+$ under conditions where $[t\text{-H}\mathbf{1}^{\mathbf{NH}}]^+$ is undetectable. A sequence of three processes is invoked to explain the formation the μ-hydride under these conditions: (i) *N*-protonation, albeit unfavorable, (ii) tautomerization of ammonium species to the terminal hydride $[t\text{-H}\mathbf{1}^{\mathbf{NH}}]^+$, and (iii) isomerization of $[t\text{-H}\mathbf{1}^{\mathbf{NH}}]^+$ to $[\mu\text{-H}\mathbf{1}^{\mathbf{NH}}]^+$. The pK_a of $[t\text{-H}\mathbf{1}^{\mathbf{NH}}]^+$ is estimated at 16, and the pK_a of $[\mu\text{-H}\mathbf{1}^{\mathbf{NH}}]^+$ is > 18.6 (MeCN scale).

The presence of this basic site results in formation of doubly protonated ammonium hydrides, in the presence of excess acid. The doubly protonated ammonium hydride $[t\text{-H}\mathbf{1}^{\mathbf{NH2}}]^{2+}$ was crystallographically characterized, and this is the first example of a crystal structure of a diiron terminal hydride that was prepared by biologically relevant protonation of a neutral diiron species. An important aspect of the crystal structure is the short distance between the hydride and the proton on the ammonium cofactor. An attractive $NH^{\delta+}$---$H^{\delta-}$ interaction may be relevant to the small separation between the first and second protonation constants, estimated at only 10^2 in CH_2Cl_2 solution. In comparison with $[t\text{-H}\mathbf{1}^{\mathbf{NH}}]^+$, the $[t\text{-H}\mathbf{1}^{\mathbf{NH2}}]^{2+}$ isomerizes to the μ-hydride more slowly, which may result from this interaction. The implied dihydrogen bonding provides

a snapshot of a step in the formation and scission of a dihydrogen molecule at the active site of the [FeFe]-H_2ase.

2.9 Experimental

Reactions were typically conducted using Schlenk techniques at room temperature. Most reagents were purchased from Aldrich and Strem. Solvents were HPLC-grade and dried by filtration through activated alumina or distilled under nitrogen over an appropriate drying agent. $HBF_4{\cdot}Et_2O$ (Sigma-Aldrich) was supplied as 51-57% HBF_4 in Et_2O (6.91 – 7.71 M). $[H(OEt_2)_2]BAr^F{}_4$ was prepared by literature methods.[48] $[Bu_4N]PF_6$ was purchased from GFS Chemicals and was recrystallized multiple times by extraction into acetone followed by precipitation by ethanol. ^{1}H NMR spectra (500 and 400 MHz) are referenced to residual solvent referenced to TMS. ^{31}P NMR spectra (202 or 161 MHz) were referenced to external 85% H_3PO_4. FT-IR spectra were recorded on a Perkin Elmer Spectrum 100 FT-IR spectrometer.

$Fe_2(adt^{NH})(CO)_4(dppv)$. A solution of $Fe_2(adt^{NH})(CO)_6$[28] (175 mg, 0.45 mmol) and dppv (179 mg, 0.45 mmol) in 15 mL of toluene was treated with a solution of anhydrous Me_3NO (34 mg, 0.45 mmol) in ca. 5 mL of MeCN. Bubbles appeared, and the reaction mixture darkened. After heating the mixture at reflux for 5 h, the FT-IR spectrum indicated complete conversion to product. Solvent was removed under vacuum, and the product was extracted into 5 mL of CH_2Cl_2. Addition of 50 mL of hexane precipitated the product. Yield: 0.260 g (80%). FT-IR, ^{1}H NMR, and ^{31}P NMR results matched reported values.[36]

$Fe_2(adt^{NH})(CO)_2(dppv)_2$, ($1^{NH}$). A solution of $Fe_2(adt^{NH})(CO)_4(dppv)$ (400 mg, 0.55 mmol) in 40 mL of toluene was treated with dppv (872 mg, 2.2 mmol) in 10 mL of toluene. The mixture was irradiated at 365 nm until the conversion was complete (~24 h) as indicated by IR spectroscopy. The solvent was removed in vacuum, and the product was extracted into ~3 mL of toluene. The green product precipitated upon addition of methanol to the toluene extract. The product was then re-extracted into ~2 mL of CH_2Cl_2, and the product precipitated as an olive-green powder upon the addition of 100 mL of hexanes. Yield: 150 mg (26%). ^{1}H NMR (500 MHz, CD_2Cl_2): δ 8.1 – 7.0 (m, 40H, $P(C_6\mathit{H}_5)_2$), 2.3 (s, 4H, $(SC\mathit{H}_2)_2NH$). ^{31}P NMR (CD_2Cl_2, 20 ºC): δ 92. ^{31}P NMR (CD_2Cl_2, -70 ºC): δ 102.6, 93.4, 92.2, 88.6. FT-IR (CH_2Cl_2): ν_{CO} = 1888, 1868 cm^{-1}. Anal. Calcd for $C_{56}H_{49}Fe_2O_2NP_4S_2{\cdot}CH_2Cl_2{\cdot}CH_3OH$ (found): C, 58.8 (58.15); H,

4.68 (4.63), N 1.18 (1.10). Diffraction quality crystals were grown at -20 ºC from a CH_2Cl_2 solution of $\mathbf{1^{NH}}$ layered with pentane at -20 °C.

[*t*-HFe$_2$(pdt)(CO)$_2$(dppv)$_2$]BAr$^F_{24}$, [*t*-H2]BAr$^F_{24}$. In a J. Young NMR tube, ~ 0.5 mL of CD_2Cl_2 was distilled and frozen onto **2** (5 mg, 0.005 mmol) and [H(OEt$_2$)$_2$]BAr$^F_{24}$ (5 mg, 0.005 mmol) in a -78 ºC bath. The sample was then thawed and analyzed by NMR spectroscopy. ^{1}H NMR (500 MHz, CD_2Cl_2): δ -3.5 (t, Fe-H, $^2J_{PH}$ = 76 Hz). ^{31}P NMR (202 MHz, CD_2Cl_2): δ 99 (s), 91 (s), 86 (s), 68 (s). Selective ^{31}P decoupled ^{1}H NMR verified that the signals at δ 91 and 86 coupled to the hydride signal. FT-IR (CH_2Cl_2, cm^{-1}): ν_{CO} = 1965, 1905, 1988.

IR Spectroscopy of [*t*-HFe$_2$(pdt)(CO)$_2$(dppv)$_2$]BAr$^F_{24}$, [*t*-H2]BAr$^F_{24}$ and [*t*-DFe$_2$(pdt)(CO)$_2$(dppv)$_2$]BAr$^F_{24}$, [*t*-D2]BAr$^F_{24}$. Into a 10 mL Schlenk flask, **2** (10 mg, 0.009 mmol) and [H(OEt$_2$)$_2$]BAr$^F_{24}$ (16 mg, 0.015 mmol) were weighed, cooled to -78 °C, and dissolved in pre-cooled CH_2Cl_2. The solution was immediately analysed by IR spectroscopy. The corresponding deuteride was prepared by an analogous procedure, utilizing [H(OEt$_2$)$_2$]BAr$^F_{24}$.

[*t*-DFe$_2$(pdt)(CO)$_2$(dppv)$_2$]BAr$^F_{24}$, [*t*-D2]BAr$^F_{24}$. Solutions of **2** (5 mg, 0.005 mmol) and [D(OEt$_2$)$_2$]BAr$^F_{24}$ (7 mg, 0.007 mmol) in CD_2Cl_2 were cooled to -35 °C. The solutions were combined in a J. Young NMR tube and placed in a -15 °C bath. The sample was then transferred to an NMR spectrometer cooled to -20 °C and analyzed by NMR spectroscopy. ^{1}H NMR does not show a high field signal corresponding to a hydride. ^{31}P NMR (202 MHz, CD_2Cl_2): δ 99.5 (s), 92 (d), 86 (d), 69 (s) ([*t*-D**2**]BAr$^F_{24}$); 88.7 (s), 87.9 (s) (*sym*-[μ-D**2**]BAr$^F_4$ (~ 5%)).

[HFe$_2$(adt^{NH})(CO)$_2$(dppv)$_2$]BAr$^F_{24}$, ([*t*-H1^{NH}]BAr$^F_{24}$), [Fe$_2$(adt^{NH})(CO)$_2$(dppv)$_2$]BAr$^F_{24}$ ([μ-H1^{NH}]BAr$^F_{24}$), and [Fe$_2$(adt^{NH2})(μ-H)(CO)$_2$(dppv)$_2$](BAr$^F_{24}$)$_2$ ([μ-H1^{NH2}](BAr$^F_{24}$)$_2$). In a J. Young NMR tube, ~ 0.5 mL of CD_2Cl_2 was distilled and frozen onto $\mathbf{1^{NH}}$ (5 mg, 0.005 mmol) and [H(OEt$_2$)$_2$]BAr$^F_{24}$ (5 mg, 0.005 mmol) in a -78 ºC bath. The sample was then thawed and analyzed by NMR spectroscopy. ^{1}H NMR (600 MHz, CD_2Cl_2, -80 ºC): δ -4.2 (t, Fe-H, $^2J_{PH}$ = 73 Hz). ^{31}P NMR (242 MHz, CD_2Cl_2, -40 ºC): δ103.2 (s), 94.5 (s), 84.0 (s), 75.1 (s). Selective ^{31}P decoupling of the ^{1}H NMR verified that only the signals at δ 94 and 84 were coupled to the hydride, presumably these correspond to dibasal phosphines attached to the FeH center. At the sample temperature of -10 ºC, a triplet of triplets at δ -14.8 (Fe-μH, J_{PH} = 25, 5 Hz) appears in the ^{1}H NMR spectrum, and singlets at δ 91.0 and 90.8 appear in the ^{31}P NMR

spectrum, which are assigned to *sym*-[μ-H**1**$^{\mathbf{NH}}$]BAr^F_{24}. Upon warming the sample to 20 ºC, signals corresponding to [*t*-H**1**$^{\mathbf{NH}}$]BAr^F_{24} disappear, and only *sym*-[μ-H**1**$^{\mathbf{NH}}$]BAr^F_{24} is observed. If the sample is then recooled to -15 C, the only species present is *sym*-[μ-H**1**$^{\mathbf{NH}}$]BAr^F_{24}, the terminal hydride does not reform. After ~10 min. at 20 ºC, an additional ^{1}H NMR multiplet at δ-13.7 appears, and four ^{31}P NMR singlets appear at δ 88.2, 85.7, 82.7, and 77.3, which are assigned to *unsym*-[μ-H**1**$^{\mathbf{NH}}$]BAr^F_{24}. After ~12 h at room temperature, the ratio of the *sym:unsym* isomers is 1:5.

Effect of $[Bu_4N]BF_4$ on Equilibrium between Tautomers [*t*-H1$^{\mathbf{NH}}$]$^+$ and [1$^{\mathbf{NH2}}$]$^+$. A 7 mM solution of [*t*-H**1**$^{\mathbf{NH}}$]BAr^F_{24} was prepared by dissolving **1**$^{\mathbf{NH}}$ (15 mg, 0.014 mmol) and $[H(Et_2O)_2]BAr^F_4$ (15 mg, 0.014 mmol) in 2 mL of CH_2Cl_2, which had been pre-cooled to -78 °C. Aliquots of a 0.6 M $[Bu_4N]BF_4$ solution were added to the solution. After each addition, 0.1 mL aliquots were removed and immediately analyzed by IR spectroscopy.

Double Protonation of $Fe_2(adt^{NH})(CO)_2(dppv)_2$, 1$^{\mathbf{NH}}$. In a J. Young NMR tube, ~ 0.5 mL of CD_2Cl_2 was distilled onto **1**$^{\mathbf{NH}}$ (5 mg, 0.005 mmol) and $[H(OEt_2)_2]BAr^F_{24}$ (10 mg, 0.010 mmol). The J. Young tube was then gently warmed to near -78 ºC before analysis by low temperature NMR spectroscopy. High field ^{1}H NMR (500 MHz, CD_2Cl_2): δ - 4.95 (t, Fe-H, $^2J_{PH}$ = 72 Hz). $^{31}P\{^1H\}$ NMR (242 MHz, CD_2Cl_2, -40 ºC): δ 98 (s), 89 (s), 76 (s), 74 (s). Decoupling experiments verified that the high field ^{1}H NMR signal is coupled to the ^{31}P NMR signals at δ 89 and 74. Upon warming the sample to room temperature, signals corresponding to [*t*-H**1**^{NH2}]$(BAr^F_{24})_2$ disappear. New signals appear at δ -15.6 (tt) in the ^{1}H NMR spectrum and δ 91.3 (s) and 88.7 (s) in the ^{31}P NMR spectrum, which correspond to *sym*-[μ-H**1**$^{\mathbf{NH2}}$]$(BAr^F_{24})_2$. Over time, signals also appear at δ -14.5 (dtd) in the ^{1}H NMR spectrum and δ 92.3 (s), 86.0 (s), 82.4 (s), 79.0 (s) in the ^{31}P NMR spectrum, which correspond to *unsym*-[μ-H**1**$^{\mathbf{NH2}}$]$(BAr^F_{24})_2$. When this solution is cooled, the signals for *sym*-[μ-H**1**$^{\mathbf{NH2}}$]$(BAr^F_{24})_2$ split into four signals at δ 96.0 (s), 93.5 (s), 89.5 (s), 86.2 (s).

Crystallization of $[t\text{-}HFe_2(adt^{NH2})(CO)_2(dppv)_2]BF_4)_2$. Crystals were obtained by treating a CH_2Cl_2 solution of **1**$^{\mathbf{NH}}$, at 0 ºC, with two equiv of $HBF_4{\cdot}Et_2O$ and layering with cold pentane. Storage at -20 ºC gave dark brown crystals.

$[Fe_2(adt^{NH})(\mu\text{-}H)(CO)_2(dppv)_2]BAr^F_{24}$, $[\mu$-H1$^{\mathbf{NH}}]BAr^F_{24}$. A 10 mL solution of **1**$^{\mathbf{NH}}$ (35 mg, 0.03 mmol) in CH_2Cl_2 was treated with a 5-mL solution of $[H(OEt_2)_2]BAr^F_{24}$ (33 mg, 0.03

mmol) in CH_2Cl_2. Within 5 min., the solution color changed from green to brown. After stirring at room temperature for 22 h, the solution was concentrated to ~ 5 mL, and the brown product was precipitated with addition of 20 mL of Et_2O. IR (CH_2Cl_2): ν_{CO} = 1948, 1969 (sh) cm^{-1}. ^1H and ^{31}P NMR data match those described above. Anal. Calcd for $C_9H_{62}BF_{24}Fe_2NO_2P_4S_2 \cdot 2CH_2Cl_2 \cdot C_4H_{10}O$ (found): C, 51.89 (52.19); H, 3.52 (3.13); N 0.64 (0.76).

Preparation of $[HN(EtOH)_3]BAr^F_{24}$. A CH_2Cl_2 solution of $N(EtOH)_3$ (0.15 mmol) was treated with $HCl \cdot Et_2O$, followed by a solution of $NaBAr^F_{24}$ in CH_2Cl_2. The mixture stirred for 3 hours, during which time, a white solid formed (NaCl). The mixture was filtered, and the filtrate was concentrated to dryness under vacuum. The product was recrystallized from CH_2Cl_2/ hexanes. ^1H NMR (500 MHz, CD_2Cl_2): δ 7.71 (BAr^F_{24} aryl protons, s, 8 H), 7.56 (BAr^F_{24} aryl protons, 4 H), 3.95, 3.24 (CH_2, t, 6 H each), 2.12 (NH, s, 1H).

Preparation of $[HNEt_3]BF_4$. A 10 mL CH_2Cl_2 solution of NEt_3 (35.8 mmol) was treated dropwise with $HBF_4 \cdot Et_2O$ (36 mmol). A white precipitate formed, and after storage at 0 °C for 1 hour, the mixture was filtered and the solid washed with ether. The product was recrystallized from CH_2Cl_2, pentane, and Et_2O. ^1H NMR (500 MHz, CD_2Cl_2): δ 7.25 (NH, t, 1 H), 3.22 (CH_2, m, 6 H), 1.39 (CH_3, t, 9 H), 3.95, 3.24 (CH_2, t, 6 H each), 2.12 (NH, s, 1H).

Preparation of $[HNMe_3]BAr^F_{24}$. Into a cooled (-40 C) flask, ~5 mL of NMe_3 was condensed (0.055 mmol). To the flask, cold Et_2O was added, followed by $HBF_4 \cdot Et_2O$. A white solid immediately formed, the mixture was filtered, and the white solid was washed with Et_2O. The resulting BF_4^- salt is insoluble in CH_2Cl_2. The $BAr^F_{24}{}^-$ salt was prepared by treating a solution of $[HNMe_3]BF_4$ (167 mg, 1.13 mmol) in 300 mL of MeOH with a solution of $NaBAr^F_{24}$ (1.0 g, 1.13 mmol) in 20 mL of MeOH. The reaction stirred at room temperature for 3 hours, after which, solvent was removed. The resulting white solid was extracted into CH_2Cl_2 and filtered, leaving $NaBF_4$. The product was recrystallized from CH_2Cl_2 and pentane. ^1H NMR (500 MHz, CD_2Cl_2): δ 7.72 (BAr^F_{24} aryl protons, t, 8 H), 7.53 (BAr^F_{24} aryl protons, s, 4 H), 2.98 (CH_3, s, 9 H).

Protonation of $\mathbf{1^{NH}}$ with Weak Acids. The following general procedure was followed for the protonation of $\mathbf{1^{NH}}$ with weak acids: Into a J. Young NMR tube, $\mathbf{1^{NH}}$ (5.0 mg, 0.005 mmol) and acid (1 equiv) were weighed and dissolved in ~ 0.75 mL of CD_2Cl_2. The samples were then analyzed by ^1H and ^{31}P NMR spectroscopy.

Electrochemistry. Electrochemical experiments were carried out on CH Instruments Model 600D Series Electrochemical Analyzer. Cyclic voltammetry experiments were conducted using a 10-mL one-compartment glass cell with a tight-fitting Teflon top. The working electrode was a glassy carbon (GC) disk (diameter = 3.00 mm). A silver wire was used as a quasi-reference electrode, and the counter electrode was a Pt wire. Ferrocene was added as an internal reference, and each cyclic voltammogram was referenced to this $Fc^{0/+}$ couple = 0.00 V. *i*R compensation was applied to all measurements using the CH Instruments software. Cell resistance was determined prior to each scan, and the correction applied to the subsequently collected cyclic voltammogram. A CYCLIC VOLTAMMOGRAM of the 0.1 M electrolyte solution was collected prior to the addition of diiron compound, in order to check the purity of the electrolyte. The diiron compound was then dissolved in the electrolyte solution and transferred to the cell. The final concentration of diiron complex was 1.0 mM.

2.10 References

(1) Fontecilla-Camps, J. C.; Volbeda, A.; Cavazza, C.; Nicolet, Y. "Structure/Function Relationships of [NiFe]- and [FeFe]-Hydrogenases." *Chem. Rev.* **2007**, *107*, 4273.

(2) Peters, J. W.; Lanzilotta, W. N.; Lemon, B. J.; Seefeldt, L. C. "X-ray Crystal Structure of the Fe-Only Hydrogenase (*CpI*) from *Clostridium pasteurianum* to 1.8 A Resolution." *Science* **1998**, *282*, 1853.

(3) Silakov, A.; Wenk, B.; Reijerse, E.; Lubitz, W. "^{14}N HYSCORE investigation of the H-cluster of [FeFe] hydrogenase: evidence for a nitrogen in the dithiol bridge." *Phys. Chem. Chem. Phys.* **2009**, *11*, 6592.

(4) Ryde, U.; Greco, C.; De Gioia, L. "Quantum Refinement of [FeFe] Hydrogenase Indicates a Dithiomethylamine Ligand." *J. Am. Chem. Soc.* **2010**, *132*, 4512.

(5) Nicolet, Y.; Lemon, B. J.; Fontecilla-Camps, J. C.; Peters, J. W. "A Novel FeS Cluster in Fe-only Hydrogenases." *Trends Biochem. Sci.* **2000**, *25*, 138.

(6) Bruschi, M.; Greco, C.; Kaukonen, M.; Fantucci, P.; Ryde, U.; De Gioia, L. "Influence of the [2Fe]H Subcluster Environment on the Properties of Key Intermediates in the Catalytic Cycle of [FeFe] Hydrogenases: Hints for the Rational Design of Synthetic Catalysts." *Angew. Chem., Int. Ed.* **2009**, *48*, 3503.

(7) Gloaguen, F.; Rauchfuss, T. B. "Small Molecule Mimics of Hydrogenase: Hydrides and Redox." *Chem. Soc. Rev.* **2009**, *38*, 100.

(8) Tard, C.; Pickett, C. J. "Structural and Functional Analogues of the Active Sites of the [Fe]-, [NiFe]-, and [FeFe]-Hydrogenases." *Chem. Rev.* **2009**, *109*, 2245.

(9) Lansing, J.; Camara, J.; Rauchfuss, T. B. **2013**, *Unpublished Result*.

(10) Reihlen, H.; von Friedolsheim, A.; Ostwald, W. "Über Stickoxyd- und Kohlenoxydverbindungen des scheinbar einwertigen Eisens und Nickels." *Justus Liebigs Ann. Chem.* **1928**, *465*, 72.

(11) Hieber, W.; Spacu, P. "Einwirkung Organischer Schwefelverbindungen auf die Carbonyle von Eisen und Kobalt." *Z. anorg. allgem. Chem.* **1937**, *233*, 852.

(12) King, R. B. "Organosulfur Derivatives of Metal Carbonyls. I. The Isolation of Two Isomeric Products in the Reaction of Triiron Dodecacarbonyl with Dimethyl Disulfide." *J. Am. Chem. Soc.* **1962**, *84*, 2460.

(13) Lawrence, J. D.; Li, H.; Rauchfuss, T. B. "Beyond Fe-only Hydrogenases: N-Functionalized 2-Aza-1,3-dithiolates $Fe_2[(SCH_2)_2NR](CO)_x$ (x = 5, 6)." *Chem. Commun.* **2001**, 1482.

(14) Li, H.; Rauchfuss, T. B. "Iron Carbonyl Sulfides, Formaldehyde, and Amines Condense To Give the Proposed Azadithiolate Cofactor of the Fe-Only Hydrogenases." *J. Am. Chem. Soc.* **2002**, *124*, 726.

(15) Angamuthu, R.; Carroll, M. E.; Ramesh, M.; Rauchfuss, T. B. "A New Route to Azadithiolato Complexes." *Eur. J. Inorg. Chem.* **2011**, 1029.

(16) Justice, A. K.; De Gioia, L.; Nilges, M. J.; Rauchfuss, T. B.; Wilson, S. R.; Zampella, G. "Redox and Structural Properties of Mixed-Valence Models for the Active Site of the [FeFe]-Hydrogenase: Progress and Challenges." *Inorg. Chem.* **2008**, *47*, 7405.

(17) Gloaguen, F.; Lawrence, J. D.; Schmidt, M.; Wilson, S. R.; Rauchfuss, T. B. "Synthetic and Structural Studies on $[Fe_2(SR)_2(CN)_x(CO)_{6-x}]^{x-}$ as Active Site Models for Fe-Only Hydrogenases." *J. Am. Chem. Soc.* **2001**, *123*, 12518.

(18) Jablonskytė, A.; Wright, J. A.; Pickett, C. J. "Mechanistic aspects of the protonation of [FeFe]-hydrogenase subsite analogues." *Dalton Trans.* **2010**, *39*, 3026.

(19) Gloaguen, F.; Lawrence, J. D.; Rauchfuss, T. B.; Bénard, M.; Rohmer, M.-M. "Bimetallic Carbonyl Thiolates as Functional Models for Fe-Only Hydrogenases." *Inorg. Chem.* **2002**, *41*, 6573.

(20) Zhao, X.; Georgakaki, I. P.; Miller, M. L.; Yarbrough, J. C.; Darensbourg, M. Y. "H/D Exchange Reactions in Dinuclear Iron Thiolates as Activity Assay Models of Fe-H_2ase." *J. Am. Chem. Soc.* **2001**, *123*, 9710.

(21) Li, P.; Wang, M.; He, C.; Li, G.; Liu, X.; Chen, C.; Åkermark, B.; Sun, L. "Influence of tertiary phosphanes on the coordination configurations and electrochemical properties of iron hydrogenase model complexes: Crystal structures of $[(\mu\text{-}S_2C_3H_6)Fe_2(CO)_{6-n}L_n]$ (L = PMe_2Ph, n = 1, 2; PPh_3, $P(OEt)_3$, n = 1)." *Eur. J. Inorg. Chem.* **2005**, 2506.

(22) van der Vlugt, J. I.; Rauchfuss, T. B.; Whaley, C. M.; Wilson, S. R. "Characterization of a Diferrous Terminal Hydride Mechanistically Relevant to the Fe-Only Hydrogenases." *J. Am. Chem. Soc.* **2005**, *127*, 16012.

(23) Adam, F. I.; Hogarth, G.; Kabir, S. E.; Richards, I. "Models of the iron-only hydrogenase: Synthesis and protonation of bridge and chelate complexes $[Fe_2(CO)_4\{Ph_2P(CH_2)_nPPh_2\}(\mu\text{-pdt})]$ (n =2-4) - evidence for a terminal hydride intermediate." *C. R. Chim.* **2008**, *11*, 890.

(24) Ezzaher, S.; Capon, J.-F.; Gloaguen, F.; Pétillon, F. Y.; Schollhammer, P.; Talarmin, J.; Pichon, R.; Kervarec, N. "Evidence for the Formation of Terminal Hydrides by Protonation of an Asymmetric Iron Hydrogenase Active Site Mimic." *Inorg. Chem.* **2007**, *46*, 3426.

(25) Barton, B. E.; Zampella, G.; Justice, A. K.; De Gioia, L.; Rauchfuss, T. B.; Wilson, S. R. "Isomerization of the hydride complexes $[HFe_2(SR)_2(PR_3)_x(CO)_{6-x}]+$ (x = 2, 3, 4) relevant to the active site models for the [FeFe]-hydrogenases." *Dalton Trans.* **2010**, *39*, 3011.

(26) Ezzaher, S.; Capon, J.-F.; Gloaguen, F.; Kervarec, N.; Pétillon, F. Y.; Pichon, R.; Schollhammer, P.; Talarmin, J. "Diiron chelate complexes relevant to the active site of the iron-only hydrogenase." *C. R. Chim.* **2008**, *11*, 906.

(27) Barton, B. E.; Olsen, M. T.; Rauchfuss, T. B. "Aza- and Oxadithiolates Are Probable Proton Relays in Functional Models for the [FeFe]-Hydrogenases." *J. Am. Chem. Soc.* **2008**, *130*, 16834.

(28) Zaffaroni, R.; Rauchfuss, T. B.; Gray, D. L.; De Gioia, L.; Zampella, G. "Terminal vs Bridging Hydrides of Diiron Dithiolates: Protonation of $Fe_2(dithiolate)(CO)_2(PMe3)_4$." *J. Am. Chem. Soc.* **2012**, *134*, 19260.

(29) Singleton, M. L.; Jenkins, R. M.; Klemashevich, C. L.; Darensbourg, M. Y. "The effect of bridgehead steric bulk on the ground state and intramolecular exchange processes of $(\mu\text{-}SCH_2CR_2CH_2S)[Fe(CO)_3][Fe(CO)_2L]$ complexes." *C. R. Chim.* **2008**, *11*, 861.

(30) Winter, A.; Zsolnai, L.; Huttner, G. "Zweikernige und dreikernige Carbonyleisenkomplexe mit 1,2- und 1,3-Dithiolatobrückenliganden." *Z. Naturforsch.* **1982**, *37b*, 1430.

(31) Lambert, J. B.; Featherman, S. I. "Conformational analysis of pentamethylene h eterocycles." *Chem. Rev.* **1975**, *75*, 611.

(32) Barton, B. E. *PhD Thesis, University Illinois at Urbana-Champaign* **2010**.

(33) Justice, A. K.; Zampella, G.; De Gioia, L.; Rauchfuss, T. B. "Lewis vs BrØnsted-Basicities of Diiron Dithiolates: Spectroscopic Detection of the "Rotated Structure" and Remarkable Effects of Ethane- vs. Propanedithiolate." *Chem. Commun.* **2007**, 2019.

(34) Geiger, W. E.; Barrière, F. "Organometallic Electrochemistry Based on Electrolytes Containing Weakly-Coordinating Fluoroarylborate Anions." *Acc. Chem. Res.* **2010**, *43*, 1030.

(35) Olsen, M. T.; Rauchfuss, T. B.; Wilson, S. R. "Role of the Azadithiolate Cofactor in Models for [FeFe]-Hydrogenase: Novel Structures and Catalytic Implications." *J. Am. Chem. Soc.* **2010**, *132*, 17733.

(36) Justice, A. K.; Zampella, G.; De Gioia, L.; Rauchfuss, T. B.; van der Vlugt, J. I.; Wilson, S. R. "Chelate Control of Diiron(I) Dithiolates Relevant to the Fe-only Hydrogenase Active Site." *Inorg. Chem.* **2007**, *46*, 1655.

(37) Izutsu, K. *Acid-Base Dissociation Constants in Dipolar Aprotic Solvents*; Blackwell Scientific Publications: Oxford, U.K., 1990; Vol. 35.

(38) Apfel, U.-P.; Troegel, D.; Halpin, Y.; Tschierlei, S.; Uhlemann, U.; Goerls, H.; Schmitt, M.; Popp, J.; Dunne, P.; Venkatesan, M.; Coey, M.; Rudolph, M.; Vos, J. G.; Tacke, R.; Weigand, W. "Models for the Active Site in [FeFe] Hydrogenase with Iron-Bound Ligands Derived from Bis-, Tris-, and Tetrakis(mercaptomethyl)silanes." *Inorg. Chem.* **2010**, *49*, 10117.

(39) Dong, W.; Wang, M.; Liu, X.; Jin, K.; Li, G.; Wang, F.; Sun, L. "An insight into the protonation property of a diiron azadithiolate complex pertinent to the active site of Fe-only hydrogenases." *Chem. Commun.* **2006**, 305.

(40) Ezzaher, S.; Gogoll, A.; Bruhn, C.; Ott, S. "Directing protonation in [FeFe] hydrogenase active site models by modifications in their second coordination sphere." *Chem. Commun.* **2010**, *46*, 5775.

(41) Ott, S.; Kritikos, M.; Åkermark, B.; Sun, L.; Lomoth, R. "A Biomimetic Pathway for Hydrogen Evolution from a Model of the Iron Hydrogenase Active Site." *Angew. Chem., Int. Ed.* **2004**, *43*, 1006.

(42) Schwartz, L.; Eilers, G.; Eriksson, L.; Gogoll, A.; Lomoth, R.; Ott, S. "Iron hydrogenase active site mimic holding a proton and a hydride." *Chem. Commun.* **2006**, 520.

(43) Lawrence, J. D.; Li, H.; Rauchfuss, T. B.; Bénard, M.; Rohmer, M.-M. "Diiron Azadithiolates as Models for the Iron-only Hydrogenase Active Site: Synthesis, Structure, and Stereoelectronics." *Angew Chem., Int. Ed.* **2001**, *40*, 1768.

(44) Das, P.; Capon, J.-F.; Gloaguen, F.; Pétillon, F. Y.; Schollhammer, P.; Talarmin, J.; Muir, K. W. "Di-Iron Aza Diphosphido Complexes: Mimics for the Active Site of Fe-Only Hydrogenase, and Effects of Changing the Coordinating Atoms of the Bridging Ligand in $[Fe_2\{\mu\text{-}(ECH_2)_2NR\}(CO)_6]$." *Inorg. Chem.* **2004**, *43*, 8203.

(45) Olsen, M. T.; Bruschi, M.; De Gioia, L.; Rauchfuss, T. B.; Wilson, S. R. "Nitrosyl Derivatives of Diiron(I) Dithiolates Mimic the Structure and Lewis Acidity of the [FeFe]-Hydrogenase Active Site." *J. Am. Chem. Soc.* **2008**, *130*, 12021.

(46) Ho, N. N.; Bau, R.; Mason, S. A. "Neutron diffraction study of the highly distorted octahedral complex $FeH_2(CO)_2[P(OPh)_3]_2$." *J. Organomet. Chem.* **2003**, *676*, 85.

(47) Custelcean, R.; Jackson, J. E. "Dihydrogen bonding: structures, energetics, and dynamics." *Chem. Rev.* **2001**, *101*, 1963.

(48) Brookhart, M.; Grant, B.; Volpe, A. F. "$[(3,5\text{-}(CF_3)_2C_6H_3)_4B]\text{-}[H(OEt_2)_2]^+$: a convenient reagent for generation and stabilization of cationic, highly electrophilic organometallic complexes." *Organometallics* **1992**, *11*, 3920.

Chapter 3.

Diiron Dithiolates as Proton Reduction Catalysts: Effect of Dithiolate Identity and Hydride Binding Mode[†]

3.1 Introduction

As discussed in Chapter 1, many diiron model complexes are electrocatalysts for the reduction of protons, but they suffer from a number of issues.[1,2] Due to their low basicity, diiron hexacarbonyl complexes must first be reduced before protonation, a sequence that is not biomimetic. The model complex, $[Fe_2(pdt)(CO)_2(CN)_2]^{2-}$ (pdt= 1,3-propanedithiolate), which is a good spectroscopic model for active site,[3,4] reduces at potentials (E_{red}= -2.74 V vs $Fc^{+/0}$) that are far more negative than those reported for the enzyme[5], thus supporting protonation rather than reduction as the first step in the catalytic cycle. Additionally, this mechanism is supported by DFT calculations.[6]

Diiron hydrides, in which the hydride bridges between the two metal centers, have also been shown to catalyze proton reduction, but these catalysts operate at high overpotentials. Additionally, the enzyme is proposed to operate via terminally bound hydride species, so bridging hydrides are not particularly relevant to the catalytic cycle of the enzyme.

Diiron models that form terminal hydrides have been reported previously, but they are generally only stable at very low temperatures (< -30 °C).[7-11] The instability of these species made studying their redox and electrocatalytic properties difficult. Our group reported that the $[t\text{-}HFe_2(pdt)(CO)_2(dppv)_2]^+$ ($[\mathbf{2}H]^+$, pdt = 1,3-propanedithiolate) undergoes protonation, albeit only with strong acids, to give a terminal hydride with a half-life of several minutes at room temperature (dppv = *cis*-$C_2H_2(PPh_2)_2$). Additionally, this terminal hydride derivative was shown to reduce at a potential ca. 100 mV less negative than the isomeric bridging hydride complex.[12]

This chapter summarizes an extensive investigation of the redox and electrocatalytic properties of $Fe_2(adt^{NH})(CO)_2(dppv)_2$ ($\mathbf{1}^{\mathbf{NH}}$) (adt^{NH} = $[(SCH_2)_2NH]^{2-}$), with parallel studies on the $Fe_2(pdt)(CO)_2(dppv)_2$ (**2**), which lacks the amine cofactor. Overall, the results indicate that the combination of a terminal hydride and the azadithiolate cofactor greatly facilitates reduction of protons to form H_2 by diiron complexes.

[†] Portions of this chapter are reproduced from the following publication with permission from the authors.
Carroll, M. E.; Barton, B. E.; Rauchfuss, T.B.; Carroll, P.J. *J. Am. Chem. Soc.* **2012**, *134*, 18843–18852.

3.2 Redox Properties of the Protonated Derivatives of $Fe_2(xdt)(CO)_2(dppv)_2$

The binding mode of the hydride (bridging vs. terminal) has a significant impact on the reduction potential of the diiron hydride complexes. In CH_2Cl_2 solutions, the μ-hydrides [μ-H**1**$^{\mathbf{NH}}$]$^+$ and [μ-H**2**]$^+$ reversibly reduce near -1.8 V (Figures 3.1, 3.2, Table 3.1). The terminal hydrides [*t*-H**1**$^{\mathbf{NH}}$]$^+$ and [*t*-H**2**]$^+$ are redox-active at milder potentials, the pdt derivative [*t*-H**2**]$^+$ reducing quasi-reversibly at –1.67 V (Figures 3.1, 3.2, Table 3.4). Reduction of [*t*-H**2**]$^+$ is a 1e$^-$ process as indicated by the similarity of the dependence of i_p vs $\nu^{1/2}$ for the couples [*t*-H**2**]$^{+/0}$ and [**2**]$^{0/+}$.[12] Former co-workers have independently established the stoichiometry of the [**2**]$^{0/+}$ couple.[13] The adt derivative, [*t*-H**1**$^{\mathbf{NH}}$]$^+$, is also reduced at a more mild potential compared to the analogous bridging hydride, but in this case, the reduction is irreversible.

The difference in reduction potentials between the isomeric hydrides is proposed to reflect differences in the localization of the reduction. In general, metal hydrides are difficult to reduce, due to the negative charge of the hydride.[14] In the case of the μ-hydride isomer, reduction is likely more delocalized between the two equivalent Fe centers.[15] When the hydride is bound to a single Fe center, reduction likely occurs at the non-hydride containing Fe center.[14] Regardless of which Fe center is reduced in the μ-hydride, it is bound to the hydride, and therefore will be more difficult to reduce than the analogous terminal hydride species, in which a non-hydride containing Fe center is reduced.

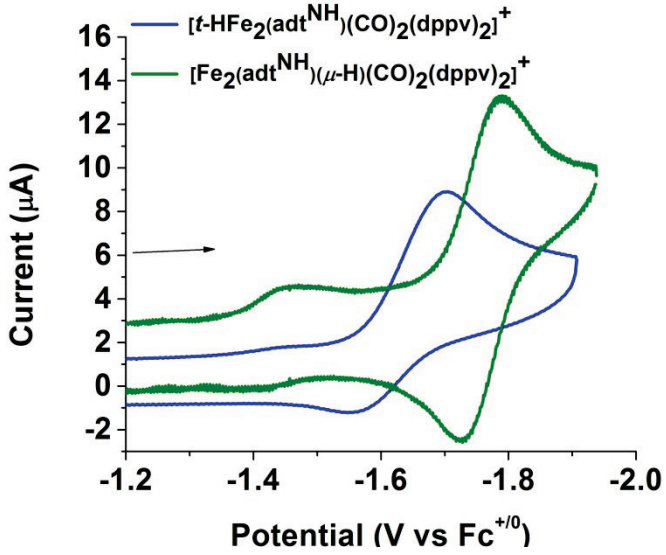

Figure 3.1. Cyclic voltammograms of $[t\text{-H1}^{NH}]^+$ (blue) and $[\mu\text{-H1}^{NH}]^+$ (green) (Conditions: 0.1 M $[Bu_4N]BAr^F{}_{24}$ in CH_2Cl_2, 1.0 mM diiron hydride, GC working electrode, Pt counter electrode, Ag wire pseudo reference electrode, Fc internal standard, Scan Rate = 0.1 V/s)

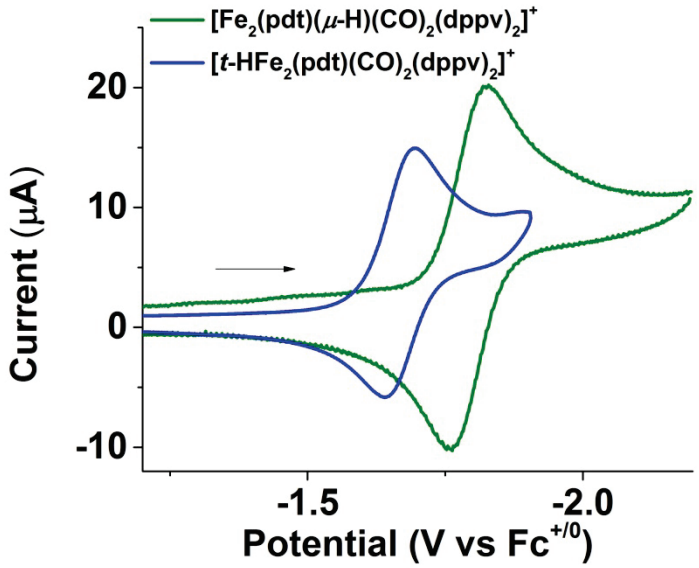

Figure 3.2. Cyclic voltammograms of $[t\text{-H2}]^+$ (blue) and $[\mu\text{-H2}]^+$ (green) (Conditions: 0.1 M $[Bu_4N]PF_6$ in CH_2Cl_2, 1.0 mM diiron hydride, GC working electrode, Pt counter electrode, Ag wire pseudo reference electrode, Fc internal standard, Scan Rate = 0.1 V/s)

Table 3.1 Electrochemical properties of protonated derivatives of 1^{NH} and 2.

Complex	$E_{1/2}$ in CH_2Cl_2 (V vs $Fc^{+/0}$)	Assignment	i_{pc}/i_{pa}
$[t\text{-}HFe_2(adt^{NH})(CO)_2(dppv)_2]^+$, $[t\text{-}H\mathbf{1}^{\mathbf{NH}}]^+$	-1.64	$[t\text{-}H\mathbf{1}^{\mathbf{NH}}]^{+/0}$	Irreversible
$[t\text{-}HFe_2(adt^{NH2})(CO)_2(dppv)_2]^{2+}$, $[t\text{-}H\mathbf{1}^{\mathbf{NH2}}]^{2+}$	-1.30	$[t\text{-}H\mathbf{1}^{\mathbf{NH2}}]^{2+/+}$	Irreversible
$[Fe_2(adt^{NH})(\mu\text{-}H)(CO)_2(dppv)_2]^+$, $[\mu\text{-}H\mathbf{1}^{\mathbf{NH}}]^+$	-1.77	$[\mu\text{-}H\mathbf{1}^{\mathbf{NH}}]^{+/0}$	1.19
$[Fe_2(adt^{NH2})(\mu\text{-}H)(CO)_2(dppv)_2]^{2+}$, $[\mu\text{-}H\mathbf{1}^{\mathbf{NH2}}]^{2+}$	-1.57	$[\mu\text{-}H\mathbf{1}^{\mathbf{NH2}}]^{2+/+}$	1.00
$[t\text{-}HFe_2(pdt)(CO)_2(dppv)_2]^+$, $[t\text{-}H\mathbf{2}]^+$	-1.67	$[t\text{-}H\mathbf{2}]^{+/0}$	1.57
$[Fe_2(pdt)(\mu\text{-}H)(CO)_2(dppv)_2]^+$, $[\mu\text{-}H\mathbf{2}]^+$	-1.80	$[\mu\text{-}H\mathbf{2}]^{+/0}$	1.07

The irreversibility of the reduction of $[t\text{-}H\mathbf{1}^{\mathbf{NH}}]^+$ is attributed to reaction between two reduced hydride species, resulting in release of H_2 (Scheme 3.1). In this scenario, two mixed valence hydride species react to form ½ equivalent of the neutral Fe(I)Fe(I) species, $\mathbf{1}^{\mathbf{NH}}$, ½ equivalent of a mixed valent Fe(II)Fe(I) species, and ½ equivalent of H_2. Evidence for this reaction is provided by the cyclic voltammogram of the hydride, $[t\text{-}H\mathbf{1}^{\mathbf{NH}}]^+$. Waves that correspond to oxidation of $\mathbf{1}^{\mathbf{NH}}$ appear in the reverse scan of the cyclic voltammogram, and their peak current is half that of the reduction wave for $[t\text{-}H\mathbf{1}^{\mathbf{NH}}]^+$ (Figure 3.3). The cyclic voltammogram suggests that half of the reduced terminal hydride species is converted to the neutral complex, $\mathbf{1}^{\mathbf{NH}}$, which is then oxidized on the reverse scan.

Scheme 3.1 Proposed H_2 forming reaction of the reduced terminal hydride.

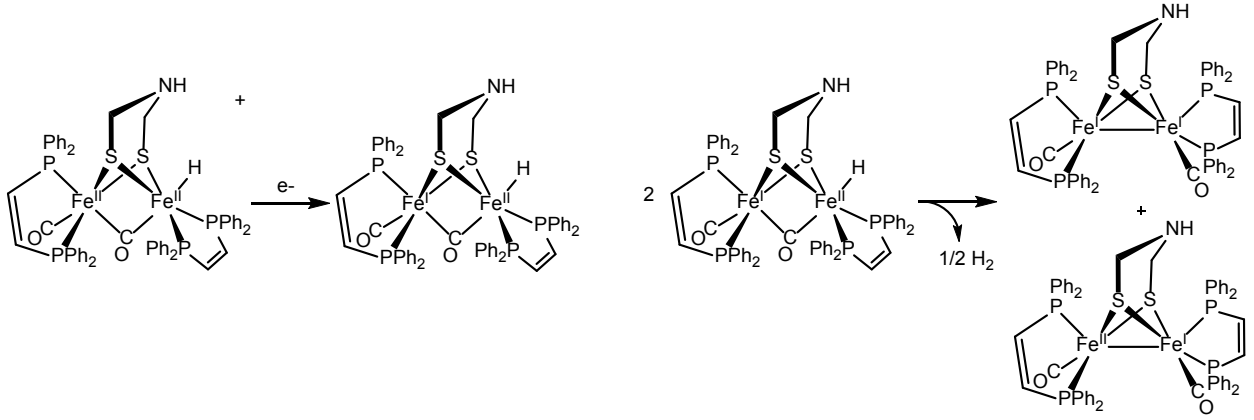

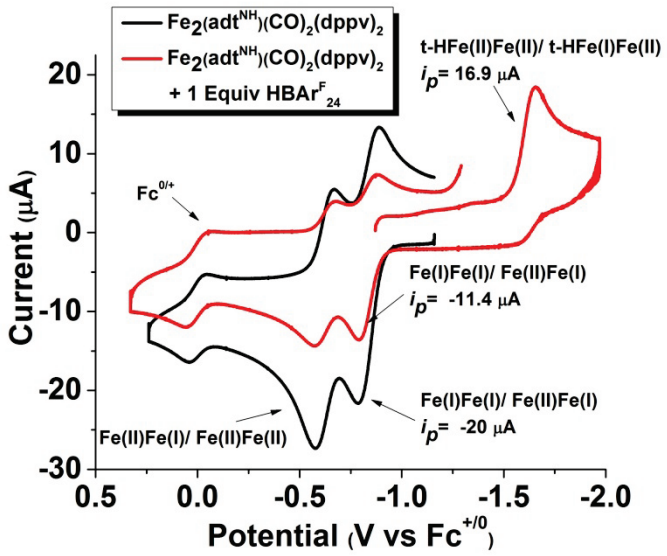

Figure 3.3. Comparison of *i* for oxidation of 1^{NH} vs *i* for reduction of $[t\text{-H}1^{NH}]^{+}$.

Reductions of the doubly protonated ammonium hydride species $[\mu\text{-H}\mathbf{1}^{NH2}]^{2+}$ and $[t\text{-H}\mathbf{1}^{NH2}]^{2+}$ occur about ~ 200 mV positive of the corresponding singly protonated species (Figure 3.4, 3.7, Table 3.1), as observed for other adt-hydrido complexes.[16-18] The ammonium hydride $[t\text{-H}\mathbf{1}^{NH2}]^{2+}$ reduces irreversibly but at the mild potential of -1.3 V (Table 3.1). Although the reduction potential is less negative than that of the singly protonated species, stronger acids are required to generate this doubly protonated species. Unlike the neutral complex, $\mathbf{1}^{NH}$, both the $[t\text{-H}\mathbf{1}^{NH}]^{+/0}$ and the $[t\text{-H}\mathbf{2}]^{+/0}$ couples proved insensitive to the electrolyte, i.e. $[Bu_4N]BAr^F{}_4$ and $[Bu_4N]PF_6$.

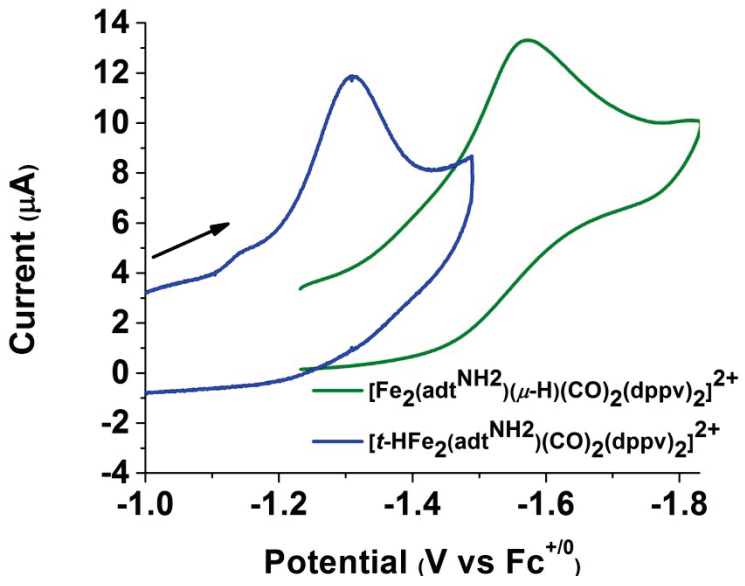

Figure 3.4. Cyclic voltammograms of $[t\text{-H1}^{NH2}]^{2+}$ (blue) and $[\mu\text{-H1}^{NH2}]^{2+}$ (green) (Conditions: 0.1 M $[Bu_4N]BAr^F{}_{24}$ in CH_2Cl_2, 1.0 mM diiron hydride, GC working electrode, Pt counter electrode, Ag wire pseudo reference electrode, Fc internal standard, Scan Rate = 0.1 V/s)

3.3 Proton Reduction Catalysis by $[t\text{-HFe}_2(pdt)(CO)_2(dppv)_2]^+$

For comparison with the catalysts that contains the amine cofactor found in the active site of [FeFe]-hydrogenase, the catalytic properties of $[t\text{-H}\mathbf{2}]^+$ were evaluated. Strong acids such $HBF_4{\cdot}Et_2O$ ($pK_a^{MeCN} = -3$)[19] are required to protonate **2**, to the terminal hydride $[t\text{-H}\mathbf{2}]^+$, which is stable for ~ 30 minutes at 0 °C. The $[t\text{-H}\mathbf{2}]^{+/0}$ couple at -1.67 V is partially reversible even at scan rates as slow as 25 mV/s. Addition of $ClCH_2CO_2H$ ($pK_a^{MeCN} = 15.3$)[19] has no effect on the electrochemical properties of $[t\text{-H}\mathbf{2}]^+$. Only strong acids, such as $HBF_4{\cdot}Et_2O$ results in an increase in current for the couple at –1.67 V, indicative of catalysis (Figure 3.5). The ratio i_c/i_p increases linearly with $[H^+]$ up to 8 equiv of acid, indicating a catalytic pathway that is second order with respect to $[H^+]$. Above this level, i_c/i_p reached a plateau near 5. In this regime, the rate of catalysis is independent of acid concentration. The turnover frequency is calculated to be ~5 s^{-1}, and the overpotential is estimated to be 1.3 V (Table 3.2). As acid is added to the solution, a second wave appears in the cyclic voltammogram at potentials negative of that for the $[t\text{-H}\mathbf{2}]^{+/0}$ couple. We initially attributed this new wave to the bridging hydride, $[\mu\text{-H}\mathbf{2}]^+$, which would accumulate if the rate of isomerization of the terminal hydride was faster than the rate of catalysis. However, control experiments, performed under identical conditions but in the absence of catalyst, indicate that this new catalytic wave is due to reduction of protons at the

glassy carbon working electrode. As the concentration of acid is increased, the wave proton reduction by the electrode dominates, suggesting that the working electrode is a better catalyst than $[t\text{-H}\mathbf{2}]^+$.

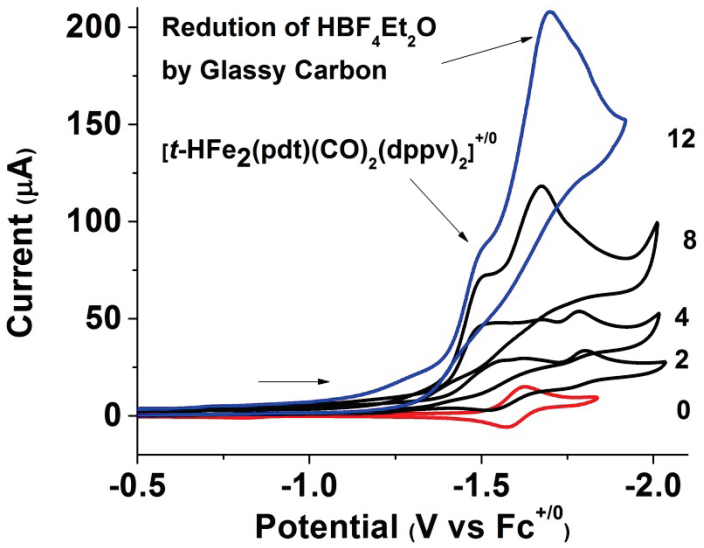

Figure 3.5. Cyclic volatamograms of $[t\text{-H2}]^+$ (generated and *in situ*) with increasing amounts of $HBF_4{\cdot}Et_2O$. (Equivalents of acid indicated to right of each cyclic voltammogram). (Conditions: 0.1 M $[Bu_4N][PF_6]$ in CH_2Cl_2, 1.0 mM $[t\text{-H2}]^+$, 0 °C, GC working electrode, Pt counter electrode, Ag wire pseudo reference electrode, Fc internal standard, Scan Rate = 0.1 V/s)

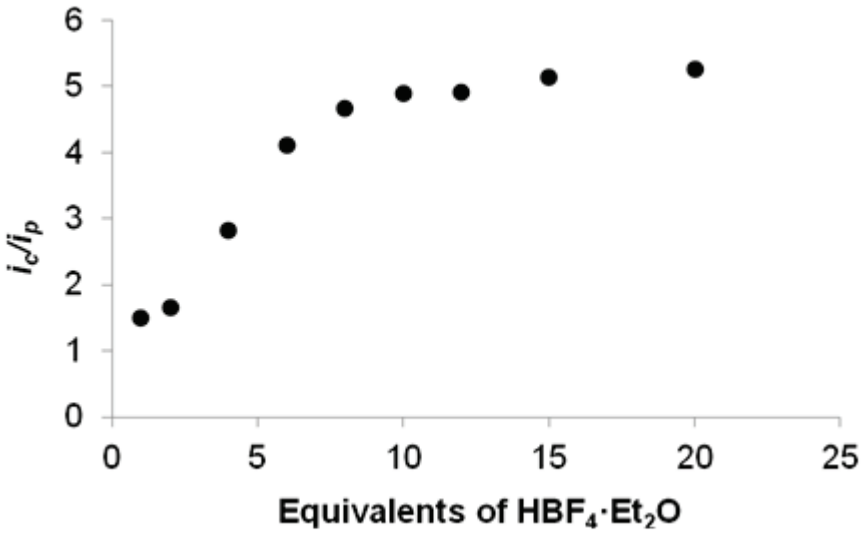

Figure 3.6. Plot of i_c/i_p vs. equivalents of $HBF_4{\cdot}Et_2O$ added to $[t\text{-H2}]^+$.

Table 3.2. Selected Electrocatalytic Properties of Protonated Derivatives of 1^{NH} and 2.

Catalyst	Acid	$(i_c/i_p)_{max}$ [a]	k (s^{-1})	E_{cat} [b] (V vs $Fc^{+/0}$)	Overpotential [c] (V)
$[HFe_2(adt^{NH})(CO)_2(dppv)_2]^+$, $[t\text{-H}\mathbf{1}^{NH}]^+$	$ClCH_2CO_2H$	69	5000	-1.49	0.71
$[HFe_2(adt^{NH}H)(CO)_2(dppv)_2]^{2+}$, $[t\text{-H}\mathbf{1}^{NH2}]^{2+}$	CF_3CO_2H	167	58000	-1.11	0.51
$[Fe_2(adt^{NH})(\mu\text{-H})(CO)_2(dppv)_2]^+$, $[\mu\text{-H}\mathbf{1}^{NH}]^+$	$ClCH_2CO_2H$	10	20	-1.72	0.90
$[HFe_2(pdt)(CO)_2(dppv)_2]^+$, $[t\text{-H}\mathbf{2}]^+$	$HBF_4\bullet Et_2O$	5	5	-1.49	1.32
$[Fe_2(pdt)(\mu\text{-H})(CO)_2(dppv)_2]^+$, $[\mu\text{-H}\mathbf{2}]^+$	$ClCH_2CO_2H$	3.5	3	-1.78	0.95

[a] i_c is the average catalytic current in the plateau region

[b] E_{cat} was calculated at each acid concentration in the linear region by the method described by Fourmond, *et al.*, considering the effects of homoconjugation for the two carboxylic acids.[20] The E_{cat} values listed are averages from each acid concentration in the linear region.

[c] Overpotential = $E^o_{HA/H2} - E_{cat}$, where $E^o_{HA/H2}$ is the standard reduction potential of the acid.[20]

3.4 Proton Reduction Catalysis by $[t\text{-}HFe_2(adt^{NH})(CO)_2(dppv)_2]^+$, $[t\text{-H}\mathbf{1}^{NH}]^+$

In contrast to the behavior of the pdt complex, the voltammetry of $[t\text{-H}\mathbf{1}^{NH}]^+$ is strongly affected by relatively weak acids. Experiments employed $[Bu_4N]BAr^F{}_{24}$ ($BAr^F{}_{24}$= tetrakis(3,5-bis(trifluoromethyl)phenyl)borate) as the electrolyte to maximize the equilibrium concentration of $[t\text{-H}\mathbf{1}^{NH}]^+$ vs its tautomer $[\mathbf{1}^{NH2}]^+$. When $[t\text{-H}\mathbf{1}^{NH}]^+$ was generated *in-situ* from $\mathbf{1}^{NH}$ and one equiv of $[H(OEt_2)_2]BAr^F{}_4$, the current for the $[t\text{-H}\mathbf{1}^{NH}]^{+/0}$ couple closely matched the current for the $[\mathbf{1}^{NH}]^{0/+}$ couple, indicating that both events correspond to one-electron couples (Figure 3.3). When $ClCH_2CO_2H$ is added to solutions of **1**, the reductive current at –1.64 V sharply increases and i_{pc} shifts to more positive potential (E_{cat} = -1.43 V), indicative of catalytic proton reduction (Figure 3.7).[21] A plot of i_c/i_p vs $[H^+]$ is linear over the range 50 to 400 equiv. The maximum i_c/i_p of ~70 corresponds to a rate of 5000 s^{-1} (Figure 3.8). The catalyst operates at an overpotential of 0.7 V (Table 3.2).

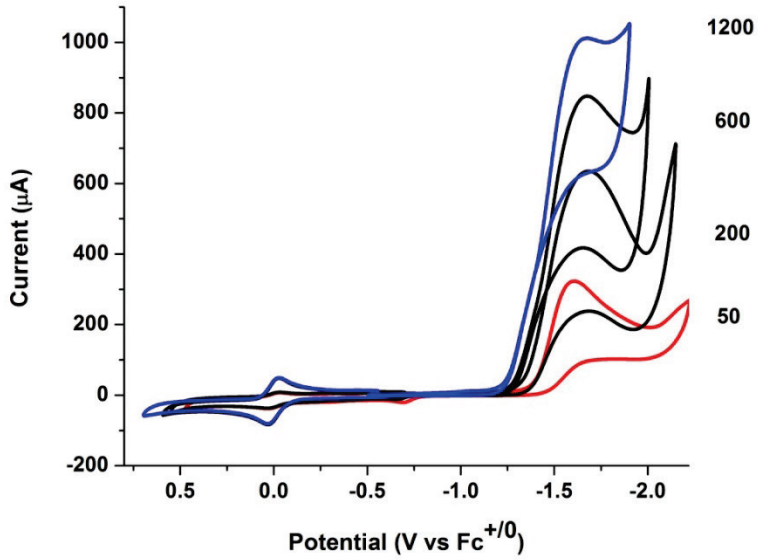

Figure 3.7. Cyclic voltammograms of a 1.00 mM solution of 1^{NH} (0 °C, 0.125 M $[Bu_4N]BAr^F{}_4$, CH_2Cl_2, scan rate = 0.5 V/s, glassy carbon working electrode, Pt counter electrode, Ag wire pseudo reference electrode, Fc internal standard) recorded with increasing equiv of $ClCH_2CO_2H$.

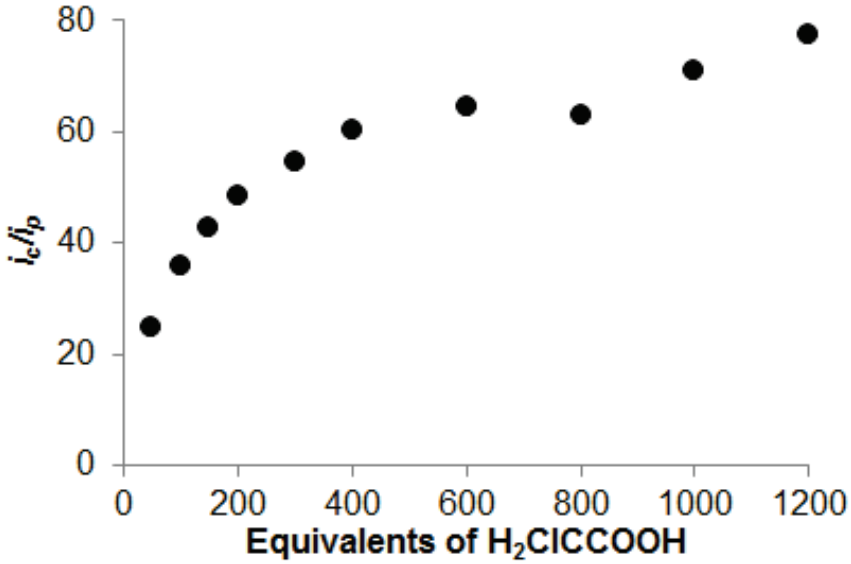

Figure 3.8. Graph of i_c/i_p vs equiv acid for the addition of $ClCH_2CO_2H$ to a 1.00 mM solution of 1^{NH}, with $[Bu_4N]BAr^F{}_4$ as supporting electrolyte .

As discussed in Chapter 1, the catalytic current, i_c, is defined by equation 3.1. In order for equation 1 to be valid in this case, i_c should be directly proportional to the concentration of catalyst, [cat], and independent of scan rate, ν. The dependence of i_c on [cat] was verified by collecting cyclic voltammograms of $[t\text{-H}\mathbf{1}^{NH}]^+$ at acid concentrations that represent the plateau

region of catalytic acitivity (Figure 3.9). The independence of i_c on ν was verified by collecting cyclic voltammograms of [*t*-H**1**$^{\mathbf{NH}}$]$^+$ in the presence of 600 equivalents of acid (plateau region conditions) at a range of ν values As shown in Figure 3.10, the independence is only reached at ν values of 0.5 V/s or greater. Therefore, equation 3.1 is only valid for this system at high scan rates, and therefore, all experiments were performed at ν = 0.5 V/s. Similar behavior has been cited in other catalytic systems, such as DuBois's $Ni(P_2N_2)_2$ system, in which scan rate independence is only reached for ν > 5 V/s.[22] In order for equation 3.3, the expression that relates i_c/i_p to turnover frequency (*k*), to hold true, i_c/i_p must be directly proportional to $1/\nu^{1/2}$, as shown in Figure 3.11.

$$i_c = nFA[cat]\sqrt{Dk[H^+]} \qquad (eq\ 3.1)$$

$$i_p = 0.4463FA[cat]\sqrt{\frac{F\nu D}{RT}} \qquad (eq\ 3.2)$$

$$i_c/i_p = \frac{n}{0.4463}\sqrt{\frac{RTk_{H2}[H^+]}{F\nu}} \qquad (eq\ 3.3)$$

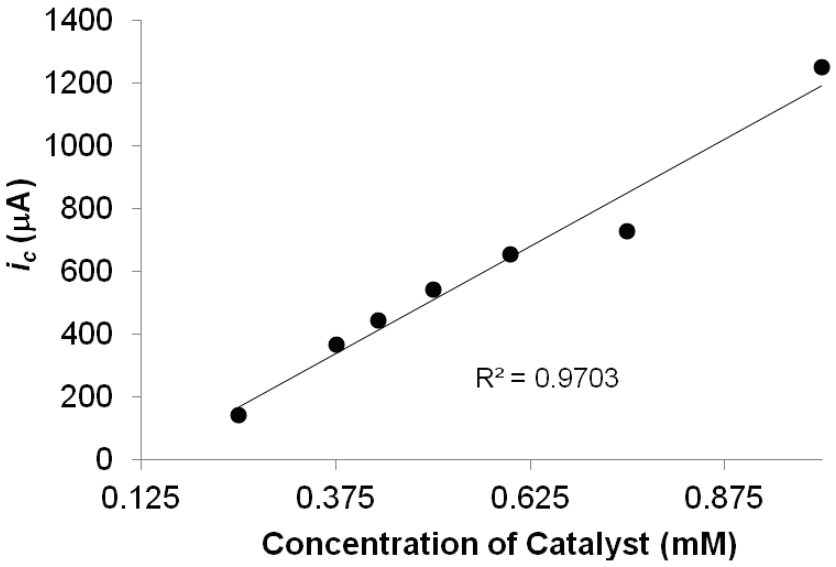

Figure 3.9. Plot of i_c vs. catalyst concetration for [*t*-H1^{NH}]$^+$ (Conditions: 0.125 M [Bu_4N][$BArF_4$] in CH_2Cl_2, 1.0 mmol $H_2ClCCOOH$, GC working electrode, Pt counter electrode, Ag wire pseudo reference electrode, Fc internal standard, 0 °C)

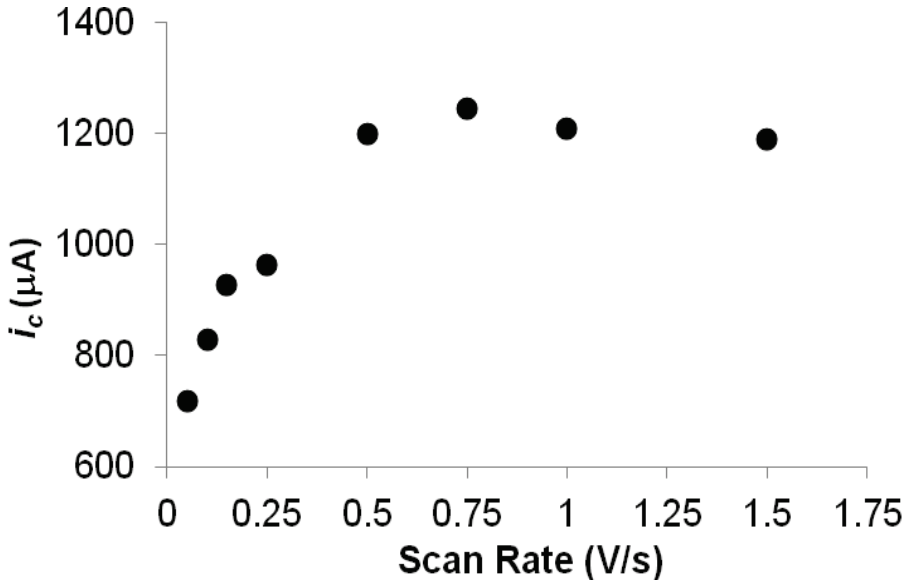

Figure 3.10. Plot of i_c vs. scan rate for [*t*-H1^{NH}]$^+$ (Conditions: 0.125 M [Bu_4N][$BArF_{24}$] in CH_2Cl_2, 1.0 mM 1^{NH}, GC working electrode, Pt counter electrode, Ag wire pseudo reference electrode, Fc internal standard, 0 °C)

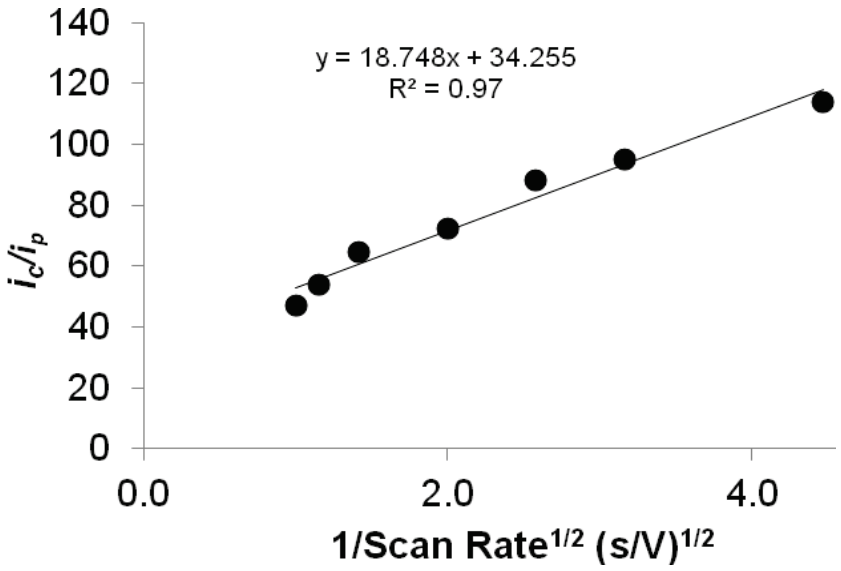

Figure 3.11. Plot of i_c/i_p vs. 1/scan rate$^{1/2}$ for [*t*-H1^{NH}]$^+$ (Conditions see Figure 3.10).

Typical electrocatalysis experiments were performed in CH_2Cl_2 due to stability issues in MeCN. However, accurate values for $E°_{HA/H2}$ have not been calculated in CH_2Cl_2, and therefore, MeCN would be a more ideal solvent for accurate overpotential calculations. In order to determine a value for E_{cat} in MeCN, electrocatalysis was perfomed quickly in this solvent. A catalytic wave appears at -1.45 V, and the current increases upon addition of excess acid (Figure 3.12). A plateau is reached after ~ 600 equiv of acid have been added (Figure 3.13). However, two additional catalytic waves appear at high acid concentration, due to unknown decomposition products. Based on these experiments, the value for E_{cat} is not significantly different in CH_2Cl_2 vs. MeCN solutions (Table 3.1), and therefore, it is a valid approximation to calculate overpotential using E_{cat} measured in CH_2Cl_2 and $E°_{HA/H2}$ calculated in MeCN.

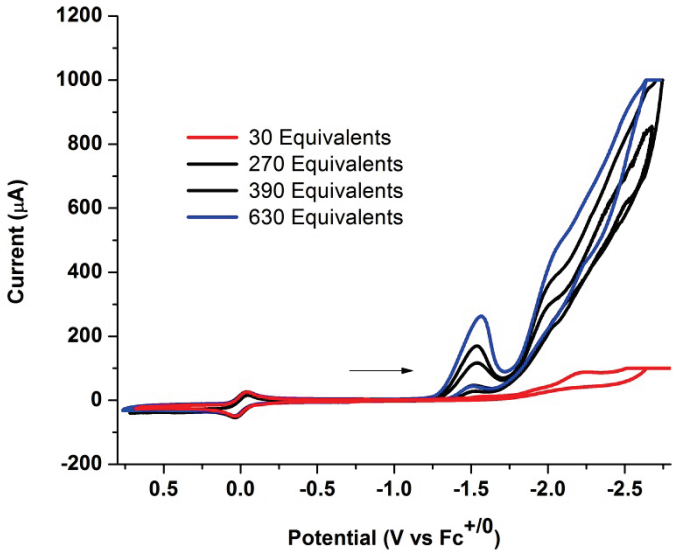

Figure 3.12. a. Cyclic volatamograms of $Fe_2(adt^{NH})(CO)_2(dppv)_2$ (1^{NH}) with increasing amounts of $Cl_2HCCOOH$. (Conditions: 0.1 M $[Bu_4N][PF_6]$ in MeCN, 1.0 mM 1^{NH}, 0 °C, GC working electrode, Pt counter electrode, Ag wire pseudo reference electrode, Fc internal standard, Scan Rate = 0.1 V/s)

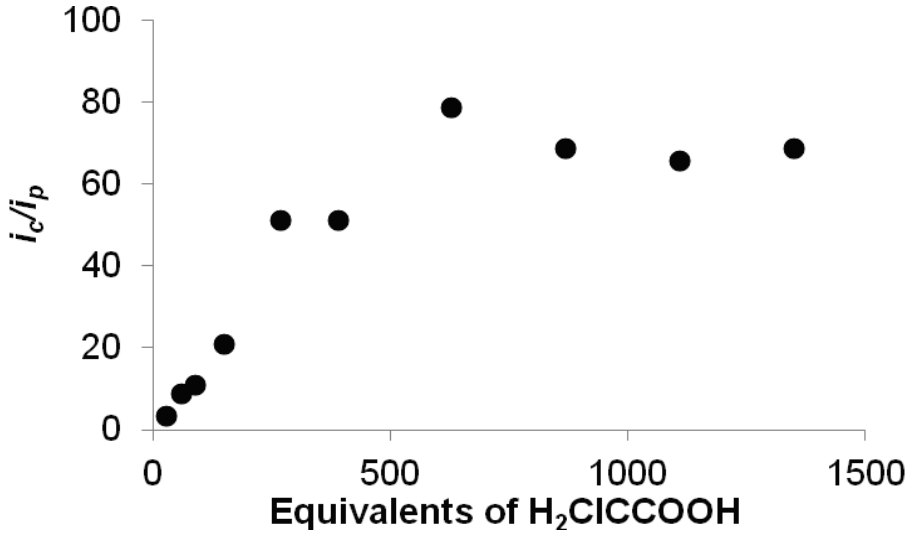

Figure 3.13 Plot of i_c/i_p vs. equivalents of acid added to a solution of 1^{NH}. (Conditions: see Figure 3.12)

As discussed in Chapter 1, when electrocatalysts reach a plateau region, the rate determining step (RDS) is independent of acid concentration, and the turnover frequency is solely dependent on the rate at which H_2 is formed by the catalyst. This step therefore involves either the formation of an H_2 complex or release of H_2 from the catalyst. In order to evaluate the RDS, electrocatalysis experiments were performed using $ClCH_2CO_2D$. In this case, the

dependence of the i_c/i_p vs [$ClCH_2CO_2D$] is linear up to 60 equiv of acid, and reaches a plateau at i_c/i_p of 18, which corresponds to a turnover frequency of 420 s^{-1} (Figures 3.14, 3.15). The rate decreases ten-fold, compared to that exhibited in experiments that utilize $ClCH_2CO_2H$ (maximum i_c/i_p = 66, k = 4500 s^{-1}). In general, hydrogen evolution by electrolysis is subject to substantial isotope effects,[23] and this aspect was observed with $\mathbf{1}^{NH}$.

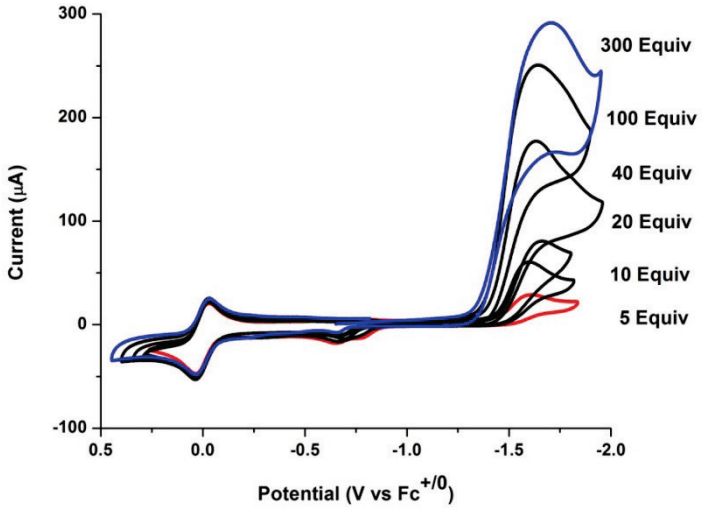

Figure 3.14. Cyclic voltamagrams of a 1.00 mM solution of $\mathbf{1}^{NH}$ (0 °C, 0.125 M [Bu_4N][BAr^F_{24}], CH_2Cl_2, scan rate = 0.5 V/s, GC working electrode, Pt counter electrode, Ag wire pseudo reference electrode, Fc internal standard) recorded with increasing equivs of $ClCH_2CO_2D$.

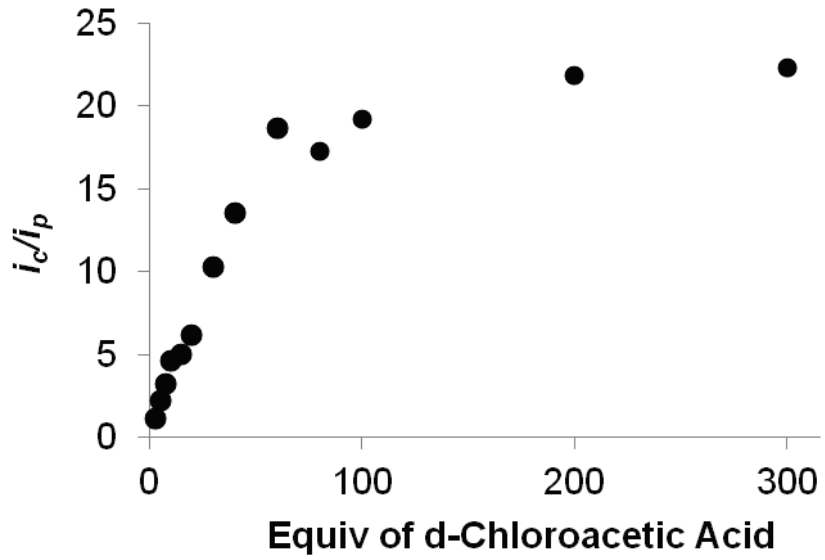

Figure 3.15. Plot of i_c/i_p vs. equivalents of acid added to a 1.00 mM solution of $\mathbf{1}^{NH}$. Conditions: see Figure 3.14.

In order to determine the Faradaic efficiency and turnover number for the catalyst, controlled-potential electrolysis of $[t\text{-H1}^{NH}]^+$ was performed. A solution of $\mathbf{1}^{NH}$ and excess $ClCH_2CO_2H$ was electrolyzed at -1.8 V vs $Fc^{+/0}$. As shown in Figure 3.16 and 3.17, the current gradually decreased over the course of ~ 6500 s, and the charge passed by the system increased. (Note that the background current due to direct reduction of protons at the working electrode has been subtracted from these plots. See Experimental for raw data.) The headspace of the cell was periodically sampled, and analyzed by gas chromatography. Based on the total charge passed by the system (Figure 3.17) and the amount of headspace measured by GC, the catalyst operates at a Faradaic efficiency of 99 ± 12 % (Table 3.3). The high yields for later time points are attributed to loss of the internal standard (CH_4) from the cell over time, leading to overestimation of the amount of H_2 present in the headspace. Therefore, a more modest estimation of the Faradaic efficiency is ~ 90%.

Table 3.3. Experimental results from controlled-potential electrolysis experiment.

Time (s)	1473	4300	5500
Total Charge (C)	0.957	2.823	3.204
Calc mmol H_2	4.96×10^{-3}	1.46×10^{-2}	1.66×10^{-2}
Calc Vol H_2 (μL)	111	328	372
Exp mmol H_2	4.32×10^{-3}	1.48×10^{-2}	1.82×10^{-2}
Exp Vol H_2 (μL)	97	332	408
Efficiency	87	101	110

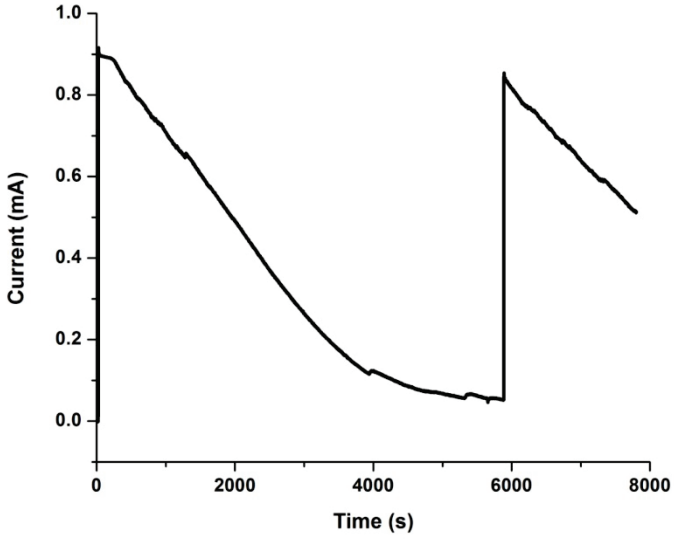

Figure 3.16. Plot of current vs time for controlled-potential electrolysis of $[t\text{-}H1^{NH}]^+$ in a CH_2Cl_2 solution of 0.1 M $[Bu_4N]PF_6$ / 10 mM $ClCH_2CO_2H$. To account for current due to direct reduction of protons at the carbon electrode, 0.21 mA has been subtracted. Time = 0 s corresponds to the time at which catalyst was added to the solution.

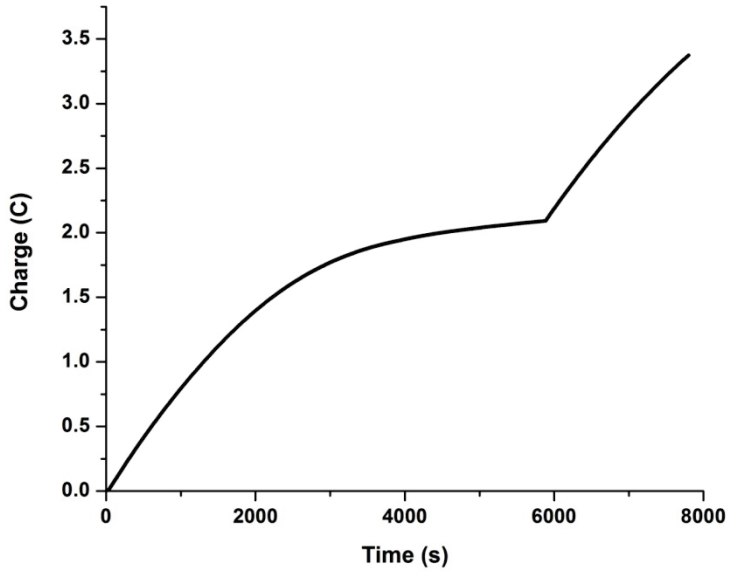

Figure 3.17. Plot of charge vs time for controlled-potential electrolysis $[t\text{-H1}^{NH}]^+$ in a CH_2Cl_2 solution of 0.1 M $[Bu_4N]PF_6$ / 10 mM $ClCH_2CO_2H$, with background correction.

If additional acid is introduced in the electrolysis cell, the current increases to the maximum exhibited at the beginning of the experiment, suggesting that catalytic activity is reactivated when acid is replenished. The turnover numbers for the duration of the experiment are shown in Table 3.4. Over the course of ~ 2 hours, 3.5 turnovers were acheived.

Table 3.4. Turnover number for catalysis by $[t\text{-H1}^{NH}]^+$, based on controlled-potential electrolysis experiment.

Time (s)	773	3600	4800	5800	7800
Charge Due to Catalyst (C)	0.629	1.90	2.02	2.08	3.38
mmol H_2 Due to Catalyst	3.26×10^{-3}	9.85×10^{-3}	1.08×10^{-2}	1.08×10^{-2}	1.75×10^{-2}
Turnover Number	0.65	1.97	2.16	2.16	3.50

3.5 Proton Reduction Catalysis by $[t\text{-HFe}_2(adt^{NH2})(CO)_2(dppv)_2]^{2+}$, $[t\text{-H1}^{NH2}]^{2+}$.

By the standards of synthetic catalysts, $[t\text{-H1}^{NH}]^+$ is a fast catalyst, but $[t\text{-H1}^{NH2}]^{2+}$ appears to be even faster. Thus, in the presence of strong acids such as $HBF_4{\cdot}Et_2O$ or trifluoroacetic acid (TFA), a catalytic wave is observed at -1.22 V. This lower potential process is assigned to electrocatalysis by $[t\text{-H1}^{NH2}]^{2+}$, the ammonium-terminal hydride that predominates in the presence of such strong acids. Monitoring the current at -1.2 V, the variation of i_c/i_p vs $[H^+]$ was found to be linear over 20 - 300 equiv (Figures 3.18, 3.19). The maximum i_c/i_p of ~167

corresponds to an estimated turnover frequency of 58,000 s^{-1} (Table 3.2). Despite the fact that stronger acids are required to generate [*t*-H**1**^{NH2}]$^{2+}$, the catalyst operates at a significantly milder potential than [*t*-H**1**^{NH}]$^{+}$, resulting in an overpotential of 0.5 V (~ 200 mV less than that for [*t*-H**1**^{NH}]$^{+}$) (Table 3.2).

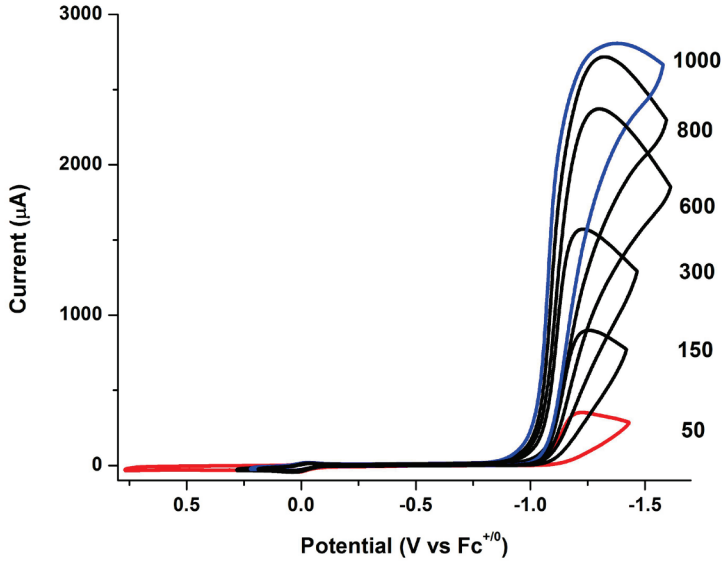

Figure 3.18 Cyclic voltammograms of a 0.5 mM solution of 1^{NH} (0 °C, 0.125 M [Bu$_4$N]BAr$^F_4$, CH_2Cl_2, scan rate = 1.0 V/s, GC working electrode, Pt counter electrode, Ag wire pseudo reference electrode, Fc internal standard) recorded with increasing equiv of CF_3CO_2H.

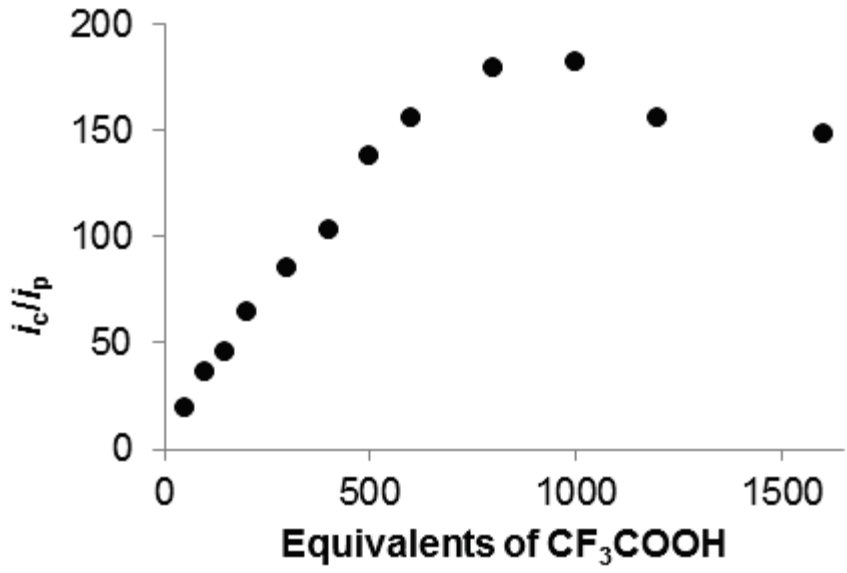

Figure 3.19. Dependence of i_c/i_p on equiv of CF_3CO_2H added to a 0.5 mM solution of $\mathbf{1}^{NH}$, with $[Bu_4N]BAr^F{}_4$ as supporting electrolyte.

Again, we verified the validity of equations 3.1 and 3.2 for the catalysis by $[t\text{-H}\mathbf{1}^{NH2}]^{2+}$. As expected, i_c/i_p is directly proportional to $1/\nu^{1/2}$ (Figure 3.20). As seen for catalysis by $[t\text{-H}\mathbf{1}^{NH}]^{+}$, i_c is only independent of n at high values of n > 0.25 V/s (Figure 3.21).

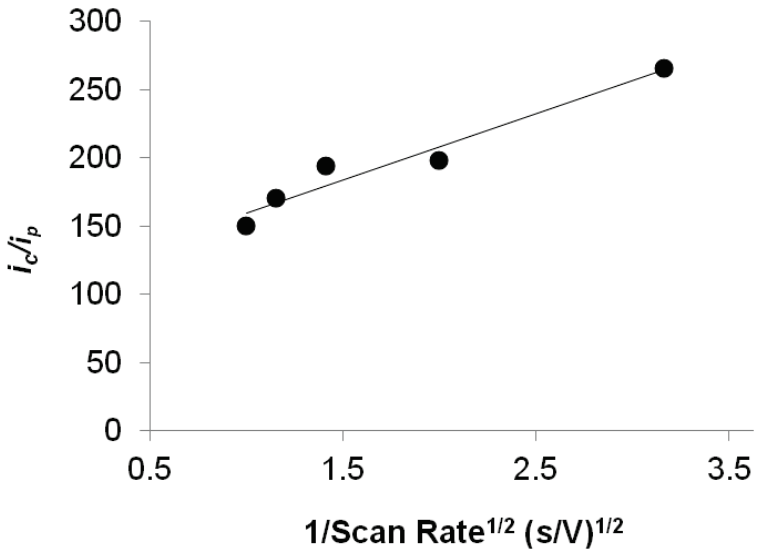

Figure 3.20 Plot of i_c/i_p vs. 1/scan rate$^{1/2}$ for $[t\text{-H}\mathbf{1}^{NH2}]^{2+}$.

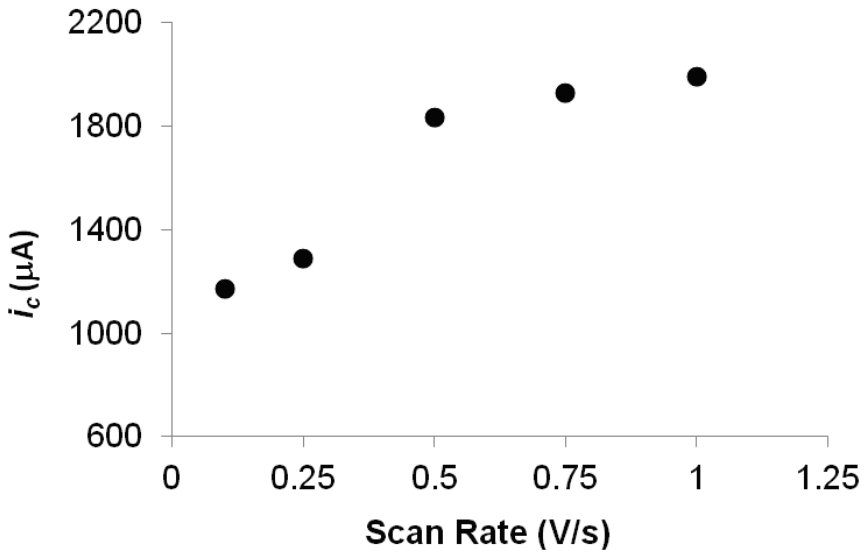

Figure 3.21. Plot of i_c vs. scan rate for [*t*-H1^{NH2}]$^{2+}$ (Conditions: 0.1 M [Bu$_4$N][BArF$_{24}$] in CH_2Cl_2, 0.5 mM 1^{NH}, GC working electrode, 0.67 M CF_3COOH, Pt counter electrode, Ag wire pseudo reference electrode, Fc internal standard, 0 °C)

In order to better probe the mechanism by which [*t*-H**1**^{NH2}]$^{2+}$ catalyzes proton reduction, we investigated catalysis in which CF_3CO_2D is substituted for CF_3CO_2H (Figures 3.22, 3.23). In this case, *k* decreases by about 15%, with the maximum i_c/i_p = 106 and k = 6600 s^{-1} (Table 3.2).

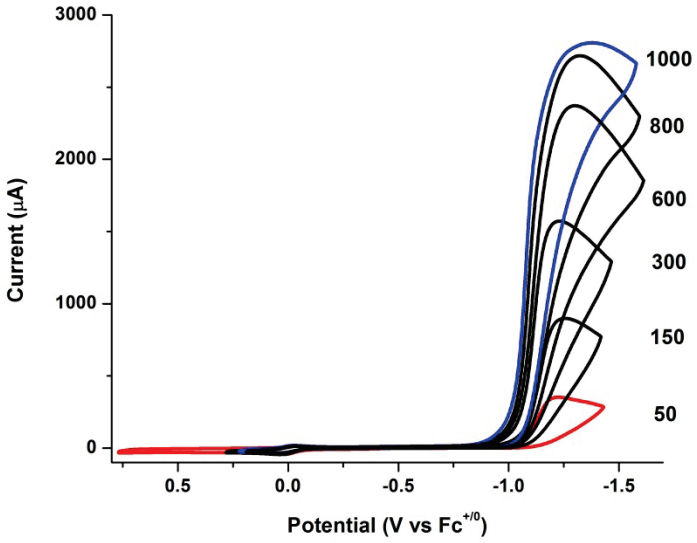

Figure 3.22. Cyclic voltamagrams of a 0.6 mM solution of 1^{NH} (0 °C, 0.005 M [Bu$_4$N][BAr$^F{}_{24}$], CH_2Cl_2, scan rate = 0.25 V/s, GC working electrode, Pt counter electrode, Ag wire pseudo reference electrode, Fc internal standard) recorded with increasing equivs of CF_3CO_2D.

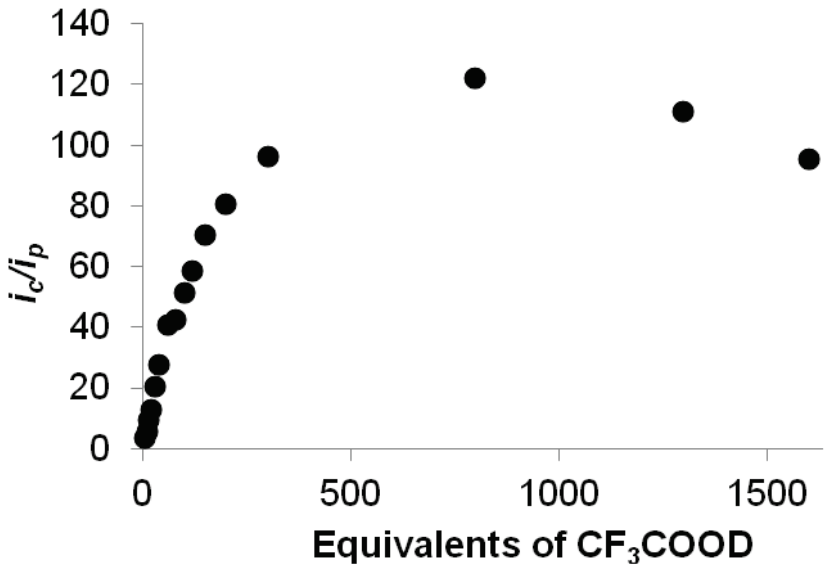

Figure 3.23. Plot of i_c/i_p vs. equiv of CF_3CO_2D added to a solution of 1^{NH}.

3.6 Proton reduction catalysis by diiron bridging hydride complexes.

As judged from electrocatalysis experiments utilizing terminal hydride diiron complexes, fast and efficient catalysis is only exhibited in for complexes that contain an azadithiolate cofactor adjacent to a hydride. Therefore, we sought to investigate the effect of changing from a terminal to a bridging hydride species, on the catalytic properties.

Electrocatalysis experiments were conducted with the bridging hydride $[\mu\text{-H}\mathbf{1}^{\mathbf{NH}}]^+$. At -1.8 V, the current increases with the addition of $ClCH_2CO_2H$ (Figure 3.24). A plot of i_c/i_p vs $[H^+]$ is linear over the range 2- 50 equiv of $ClCH_2CO_2H$, but begins to plateau at 60 equiv, corresponding to an i_c/i_p of ~10 (Figure 3.25). The catalytic rate is estimated to be 20 s^{-1}. The μ-hydride operates at an overpotential of 0.9 V, which is 200- 400 mV higher than the overpotentials for the terminal hydride species (Table 3.2). Based on these results, both the azadithiolate cofactor and terminal hydride are necessary for fast and efficient proton reduction catalysis by diiron hydrides.

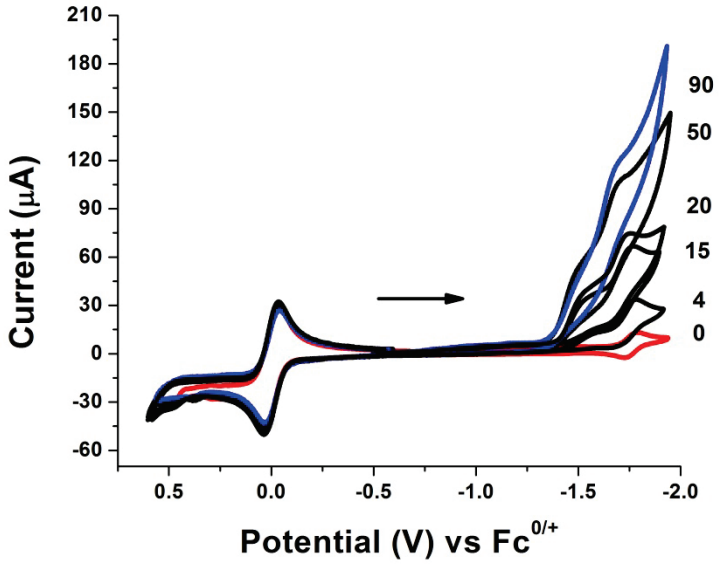

Figure 3.24. a. Cyclic volatamograms of $[\mu\text{-HFe}_2(\text{adt})(\text{CO})_2(\text{dppv})_2]^+$ ($[\mu\text{-H1}^{\text{NH}}]^+$) with increasing amounts of $Cl_2HCCOOH$. (Conditions: 0.1 M $[Bu_4N][PF_6]$ in CH_2Cl_2, 1.0 mM $[\mu\text{-1H}]^+$, 0 °C, GC working electrode, Pt counter electrode, Ag wire pseudo reference electrode, Fc internal standard, Scan Rate = 0.1 V/s) (Equivalents of acid indicated to right of each cyclic

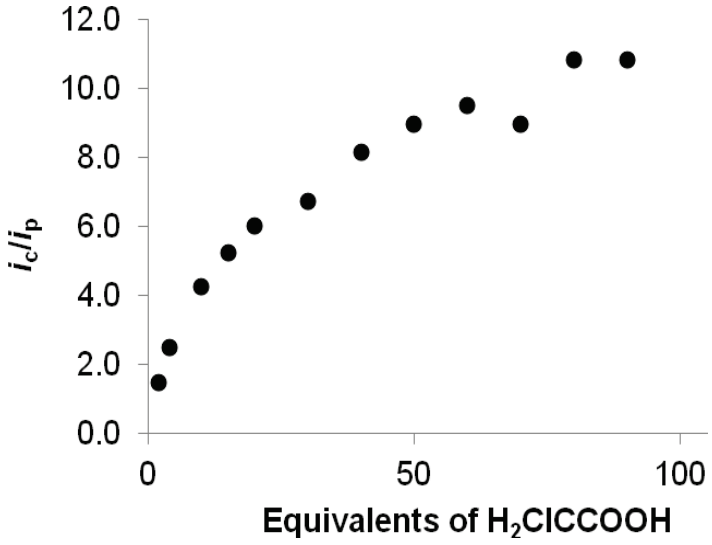

Figure 3.25. Plot of i_c/i_p vs equivalents of $Cl_2HCCOOH$ added to a solution of $[\mu\text{-HFe}_2(\text{adt})(\text{CO})_2(\text{dppv})_2]^+$.

For completeness, we studied the catalytic properties of $[\mu\text{-H}\mathbf{2}]^+$, which led to an interesting result. Unlike the analogous terminal hydride complex, $[t\text{-H}\mathbf{2}]^+$, which is only reactive towards strong acids, $[\mu\text{-H}\mathbf{2}]^+$ is reactive towards weak acid. Addition of $ClCH_2CO_2H$ to a solution of $[\mu\text{-H}\mathbf{2}]^+$ results in an increase in the current for the -1.8 V couple (Figure 3.26).

Plots of i_c/i_p vs $[H^+]$ are linear up to 10 equiv of acid, and the rate of catalysis by this derivative is calculated to be ~3 s^{-1} (Figure 3.27). The overpotential is estimated to be 0.95 V for this very slow process.[21] These data suggest that the bridging hydride, $[\mu\text{-H}\mathbf{2}]^+$, is actually a slightly better catalyst than the analogous terminal hydride, $[t\text{-H}\mathbf{2}]^+$, in that it catalyzes proton reduction with weak acids, resulting in a slightly lower overpotential. The reactivity with weak acids also gives some indication into the mechanism by which the bridging hydrides opertate (See section 3.7).

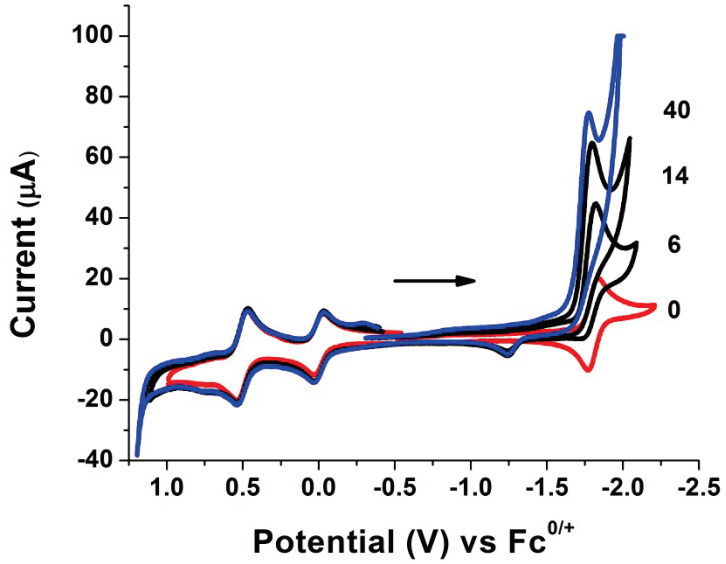

Figure 3.26. Cyclic volatamograms of $[\mu\text{-H2}]PF_6$ with increasing amounts of $Cl_2HCCOOH$ (Equivalents of acid indicated to right of each cyclic voltammogram). (Conditions: 0.1 M $[Bu_4N]PF_6$ in CH_2Cl_2, 1.0 mM $[\mu\text{-H2}]^+$, 20 °C, GC working electrode, Pt counter electrode, Ag wire pseudo reference electrode, Fc internal standard, Scan Rate = 0.1 V/s)

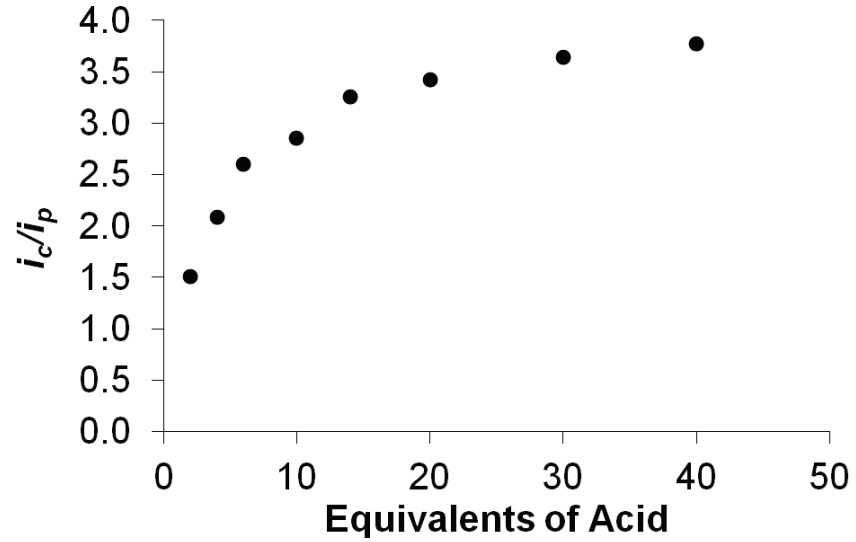

Figure 3.27. Plot of i_c/i_p vs. equivalents of acid added to solution of [μ-H2]PF_6.

3.7 Proposed mechanisms of proton reduction catalysis by diiron hydrides.

As discussed above, catalysts that contain two biologically relevant components, the azadithiolate cofactor and a terminal hydride, operate at very fast rates and low overpotentials. As judged from spectroscopic and electrochemical data, some details of the mechanism by which proton reduction catalysis can be inferred.

Protonation studies on $\mathbf{1}^{\mathbf{NH}}$ have shown that initial protonation occurs at the adt amine to form an ammonium species (Scheme 3.2, A), and then the proton is relayed to an Fe center, forming the terminal hydride, [*t*-H$\mathbf{1}^{\mathbf{NH}}$]$^+$ (Scheme 3.2, B). The strength of the acid determines the next step in the mechanism. When weaker acids, such as $ClCH_2CO_2H$ ($pK_{a\text{-}}^{MeCN}$= 15.3)[19], are used, a catalytic wave is present at ~-1.6 V. This potential corresponds with that at which [*t*-H$\mathbf{1}^{\mathbf{NH}}$]$^+$ is reduced, indicating that this terminal hydride species is the active catalyst. Prior to additional protonation steps, [*t*-H$\mathbf{1}^{\mathbf{NH}}$]$^+$ must first be reduced by one electron (Scheme 3.2, C). Reduction of [*t*-H$\mathbf{1}^{\mathbf{NH}}$]$^+$ results in formation of a reduced hydride species, and after this step, an additional protonation, reduction, and release of H_2 must occur to reform $\mathbf{1}^{\mathbf{NH}}$ (Scheme 3.2, D).

Scheme 3.2 Proposed mechanism for catalysis by azadithiolate terminal hydride complexes.

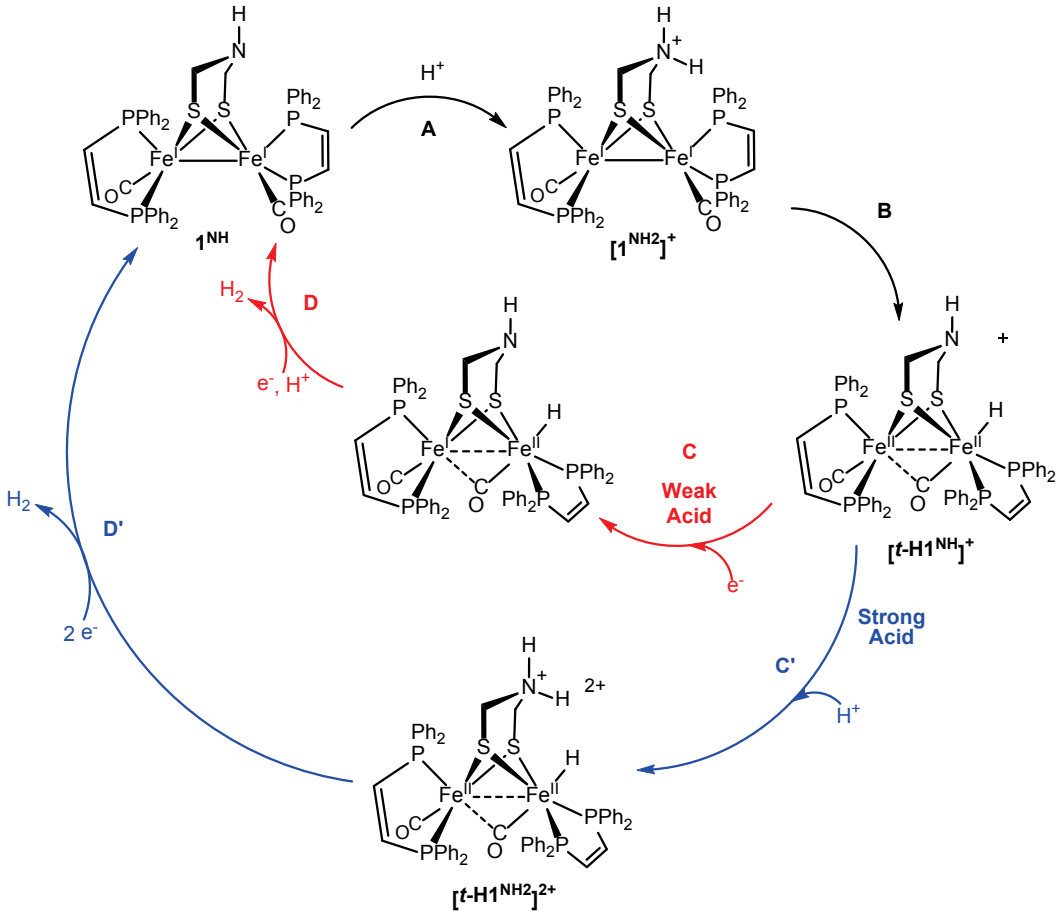

When a stronger acid is used, such as CF_3COOH (pK_{a}^{MeCN}= 12.7)[19], the reductive current at -1.3 V, corresponding to [*t*-H**1**^{NH2}]$^{2+}$, increases, suggesting that [*t*-H**1**^{NH2}]$^{2+}$ is the active catalyst (Scheme 3.2, C'). As judged from crystallographic data, there is a short distance between the hydride and the proton on the ammonium cofactor in [*t*-H**1**^{NH2}]$^{2+}$. This dihydrogen bond provides a unique insight into a probable intermediate in the evolution of hydrogen. Upon reduction, these couple to form H_2 (either in the form of a dihydrogen complex or as free H_2). The exact details of this final step are not obvious, but it necessarily involves two additional electron transfers, release of H_2 and reformation of **1**^{NH} (Scheme 3.2, D').

For catalysis by both [*t*-H**1**^{NH}]$^{+}$ and [*t*-H**1**^{NH2}]$^{2+}$, the final steps in the mechanism and the exact nature of the rate determining step are not obvious. From electrocatalysis experiments, it is known that the rate determining step is independent of acid concentration. Therefore, there are a two possible rate limiting steps; (i) coupling of the ammonium proton with the hydride to form a

dihydrogen complex or (ii) release of dihydrogen from the catalyst. In either case, the rate of catalysis would be decreased when protic acids are replaced with the equivalent deutero acid, which was observed in such experiments.

For both adt terminal hydride complexes, the presence of a pendant base (the adt amine) is important to the rate of catalysis. Further proof for the importance of this amine cofactor is provided by the poor catalytic activity exhibited by the analogous pdt complex, $[t\text{-H}\mathbf{2}]^+$. The pdt and adt complexes have similar thermodynamic properties, based on spectroscopic and electrochemical data. Most importantly, the singly protonated terminal hydride complexes, $[t\text{-H}\mathbf{1}^{\mathbf{NH}}]^+$ and $[t\text{-H}\mathbf{2}]^+$ are reduced at nearly identical potentials (Table 3.1), and so the differences in catalytic activities are not attributed to electronic differences.

A proposed mechanism for proton reduction catalyzed by $[t\text{-H}\mathbf{2}]^+$ is shown in Scheme 3.3. Based on spectroscopic data, **2** is protonated to form the terminal hydride species $[t\text{-H}\mathbf{2}]^+$ (Scheme 3.3, A). Protonation of **2** is only achieved with strong acids, indicating that **2** is not an easily protonated complex. The terminal hydride species is reduced at -1.68 V to form a reduced hydride (Scheme 3.3, B). The reduced hydride must then be protonated and form a dihydrogen complex (Scheme 3.3, C). The dihydrogen complex is reduced and releases H_2, to reform **2**, with uncertainty associated with the order of these two steps (Scheme 3.3, D).

Again, the rate determining step is independent of acid concentration, and so it could be either C or D. In C, the reduced hydride must be protonated, but there is no obvious basic site at which this protonation may occur. The iron centers are coordinatively saturated, so a ligand may have to dissociate, in order to open a site for protonation. The requirement of a structural rearrangement may be the cause of the slow rate of catalysis. Conversely, protonation could occur directly at the Fe-H bond, forming a dihydrogen complex. In either case, the rate of protonation would be slow, regardless of the concentration of acid. The alternative rate determining step, D, involves loss of H_2 from the diiron complex. The low catalytic activity for $[t\text{-H}\mathbf{2}]^+$ is likely due to the lack of a pendant base. Aside from the work presented here, there are other examples in which very high rates of proton reduction catalysis are only achieved when a metal hydride is located adjacent to a pendant base. For example, DuBois and coworkers Ni tetraphosphine complexes achieve the highest rates when bases are incorporated into the second coordination sphere. The presence of a pendant base effectively increases the concentration of

protons near the metal hydride, which in turns aids in coupling the proton and hydride, in order to form dihydrogen.

Scheme 3.3 Proposed mechanism for proton reduction catalysis by [*t*-H2]$^+$.

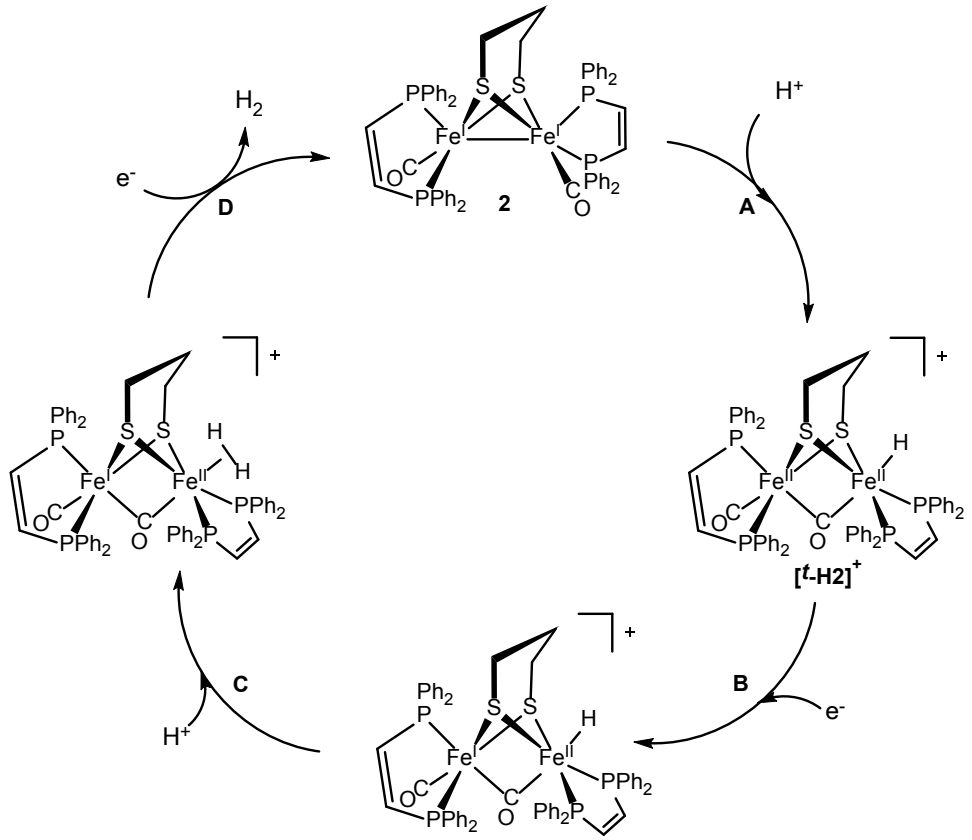

Further support for the necessity of a hydride adjacent to a pendant base comes from studies on catalytic properties of bridging hydrides. Both bridging hydride species, [μ-H**1**$^{\mathbf{NH}}$]$^+$ and [μ-H**2**]$^+$ are poor proton reduction catalysts, and this is likely due to the absence of a basic site to help couple the proton and hydride.

Based on electrocatalysis studies, the bridging hydrides catalyze proton reduction by an entirely different mechanism than the analogous terminal hydrides. In the terminal hydride mechanisms, the neutral species, either **1**$^{\mathbf{NH}}$ or **2**, are generated, and the terminal hydrides are reformed. There are several lines of evidence that suggest that the neutral complexes are not reformed in the bridging hydride mechanism. For catalysis by [μ-H**2**]$^+$, reformation of **2** would require protonation to form [*t*-H**2**]$^+$. However, [μ-H**2**]$^+$ is catalytically active with weak acid, which, from protonation studies, is unable to protonate **2**. Therefore, the mechanism cannot involve formation and subsequent protonation of **2**.

Similarly, if $\mathbf{1}^{\mathbf{NH}}$ was generated during the course of catalysis by $[\mu\text{-H}\mathbf{1}^{\mathbf{NH}}]^{+}$, then after one cycle, $[t\text{-H}\mathbf{1}^{\mathbf{NH2}}]^{2+}$ would form, and being a very active catalyst, would dominate the catalytic cycle. In other words, once the terminal hydride formed, it would catalyze proton reduction at a faster rate than it would isomerize to the bridging hydride. The fact that the bridging hydride is an active catalyst and terminal hydride does not take over after one cycle indicates that formation of $\mathbf{1}^{\mathbf{NH}}$ does not occur.

Based on these results, a mechanism is proposed in which the bridging hydride acts as a "spectator" ligand (Scheme 3.4). A similar mechanism has been proposed by Talarmin for catalysis by $[Fe_2(pdt)(\mu\text{-H})(CO)_4(dppe)]^{+}$, which does not exhibit formation of $Fe_2(pdt)(CO)_4(dppe)$ during the catalytic cycle.[24]

Scheme 3.4 Proposed mechanism for proton reduction catalysis by bridging hydride complexes.

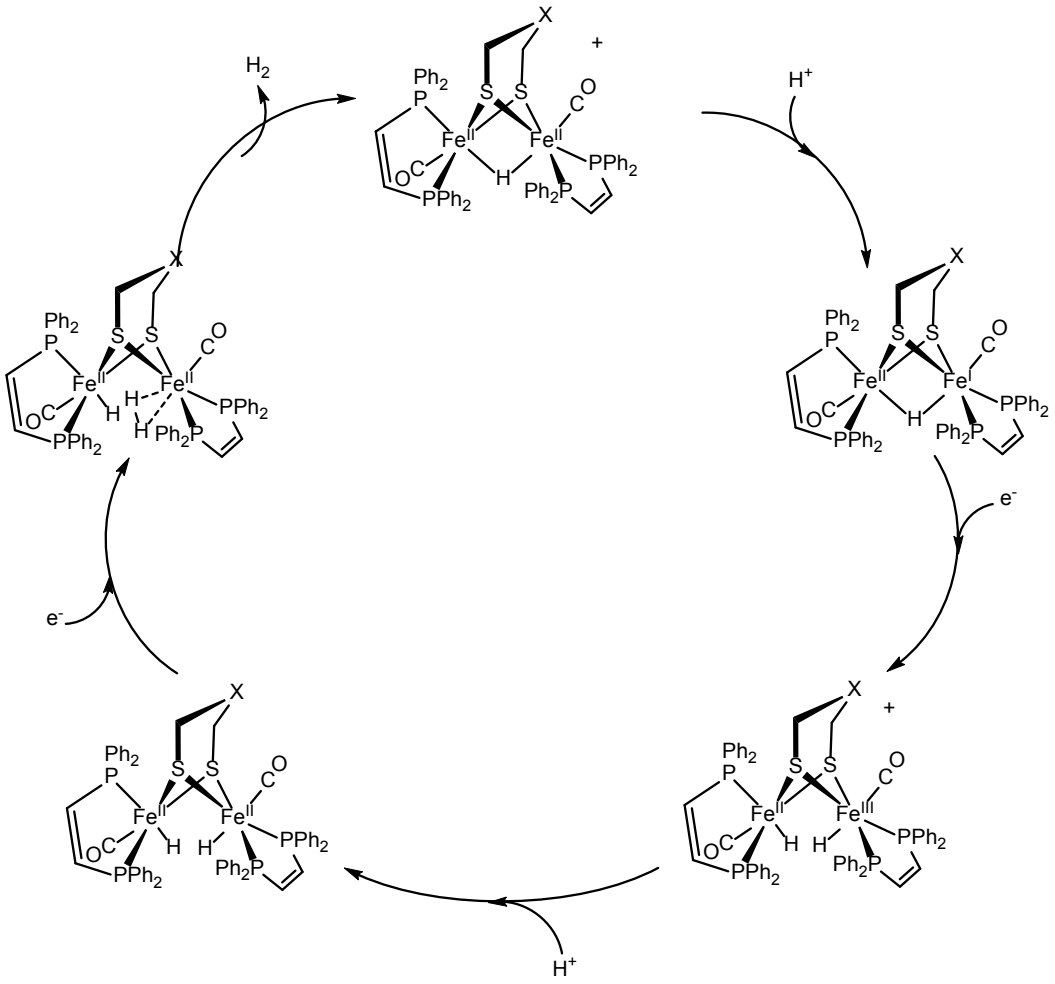

3.8 Conclusions

Hydrogen evolution by biomimetic diiron dithiolates is accelerated by the amine cofactor, to which the hydride ligand must be adjacent. The protonated derivatives of $\mathbf{1}^{\mathbf{NH}}$ and **2** exhibit very different catalytic properties, although the neutral complexes are almost indistinguishable spectroscopically. For both the pdt and adt derivatives, the terminal hydrides reduce at potentials that are 100 - 200 mV more positive than the corresponding bridging hydrides. The difference in reduction potentials between the isomeric hydrides is proposed to reflect differences in the localization of the reduction; the terminal hydride reduction is localized on the non-hydride containing Fe center, whereas the bridging hydride negative charge is delocalized over both Fe centers, making them equally difficult to reduce.

As mentioned above, the best diiron hydride catalysts contain an amine cofactor and a terminal hydride ligand, two components that are also found in the [FeFe]-hydrogenases. The high rates associated with these complexes are attributed to the ability of the amine to be protonated, which effectively increases the concentration of acid near the hydride, in turn, aiding in coupling the hydride and the proton to form H_2. The slow rates for the pdt complex, $[t\text{-H}\mathbf{2}]^+$, are due to the lack of an internal base. Structural rearrangements are necessary for the coupling of the hydride and protons, thus slowing the process. The corresponding bridging hydrides are also poor catalysts. These catalyze proton reduction via a mechanism that is unrelated to that proposed for the natural systems.

Although the bio-inspired complexes described in this report are highly active proton reduction catalysts,[22,25] challenges remain. These biomimetic catalysts suffer from relatively negative reduction potentials leading to high overpotentials.[26] A future goal for this system may involve use of less electron donating diphsophine ligands, so that the complexes are reduced at more mild potentials. A tetraphosphine system would still be employed because it aids in stabilization of terminal hydride species. A potential class of diphosphine ligands is fluorinated derivatives of 1,2-diphenylphosphinobenzene (Scheme 3.5).

Scheme 3.5 Proposed modification to diiron tetraphosphine catalysts.

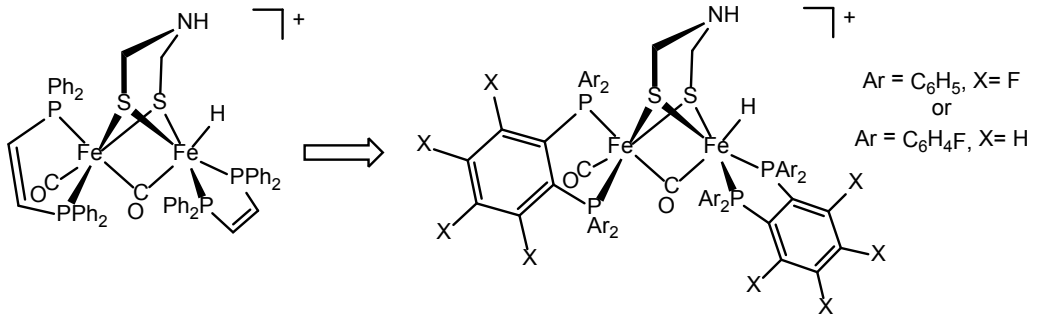

In the design of new catalysts, it is important to properly balance the basicity of the amine and the Fe centers. If the diphosphines are not electron donating enough, then the Fe centers may be less basic than the amine. In this case, protonation would occur at the amine, but the proton would not be transferred to a Fe center. This situation is exhibited by the related complexes, $Fe_2(adt^{iPr})(CO)_2(dppe)$ and $Fe_2(adt^{iPr})(CO)_2(phen)$. In these compounds, the amine is more basic than the Fe centers, so the kinetic products of protonation are ammonium species, which do not isomerize to corresponding Fe hydride complexes.[27] In order to balance the basicities of the amine and the Fe centers, a mixture of diphosphine ligands may be necessary. Another possible solution to the high overpotential involves incorporation of redox-active center to mediate the proton-coupled electron transfer that is implicated for the breaking and making of the H-H bond.[28,29]

3.9 Experimental

General procedures for electrochemical experiments. Electrochemical experiments were carried out on CH Instruments Model 600D Series Electrochemical Analyzer or a BAS-100 Electrochemical Analyzer. Cyclic voltammetry experiments were conducted using a 10-mL one-compartment glass cell with a tight-fitting Teflon top. The working electrode was a glassy carbon (GC) disk (diameter = 3.00 mm). A silver wire was used as a quasi-reference electrode, and the counter electrode was a Pt wire. Ferrocene was added as an internal reference, and each cyclic voltammogram was referenced to this $Fc^{0/+}$ couple = 0.00 V. *i*R compensation was applied to all measurements using the CH Instruments or BAS software. Cell resistance was determined prior to each scan, and the correction applied to the subsequently collected cyclic voltammogram. During prolonged experiments, additional solvent was added to compensate for

evaporative loss. Between scans, the solution was purged briefly with N_2 and the working GC electrode was removed and polished. The duration of typical electrochemical titrations was 30 min. For all experiments, the electrolyte solution was prepared and sparged in the cell, which was fitted with electrodes. A cyclic voltammogram of the electrolyte was collected prior to the addition of Fe_2 compound, in order to check the purity of the electrolyte. The diiron compound was then dissolved in the electrolyte solution and transferred to the cell. For all electroctalysis experiments, a control experiment was performed under identical conditions but in the absence of catalyst. These control experiments were used to subtract the contribution of the electrode from the catalytic current.

Cyclic voltammetry of diiron hydrides. cyclic voltammogram's of terminal hydride species were collected by *in-situ* generation of the terminal hydrides, due to their instability. A solution of 0.1 M supporting electrolyte (either $[Bu_4N]BAr^F{}_{24}$ or $[Bu_4N]PF_6$) and 1.0 mM neutral complex (**1**^{NH} or **2**) at 0 °C was treated with 1-2 equivalents of $[H(OEt_2)_2]BAr^F{}_{24}$. The corresponding bridging hydrides were isolated at their BF_4^- or PF_6^- salts, and these were analyzed by cyclic voltammogram.

Proton reduction catalysis by [*t*-HFe$_2$(pdt)(CO)$_2$(dppv)$_2$]$^+$, [*t*-H2]$^+$. A 4-mL CH_2Cl_2 solution of **2** (4.3 mg, 0.004 mmol) and $[Bu_4N]PF_6$ (308 mg, 0.0.8 mmol) was cooled to 0 ºC. The solution was then treated with aliquots of a 0.2 M solution of $HBF_4{\cdot}Et_2O$ in CH_2Cl_2 via a micropipette. After each addition, a cyclic voltammogram was collected at ν= 0.5 V/s, and the value of i_c was recorded. Addition of acid continued until the value of i_c/i_p remained constant. As the concentration of acid increased, a wave at more negative potential appears, but this is attributed to reduction of protons directly at the glassy carbon electrode.

Proton reduction catalysis by [*t*-HFe$_2$(adt^{NH})(CO)$_2$(dppv$_2$)]$^+$, [*t*-H1^{NH}]$^+$. A 2-mL CH_2Cl_2 solution of **1**^{NH} (2.0 mg, 0.002 mmol) and $[NBu_4]BAr^F{}_{24}$ (276 mg, 0.25 mmol) was cooled to 0 ºC. A cyclic voltammogram was recorded in the absence of acid, in order to obtain a value for i_p. The solution was then treated with aliquots of a 2 M solution of HCl_2CCO_2H in CH_2Cl_2 via a micropipette. After each addition, a cyclic voltammogram was collected at ν= 0.5 V/s, and the value of i_c was recorded. Addition of acid continued until the value of i_c/i_p remained constant. A similar experiment was performed in MeCN solution, in which case, a second reduction wave is observed at -1.8 V that also increases with addition of acid. The species responsible for this wave is unknown.

Catalyst concentration dependence for [*t*-HFe$_2$(adt^{NH})(CO)$_2$(dppv$_2$)]$^+$, [*t*-H1^{NH}]$^+$. A 1.5-mL CH_2Cl_2 solution of 1.0 mM **1**^{NH} (1.5 mg, 0.0015 mmol), 0.125 M $[Bu_4N]PF_6$, 0.67 M $H_2ClC_2O_2H$ (667 equiv), and a ferrocene reference was cooled to 0 °C. A cyclic voltammogram was obtained at ν = 1 V/s. To the solution, 0.5 mL aliquots of a 0.125 M $[Bu_4N]PF_6$ were added, and a cyclic voltammogram was collected at each concentration.

Scan rate dependence for catalysis by [*t*-HFe$_2$(adt^{NH})(CO)$_2$(dppv$_2$)]$^+$, [*t*-H1^{NH}]$^+$. A 2-mL CH_2Cl_2 solution of 1.0 mM **1** (2.1 mg, 0.002 mmol), 0.125 M $[Bu_4N]PF_6$, and a ferrocene reference was cooled to 0 °C and treated with 600 μL of 2.0 M H_2ClCCO_2H (600 equiv). Cyclic voltammograms were obtained at a range of scan rates.

Proton reduction catalysis by [*t*-DFe$_2$(adt^{NH})(CO)$_2$(dppv)$_2$]$^+$, [*t*-D1^{NH}]$^+$. A 2-mL CH_2Cl_2 solution of **1**^{NH} (2.0 mg, 0.002 mmol) and $[NBu_4]BAr^F{}_{24}$ (276 mg, 0.25 mmol) was cooled to 0 ºC. A cyclic voltammogram was recorded in the absence of acid, in order to obtain a value for i_p. The solution was then treated with aliquots of a 1 M solution of HCl_2CCO_2D in CH_2Cl_2 via a micropipette. After each addition, a cyclic voltammogram was collected at ν= 0.5 V/s, and the value of i_c was recorded. Addition of acid continued until the value of i_c/i_p remained constant.

Controlled-potential electrolysis of [*t*-HFe$_2$(adt^{NH})(CO)$_2$(dppv)$_2$]$^+$, [*t*-H1^{NH}]$^+$. A two compartment electrolysis cell was used, in which the compartments were separated by a medium glass frit (Figure 3.28). The main compartment contains three necks, which were fitted with a septum, a reticulated vitreous carbon working electrode (45 ppi Duocel carbon from ERG Materials and Aerospace Corporation, 1 cm x 1cm x 0.5 cm) connected to Nichrome wire by Ag epoxy (MG Chemicals Silver Conductive Epoxy, Cat No. 8331-14G) (Figure 3.29), and a $Ag/AgNO_3$ reference electrode (contained in a Vycor (purchased from BASi, Part# MF 2064) fritted glass tube) (Figure 3.30). The second compartment consists of a glass tube that was fitted with a Pt wire counter electrode, containing a Viton O-Ring (1.6 mm x 7.1 mm, McMaster 9263K137) to seal the compartment (Figure 3.31).

Figure 3.28. Controlled potential electrolysis cell, fitted with electrodes.

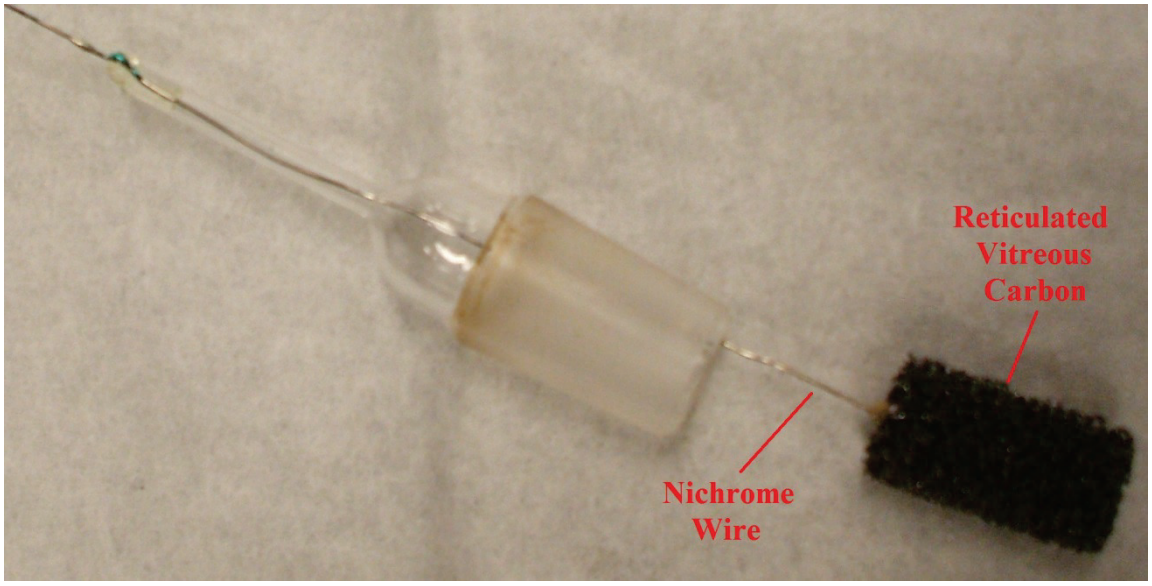

Figure 3.29. Reticulated vitreous carbon working electrode used for controlled potential electrolysis experiments.

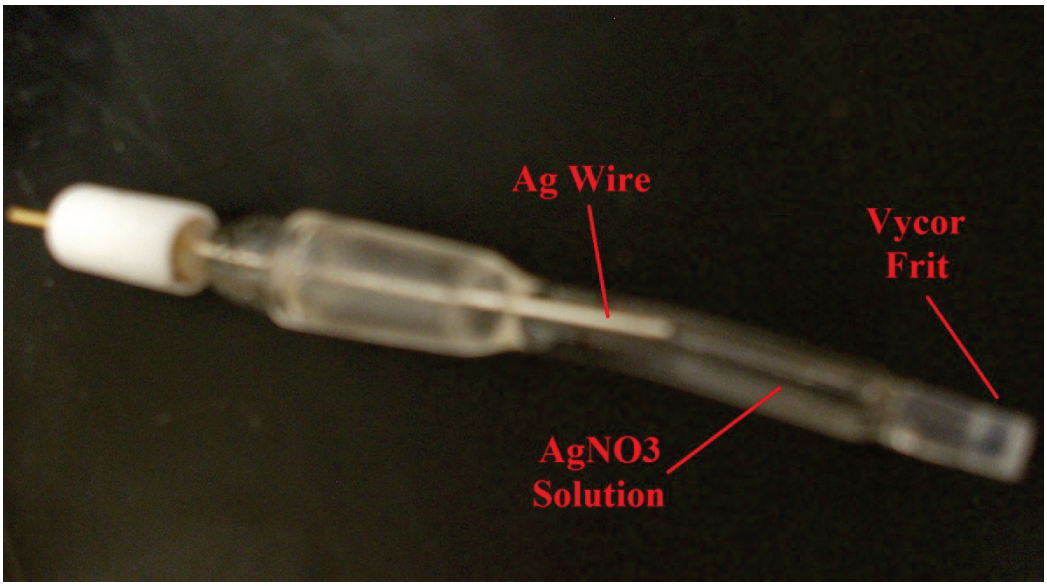

Figure 3.30 Ag/$AgNO_3$ reference electrode used for controlled potential electrolysis experiments.

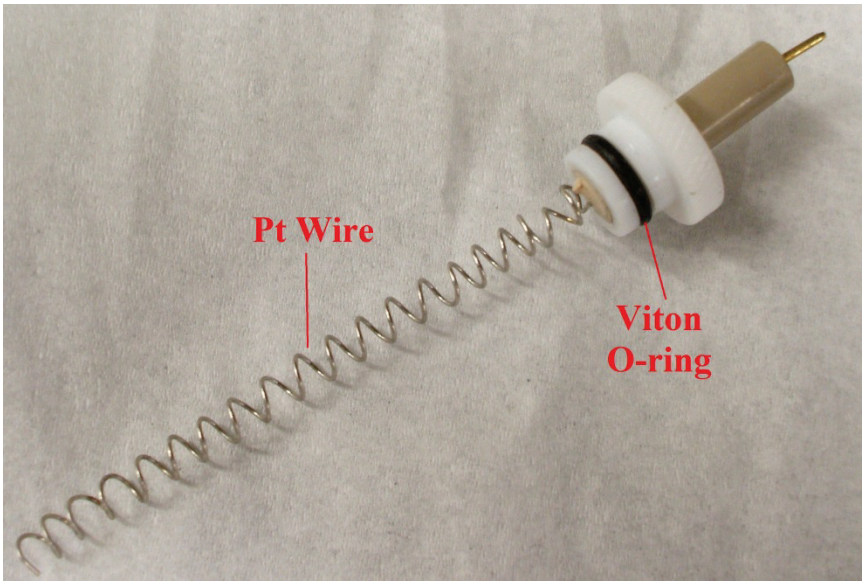

Figure 3.31. Pt counter electrode used for controlled potential electrolysis experiments.

To the main and Pt compartments of the cell, 10 mL and 7 mL, respectively, of a CH_2Cl_2 solution of 0.1 M $[Bu_4N]PF_6$ / 0.01 M $ClCH_2CO_2H$ was added. The solution was cooled to 0 ºC in an ice bath, and 100 µL of CH_4 was injected as an internal standard. The solution was then electrolyzed at -1.8 V vs $Fc^{+/0}$, until the current remained constant (~ 700 s, 0.21 mA). At this point, $\mathbf{1}^{\mathbf{NH}}$ (0.005 mmol) was added to the cell, causing the current to increase to 1.1 mA. The current gradually decreased, and after 6500 s it was within 5% of the background current. Upon

addition of 0.1 mmol of $ClCH_2CO_2H$ (0.2 mL of 0.5 M stock solution), the current once again increased to 1.1 mA and gradually decreased (Figures 3.32. 3.33).

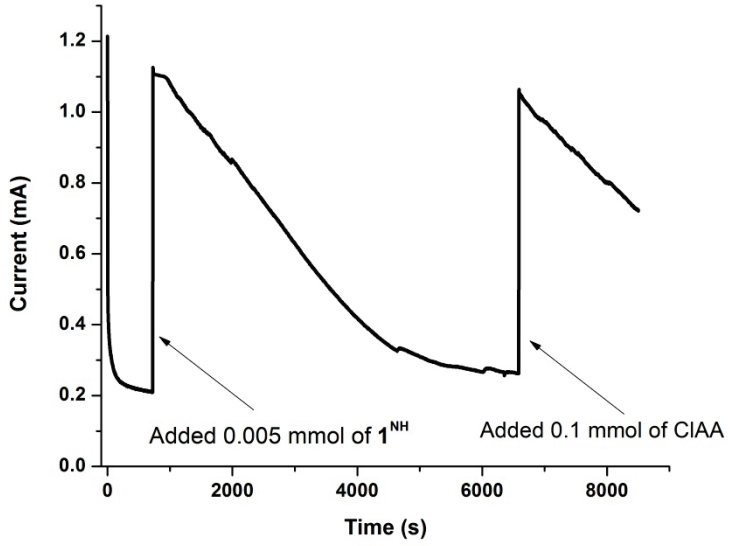

Figure 3.32. Plot of current vs time for controlled-potential electrolysis of [*t*-H1^{NH}]$^+$ in a CH_2Cl_2 solution of 0.1 M [Bu_4N]PF_6 / 10 mM $ClCH_2CO_2H$.

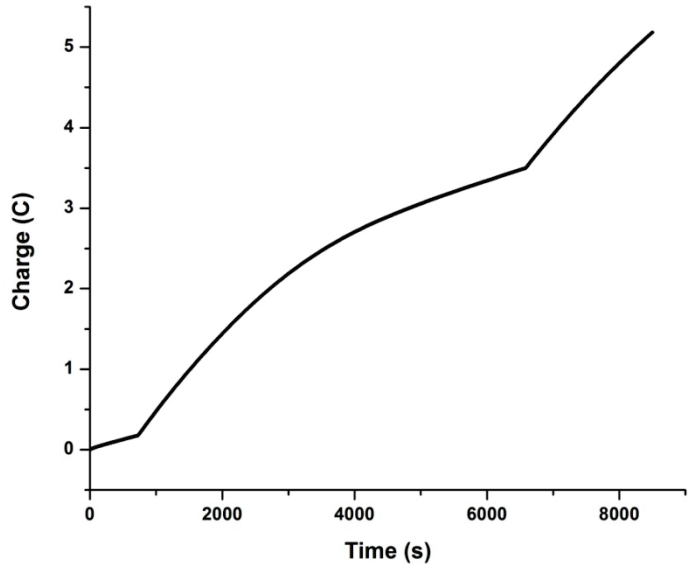

Figure 3.33. Plot of charge vs time for controlled-potential electrolysis of [*t*-H1^{NH}]$^+$ in a CH_2Cl_2 solution of 0.1 M [Bu_4N]PF_6 / 10 mM $ClCH_2CO_2H$.

During the first 6500 s of the experiment, 500 μL of headspace was periodically removed through the septum, using a Hamilton 500 μL gas-tight syringe, and injected on an Agilent

7820A gas chromatograph. The experimental yield of H_2 was calculated based on the areas of the H_2 and CH_4 peaks. The average current efficiency was calculated to be 99 ± 12 %.

Based on initial electrolysis in the absence of catalyst, 0.21 mA of the total current is due to reduction of protons at the carbon working electrode. Therefore, in turnover number calculations, 0.21 mA was subtracted from the total current, in order to calculate the charge passed due to the catalyst, and therefore the total amount of H_2 produced by the catalyst.

Proton reduction catalysis by $[t\text{-}HFe_2(adt^{NH2})(CO)_2(dppv)_2]^{2+}$, $[t\text{-}H1^{NH2}]^{2+}$. A 2-mL CH_2Cl_2 solution of **1** (2.0 mg, 0.002 mmol) and $[NBu_4]BAr^F{}_4$ (414 mg, 0.37 mmol) was cooled to 0 ºC. A cyclic voltammogram was recorded in the absence of acid, in order to obtain a value for i_p. The solution was then treated with aliquots of a 5 M solution of CF_3CO_2H in CH_2Cl_2 via a micropipette. After each addition, a cyclic voltammogram was collected at ν = 0.25 V/s, and the value of i_c was recorded. Addition of acid continued until the value of i_c/i_p remained constant.

Scan rate dependence for catalysis by $[t\text{-}HFe_2(adt^{NH2})(CO)_2(dppv_2)]^{2+}$, $[t\text{-}H1^{NH2}]^{2+}$. A 2.5-mL CH_2Cl_2 solution of 0.6 mM **1** (1.5 mg, 0.0015 mmol), 0.1 M $[Bu_4N]PF_6$, and a ferrocene reference was cooled to 0 °C and treated with 125 μL of CF_3CO_2H (1200 equiv). Cyclic voltammograms were obtained at a range of scan rates.

Proton reduction catalysis by $[t\text{-}DFe_2(adt^{ND})(CO)_2(dppv)_2]^{2+}$, $[t\text{-}D1^{ND}]^{2+}$. A 3-mL CH_2Cl_2 solution of $\mathbf{1}^{NH}$ (2.0 mg, 0.002 mmol) and $[NBu_4]BAr^F{}_4$ (166 mg, 0.15 mmol) was cooled to 0 ºC. A cyclic voltammogram was recorded in the absence of acid, in order to obtain a value for i_p. The solution was then treated with aliquots of a 1.8 M solution of CF_3CO_2D in CH_2Cl_2 via a micropipette. After each addition, a cyclic voltammogram was collected at ν = 0.25 V/s, and the value of i_c was recorded. Addition of acid continued until the value of i_c/i_p remained constant.

Proton reduction catalysis by $[Fe_2(adt^{NH})(\mu\text{-}H)(CO)_2(dppv)_2]BAr^F{}_4$, $[\mu\text{-}H1^{NH}]BAr^F{}_{24}$. A 5-mL CH_2Cl_2 solution of $[\mu\text{-}H\mathbf{1}^{NH}]BAr^F{}_{24}$ (9.7 mg, 0.005 mmol) and $[NBu_4]PF_6$ (193 mg, 0.5 mmol) was cooled to 0 ºC. A cyclic voltammogram was collected in the absence of acid, in order to obtain a value for i_p. The solution was then treated with aliquots of a 0.25 M solution of HCl_2CCO_2H in CH_2Cl_2 via a micropipette. After each addition, a cyclic voltammogram was collected at ν = 0.1 V/s, and the value of i_c was recorded. Addition of acid continued until the value of i_c/i_p remained constant.

Proton reduction catalysis by $[Fe_2(pdt)(\mu\text{-}H)(CO)_2(dppv)_2]PF_6$, $[\mu\text{-}H2]PF_6$. A 5-mL CH_2Cl_2 solution of $[\mu\text{-}H\mathbf{2}]PF_6$ (9.7 mg, 0.005 mmol) and $[Bu_4N]PF_6$ (193 mg, 0.5 mmol) was cooled

to 0 ºC. A cyclic voltammogram was collected in the absence of acid, in order to obtain a value for i_p. The solution was then treated with aliquots of a 0.25 M solution of HCl_2CCO_2H in CH_2Cl_2 via a micropipette. After each addition, a cyclic voltammogram was collected at $\nu = 0.1$ V/s, and the value of i_c was recorded. Addition of acid continued until the value of i_c/i_p remained constant.

3.10 References

(1) Gloaguen, F.; Rauchfuss, T. B. "Small Molecule Mimics of Hydrogenase: Hydrides and Redox." *Chem. Soc. Rev.* **2009**, *38*, 100.

(2) Tard, C.; Pickett, C. J. "Structural and Functional Analogues of the Active Sites of the [Fe]-, [NiFe]-, and [FeFe]-Hydrogenases." *Chem. Rev.* **2009**, *109*, 2245.

(3) Gloaguen, F.; Lawrence, J. D.; Rauchfuss, T. B. "Biomimetic Hydrogen Evolution Catalyzed by an Iron Carbonyl Thiolate." *J. Am. Chem. Soc.* **2001**, *123*, 9476.

(4) Gloaguen, F.; Lawrence, J. D.; Schmidt, M.; Wilson, S. R.; Rauchfuss, T. B. "Synthetic and Structural Studies on $[Fe_2(SR)_2(CN)_x(CO)_{6-x}]^{x-}$ as Active Site Models for Fe-Only Hydrogenases." *J. Am. Chem. Soc.* **2001**, *123*, 12518.

(5) Vincent, K. A.; Parkin, A.; Armstrong, F. A. "Investigating and Exploiting the Electrocatalytic Properties of Hydrogenases." *Chem. Rev.* **2007**, *107*, 4366.

(6) Bruschi, M.; Greco, C.; Kaukonen, M.; Fantucci, P.; Ryde, U.; De Gioia, L. "Influence of the [2Fe]H Subcluster Environment on the Properties of Key Intermediates in the Catalytic Cycle of [FeFe] Hydrogenases: Hints for the Rational Design of Synthetic Catalysts." *Angew. Chem., Int. Ed.* **2009**, *48*, 3503.

(7) van der Vlugt, J. I.; Rauchfuss, T. B.; Whaley, C. M.; Wilson, S. R. "Characterization of a Diferrous Terminal Hydride Mechanistically Relevant to the Fe-Only Hydrogenases." *J. Am. Chem. Soc.* **2005**, *127*, 16012.

(8) Adam, F. I.; Hogarth, G.; Kabir, S. E.; Richards, I. "Models of the iron-only hydrogenase: Synthesis and protonation of bridge and chelate complexes $[Fe_2(CO)_4\{Ph_2P(CH_2)_nPPh_2\}(\mu\text{-pdt})]$ (n =2-4) - evidence for a terminal hydride intermediate." *C. R. Chim.* **2008**, *11*, 890.

(9) Ezzaher, S.; Capon, J.-F.; Gloaguen, F.; Pétillon, F. Y.; Schollhammer, P.; Talarmin, J.; Pichon, R.; Kervarec, N. "Evidence for the Formation of Terminal Hydrides by Protonation of an Asymmetric Iron Hydrogenase Active Site Mimic." *Inorg. Chem.* **2007**, *46*, 3426.

(10) Barton, B. E.; Zampella, G.; Justice, A. K.; De Gioia, L.; Rauchfuss, T. B.; Wilson, S. R. "Isomerization of the hydride complexes $[HFe_2(SR)_2(PR_3)_x(CO)_{6-x}]^+$ (x = 2, 3, 4) relevant to the active site models for the [FeFe]-hydrogenases." *Dalton Trans.* **2010**, *39*, 3011.

(11) Ezzaher, S.; Capon, J.-F.; Gloaguen, F.; Kervarec, N.; Pétillon, F. Y.; Pichon, R.; Schollhammer, P.; Talarmin, J. "Diiron chelate complexes relevant to the active site of the iron-only hydrogenase." *C. R. Chim.* **2008**, *11*, 906.

(12) Barton, B. E.; Rauchfuss, T. B. "Terminal Hydride in [FeFe]-Hydrogenase Model Has Lower Potential for H2 Production Than the Isomeric Bridging Hydride." *Inorg. Chem.* **2008**, *47*, 2261.

(13) Justice, A. K.; De Gioia, L.; Nilges, M. J.; Rauchfuss, T. B.; Wilson, S. R.; Zampella, G. "Redox and Structural Properties of Mixed-Valence Models for the Active Site of the [FeFe]-Hydrogenase: Progress and Challenges." *Inorg. Chem.* **2008**, *47*, 7405.

(14) Lever, A. B. P. "Electrochemical parametrization of metal complex redox potentials, using the ruthenium(III)/ruthenium(II) couple to generate a ligand electrochemical series." *Inorg. Chem.* **1990**, *29*, 1271.

(15) Jablonskya, A.; Wright, J. A.; Fairhurst, S. A.; Peck, J. N. T.; Ibrahim, S. K.; Oganesyan, V. S.; Pickett, C. J. "Paramagnetic Bridging Hydrides of Relevance to Catalytic Hydrogen Evolution at Metallosulfur Centers." *J. Am. Chem. Soc.* **2011**, *133*, 18606.

(16) Wang, F.; Wang, M.; Liu, X.; Jin, K.; Dong, W.; Sun, L. "Protonation, electrochemical properties and molecular structures of halogen-functionalized diiron azadithiolate complexes related to the active site of iron-only hydrogenases." *Dalton Trans.* **2007**, 3812.

(17) Ott, S.; Kritikos, M.; Åkermark, B.; Sun, L.; Lomoth, R. "A Biomimetic Pathway for Hydrogen Evolution from a Model of the Iron Hydrogenase Active Site." *Angew. Chem., Int. Ed.* **2004**, *43*, 1006.

(18) Schwartz, L.; Eilers, G.; Eriksson, L.; Gogoll, A.; Lomoth, R.; Ott, S. "Iron hydrogenase active site mimic holding a proton and a hydride." *Chem. Commun.* **2006**, 520.

(19) Izutsu, K. *Acid-Base Dissociation Constants in Dipolar Aprotic Solvents*; Blackwell Scientific Publications: Oxford, U.K., 1990; Vol. 35.

(20) Fourmond, V.; Jacques, P.-A.; Fontecave, M.; Artero, V. "H_2 Evolution and Molecular Electrocatalysts: Determination of Overpotentials and Effect of Homoconjugation." *Inorg. Chem.* **2010**, *49*, 10338.

(21) Felton, G. A. N.; Glass, R. S.; Lichtenberger, D. L.; Evans, D. H. "Iron-Only Hydrogenase Mimics. Thermodynamic Aspects of the Use of Electrochemistry to Evaluate Catalytic Efficiency for Hydrogen Generation." *Inorg. Chem.* **2006**, *45*, 9181.

(22) Helm, M. L.; Stewart, M. P.; Bullock, R. M.; Rakowski DuBois, M.; DuBois, D. L. "A Synthetic Nickel Electrocatalyst with a Turnover Frequency Above 100,000 s^{-1} for H_2 Production." *Science* **2011**, *333*, 863.

(23) Miller, M. A.; Carey, A. A. In *Ullmann's Encyclopedia of Industrial Chemistry*; Wiley-VCH: Weinheim, 2000.

(24) Ezzaher, S.; Capon, J.-F.; Dumontet, N.; Gloaguen, F.; Pétillon, F. Y.; Schollhammer, P.; Talarmin, J. "Electrochemical study of the role of a H-bridged, unsymmetrically disubstituted diiron complex in proton reduction catalysis." *J. Electroanal. Chem.* **2009**, *626*, 161.

(25) Cheah, M. H.; Tard, C.; Borg, S. J.; Liu, X.; Ibrahim, S. K.; Pickett, C. J.; Best, S. P. "Modeling [Fe-Fe] Hydrogenase: Evidence for Bridging Carbonyl and Distal Iron Coordination Vacancy in an Electrocatalytically Competent Proton Reduction by an Iron Thiolate Assembly That Operates through Fe(0)-Fe(II) Levels." *J. Am. Chem. Soc.* **2007**, *129*, 11085.

(26) Fontecilla-Camps, J. C.; Volbeda, A.; Cavazza, C.; Nicolet, Y. "Structure/Function Relationships of [NiFe]- and [FeFe]-Hydrogenases." *Chem. Rev.* **2007**, *107*, 4273.

(27) Ezzaher, S.; Orain, P.-Y.; Capon, J.-F.; Gloaguen, F.; Pétillon, F. Y.; Roisnel, T.; Schollhammer, P.; Talarmin, J. "First insights into the protonation of dissymetrically disubstituted di-iron azadithiolate models of the [FeFe]H2ases active site." *Chem. Commun.* **2008**, 2547.

(28) Camara, J. M.; Rauchfuss, T. B. "Mild Redox Complementation Enables H2 Activation by [FeFe]-Hydrogenase Models." *J. Am. Chem. Soc.* **2011**, *133*, 8098.

(29) Camara, J. M.; Rauchfuss, T. B. "Combining acid–base, redox and substrate binding functionalities to give a complete model for the [FeFe]-hydrogenase." *Nature Chem.* **2012**, *4*, 26.

Chapter 4.

Active-Site Models for the Nickel-Iron Hydrogenases: Effects of Ligands on Reactivity and Catalytic Properties[†]

4.1 Introduction

[NiFe]-hydrogenases are more common in nature than the [FeFe]-hydrogenases, and are also far more tolerant of O_2.[1] The bimetallic active site of [NiFe]-hydrogenase consists of a distorted square planar Ni(SCys) unit, bridged to an $Fe(CN)_2(CO)$ unit, via two of the SCys ligands. The active site is not directly tethered to a 4Fe4S cluster, as in [FeFe]-hydrogenase, but a 4Fe4S cluster is located close to the active site, aids in electron transfer.[2] The Ni center is redox active, cycling between Ni(II) and Ni(III), whereas the Fe center is redox inactive, remaining in the ferrous state.[3]

[NiFe]-hydrogenase can be purified in air but is isolated as an inactive form, Ni-B, an EPR active Ni(III) state. This inactive state is proposed to contain a hydroxide ligand that bridges the Ni and Fe centers (Scheme 4.1). Under reducing conditions, Ni-B is converted to Ni-SI_R, via reduction to Ni(II). An active state, Ni-SI_A forms upon loss of the hydroxide ligand. Proposed mechanisms by which the enzyme operates are highly speculative. The main barrier to detailed mechanistic studies is the fact that hydrogenic substrates cannot be located, for example by X-ray crystallography, or studied by NMR spectroscopy. EPR methods have been used to characterize paramagnetic states, for example Ni-C, which is proposed to form upon reduction and protonation of Ni-SI_A.[4] A hydride ligand bridging Ni(III) and Fe(II) centers has been observed by pulsed EPR techniques.[5-7] Additional proton and electron transfers form Ni-R, which is proposed to contain a bridging hydride and a protonated SCys. The proton couples with the hydride, forming a dihydrogen complex, prior to release of H_2, reforming Ni-SI_A.[3]

[†] Portions of this chapter are reproduced from the following publication with permission from the authors.
Carroll, M. E.; Barton, B. E.; Gray, D. L.; Mack, A. E.; Rauchfuss, T.B. *Inorg. Chem.* **2011**, *50*, 9554–9563.

Scheme 4.1. Structures of the inactive and active forms of [NiFe]-hydrogenase and proposed mechanism of proton reduction.

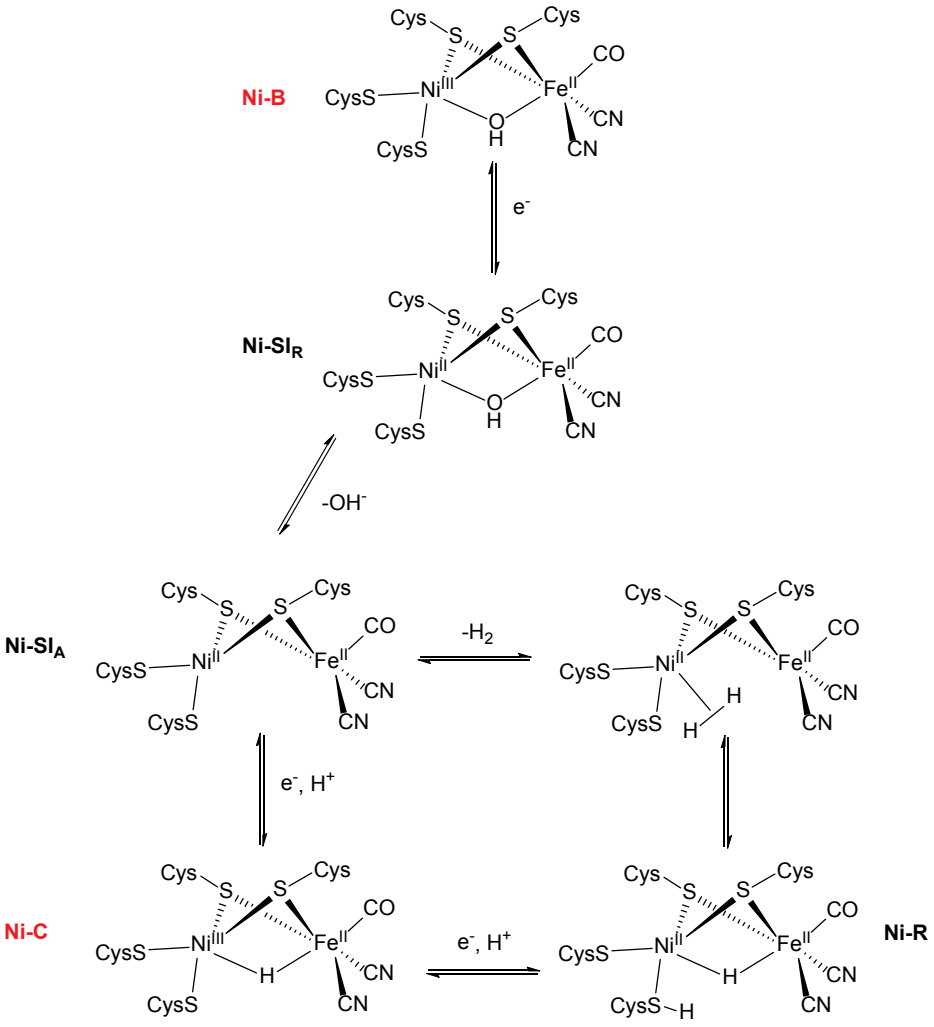

As with the [FeFe]-hydroganses, extensive work has focused on the synthesis of small molecule mimics for [NiFe]-hydrogense. Before the structural characterization in 1995, Fe was not known to be present in the active site, so early modeling efforts focused on the synthesis of NiS_4 complexes.[8,9] After the active site was found to consist of a Ni-Fe core, work focused on synthesis of monomeric Fe complexes that mimic the Fe center in the active site.[10] One notable example is $[CpFe(CO)(CN)_2]^-$ (Cp= $C_5H_5^-$), in which the Cp ligand is meant to mimic the electronic influence of the Ni center in the active site, and the IR spectrum closely matches that for the inactive forms, Ni-A and Ni-B.[11]

Heterobimetallic complexes of Ni and Fe were rare at the time that the structure of

[NiFe]-hydrogenase was determined, opening a new field for synthetic chemists. Extensive research has focused on the synthesis of NiFe complexes. One early class of model complexes contained Ni centers bound to N_2S_2 ligands.[10] One or both thiolate ligands on Ni bridge to the Fe center, mimicking one aspect of the active site structure. However, in general, the Ni-Fe distances are longer than that found in the enzyme. Two examples reported by Schroder and co-workers (Scheme 4.2), feature shorter Ni-Fe distances and bridging thiolate ligands. The Ni(salen) complex contains a non-biologically relevant Fe(0) center.[12,13]

Scheme 4.2 NiFe model complexes with N_2S_2 ligands.

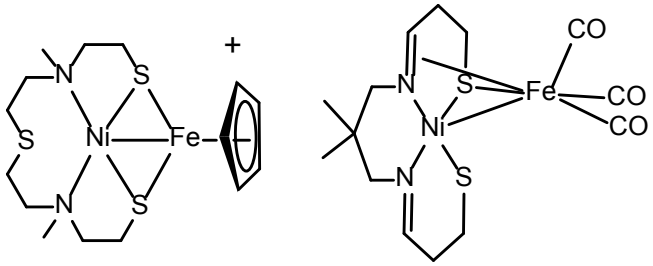

Numerous NiFe complexes with "NiS_4" centers have been synthesized. One class utilizes chelating S_4 ligands, which contain two thiolates and two thioethers. In general, the resulting NiFe complexes exhibit long Ni-Fe distances. Furthermore, the geometry at the Ni center is constrained to square planar, in contrast to the distorted tetrahedral geometry found in the active site. A number of models containing Ni tetrathiolates have been reported. The complexes reported by Tatsumi and co-workers (Scheme 4.3) contain a NiS_4 center, Fe bound to both CN^- and CO ligands, and Ni-Fe and M-S distances similar to those found in the active site (Scheme 4.3). However, these complexes are unstable at temperatures higher than -20 °C, and the Fe center is coordinatively saturated and does not undergo decarbonylation.

Scheme 4.3 Tatsumi's NiFe model complexes with Ni tetrathiolate and $Fe(CO)_2(CN)_2$ centers.

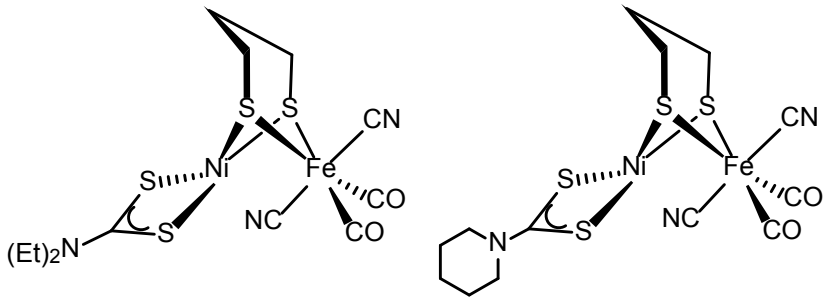

As discussed in Chapter 1, a large body of work has focused on the synthesis of functional NiRu models for the active site of [NiFe]-hydrogenase. Relevant to this work, Ogo and co-workers reported that the NiRu complex heterolytically cleaves H_2, forming a NiRu-hydride in water, along with a decrease in the pH of the reaction solution.[14] Very recently, the same group reported a NiFe model that can catalytically oxidize H_2, via a NiFe hydride complex (Scheme 4.4).

Scheme 4.4 Activation of H_2 by NiRu and NiFe models for [NiFe]-hydrogenase.

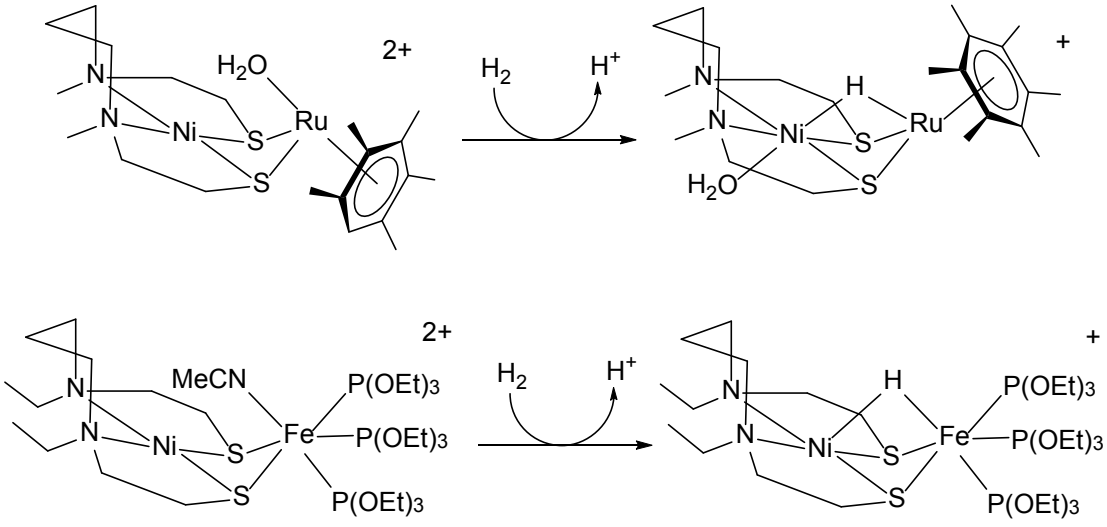

As of 2009, no NiFe models containing hydride ligands had been reported. This situation represented a major deficiency in the area, since hydride intermediates are proposed to be present in the catalytic cycle of the enzyme. Schröder and co-workers had reported the synthesis of (dppe)Ni(pdt)$Fe(CO)_3$, **1**, (pdt= 1,3-propanedithiolate, dppe = $Ph_2PCH_2CH_2PPh_2$) but claimed that the complex is unstable.[12] A former group member, Dr. Bryan Barton, found that **1** was

robust, reversibly protonated to give a hydride, and was amenable to substitution reactions.[15] Additionally, the hydride complex [(dppe)Ni(pdt)(μ-H)Fe(CO)$_3$]BF$_4$ ([**1**H]$^+$), the first crystallographically characterized NiFe hydride, was found to catalyze hydrogen evolution from acids at about –1.3 V vs Fc$^{+/0}$.[16] Barton also described changes in the iron subsite, leading to derivatives of the type [(dppe)Ni(pdt)(μ-H)Fe(CO)$_{3-x}$(PR$_3$)]BF$_4$, which also catalyze proton reduction.[16]

Dr. Bryan Barton previously reported that the reaction of Ni(xdt)$_2$(diphosphine) with Fe$_2$(CO)$_9$ gives the NiFe complexes in relatively good yield, but also results in undesirable co-formation of Fe$_2$(xdt)(CO)$_6$ (Scheme 4.5).[16] Therefore, in collaboration with Dr. Bryan Barton and Amanda Mack, we developed a new route to such complexes that involves reaction of ferrous carbonyls and Ni(xdt)(diphosphine), forming a μ-I intermediate, followed by reduction (Scheme 4.5). Our group had reported a related reaction of Fe(pdt)(CO)$_2$(dppe) with NiCl$_2$(dppe) to afford salts of [(dppe)Ni(pdt)(μ-Cl)Fe(CO)(dppe)]$^+$.[17] Until this work, we had not succeeded in converting such halide-bridged intermediates to the corresponding hydrides.

This chapter describes the influence of the dithiolate and the ligands on nickel on spectroscopic and catalytic properties of NiFe models. Unlike the active site of the [FeFe]-hydrogenase, the Ni and Fe centers in the [NiFe]-hydrogenases are linked by cysteinyl thiolates, but our previous models employed propanedithiolate, so variations of the thiolate were targeted. Furthermore, the terminal ligands on Ni in the protein are alkylthiolates, which are better donor ligands than arylphosphines.[18] Therefore, we sought to install more electron donating phosphine ligands on the Ni center.

4.2 Synthesis of (diphosphine)Ni(xdt)Fe(CO)$_3$ Complexes.

The reaction of Fe$_2$(CO)$_9$ and Ni(xdt)(diphosphine) provides a reliable route to complexes of the type (diphosphine)Ni(xdt)Fe(CO)$_3$ but generates substantial amounts of Fe$_2$(dithiolate)(CO)$_6$. An alternative method that circumvents this side reaction was developed that employs FeI$_2$(CO)$_4$ as an Fe source. Thus, the reaction of FeI$_2$(CO)$_4$ and Ni(pdt)(dppe) followed by addition of two equiv of Cp$_2$Co afforded **1** in ~30% yield. Using the Fe$_2$(CO)$_9$ and the FeI$_2$(CO)$_4$ methods, we were able to generate complexes in which pdt had been changed to edt (Scheme 4.5). We also sought to replace dppe with a more electron donating diphosphine ligand. We initially attempted to prepare Fe(CO)$_3$ derivatives of Ni(pdt)(dmpe), but these species were unstable. We ultimately replaced dppe with dcpe (dcpe= Cy$_2$PCH$_2$CH$_2$PCy$_2$)

(Table 4.1). This replacement resulted in stable complexes, likely due to the fact that dcpe is bulkier dmpe, which were also significantly more basic.[19]

The $FeI_2(CO)_4$ method is proposed to proceed via the intermediacy of the μ-iodo cations $[(diphsophine)Ni(xdt)(\mu\text{-}I)Fe(CO)_3]^+$ (Scheme 4.5). IR spectra of these reaction solutions feature ν_{CO} bands resembling those for the corresponding hydride cations, but are shifted to higher energies by about 20 cm^{-1}. Spectra were somewhat more complicated than expected, probably owing to sample decomposition. Treatment of a CH_2Cl_2 solution of purified **1** with I_2 gave a similar but simpler FT-IR spectrum (Figure 4.1).

Scheme 4.5 Synthesese of (diphsophine)Ni(xdt)Fe(CO)$_3$ complexes, 1-4.

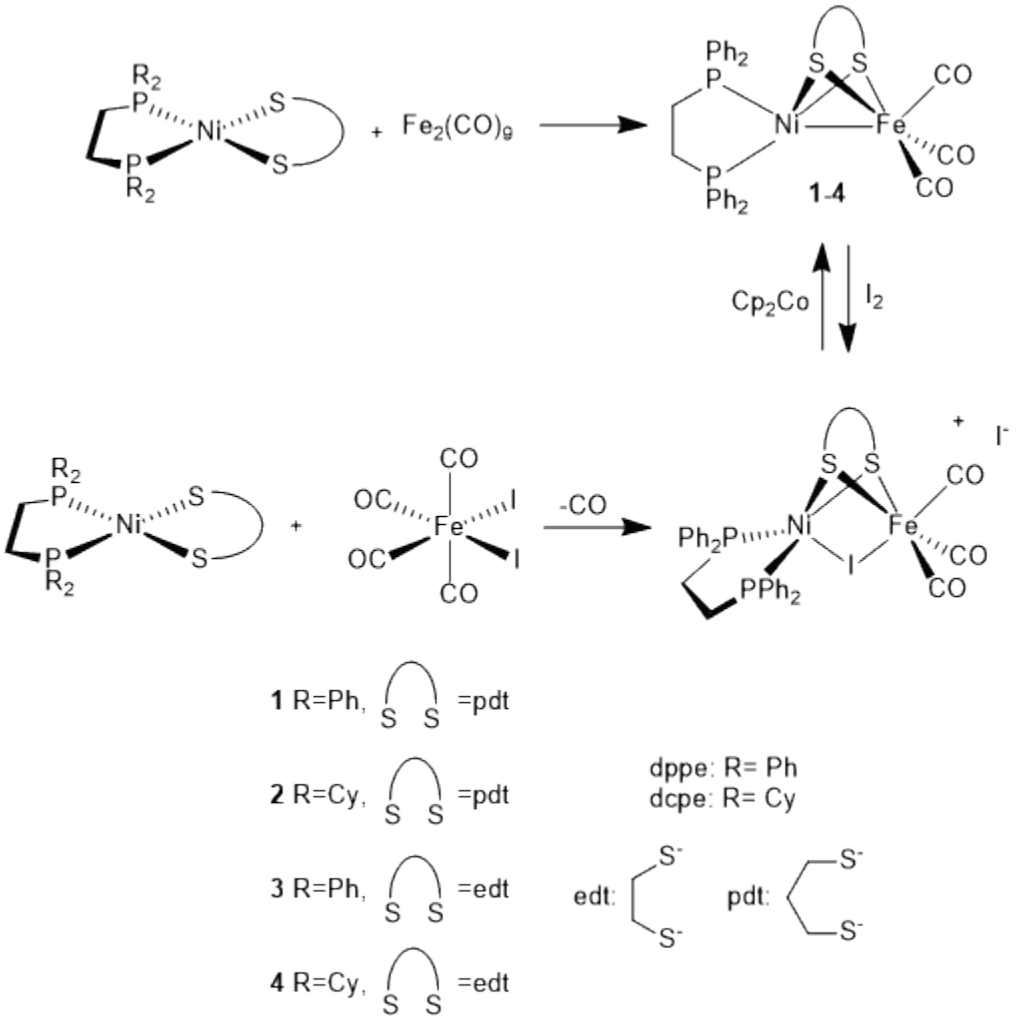

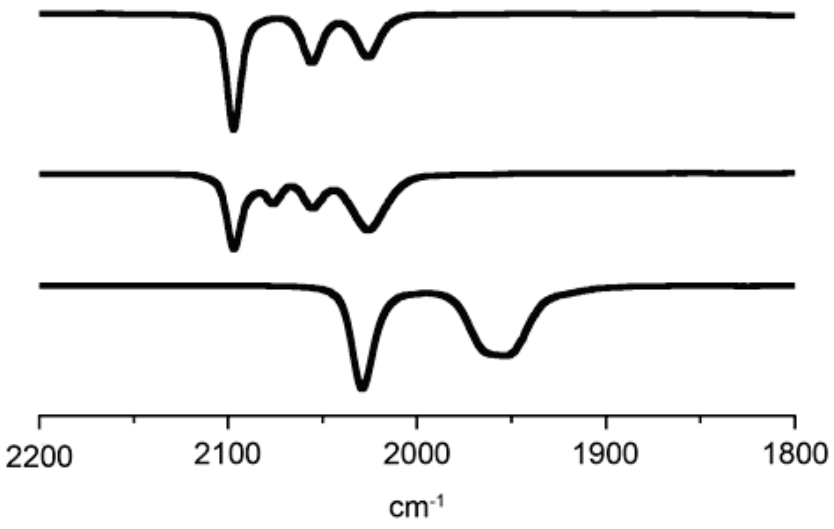

Figure 4.1. IR spectra (CH_2Cl_2 solutions, from top): (dppe)Ni(pdt)Fe(CO)$_3$ + I_2 (top), intermediate [(dppe)Ni(pdt)(μ-I)Fe(CO)$_3$]I from the reaction of Ni(pdt)(dppe) + $FeI_2(CO)_4$, (middle), and (dppe)Ni(pdt)Fe(CO)$_3$ (bottom).

Table 4.1 Spectroscopic data for (diphsophine)Ni(xdt)Fe(CO)$_3$ complexes (1-4) and the corresponding μ-iodide intermediate.

Complex	ν_{CO} (cm^{-1}) (μ-I intermediate)	^{31}P NMR (δ)
(dppe)Ni(pdt)Fe(CO)$_3$, **1**	2028, 1952 (2096, 2054, 2023)	63.6
(dcpe)Ni(pdt)Fe(CO)$_3$, **2**	2014, 1940 (2095, 2053, 2021)	81.0
(dppe)Ni(edt)Fe(CO)$_3$, **3**	2030, 1959 (2095, 2046, 2028)	65.0
(dcpe)Ni(edt)Fe(CO)$_3$, **4**	2015, 1940 (2096, 2075, 2053, 2029)	94.1

In an effort to stabilize the μ-iodide intermediate, we investigated the reaction of $FeI_2(CO)_4$ with Ni(Me_2pdt)(dppe), where Me_2pdt is 2,2,-dimethyl-1,3-propanedithiolate. The Ni complex of this bulky dithiolate[20] reacts with the iron reagent in the expected way as judged by IR spectra, and a more stable μ-iodide intermediate was formed, which could be recrystallized (Figure 4.2). We attempted to crystallize this intermediate, but the initial tricarbonyl product degraded to the ferrous iodide derivative NiFe(Me_2pdt)(dppe)I_2, which was characterized by single crystal X-ray diffraction (Figure 4.3). As for other Ni(II)Fe(II) species, the Ni-Fe distance

suggests the absence of metal-metal bonding.[10] Related adducts of ferrous iodide with two thiourea ligands are known.[21] The formation of the ferrous iodide complex is proposed to occur via attack of the iodide counteranion at $[(dppe)Ni(Me_2pdt)(\mu\text{-}I)Fe(CO)_3]^+$ concomitant with dissociation of the CO ligands (Scheme 4.6). A co-worker, David Schilter, later found that the analogous complex, $(dppe)Ni(pdt)FeI_2$, formed via reaction of $Ni(dppe)(pdt)$ with a source of FeI_2.[22]

Scheme 4.6 Proposed formation of $[(dppe)Ni(Me_2pdt)(\mu\text{-}I)Fe(CO)_3]I$ and decomposition to $(dppe)Ni(Me_2pdt)FeI_2$.

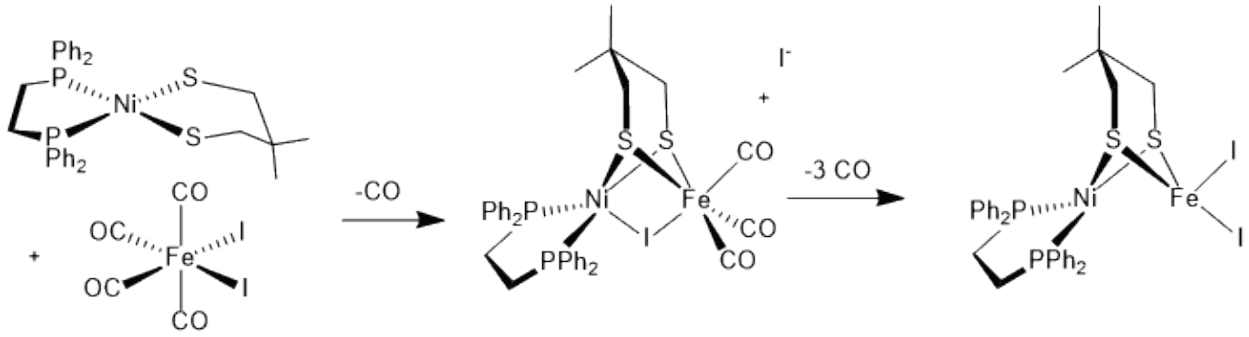

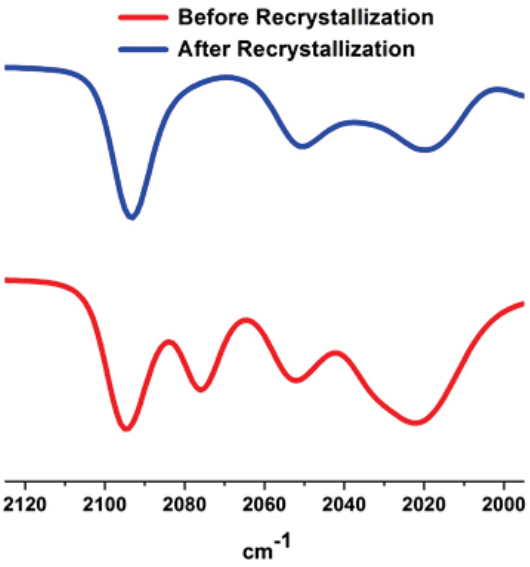

Figure 4.2. IR spectra of $[Ni(dppe)(Me_2pdt)(\mu\text{-}I)Fe(CO)_3]I$ in CH_2Cl_2; initial reaction mixture at -78 °C (red) and recrystallized product at -78 °C (blue).

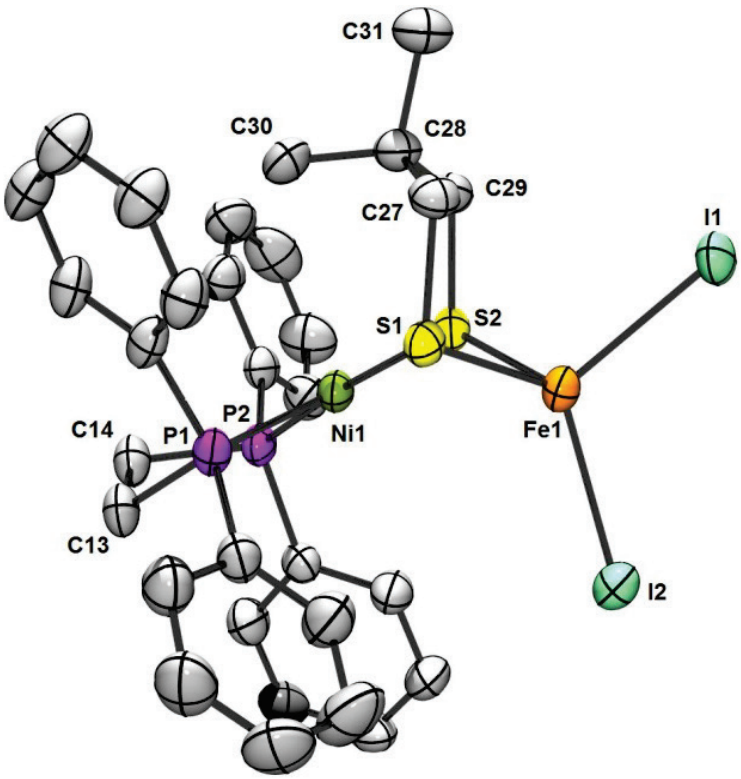

Figure 4.3. Structure of NiFe(Me_2pdt)(dppe)I_2. Selected distances (Å): Ni--Fe, 3.057; Ni1 P2 2.1703(12); Ni(1)-P(1), 2.1748(12); Ni(1)-S(2), 2.2296(12); Ni(1)-S(1), 2.2445(12); Fe(1)-S(2), 2.3806(12); Fe(1)-S(1), 2.3841(12); Fe(1)-I(2), 2.6165(7); Fe(1)-I(1), 2.6458(7).

Using the ferrous iodide method, we prepared three new NiFe tricarbonyl complexes: (dcpe)Ni(pdt)Fe$(CO)_3$ (**2**), (dppe)Ni(edt)Fe$(CO)_3$ (**3**), and (dcpe)Ni(edt)Fe$(CO)_3$ (**4**), which are spectroscopically similar to (dppe)Ni(pdt)Fe$(CO)_3$ (edt= 1,2-ethanedithiolate).[12] The IR spectra of the new edt complexes contain two CO bands, at energies similar to those previously reported for **1** (Figures 4.4, 4.5).[15] Substitution of dppe with dcpe causes the CO bands to shift ~ 15- 20 cm^{-1} lower in energy (Table 4.1) Furthermore, all are stereochemically nonrigid as indicated by the observation of single ^{31}P NMR signals for each. Reminiscent of the observations on **1**,[16] the ^{31}P NMR spectrum of **3** consists of a singlet at room temperature, but at lower temperatures the singlet decoalesces into two signals, which are likely unresolved doublets (Figure 4.6). The presence of a singlet at room temperature is due to rotation of the dppe, which slows at low temperatures, leading the presence of two inequivalent phosphorus centers (Scheme 4.7). For the analogous edt-dcpe complex **4**, the ^{31}P NMR signal remains a sharp singlet at –70 ºC.

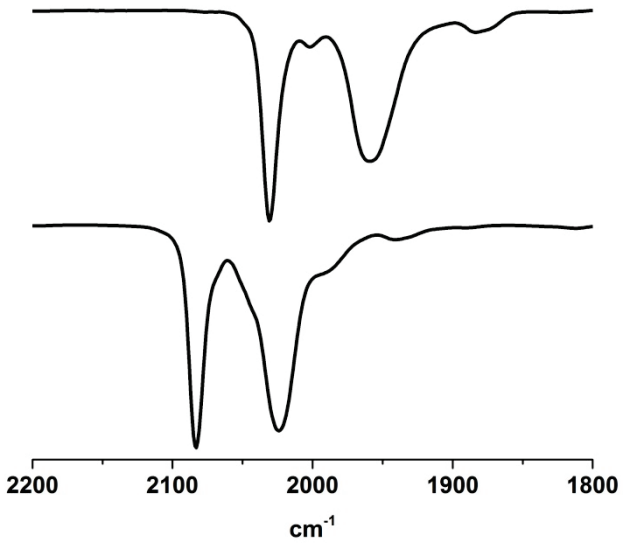

Figure 4.4. IR spectra of (dppe)Ni(edt)Fe(CO)$_3$, 3, (top) and [(dppe)Ni(edt)(μ-H)Fe(CO)$_3$]BF$_4$, [3H]BF$_4$ (bottom) in CH_2Cl_2.

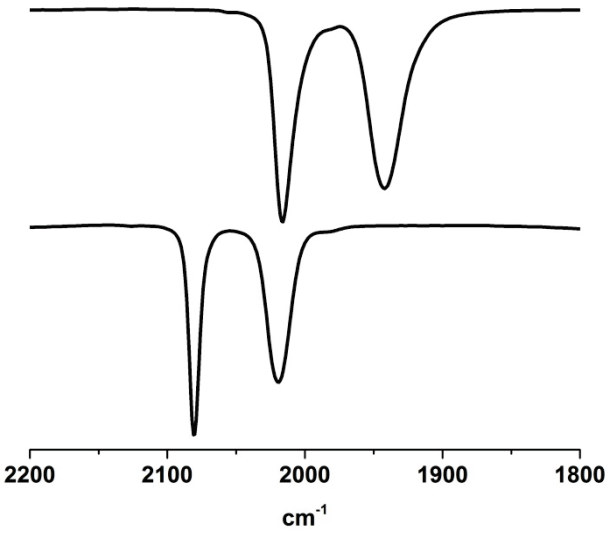

Figure 4.5. IR spectra of (dcpe)Ni(edt)Fe(CO)$_3$, 4, (top) and [(dcpe)Ni(edt)(μ-H)Fe(CO)$_3$]BF$_4$, [4H]BF$_4$ (bottom) in CH_2Cl_2.

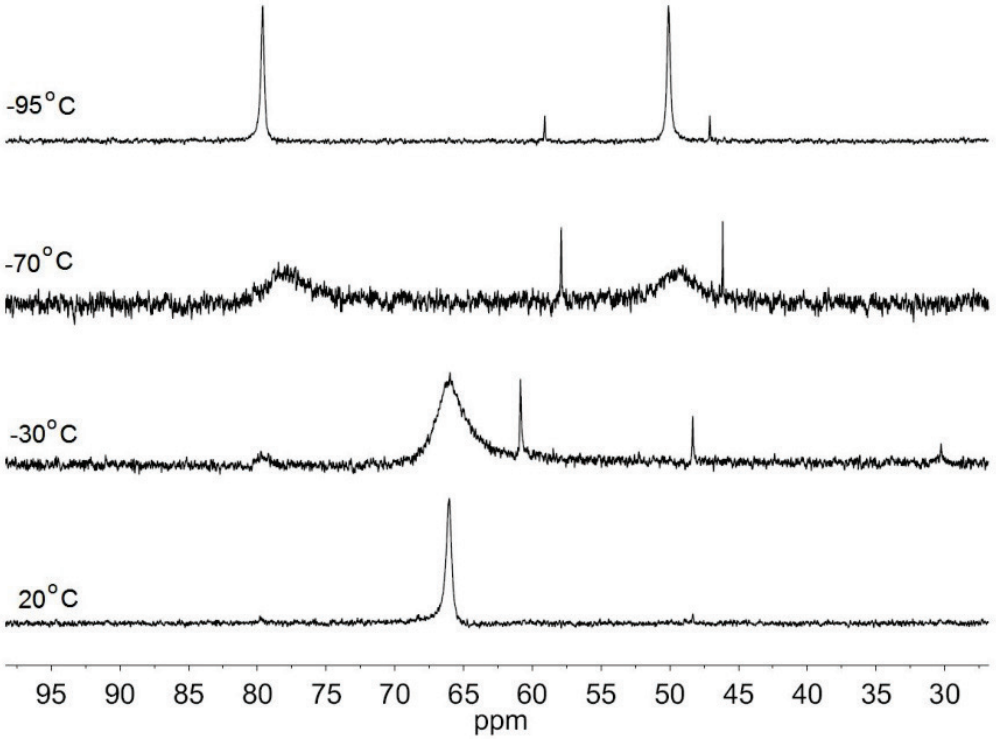

Figure 4.6. $^{31}P\{^{1}H\}$ NMR spectra of 3 (500 MHz, THF-d_8 solution) at various temperatures. The signal at ~δ60 corresponds to Ni(edt)(dppe), and the signal at ~δ47 is unassigned.

Scheme 4.7 Dynamic process associated with dppe ligand in 3.

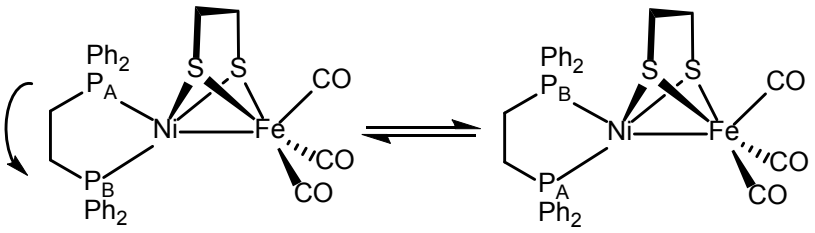

4.3 Redox Properties of (diphsophine)Ni(xdt)Fe(CO)$_3$ Complexes.

As previously reported, **1** oxidizes reversibly at -0.57 V vs $Fc^{0/+}$ in benzonitrile solution with $[NBu_4]PF_6$ as electrolyte.[16] As a solvent for the neutral complexes, benzonitrile is superior to MeCN. Redox potentials are assumed to be the same in both solvents, i.e. $E^{PhCN} = E^{MeCN}$.[23] The analogous dcpe complex, **2**, oxidizes reversibly at –0.82 V vs $Fc^{0/+}$, 250 mV milder than the $[\mathbf{1}]^{0/+}$ couple (Figure 4.7). Similarly, the dcpe-edt complex **4** oxidizes at -0.74 V, 300 mV milder than the $[\mathbf{3}]^{0/+}$ couple. Thus, the basicity of the diphosphine significantly affects the redox

potentials, but the identity of the dithiolate bridge has little effect. For **1**-**4**, a second irreversible oxidation is observed at more positive potentials (Table 4.2). We assign all couples to one-electron events, as was verified for **1**.[16]

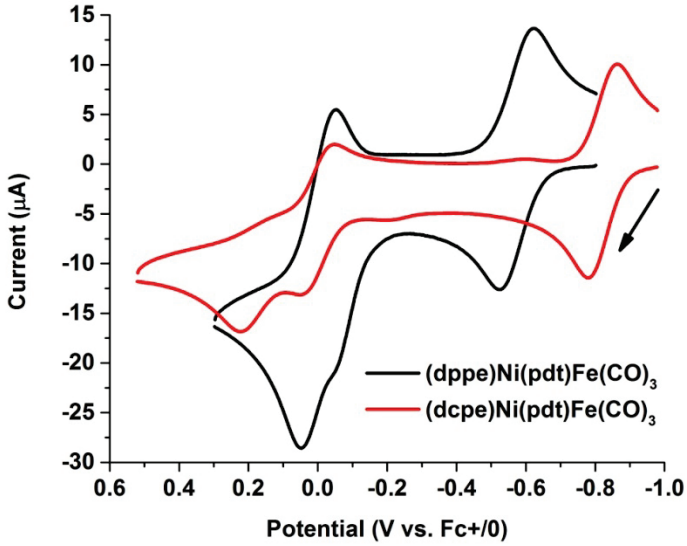

Figure 4.7 Cyclic voltammograms of 1 (black) and 2 (red) in PhCN , with. (Conditions: 1.0 mM NiFe compound, 0.1 M $[Bu_4N]PF_6$ as supporting electrolyte, glassy carbon working electrode, silver wire pseudo reference electrode, Pt counter electrode)

Table 4.2. Selected Electrochemical Properties (V vs $Fc^{+/0}$) of $Fe^{I}Ni^{I}$ Complexes. *Conditions:* scan rate 100 mV/s, benzonitrile solution.

Compound	$E_{1/2}$, $NiFe^{0/+}$	i_{pa}/i_{pc}	E_{pa}[a], $NiFe^{+/2+}$
(dppe)Ni(pdt)Fe(CO)$_3$, **1**	-0.580	0.93	-0.036
(dcpe)Ni(pdt)Fe(CO)$_3$, **2**	-0.820	0.95	+ 0.220
(dppe)Ni(edt)Fe(CO)$_3$, **3**	-0.540	0.33	-0.075
(dcpe)Ni(edt)Fe(CO)$_3$,**4**	-0.740	0.80	+ 0.027

[a] E_{pa} = peak potential for cathodic peak for second oxidation, this couple being irreversible.

4.4 Characterization of New NiFe Hydrides.

Protonation of the reduced species **2**, **3**, and **4** with HBF_4•Et_2O gave the corresponding hydrides, the new salts being [(dcpe)Ni(pdt)(μ-H)Fe(CO)$_3$]BF_4 ([**2**H]BF_4), [(dppe)Ni(edt)(μ-H)Fe(CO)$_3$]BF_4 ([**3**H]BF_4), and [(dcpe)Ni(edt)(μ-H)Fe(CO)$_3$]BF_4 ([**4**H]BF_4). These complexes were also characterized by ^{31}P and ^{1}H NMR spectroscopy (Table 4.3). The protonation can also

be monitored by IR spectroscopy; the CO bands shift by ~60 cm^{-1} to higher energy upon protonation (Figures 4.4, 4.5, Table 4.3). Illustrative of the stability of these complexes, the NMR spectrum of a CD_2Cl_2 solution of the edt-dppe cation $[\mathbf{3}H]^+$ remains unchanged in the presence of 500 equiv trifluoroacetic acid after 5 h at room temperature.

Table 4.3 Spectroscopic data for [(diphsophine)Ni(xdt)(μ-H)Fe(CO)$_3$]BF$_4$ complexes ([1H]$^+$-[4H]$^+$).

Complex	ν_{CO} (cm^{-1})	^{31}P NMR (δ ppm)	High Field ^{1}H NMR (δ ppm)
[(dppe)Ni(pdt)(μ-H)Fe(CO)$_3$]BF$_4$ [**1**H]BF	2082, 2024	71.0	-3.53
[(dcpe)Ni(pdt)(μ-H)Fe(CO)$_3$]BF$_4$ [**2**H]BF	2078, 2017	89.8	-3.0
[(dppe)Ni(edt)(μ-H)Fe(CO)$_3$]BF$_4$ [**3**H]BF	2084, 2025	72.7	-5.7
[(dcpe)Ni(pdt)(μ-H)Fe(CO)$_3$]BF$_4$ [**4**H]BF	2080, 2019	92.0	-5.3

A former co-worker, Amanda Mack, successfully crystallized a salt of $[\mathbf{2}H]^+$, which along with $[\mathbf{3}H]^+$, was characterized by single crystal X-ray diffraction (Figure 4.8, Table 4.4). Overall, the NiFe cations closely resemble $[\mathbf{1}H]^+$.[15] In the crystallographic analyses, the hydride ligands were located and refined. The Ni-H-Fe linkage is unsymmetrical in all cases, with the Fe-H distance shorter than the Ni-H distance by 0.18 and 0.37 Å for $[\mathbf{2}H]BF_4$ and $[\mathbf{3}H]BF_4$, respectively. At 2.68 Å, the Ni-Fe distance in the bulkier dcpe complex $[\mathbf{2}H]^+$ is elongated relative to those of 2.61 and 2.60 Å in $[\mathbf{1}H]^+$ and $[\mathbf{3}H]^+$, respectively.[15]

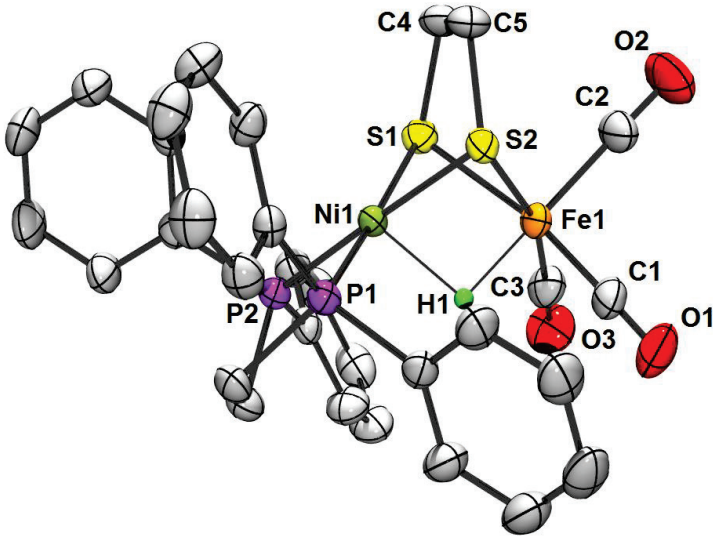

Figure 4.8. Molecular structure of the cation in $[(dppe)Ni(edt)(\mu\text{-}H)Fe(CO)_3]^+$ ($[3H]^+$). Hydrogen (except the hydride ligand) atoms and BF_4^- are not shown. Selected distances (Å): Ni-Fe, 2.5958(6); Ni-S(1), 2.1969(9); Ni-S(2), 2.2128(9); Fe-S(1), 2.3152(9); Fe-S(2), 2.328(1); Ni-H, 1.84(3); Fe-H, 1.58(4).

Table 4.4 Selected bond distances (Å) for $[(diphsophine)Ni(xdt)(H)Fe(CO)_3]BF_4$.

Compound	Ni-Fe	Ni-H	Fe-H	Δ (Ni-H, Fe-H)
[**1**H]BF_4	2.61	1.64	1.46	0.18
[**2**H]BF_4	2.68	1.91	1.53	0.38
[**3**H]BF_4	2.59	1.84	1.58	0.26

A substituted edt derivative, $[(dppe)Ni(edt)(\mu\text{-}H)Fe(CO)_2(PPh_3)]BF_4$ ([**5**H]BF_4), was prepared by reaction of [**3**H]BF_4 with PPh_3 (Scheme 4.8). Progress of reaction may be monitored by IR spectroscopy; bands shift by ~50 cm^{-1} to lower energy (Figure 4.9). Interestingly, NMR spectra indicate the presence of two isomers in a ratio of ~2:1 (Figures 4.10, 4.11). Each isomer exhibits a doublet-of-triplets in the hydride region of the ^1H NMR spectrum, implying that J_{PH} are insensitive to stereochemistry. For $[HNiFe(pdt)(dppe)(PPh_3)(CO)_2]BF_4$, we had previously detected trace amounts of a second isomer, but the mole fraction was so small that the nature of this minor component was unclear.[16] By comparisons of the ^1H NMR shifts with those for the pdt derivatives, the major isomer in [**5**H]BF_4 is unsymmetrical (as is the predominant isomer of $[(dppe)Ni(pdt)(\mu\text{-}H)Fe(CO)_2(PPh_3)]BF_4$),[16] with the PPh_3 ligand in a basal position (Scheme 4.9). The occurrence of about 50% of an isomer with PPh_3 in the apical

position apparently reflects the moderate steric profile of edt vs pdt.

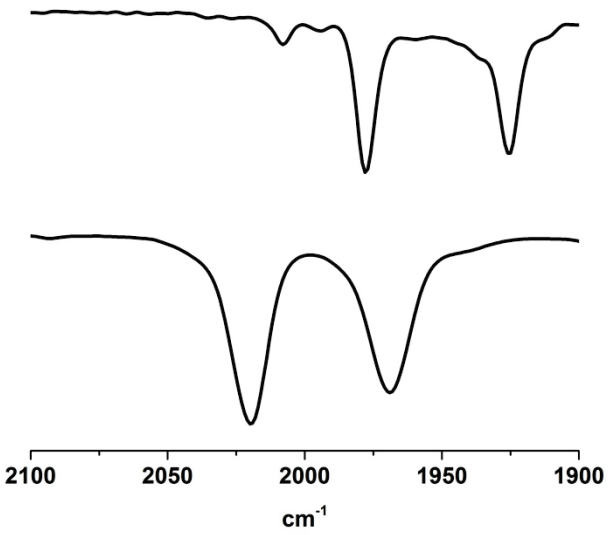

Figure 4.9. IR spectra of (dppe)Ni(edt)Fe(CO)$_2$(PPh$_3$), 5, (top) and [(dppe)Ni(edt)(μ-H)Fe(CO)$_2$(PPh$_3$)]BF$_4$, [5H]BF$_4$ (bottom) in CH$_2$Cl$_2$.

Scheme 4.8 Synthesis of [(dppe)Ni(edt)(μ-H)Fe(CO)$_2$(PPh$_3$)]BF$_4$ ([5H]BF$_4$).

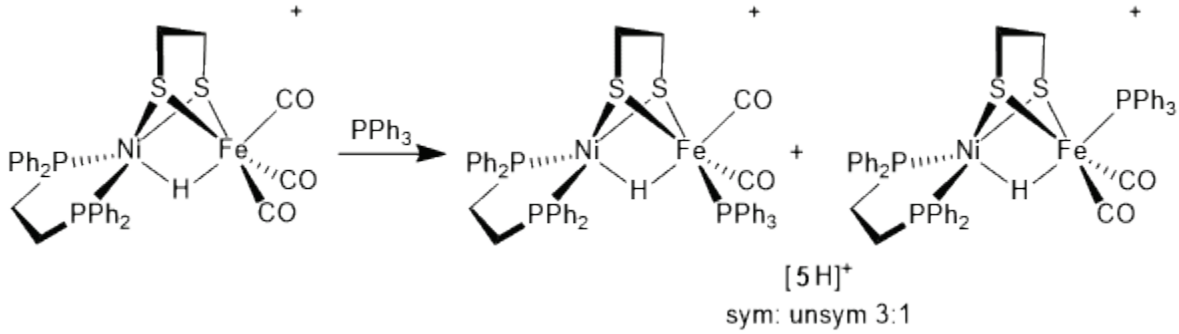

The sym- and unsym-isomers of [**5**H]$^+$ do not readily interconvert (Scheme 4.10) although variable temperature ^{31}P NMR spectra indicate that the unsym isomer is dynamic on the NMR timescale such that only one signal is observed for the dppe ligand in each isomer. When a CD_2Cl_2 solution of [**5**H]$^+$ is cooled, the signal assigned to the dppe on the unsym isomer broadens (Figure 4.11). Although not examined explicitly, it is likely that dppe in the symmetric isomer is also nonrigid (Scheme 4.9). These observations underscore the stereochemical flexibility of the square pyramidal nickel sites in these hydrido complexes. Deprotonation of the [**5**H]$^+$ with Et_3N gave the neutral complex **5**, which was characterized by IR and ^{1}H and ^{31}P NMR spectroscopy (Figures 4.9, 4.12).

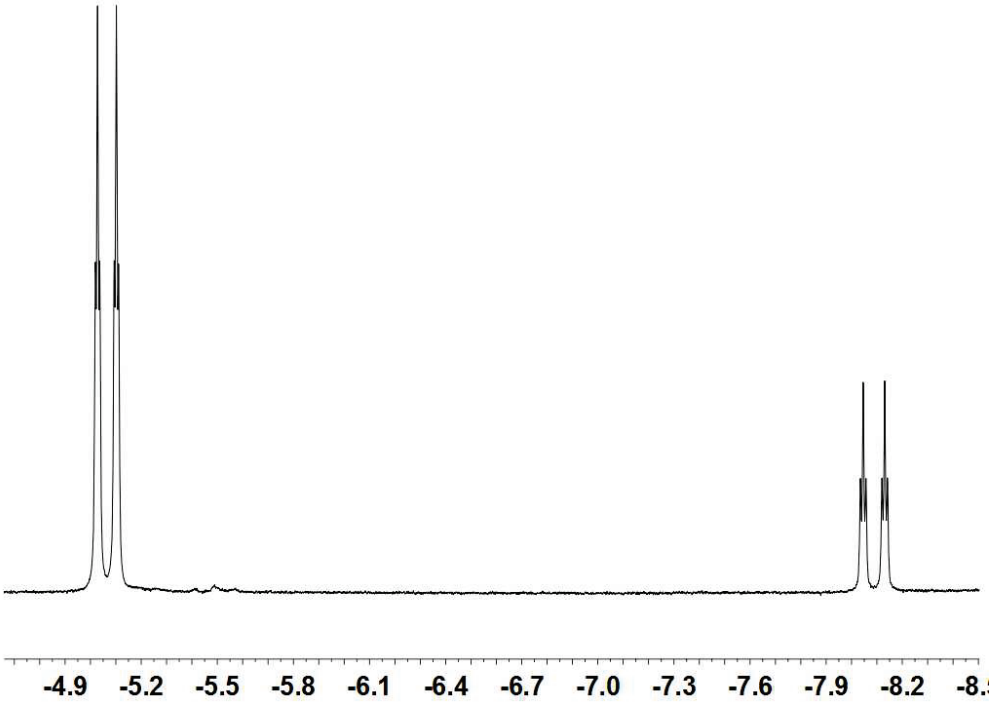

Figure 4.10. High field region of [1] [(dppe)Ni(edt)(μ-H)Fe(CO)$_2$(PPh$_3$)]BF$_4$, [5H]BF$_4$ in CD$_2$Cl$_2$. Signal at δ -5.0 ppm corresponds to the unsymmetrical isomer, and the signal at δ -8 ppmcorresponds to the symmetrical isomer.

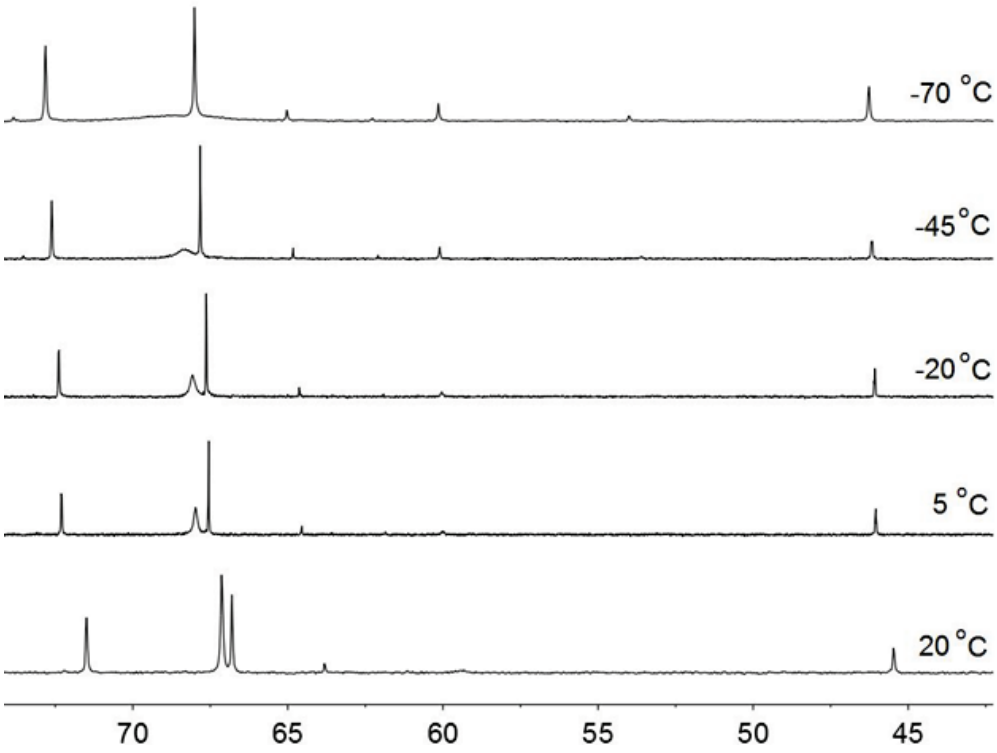

Figure 4.11. Variable temperature $^{31}P\{^{1}H\}$ NMR (202 MHz, CD_2Cl_2) spectrum of $[(dppe)Ni(edt)(\mu\text{-}H)Fe(CO)_2(PPh_3)]BF_4$. The signal at δ 68, assigned to the phosphorus centers of dppe on the unsymmetrical isomer, broadens at –70 ºC, indicative of slowed rotation of the dppe ligand at the Ni center. The signal at δ 45 is assigned to PPh_3 on the symmetrical isomer. Signals at δ 72 and 66 correspond to PPh_3 on the unsymmetrical isomer and dppe on the symmetrical isomer, but further assignments cannot be made, based on this data.

Scheme 4.9. Possible dynamic equilibria for [(dppe)Ni(edt)(μ-H)Fe(CO)$_2$(PPh$_3$)]BF$_4$, [5H]BF$_4$. ([5H]BF$_4$).

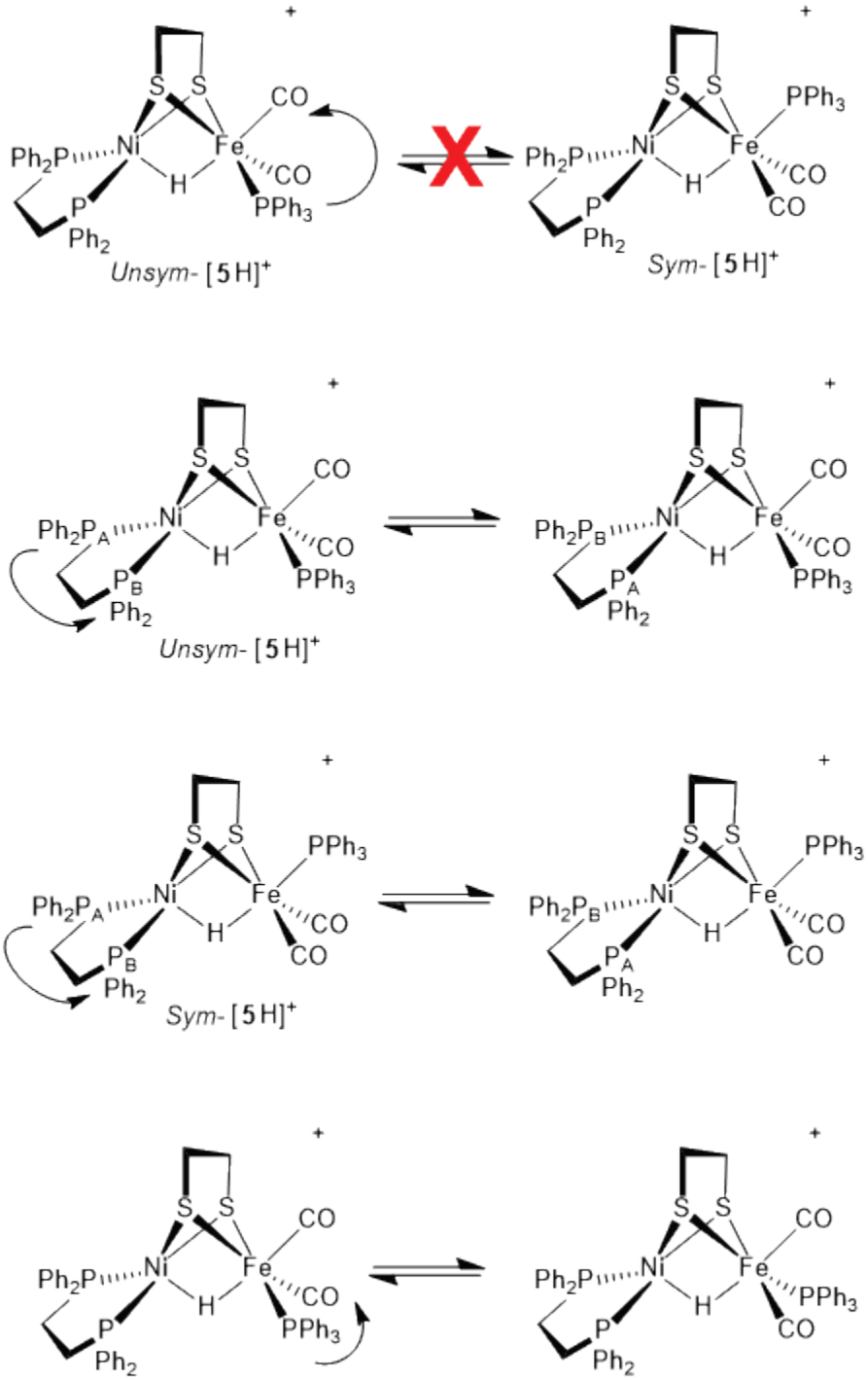

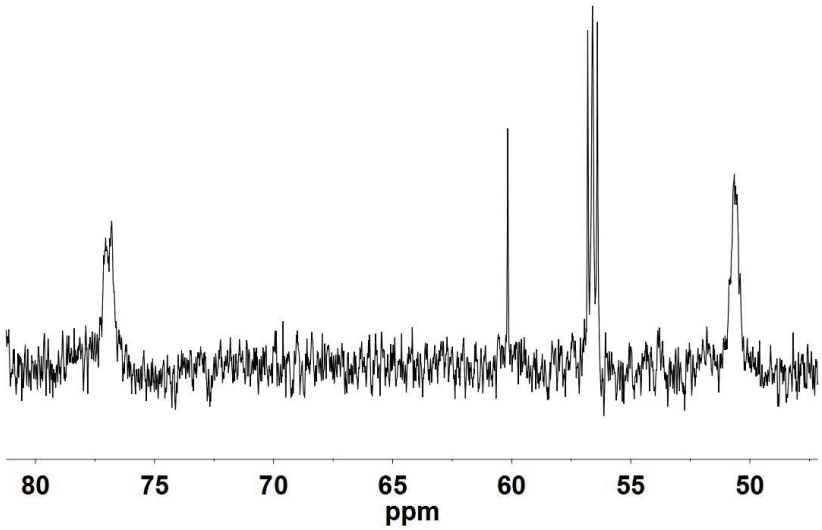

Figure 4.12. ^{31}(dppe)Ni(edt)Fe(CO)$_2$(PPh$_3$) 5 in CD_2Cl_2. Signal at δ ~ 60 corresponds Ni(edt)(dppe), which is decomposition product associated with deprotonation of [5H]BF_4.

4.5 Redox Properties of NiFe Hydrides, [(diphosphine)Ni(xdt)(μ-H)Fe(CO)$_3$]BF_4.

The reduction of the hydrides was also examined. For the couple [**1**H]$^{+/0}$, E^{MeCN} is –1.29 V vs $Fc^{0/+}$. The [**1**H]$^{+/0}$ couple is partially reversible, whereas little reversibility was detected in the couples [**2**H]$^{+/0}$, [**3**H]$^{+/0}$, [**4**H]$^{+/0}$, and [**5**H]$^{+/0}$ (Table 4.4.). Changing the solvent to CH_2Cl_2 did not substantially improve the reversibility of the reduction of any of the hydrides. In the case of [**1**H]$^{+/0}$, varying the scan rate from 100 to 750 mV/s improved the reversibility from i_{pa}/i_{pc} from 0.26 to 0.8. The [**2**H]$^{+/0}$ couple occurs at potential that is ~ 200 mV negative of that for the [**1**H]$^{+/0}$ (Figure 4.13). Similarly, the reduction potentials of the edt hydrides, [**3**H]$^{+/0}$ and [**4**H]$^{+/0}$ are separated by ~ 80 mV (Figure 4.14). This difference is attributed to the influence of the more basic dcpe ligand in [**2**H]$^+$ and [**4**H]$^+$.

Substitution at the Fe center was also found to affect the redox properties of the hydrides. Dr. Bryan Barton reported that the reduction of [(dppe)Ni(pdt)(μ-H)Fe(PPh$_3$)(CO)$_2$]BF_4 occurs at -1.49 V, which is 200 mV negative of the potential at which [**1**H]$^+$ is reduced.[16] Similarly, the reduction potential shifts by ~ 100 mV when CO is substituted with PPh_3 in the analogous edt complexes, [**3**H]$^+$ and [**5**H]$^+$. Based on these results, substitutions at Ni and Fe have similar effects on the reduction potentials of the NiFe hydride complexes.

Comparison of Lever electrochemical parameters for the relevant ligands supports the claim that reduction is not localized on the Fe center. The difference in Lever parameters between CO and PPh_3 is 0.6 V,[18] which is three to six times greater than the differences in reduction potentials for substituting CO with PPh_3 in the NiFe hydrides. If the reduction was localized at the Fe center, then we would expect a change in the reduction potential that is closer to the difference in the Lever parameters.

Similar analysis for substitution at the Ni center is complicated by the fact that the Lever parameter for dcpe has not been reported. However, the difference in Lever parameters between dppe and the methyl substituted diphosphine, dmpe (1,2-bis(dimethylphosphino)ethane), is only ~ 100 mV.[18] Assuming that dcpe has a similar Lever parameter to dmpe (within 100-200 mV), we can conclude that changing the diphosphine at Ni from dppe to dcpe should change the reduction potential of the NiFe hydride by 100-200 mV. Based on the data in hand, we cannot make a definitive conclusion concerning the localization of this reduction event; it may occur at the Ni center or be delocalized between the two metal centers.

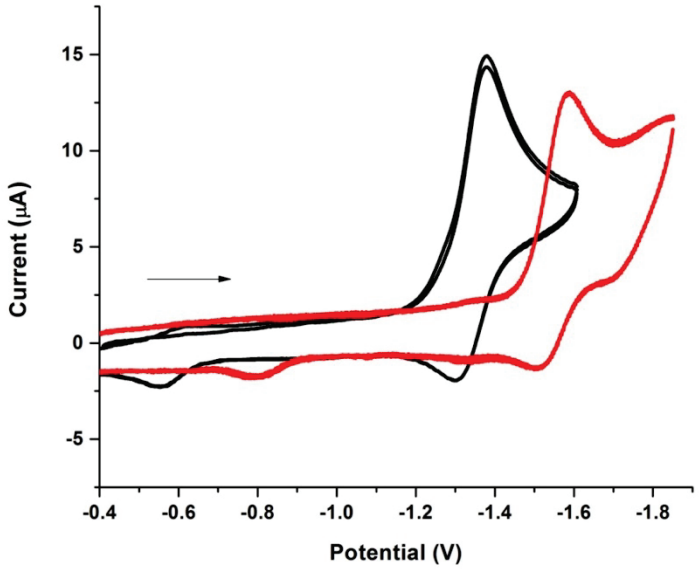

Figure 4.13. Cyclic voltammograms of [(dppe)Ni(pdt)(μ-H)Fe(CO)$_3$]BF_4, [1]BF_4, (black) and [(dcpe)Ni(pdt)(μ-H)Fe(CO)$_3$]BF_4, [2]BF_4, (red) in CH_2Cl_2. (Conditions: 1.0 mM NiFe compound, 0.1 M [Bu_4N]PF_6 as supporting electrolyte, glassy carbon working electrode, silver wire pseudo reference electrode, Pt counter electrode)

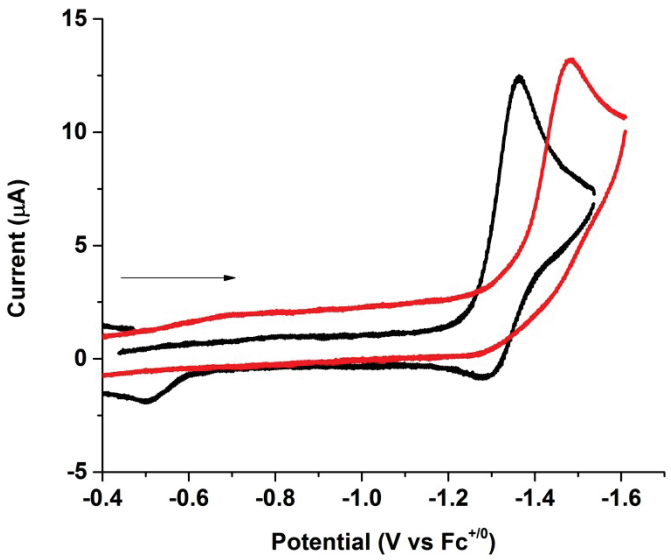

Figure 4.14. Cyclic voltammograms of [(dppe)Ni(edt)(μ-H)Fe(CO)$_3$]BF$_4$, [3]BF$_4$, (black) and [(dcpe)Ni(edt)(μ-H)Fe(CO)$_3$]BF$_4$, [4]BF$_4$, (red) in CH_2Cl_2. (Conditions: 1.0 mM NiFe compound, 0.1 M [Bu$_4$N]PF$_6$ as supporting electrolyte, glassy carbon working electrode, silver wire pseudo reference electrode, Pt counter electrode)

The irreversibility of the hydride couples is due to an intermolecular conversion of the reduced, neutral hydrides ([**1**H]^0-([**4**H]^0) into the neutral unprotonated complexes (Scheme 4.10). There are two possible mechanisms by which this reaction may occur. Two reduced hydride species, **3**H, may couple (each donating a hydrogen atom), to form H_2 and 2 equivalents of **3**. The second mechanism involves coupling of a proton from [**3**H]$^+$ and a hydride from **3**H, releasing one equivalent each of H_2, **3**$^+$, and **3**. Evidence for this reaction is indicated in the CV of [**3**H]$^+$, in which an oxidation at -0.58 V is present on the reverse scan. Additionally, when the CV is cycled multiple times, without stirring the solution, the current corresponding to [**3**]$^{+/0}$ increases, while that for [**3**H]$^{+/0}$ decreases (Figure 4.15). Within the solvent window (1.5 V to -1.5V), no other anodic events occur, which would correspond to oxidation of the hydride complexes. The absence of such an event implies that if oxidation of the hydride complexes occurs, it requires very positive potentials.

Scheme 4.10. Proposed decomposition of $[3H]^0$.

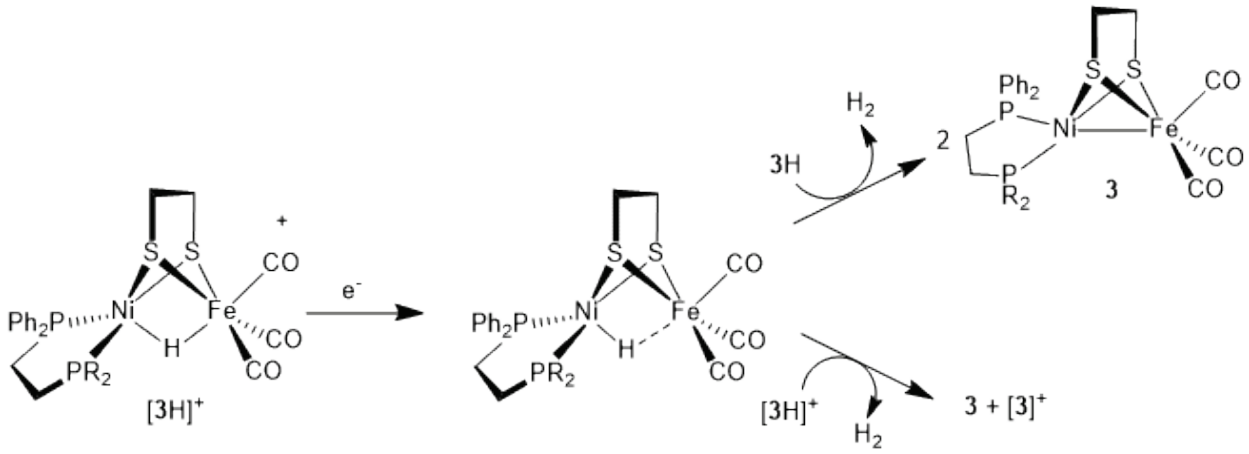

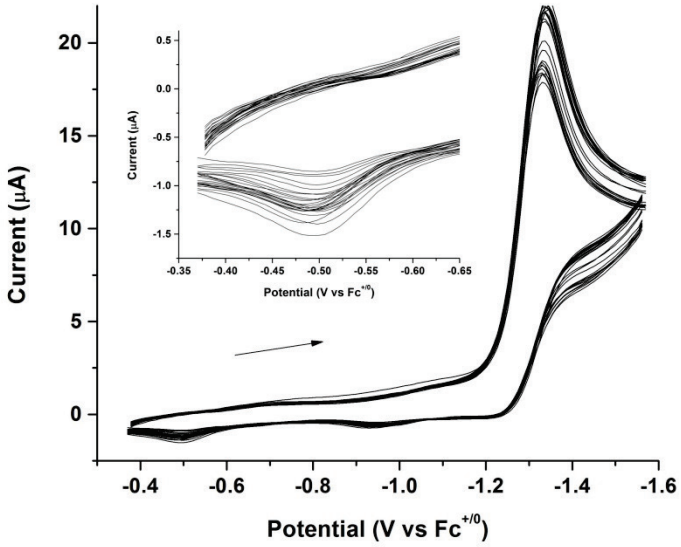

Figure 4.15. Cyclic voltammogram of $[(dppe)Ni(edt)(\mu\text{-}H)Fe(CO)_3]BF_4$, $[3]BF_4$, in CH_2Cl_2 scanning 20 segments, with stirring the solution. (Conditions: 1.0 mM NiFe compound, 0.1 M $[Bu_4N]PF_6$ as supporting electrolyte, glassy carbon working electrode, silver wire pseudo reference electrode, Pt counter electrode) (Inset: Region in which oxidation of 3 occurs)

Table 4.5. Selected Electrochemical Properties (V vs $Fc^{+/0}$) of [(diphsophine)Ni(xdt)(μ-H)$Fe(CO)_3$]BF_4 complexes ($[1H]^+$-$[4H]^+$) CH_2Cl_2.[a]

Complex	$E([HNiFe]^{+/0})$ (MeCN)	i_{pa}/i_{pc} (MeCN)	$E([HNiFe]^{+/0})$ (CH_2Cl_2)	i_{pa}/i_{pc} (CH_2Cl_2)
[(dppe)Ni(pdt)(μ-H)$Fe(CO)_3$]BF_4 [**1**H]BF	-1.29	0.26	-1.34	0.26
[(dcpe)Ni(pdt)(μ-H)$Fe(CO)_3$]BF_4 [**2**H]BF	-1.49	0.11	-1.56	0.10
[(dppe)Ni(pdt)(μ-H)$Fe(PPh_3)(CO)_2$]BF_4	-1.49 [b]	0.06 [b]	-	-
[(dppe)Ni(edt)(μ-H)$Fe(CO)_3$]BF_4 [**3**H]BF	-1.33	0	-1.33	0.08
[(dcpe)Ni(pdt)(μ-H)$Fe(CO)_3$]BF_4 [**4**H]BF	-1.41	0	-1.47	0
[(dppe)Ni(edt)(μ-H)$Fe(PPh_3)(CO)_2$]BF_4, [**5**H]BF_4	-1.54	0	-1.47	0

[a]*Conditions:* 0.5 M catalyst, scan rate 100 mV/s; [b]Value obtained from reference 16.

4.6 Electrocatalysis.

These experiments employed CH_2Cl_2 solutions of the hydride salts; MeCN solutions are stable only for a few minutes at room temperature. As can be seen in Table 4.4, the reduction potentials for CH_2Cl_2 and MeCN solutions are similar, which is relevant to estimation of overpotantials. Due to low stability of the hydrides in MeCN, catalysis was performed in CH_2Cl_2. As discussed in Chapter 1, values of $E°_{HA/H2}$ for a variety of acids have been reported in MeCN but not CH_2Cl_2. Because there is little variation in the reduction potentials of the hydrides upon changing solvent, the overpotential estimates using E_{cat} values in CH_2Cl_2 and $E°_{HA/H2}$ in MeCN are fairly accurate. For each hydride complexes, the i_{pc} increases with the addition of the acid indicating catalytic reduction of protons. For the less basic dppe derivatives, we used trifluoroacetic acid (pK_a^{MeCN} = 12.6),[24] whereas for the more basic catalysts, the weaker chloroacetic acid (pK_a^{MeCN} = 15.3)[24] was used. So long as the pK_a of the acid is below that of the NiFe hydride catalyst, the nature of the acid has little influence on rates in the plateau region.

For $[\mathbf{2}H]^+$, the observed value of $[i_c/i_p]_{max}$ of ~15 corresponds to an acid-independent turnover frequency of ~50 s^{-1}, about twice the rate of the related dppe derivative [16] (Figures 4.16, 4.17, Table 4.6).

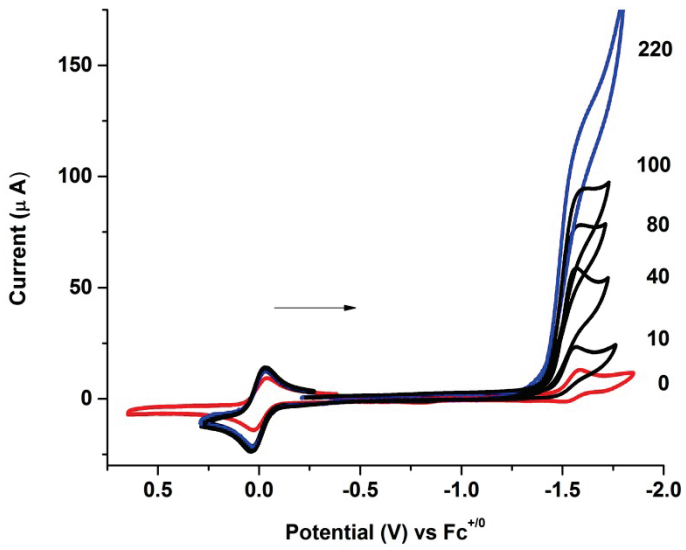

Figure 4.16. Cyclic voltammograms of [(dcpe)Ni(pdt)(μ-H)Fe(CO)$_3$]BF$_4$, [2]BF$_4$, in CH_2Cl_2, with increasing equivalents of $H_2ClC_2O_2H$. (Conditions: 1.0 mM NiFe compound, 0.1 M [Bu$_4$N]PF$_6$ as supporting electrolyte, glassy carbon working electrode, silver wire pseudo reference electrode, Pt counter electrode)

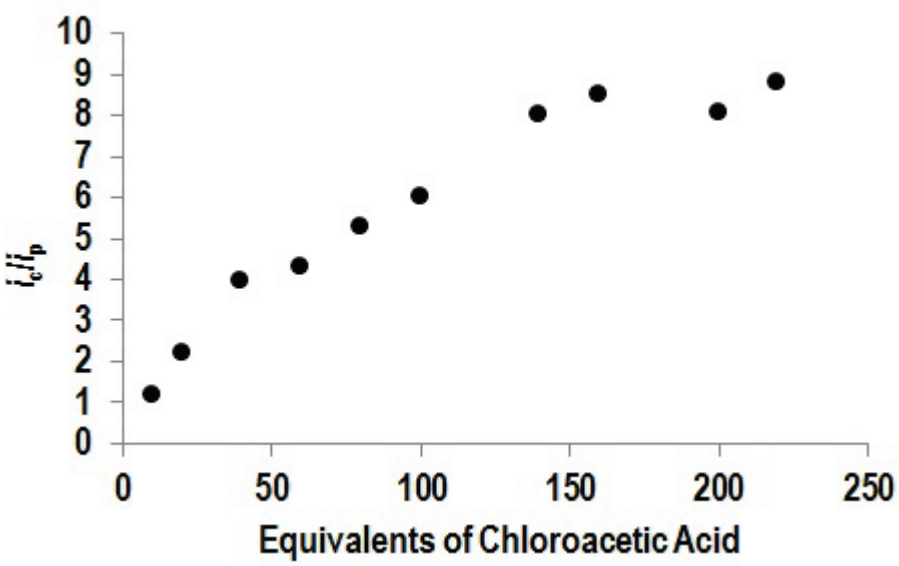

Figure 4.17. Plot of i_c/i_p vs equivalents of $H_2ClC_2O_2H$ added to a CH_2Cl_2 solution of [(dcpe)Ni(pdt)(μ-H)Fe(CO)$_3$]BF$_4$, [2]BF$_4$.

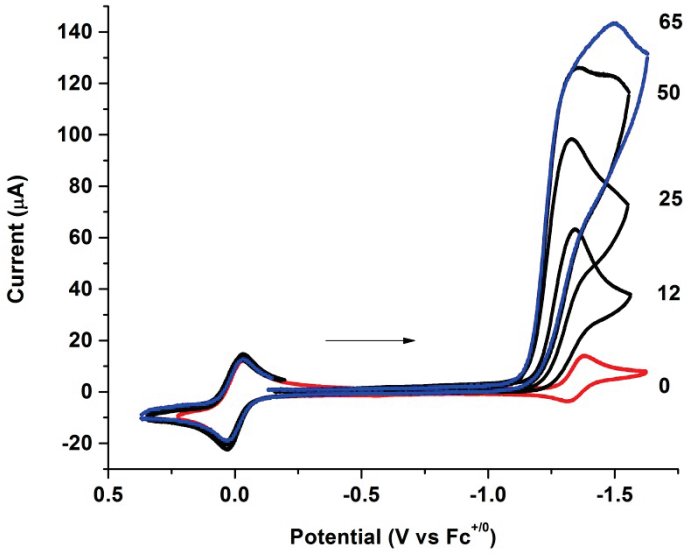

Figure 4.18. Cyclic voltammograms of [(dppe)Ni(pdt)(μ-H)Fe(CO)$_3$]BF$_4$, [1]BF$_4$, in CH$_2$Cl$_2$, with increasing equivalents of CF$_3$CO$_2$H. (Conditions: 1.0 mM NiFe compound, 0.1 M [Bu$_4$N]PF$_6$ as supporting electrolyte, glassy carbon working electrode, silver wire pseudo reference electrode, Pt counter electrode)

Like the propanedithiolate [**1**H]$^+$, the ethanedithiolate [**3**H]$^+$ catalyzes hydrogen evolution from CF_3CO_2H. E_{cat} for [**1**H]$^+$ and [**3**H]$^+$ differ by only 140 mV, but [**3**H]$^+$ is far more active (Figure 4.18-4.20). Specifically, the observed $[i_c/i_p]_{max}$ of 35-40 indicates a turnover frequency of 240-310 s^{-1}. This rate is about 10x that of [**1**H]$^+$ and is comparable to many nickel-diaminodiphosphine catalysts.[25] When the catalyst concentration was halved (0.25 mM vs 0.5 mM), the rate in the acid-independent regime remained unchanged, verifying that the rate is independent of catalyst concentration.

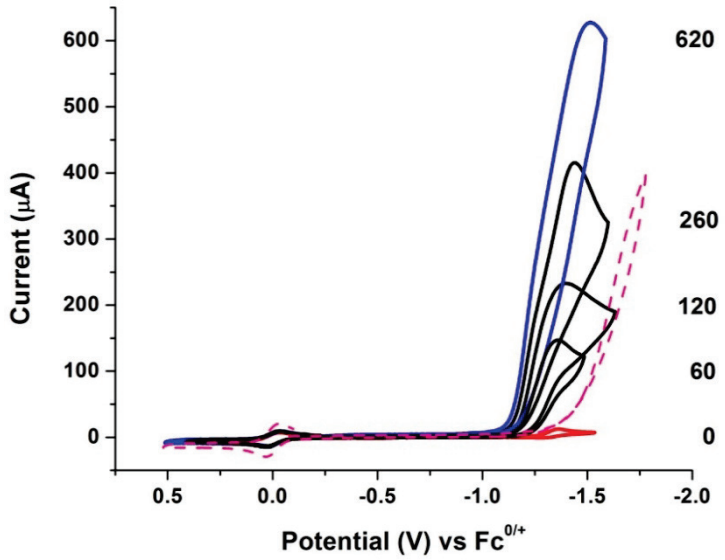

Figure 4.19. Cyclic voltammograms of [(dppe)Ni(edt)(μ-H)Fe(CO)$_3$]BF$_4$, [3]BF$_4$, in CH$_2$Cl$_2$, with increasing equivalents ofCF$_3$CO$_2$H. Dashed red line indicates potential at which direct reduction of acid at glassy carbon occurs. (Conditions: 1.0 mM NiFe compound, 0.1 M [Bu$_4$N]PF$_6$ as supporting electrolyte, glassy carbon working electrode, silver wire pseudo reference electrode, Pt counter electrode)

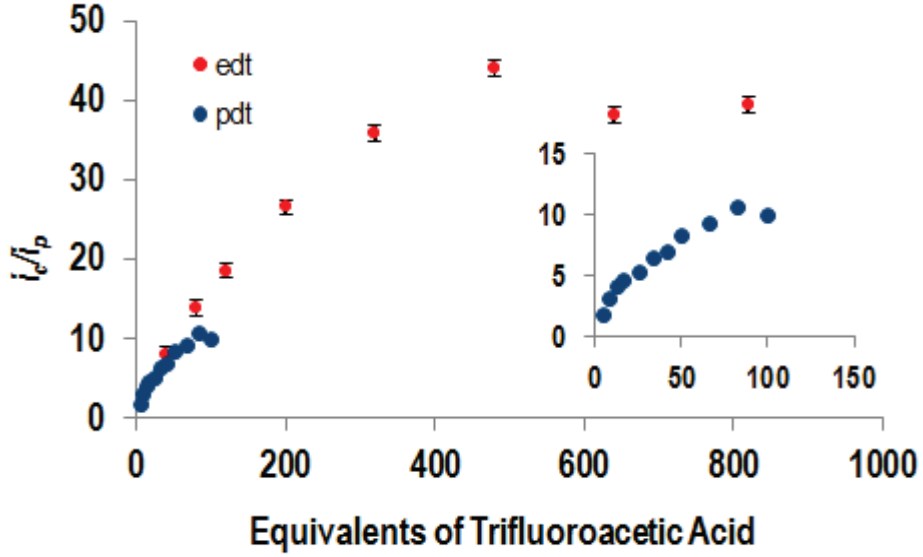

Figure 4.20. Plot of i_c/i_p vs equivalents of CF$_3$CO$_2$H added to a CH$_2$Cl$_2$ solution of [(dppe)Ni(pdt)(μ-H)Fe(CO)$_3$]BF$_4$, [1]BF$_4$, (blue) and [(dppe)Ni(edt)(μ-H)Fe(CO)$_3$]BF$_4$, [3]BF$_4$, (red). Inset: Zoomed in plot for [1]BF$_4$.

As judged by the 2-fold increase in rate on changing the diphosphine from dppe to dcpe in pdt complexes ($[\mathbf{1}H]^+$ vs $[\mathbf{2}H]^+$), we anticipated that the edt dcpe complex $[\mathbf{2}H]^+$ would be an even faster catalyst than $[\mathbf{3}H]^+$, the corresponding dppe complex. The reductive current for the $[\mathbf{2}H]^{+/0}$ couple increases with addition of chloroacetic acid, but it plateaus at i_c/i_p value of ~9, corresponding to a turnover frequency of 20 s^{-1}, which is ~10 times *less* than that for $[\mathbf{3}H]^+$ (Figures 4.21, 4.22).

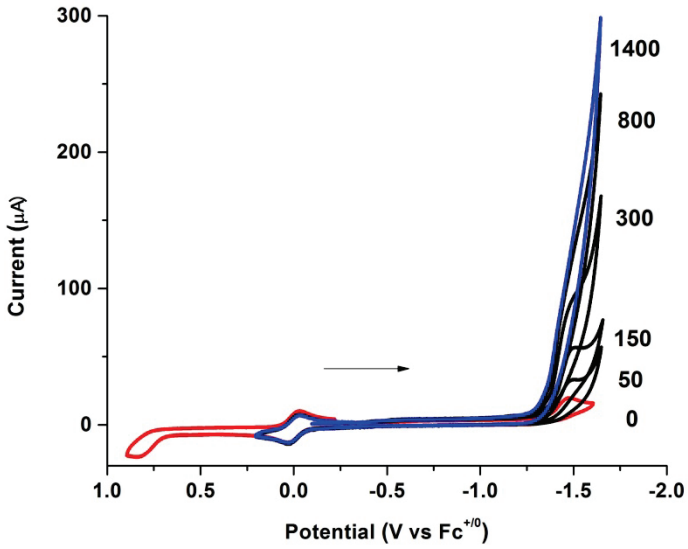

Figure 4.21 Cyclic voltammograms of [(dcpe)Ni(edt)(μ-H)Fe(CO)$_3$]BF_4, [4]BF_4, in CH_2Cl_2, with increasing equivalents of $H_2ClC_2O_2H$. (Conditions: 1.0 mM NiFe compound, 0.1 M $[Bu_4N]PF_6$ as supporting electrolyte, glassy carbon working electrode, silver wire pseudo reference electrode, Pt counter electrode)

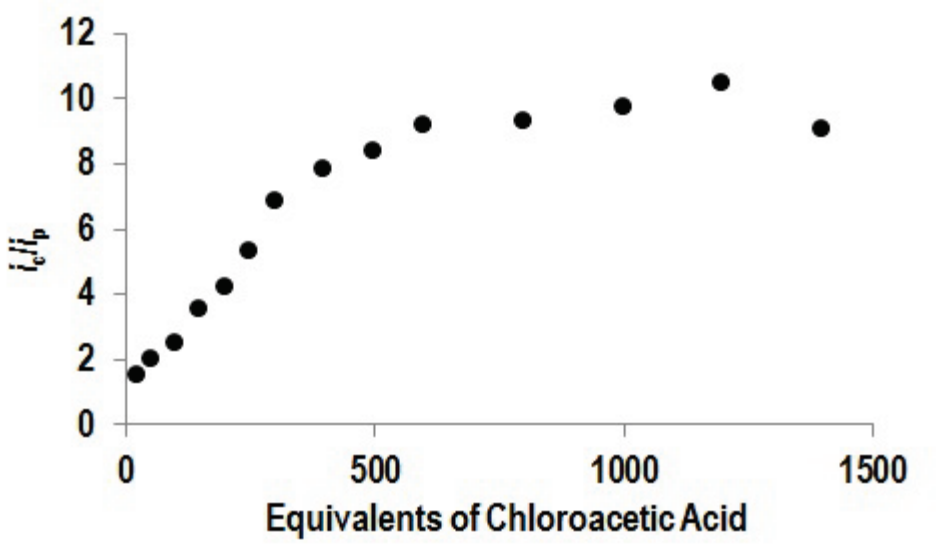

Figure 4.22. Plot of i_c/i_p vs equivalents of $H_2ClC_2O_2H$ added to a CH_2Cl_2 solution of [(dcpe)Ni(edt)(μ-H)Fe(CO)$_3$]BF_4, [4]BF_4.

We previously reported that substitution of CO with PPh_3 in [**1**H]$^+$ resulted in a two-fold increase in the rate of catalysis.[16] When the analogous substitution is made with the ethanedithiolate [**3**H]$^+$, increasing amounts of CH_2ClCO_2H cause an increase in the reductive current at -1.5 V, due to the [**5**H]$^{+/0}$ couple (Figure 4.23). Graphs of i_c/i_p vs, acid concentration begin to plateau at ~ 500 equiv of acid, corresponding to i_c/i_p of 25 (Figure 4.24). However, the value of i_c/i_p decreases with additional acid, an effect we tentatively attribute to catalyst decomposition. Based on these results, [**5**H]$^+$ operates at a slower rate than the analogous tricarbonyl derivative [**3**H]$^+$. Note, however, that [**5**H]$^+$ exists as a mixture of two isomers, in a ratio of ~2:1, and one of the two isomers may be a more active catalyst.

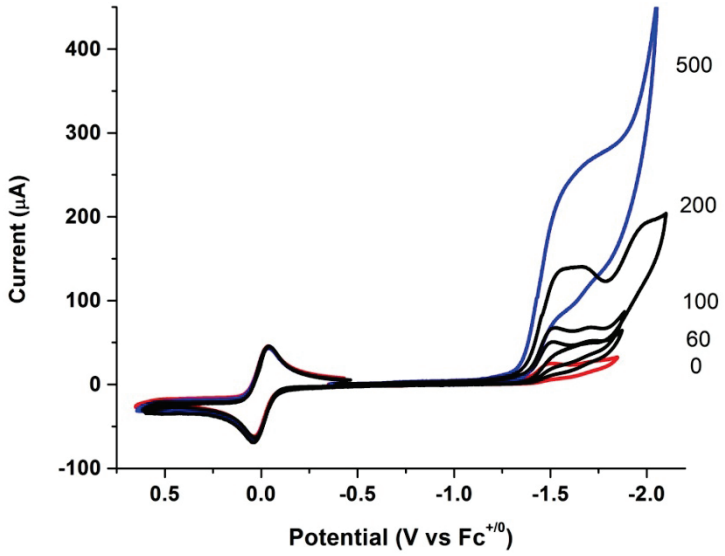

Figure 4.23 Cyclic voltammograms of [(dppe)Ni(edt)(μ-H)Fe(CO)$_2$(PPh$_3$)]BF$_4$, [5]BF$_4$, in CH$_2$Cl$_2$, with increasing equivalents of H$_2$ClC$_2$O$_2$H. (Conditions: 1.0 mM NiFe compound, 0.1 M [Bu$_4$N]PF$_6$ as supporting electrolyte, glassy carbon working electrode, silver wire pseudo reference electrode, Pt counter electrode)

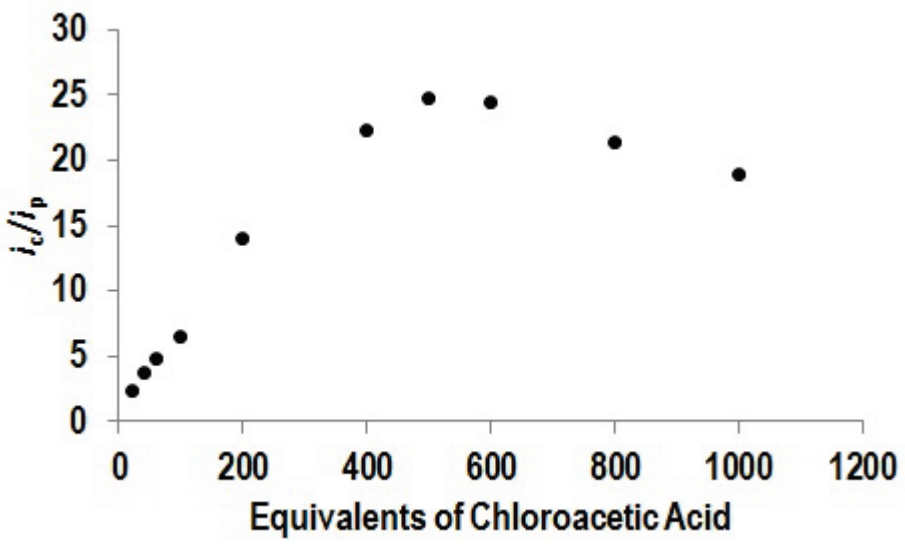

Figure 4.24. Plot of i_c/i_p vs equivalents of H$_2$ClC$_2$O$_2$H added to a CH$_2$Cl$_2$ solution of [(dppe)Ni(edt)(μ-H)Fe(CO)$_2$(PPh$_3$)]BF$_4$, [5]BF$_4$.

Table4.6. Parameters for Hydrogen Evolution Catalyzed by NiFe Hydrides in CH_2Cl_2 Solution (Potentials in V vs $Fc^{0/+}$).

Hydride catalyst, Proton source	E_{cat}	Overpotential	Rate (s^{-1})	pK_a of Hydride
[**1**H]BF_4 CF_3CO_2H	-1.20	0.54	20	10.7
[**2**H]BF_4 $H_2ClC_2O_2H$	-1.46	0.64	50	~13.6
[**3**H]BF_4 CF_3CO_2H	-1.23	0.57	240 -310	11.3
[**4**H]BF_4 $H_2ClC_2O_2H$	-1.45	0.65	20	13.6
[**5**H]BF_4 $H_2ClC_2O_2H$	-1.45	0.65	60-120	14.0

4.7 Determination of pK_a Values of NiFe Hydrides

The pK_a values of the NiFe hydrides, [**1**H]$^+$- [**5**H]$^+$ were determined by reaction of one equivalent of NiFe hydride with a base that partially deprotonates the hydride. The ratio of [NiFeH]:NiFe was then measured via ^{31}P NMR spectroscopy. The pK_a values for [**1**H]$^+$- [**5**H]$^+$ are listed in Table 4.7, along with [(dppe)Ni(pdt)(μ-H)Fe(CO)$_2$(PPh_3)]$^+$, which is included for ease of comparison.

Based on these values, changes in the electronic structure at the Fe center have a larger impact on the pK_a value that changes at Ni. Changing dppe on Ni to dcpe, causes an increase in pK_a of ~ 2.5-3 units, whereas, substituting a CO ligand on Fe with PPh_3 increases the pK_a by ~ 3.5 units.

These data are consistent with the crystal structures of the hydride complexes, which show that the hydride ligands are closer to the Fe centers than Ni. Therefore, the hydride is more tightly bound to Fe, and so the pK_a of the complex is more strongly affected by changes at the Fe center.

Table 4.7. pK_a values for NiFe hydrides

Hydride catalyst	pK_a of Hydride
[(dppe)Ni(pdt)(μ-H)Fe(CO)$_3$]BF$_4$ [**1**H]BF$_4$[a]	10.7
[(dcpe)Ni(pdt)(μ-H)Fe(CO)$_3$]BF$_4$ [**2**H]BF$_4$[b]	~13.6
[(dppe)Ni(pdt)(μ-H)Fe(CO)$_2$(PPh$_3$)]BF$_4$[b]	14.9
[(dppe)Ni(edt)(μ-H)Fe(CO)$_3$]BF$_4$ [**3**H]BF$_4$[a]	11.3
[(dcpe)Ni(edt)(μ-H)Fe(CO)$_3$]BF$_4$ [**4**H]BF$_4$[b]	13.6
[(dppe)Ni(edt)(μ-H)Fe(CO)$_2$(PPh$_3$)]BF$_4$ [**5**H]BF$_4$[b]	14.0

[a] Base: Aniline, pK_a^{MeCN} = 10.7
[b] Base: 4-Methoxypyridie, pK_a^{MeCN} = 14.2

4.8 Conclusion

The [NiFe]-hydrogenases operate via intermediates with a Ni(xdt)(μ-H)Fe core, and the complexes reported herein are new examples of such bioinspired catalytic intermediates.[16] We explored the effect of coligands (on nickel) and the dithiolate on the catalytic and other chemical properties of dithiolato NiFe hydrides.

A promising new entry to these complexes proceeds via the reaction of nickel dithiolates with $FeI_2(CO)_4$. This ferrous carbonyl iodide and the related bromide have been widely used for the preparation of ferrous carbonyls.[26-35] Typical substitution reactions of $FeI_2(CO)_4$ replace one or more CO ligands with 2e$^-$ donors to give complexes of the type $FeI_2L_2(CO)_2$ or $[FeX_3(CO)_3]^-$.[30,34] The intermediate [(diphosphine)Ni(dithiolate)(μ-I)Fe(CO)$_3$]$^+$ is structurally analogous to the hydrido cations. Our group had characterized [(dppe)Ni(pdt)(μ-Cl) Fe(dppe) (CO)]$^+$.[15,17] Both the μ-hydride and the μ-iodo tricarbonyls reduce readily to give the targeted Ni(I)Fe(I) derivatives. It is curious that the μ-iodo complexes are more labile than the corresponding μ-hydrido cations. This difference is ascribed to the influence of the strong sigma-donor hydride which stabilizes CO ligands on these midvalent complexes.[36]

It is instructive to compare these [(diphosphine)Ni(xdt)(μ-H)(CO)$_{3-x}$(PR$_3$)$_x$]$^+$ catalysts and other NiFe-based catalysts. The present type are simpler to analyze since the hydride complexes are directly observable the catalytic cycle. In contrast, for other Ni-Fe systems, the catalysts are

generated in situ and are not observed spectroscopically.[6,15,18] Most active site models for the NiFe-hydrogenases use Ni centers bound to diaminodithiolate (S_2N_2) ligands.[37-41] Such tetradentate ligands probably constrain Ni to a square-planar geometry,[42] although square-pyramidal or trans-octahedral NiS_2N_2 centers have been observed for Ni-Ru system in which the fifth and sixth site are occupied by hydride and aquo ligands.[43] In the Ni-diphosphine catalysts, the coordination sphere at Ni is proposed to alternate between square-pyramidal (with a bridging hydride), tetrahedral, and, possibly, square planar geometries (Scheme 4.11).

With respect to altering the basicities and reduction potentials, this work revealed that terminal ligands on nickel are more influential than changes in the dithiolate. On the other hand, the nature of the dithiolate more strongly affects catalytic rates. The pK_a's of $[\mathbf{1}H]^+$ vs $[\mathbf{2}H]^+$ differ by 2 units in PhCN solution. The diphosphine dcpe is known to substantially enhance the basicity of its complexes relative to dppe. Angelici has shown that $Fe(CO)_3$(dcpe) is more basic than $Fe(CO)_3$(dppe) by about 4 p$K_a^{C2H4Cl2}$ units.[19] Thus, it appears that the dcpe vs dppe effect is attenuated in the bimetallic system. In contrast, the change of $Fe(CO)_3$ to $Fe(PPh_3)(CO)_2$ leads to a ΔpK_a = 3-4.

The differing effect of substitution at Fe vs Ni suggests that the hydride is more strongly bonded to Fe. An approximate thermodynamic analysis suggests that increasing the basicity of the diphosphine more strongly affects the redox properties of the NiFe complexes than their basicities. The $[(dcpe)Ni(pdt)Fe(CO)_3]^{0/+}$ couple is 250 mV more negative than the $[(dppe)Ni(pdt)Fe(CO)_3]^{0/+}$ couple in MeCN solution (Table 4.2). A similar effect is seen for the dppe-edt and dcpe-edt complexes. The finding that the Ni-center more strongly affects the redox potential (6.88 kcal/mol at 298 K) than the basicity (2.6 kcal/mol at 298 K) suggests that oxidation of the Fe(I)Ni(I) complexes is localized at Ni, i.e. corresponding to the couple $Fe^{I}Ni^{I}/Fe^{I}Ni^{II}$. Substitution of dcpe for dppe also causes the reduction of the hydrides to become more difficult by 200-250 mV. Therefore, compounds containing more basic diphosphines on Ni will necessarily have higher overpotentials for electrocatalytic reduction of protons. Trends in the basicities and redox potentials for the new NiFe complexes suggest that protonation occurs primarily at the Fe center, whereas reduction is likely shared over both Ni and Fe.

The new NiFe hydrides, like others of this type,[16] are active electrocatalysts for the production of hydrogen. The best catalysts operate at overpotentials of ~600 mV at limiting rates near ca. 300 s^{-1}. Relative to the pdt derivatives, the edt-derived catalyst $[\mathbf{3}H]^+$ displays

faster turnover rates, while maintaining the same overpotential. Complexes $[\mathbf{1}H]^+$ and $[\mathbf{3}H]^+$ exhibit very similar spectroscopic properties as well as similar reduction potentials and acidities. At 298 K, a 10x increase in rate requires a change in activation energy of 2.6 kcal.

The rate determining step, at high acid concentrations (i.e. in the acid independent regime) is likely an intramolecular processes. As pointed out by Fraze et al.,[23] such intramolecular processes could include the coupling of two hydride ligands to form a bound dihydrogen or subsequent dissociation of H_2 from the metal. If two hydride ligands couple to form a dihydrogen complex, it is likely via hydride ligands located on the same metal, as coupling of two metal hydrides is generally orbitally forbidden.[44] Alternatively, the mechanism could be analogous to the [FeFe]-hydrogenases, that is a thiolate ligand could be protonated, then transfer the proton to the hydride ligand on Fe, forming a dihydrogen complex.

The mechanism of hydrogen evolution by these Ni-Fe models begins with the reduction of the Fe(II)-Ni(II) hydride (Figure Scheme 4.12). In this respect, there exists close parallels between the catalytic cycles for the μ-hydrides of Ni-Fe dithiolates and Fe(II)-Fe(II) dithiolates.[45] Neither model system however follows the pathways likely for the biological catalysts: the [NiFe]-hydrogenases do not operate via Fe(I) intermediates[10,46,47] and the [FeFe]-hydrogenases do not operate via bridging hydrides.[48] It is however encouraging that the basic design inspired by biology is rather forgiving despite differences in geometry at Ni, terminal ligation at Fe and Ni, and the nature of the μ-thiolates. One possible reason for the high activity may be the flexibility of the coordination geometry of the nickel sites in both (diphosphine)Ni(xdt)Fe$(PR_3)_x(CO)_{3-x}$ and the protonated derivatives [(diphosphine)Ni(xdt)(μ-H)Fe$(PR_3)_x(CO)_{3-x}]^+$. The Ni centers in (diphosphine)Ni(xdt)Fe$(PR_3)_x(CO)_{3-x}$ are stereochemically nonrigid, as indicated by variable temperature ^{31}P NMR spectra. Additionally, the geometry at the Ni centers varies based on redox and protonation state of the metal. The Ni(I) centers in (diphosphine)Ni(xdt)Fe$(PR_3)_x(CO)_{3-x}$ are tetrahedral, whereas the Ni(II) centers in [(diphosphine)Ni(xdt)(μ-H)Fe$(PR_3)_x(CO)_{3-x}]^+$ are square planar.

Scheme 4.11. Proposed mechanism of proton reduction catalysis by NiFe hydrides.

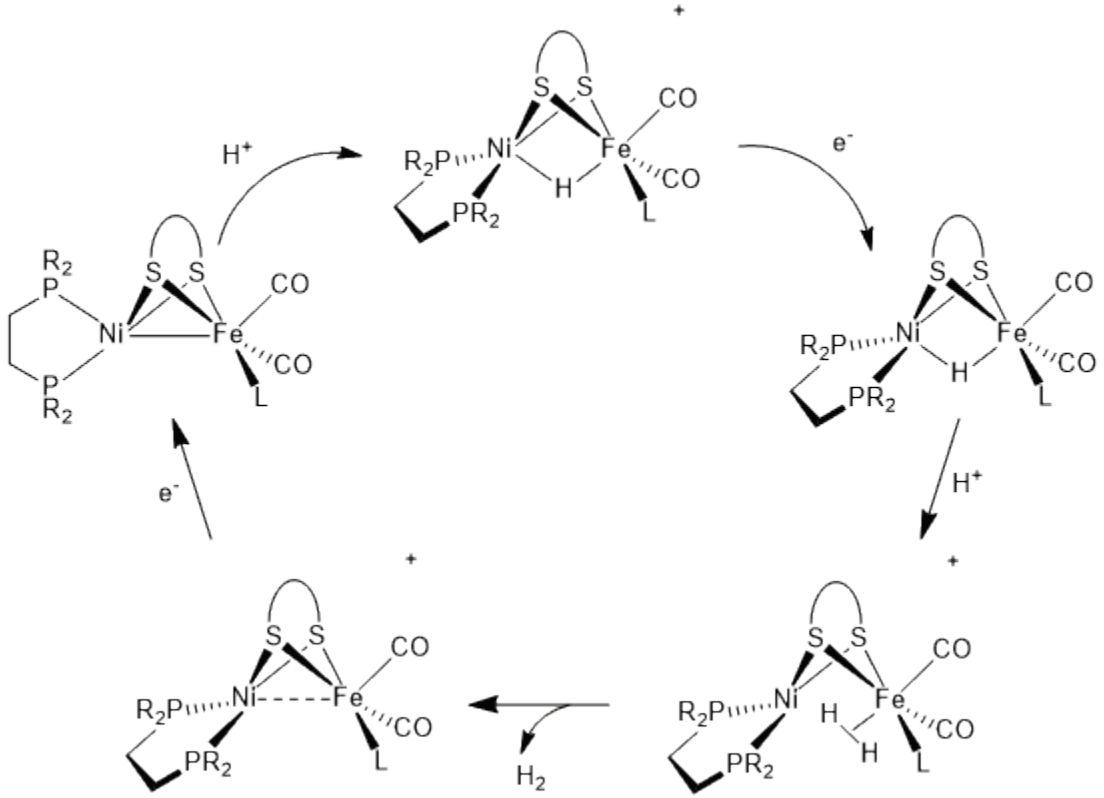

4.9 Experimental

Reactions were typically conducted using Schlenk techniques at room temperature. Most reagents were purchased from Aldrich and Strem. Solvents were HPLC-grade and dried by filtration through activated alumina or distilled under nitrogen over an appropriate drying agent. Ni(pdt)(dppe),[49] $Ni(SPh)_2$(dppe),[50] $Ni(SPh)_2$(dmpe),[16] $NiCl_2$(dppbz),[51] $NiCl_2$(dcpe),[52] $NiCl_2$(dppf),[53] $NiCl_2$(dppp),[54,55] and **1**[12] were prepared according to modified literature procedures. Chromatography was conducted with Siliaflash® P60 from Silicycle (230-400 mesh). $HBF_4 \cdot Et_2O$ (Sigma-Aldrich) was supplied as 51-57% HBF_4 in Et_2O (6.91 – 7.71 M). A 2.0 M solution of HCl in Et_2O was purchased from Sigma-Aldrich. Bu_4NPF_6 was purchased from GFS Chemicals and was recrystallized multiple times by extraction into CH_2Cl_2 followed by precipitation by hexane. ^1H NMR spectra (500 or 400 MHz) are referenced to residual solvent referenced to TMS. $^{31}P\{^1H\}$ NMR spectra (202 or 161 MHz) were referenced to external 85% H_3PO_4. FT-IR spectra were recorded on a Perkin Elmer Spectrum 100 FT-IR spectrometer.

$NiCl_2$(dcpe). The published synthesis was followed,[52] but no NMR data had been

reported. $^{31}P\{^1H\}$ NMR (CD_2Cl_2): δ 81.2 (s). ^1H NMR (CD_2Cl_2): δ 1.2-2.6 (broad m).

Ni(edt)(dcpe). A solution of 1.12 g (2.00 mmol) of $NiCl_2$(dcpe) in 20 mL of CH_2Cl_2 was treated with 0.188 g (2.00 mmol) of 1,2-ethanedithiol followed by 0.405 g (4.00 mmol) of triethylamine. The mixture was stirred for 30 min., during which time the color of the reaction solution deepened. Solvent was removed under reduced pressure, and the residue was washed with 3 x 10 mL portions of MeOH. The remaining orange solid was recrystallized by the addition of hexanes to a CH_2Cl_2 solution, and the resulting orange crystals were washed with 10 mL portions of hexanes and MeOH. Yield: 1.00 g (60%). ^{31}P NMR (CD_2Cl_2): δ 78.4 (s). Anal. Calcd for $C_{28}H_{52}NiP_2S_2 \cdot CH_2Cl_2 \cdot 2C_6H_{14}$ (found): C 59.28 (59.58); H, 9.95 (9.24).

Ni(Me_2pdt)(dppe). A solution of $NiCl_2$(dppe) (2.65 g, 5.0 mmol) in 200 mL of CH_2Cl_2 was treated with 0.79 g (5.8 mmol) of Me_2pdtH_2, followed by 1.58 mL (11.6 mmol) of triethylamine causing the orange solution to become dark red. After stirring for 10 min., the solution was reduced to half volume, transferred to a separatory funnel, and extracted into an equal volume of water. The volume of the CH_2Cl_2 layer was reduced, diluted with hexanes, and stored at -20 °C, resulting in dark red crystals, which were washed with hexanes. Yield: 1.8 g (61%). ^1H NMR ($CDCl_3$): δ 7.84(*d*), 7.44 (*m*) (dppe C_6H_5), 2.25 (*d*) ($S(CH_2)_2C$), 2.14 (*d*) ($P(CH_2)_2P$), 0.96 (*s*) ($C(CH_3)_2$). ^{31}P NMR ($CDCl_3$): δ55.9 (s).

[(dppe)Ni(Me_2pdt)(μ-I)Fe$(CO)_3$]$^+$ and (dppe)Ni(Me_2pdt)FeI_2. In a 50-mL Schlenk were dissolved 0.140 g (0.24 mmol) of $FeI_2(CO)_4$ and 0.100 g (0.24 mmol) of Ni(Me_2pdt)(dppe) in 5 mL of CH_2Cl_2. After stirring the solution for 5 min., the IR spectrum of the mixture showed ν_{CO} = 2095, 2075, 2053, and 2020 cm^{-1}. To the red solution, 20 mL of hexanes was added to precipitate a red solid. The IR spectrum of the red solid contains ν_{CO} = 2095, 2053, and 2020 cm^{-1}, which is similar to that for the species formed by reaction of **1** with I_2. The red solid was extracted into 5 mL of CH_2Cl_2, and this solution was treated with one equiv of $NaBF_4$. After stirring for 1 h, the mixture was filtered through Celite, the filtrate was concentrated to 2 mL, and hexanes were layered over the solution. After storage at –20 ºC, red and brown crystals had formed, which were identified as NiI_2(dppe) and NiFe(Me_2pdt)I_2(dppe), respectively, by X-ray diffraction.

(dppe)Ni(pdt)$Fe(CO)_3$ and [(dppe)Ni(pdt)(μ-I)$Fe(CO)_3$]I. The procedure developed for NiFe(pdt)(dcpe)$(CO)_3$ was applied to the synthesis of **1**.[16] Yield: 0.22 g (38%). A solution of 30 mg (0.0426 mmol) of **1** in 5 mL of CH_2Cl_2 was cooled in a –78 ºC bath and then treated with

10.8 mg (0.0426 mmol) of solid I_2. A 0.5-mL sample was removed and checked by FT-IR spectroscopy: ν_{CO} = 2095, 2055, 2025 cm^{-1} (see Figure 2).

(dppe)Ni(edt)Fe(CO)$_3$ and [(dppe)Ni(edt)(μ-H)Fe(CO)$_3$]BF$_4$, 3 and [3H]BF$_4$. A 100-mL Schlenk flask was charged with 0.382 g (0.91 mmol) of $FeI_2(CO)_4$ and 0.500 g (0.91 mmol) of Ni(edt)(dppe) and cooled to –78 °C. 30 mL of CH_2Cl_2 was added to the cooled mixture, resulting in a dark brown homogeneous solution. A 0.5-mL sample was removed (using an ambient temperature syringe) and checked by FT-IR spectroscopy to confirm the formation of the proposed μ-iodo intermediate (see Table 1). The remaining cold reaction solution was then treated with a pre-cooled (–78 °C) solution of 0.344 g (1.82 mmol) of Cp_2Co in 20 mL of CH_2Cl_2, which was transferred via cannula. The reaction solution became brown-green and was allowed to warm to room temperature. After stirring for 20 min. at room temperature, the reaction mixture was evaporated under reduced pressure, and the dark green residue was washed with 2 x 30 mL of MeCN. The dark green residue was extracted into 20 mL of CH_2Cl_2, and the dark green product was precipitated by addition of 30 mL of hexanes. Yield: 0.42 g (71%). $^{31}P\{^1H\}$ NMR (CD_2Cl_2): δ 65 (s). IR (CH_2Cl_2): ν_{CO} 2029, 1957 cm^{-1}. The protonation was conducted analogously to the protonation of **1**. ^1H NMR (CD_2Cl_2): δ -5.7 (br s, 1H). $^{31}P\{^1H\}$ (CD_2Cl_2): δ 72.7. IR (CH_2Cl_2): ν_{CO} = 2084, 2025 cm^{-1}. Anal. Calcd for $C_{31}H_{29}BF_4FeNiO_3P_2S_2$ (found): C, 44.59 (44.40, 43.72); H, 3.63 (3.62, 3.5).

(dcpe)Ni(edt)Fe(CO)$_3$ and [(dcpe)Ni(pdt)(μ-H)Fe(CO)$_3$]BF$_4$, 4 and [4H]BF$_4$. A 100-mL Schlenk flask was charged with 0.62 g (1.46 mmol) of $FeI_2(CO)_4$ and 0.84 g (1.46 mmol) of Ni(edt)(dcpe). To the mixture was added 20 mL of CH_2Cl_2 at room temperature resulting in a brown solution. After stirring for 15 min. at room temperature, the solution was treated with 0.55 g (2.92 mmol) of Cp_2Co, and was allowed to stir for 30 mins. The reaction mixture was evaporated under reduced pressure, and the dark brown solid was washed with 4 x 15 mL portions of MeCN (until washings were clear). The crude product was filtered through a pad of silica gel with CH_2Cl_2 to remove unreacted starting Ni(edt)(dcpe). The CH_2Cl_2 solution was then concentrated to dryness under vacuum. The product could not be purified beyond removal of unreacted starting material.$^{31}P\{^1H\}$ NMR (CD_2Cl_2): δ 94.1(s). The protonation was conducted analogously to the protonation of **1**. ^1H NMR (CD_2Cl_2): δ -5.3 (br s, 1H). $^{31}P\{^1H\}$ (CD_2Cl_2): δ 92.0. IR (CH_2Cl_2): ν_{CO} = 2080, 2019 cm^{-1}.

[(dppe)Ni(edt)(μ-H)Fe(CO)$_2$(PPh$_3$)]BF$_4$ and (dppe)Ni(edt)(μ-H)Fe(CO)$_2$(PPh$_3$), [5H]BF$_4$ and 5. In a 250-mL round bottomed Schlenk flask, 0.760 g (0.98 mmol) of [HNiFe(edt)(dppe)(CO)$_3$]BF$_4$ was dissolved in 80 mL of THF. The solution was treated with 2.5 g (9.8 mmol) of PPh_3. After stirring the solution for 2 h at 40 ºC, the solvent was removed in vacuum, yielding a red oil, which was washed with 3 x 40 mL portions of hexanes. The resulting reddish-brown powder was recrystallized by layering a CH_2Cl_2 solution with hexanes, which yielded orange crystals. Yield: 0.80 g (80%). ^{1}H NMR (CD_2Cl_2): -5.13 (dt), -8.15 (dt). ^{31}P^{1}H NMR (CD_2Cl_2): 71.5 (s, PPh_3 *unsym* or dppe *sym*), 67.1 (s, dppe *unsym*), 66.8 (s, PPh_3 *unsym* or dppe *sym*), 45.5 (s, PPh_3, *sym*). IR (CH_2Cl_2): ν_{CO} = 2019, 1968 cm^{-1}. Anal. Calcd for $C_{48}H_{44}BF_4FeNiO_2P_3S_2 \cdot CH_2Cl_2$ (found): C, 53.69 (53.34); H, 4.23 (4.48). IR (CH_2Cl_2): ν_{CO} = 2014, 1962 cm^{-1}.

A solution of 0.265 g (0.26 mmol) of [HNiFe(edt)(dppe)(PPh_3)(CO)$_2$]BF$_4$ in 20 mL of CH_2Cl_2 and 5 mL of MeOH was treated with 0.014 g (0.26 mmol) NaOMe in 10 mL of MeOH. The mixture stirred for 4 h, during which time the solution changed color from orange to green. Solvent was removed under vacuum, and the resulting green residue was washed with 3 x 15 mL portions of water and 3 x 10 mL portions of MeOH. The complex decomposes to form Ni(edt)(dppe), so a small amount of this complex is present in the ^{31}P NMR spectrum (δ 60 ppm). ^{31}P^{1}H NMR (CD_2Cl_2 , 20^{o}C): 77.02 (d, dppe), 58.81 (m, PPh_3), 50.68 (br, dppe). IR (CH_2Cl_2): ν_{CO} = 1968, 1912 cm^{-1}.

Determination of pK_a values of NiFe Hydrides. In general, 1 equiv of NiFe hydride and 1 equiv of base were dissolved in benzonitrile. For dppe complexes, [**1**H]$^+$ and [**3**H]$^+$, aniline was used (pK_a^{MeCN} = 10.7)[24], and for dcpe an d PPh_3 substituted complexes [**2**H]$^+$, [**4**H]$^+$, and [**5**H]$^+$, 4-Methoxypyridie was used (pK_a^{MeCN} = 14.2)[24]. The solution was allowed to equilibrate for ~ 1 hour, prior to analysis by ^{31}P NMR. The spectra were checked periodically, until they remained unchanged (typically ~ 24 h). A ratio of [NiFeH]$^+$:NiFe was determined by integration of the ^{31}P NMR spectra. The pK_a values were then determined using equation 5, which is derived based on the equilibria defined in equations 1-3 and equation 4.

$$NiFeH^+ \rightleftharpoons NiFe + H^+ \quad K_a(NiFeH^+) \quad (1)$$

$$B + H^+ \rightleftharpoons BH^+ \quad -K_a(BH^+) \quad (2)$$

$$NiFeH^+ + B \rightleftharpoons NiFe + BH^+ \quad K_{eq} = \frac{[NiFe][BH^+]}{[NiFeH^+][B]} \quad (3)$$

$$K_{eq} = K_a(NiFeH^+) - K_a(BH^+) \quad (4)$$

$$\frac{[NiFe][BH^+]}{[NiFeH^+][B]} = K_a(NiFeH^+) - K_a(BH^+)$$

$$-\log\frac{[NiFe][BH^+]}{[NiFeH^+][B]} = pK_a(NiFeH^+) - pK_a(BH^+)$$

$$\log\frac{[NiFeH^+][B]}{[NiFe][BH^+]} = pK_a(NiFeH^+) - pK_a(BH^+)$$

$$pK_a(NiFeH^+) = \log\frac{[NiFeH^+][B]}{[NiFe][BH^+]} + pK_a(BH^+) \quad (5)$$

Electrochemistry. The nickel-iron hydrides presented in this paper degrade to uncharacterized products in MeCN solution ($t_{1/2}$ ~ 60 min). For this reason, most electrochemical measurements were conducted in CH_2Cl_2 solutions. Cyclic voltammetry experiments were conducted using a 20-mL one-compartment glass cell with a tight-fitting Teflon top using a BAS-100 Electrochemical Analyzer. The working electrode was a glassy carbon (GC) disk (diameter = 3.00 mm). A silver wire was used as a quasireference electrode, and the counter electrode was a Pt wire. The electrolyte was 0.1 M $[Bu_4N]PF_6$. Ferrocene (sufficient to give ~1 mM solution) was added as an internal reference, and each cyclic voltammagram was referenced to this $Fc^{0/+}$ couple = 0.00 V. *i*R compensation was applied to all measurements using the BAS software. Cell resistance was determined prior to each scan, and the correction applied to the subsequently collected cyclic voltammagram. To account for catalysis by the GC electrode, control experiments were recorded at the same scan rate and potential range, and this current was subtracted as background. During prolonged experiments, additional solvent was added to compensate for evaporative loss. For measurements of i_p vs $[H^+]$, the total volume of acid solution (~20 μL aliquots of 0.5 M acid) was less than 5% of the sample volume, and this effect was ignored. Between scans, the solution was purged briefly with

N_2 and the working GC electrode was removed and polished. The duration of typical electrochemical titrations was 30 min.

Crystallography. *[(dppe)Ni(edt)(μ-H)Fe(CO)$_3$]B$_2$OHF$_6$·CH$_2$Cl$_2$:* A structural model consisting of the host ion pair plus one disordered dichloromethane solvate molecule was developed. Like bond distances and angles were restrained to be similar between the two orientations of the disordered dichloromethane solvate molecule (esd 0.01 and 0.02 respectively). Similar displacement amplitudes (esd 0.01) were imposed on disordered sites overlapping by less than the sum of van der Waals radii. Additionally, the displacement parameters were restrained to approximate to isotropic behavior for all disordered sites. The metal hydride was located in the difference map. The metal hydride distance was allowed to refine, but the H atom *U*'s were assigned as 1.5x U_{eq} of the carrier atom (The carrier atom was assumed to be Fe1 because the Fe-H distance was shorter than the Ni-H distance). The hydroxyl atom on the counterion[56] was located in the difference map. The O-H bond distance was allowed to refine, but the H atom *U*'s were assigned as 1.5x U_{eq} of the carrier O atom. The hydroxyl H atom was found to be hydrogen bonding to F5 on the counterion. Remaining H atoms were included as riding idealized contributors and their *U*'s were assigned as 1.2x carrier U_{eq}.

(dppe)Ni(Me$_2$pdt)FeI$_2$: A structural model consisting of the host plus 1/2 a disordered hexane solvate molecule per asymmetric unit was developed; however, positions for the idealized solvate molecules were poorly determined. This model converged with $w_{R2} = 0.1387$ and $R_1 = 0.0514$ for 366 parameters with 0 restraints against 6177 data. Since positions for the solvate molecules were poorly determined, a second structural model was refined with contributions from the solvate molecules removed from the diffraction data using the bypass procedure in PLATON.[57] No positions for the host network differed by more than two su's between these two refined models. The electron count from the "squeeze" model converged in good agreement with the number of solvate molecules predicted by the complete refinement. The "squeeze" data are reported here. Methyl H atom positions, R-CH_3, were optimized by rotation about R-C bonds with idealized C-H, R--H and H--H distances. Remaining H atoms were included as riding idealized contributors. Methyl H atom *U*'s were assigned as 1.5x U_{eq} of the carrier atom; remaining H atom *U*'s were assigned as 1.2x carrier U_{eq}.

4.10 References

(1) Vignais, P. M.; Billoud, B. "Occurrence, Classification, and Biological Function of Hydrogenases: An Overview." *Chem. Rev.* **2007**, *107*, 4206.

(2) Volbeda, A.; Charan, M.-H.; Piras, C.; Hatchikian, E. C.; Frey, M.; Fontecilla-Camps, J. C. "Crystal Structure of the Nickel-Iron Hydrogenase from *Desulfovibria gigas*." *Nature* **1995**, *373*, 580.

(3) Armstrong, F. A. "Hydrogenases: active site puzzles and progress." *Current Opinion in Chem. Biology* **2004**, *8*, 133.

(4) Foerster, S.; Stein, M.; Brecht, M.; Ogata, H.; Higuchi, Y.; Lubitz, W. "Single Crystal EPR Studies of the Reduced Active Site of [NiFe] Hydrogenase from Desulfovibrio vulgaris Miyazaki F." *J. Am. Chem. Soc.* **2003**, *125*, 83.

(5) Fan, C.; Teixeira, M.; Moura, J.; Moura, I.; Huynh, B. H.; Le, G. J.; Peck, H. D., Jr.; Hoffman, B. M. "Detection and characterization of exchangeable protons bound to the hydrogen-activation nickel site of Desulfovibrio gigas hydrogenase: a proton and deuterium Q-band ENDOR study." *J. Am. Chem. Soc.* **1991**, *113*, 20.

(6) Brecht, M.; van Gastel, M.; Buhrke, T.; Friedrich, B.; Lubitz, W. "Direct Detection of a Hydrogen Ligand in the [NiFe] Center of the Regulatory H_2-Sensing Hydrogenase from Ralstonia eutropha in Its Reduced State by HYSCORE and ENDOR Spectroscopy." *J. Am. Chem. Soc.* **2003**, *125*, 13075.

(7) Foerster, S.; van, G. M.; Brecht, M.; Lubitz, W. "An orientation-selected ENDOR and HYSCORE study of the Ni-C active state of Desulfovibrio vulgaris Miyazaki F hydrogenase." *J Biol Inorg Chem* **2005**, *10*, 51.

(8) Halcrow, M. A.; Christou, G. "Biomimetic Chemistry of Nickel." *Chem. Rev.* **1994**, *94*, 2421.

(9) Bouwman, E.; Reedijk, J. "Structural and functional models related to the nickel hydrogenases." *Coord. Chem. Rev.* **2005**, *249*, 1555.

(10) Tard, C.; Pickett, C. J. "Structural and Functional Analogues of the Active Sites of the [Fe]-, [NiFe]-, and [FeFe]-Hydrogenases." *Chem. Rev.* **2009**, *109*, 2245.

(11) Darensbourg, D. J.; Reibenspies, J. H.; Lai, C.-H.; Lee, W.-Z.; Darensbourg, M. Y. "Analysis of an Organometallic Iron Site model for the Heterodimetallic Unit of [NiFe]Hydrogenase." *J. Am. Chem. Soc.* **1997**, *119*, 7903.

(12) Zhu, W.; Marr, A. C.; Wang, Q.; Neese, F.; Spencer, D. J. E.; Blake, A. J.; Cooke, P. A.; Wilson, C.; Schröder, M. "Modulation of the electronic structure and the Ni-Fe distance in heterobimetallic models for the active site in [NiFe] hydrogenase." *Proc. Natl. Acad. Sci.* **2005**, *102*, 18280.

(13) Stenson, P. A.; Marin-Becerra, A.; Wilson, C.; Blake, A. J.; McMaster, J.; Schröder, M. "Formation of [(L)Ni(μ_2-S)$_x${Fe(CO)$_3$}$_x$] adducts (x = 1 or 2): analogues of the active site of [NiFe] hydrogenase." *Chem. Commun.* **2006**, 317.

(14) Ogo, S.; Kabe, R.; Uehara, K.; Kure, B.; Nishimura, T.; Menon, S. C.; Harada, R.; Fukuzumi, S.; Higuchi, Y.; Ohhara, T.; Tamada, T.; Kuroki, R. "A Dinuclear Ni(mu-H)Ru Complex Derived from H2." *Science* **2007**, *316*, 585.

(15) Barton, B. E.; Whaley, C. M.; Rauchfuss, T. B.; Gray, D. L. "Nickel-Iron-Dithiolato-Hydrides Relevant to the [NiFe]-Hydrogenase Active Site." *J. Am. Chem. Soc.* **2009**, *131*, 6942.

(16) Barton, B. E.; Rauchfuss, T. B. "Hydride-Containing Models for the Active Site of the Nickel-Iron Hydrogenases." *J. Am. Chem. Soc.* **2010**, *132*, 14877.

(17) Whaley, C. M. *Ph.D. Thesis, University Illinois at Urbana-Champaign, Urbana, IL* **2009**.

(18) Lever, A. B. P. "Electrochemical parametrization of metal complex redox potentials, using the ruthenium(III)/ruthenium(II) couple to generate a ligand electrochemical series." *Inorg. Chem.* **1990**, *29*, 1271.

(19) Sowa, J. R., Jr.; Zanotti, V.; Facchin, G.; Angelici, R. J. "Calorimetric studies of the heats of protonation of the metal in Fe(CO)$_3$(bidentate phosphine, arsine) complexes: effects of chelate ligands on metal basicity." *J. Am. Chem. Soc.* **1992**, *114*, 160.

(20) Singleton, M. L.; Jenkins, R. M.; Klemashevich, C. L.; Darensbourg, M. Y. "The effect of bridgehead steric bulk on the ground state and intramolecular exchange processes of (μ-SCH$_2$CR$_2$CH$_2$S)[Fe(CO)$_3$][Fe(CO)$_2$L] complexes." *C. R. Chim.* **2008**, *11*, 861.

(21) Bierbach, U.; Saak, W.; Haase, D.; Pohl, S. "Tetra-iodo-bis(μ2-trans-1,2-bis(3-methylthiourea)cyclohexane-S,S')-di-iron(ii) and related thiourea complexes of FeI2." *Z. Naturforsch.* **1990**, *B45*, (1990).

(22) Schilter, D.; Rauchfuss, T. B. "Unpublished Result." **2013**.

(23) Fraze, K.; Wilson, A. D.; Appel, A. M.; Rakowski DuBois, M.; DuBois, D. L. "Thermodynamic Properties of the Ni-H Bond in Complexes of the Type [HNi(P$_2$RN$_2$R')$_2$](BF$_4$) and Evaluation of Factors That Control Catalytic Activity for Hydrogen Oxidation/Production." *Organometallics* **2007**, *26*, 3918.

(24) Izutsu, K. *Acid-Base Dissociation Constants in Dipolar Aprotic Solvents*; Blackwell Scientific Publications: Oxford, U.K., 1990; Vol. 35.

(25) Kilgore, U. J.; Roberts, J. A. S.; Pool, D. H.; Appel, A. M.; Stewart, M. P.; Rakowski DuBois, M.; Dougherty, W. G.; Kassel, W. S.; Bullock, R. M.; DuBois, D. L. "$[Ni(PPh_2NC_6H_4X_2)_2]_2^+$ Complexes as Electrocatalysts for H2 Production: Effect of Substituents, Acids, and Water on Catalytic Rates." *J. Am. Chem. Soc.* **2011**, *133*, 5861.

(26) Hieber, W.; Bader, G. "Reaktionen und Derivate des Eisencarbonyls, II.: Neuartige Kohlenoxyd-Verbindungen von Eisenhalogeniden." *Ber.* **1928**, *61B*, 1717.

(27) Manuel, T. A. "Some Tertiary Phosphine-Iron Carbonyl Compounds." *Inorg. Chem.* **1963**, *2*, 854.

(28) Cohen, I. A.; Basolo, F. "Kinetics of substitution reactions of dihalo tetracarbonyliron(II) compounds with different reagents." *J. Inorg. Nucl. Chem.* **1966**, *28*, 511.

(29) Li, B.; Liu, T.; Popescu, C. V.; Bilko, A.; Darensbourg, M. Y. "Synthesis and Mossbauer Characterization of Octahedral Iron(II) Carbonyl Complexes $FeI_2(CO)_3L$ and $FeI_2(CO)_2L_2$: Developing Models of the [Fe]-H2ase Active Site." *Inorg. Chem.* **2009**, *48*, 11283.

(30) Bellachioma, G.; Cardaci, G.; Macchioni, A.; Venturi, C.; Zuccaccia, C. "Reductive elimination of halogens assisted by phosphine ligands in $Fe(CO)_4X_2$ (X=I,Br) complexes." *J. Organomet. Chem.* **2006**, *691*, 3881.

(31) Moreland, A. C.; Rauchfuss, T. B. "Binding of p-Acceptor Ligands to Triamine Iron(II) Complexes." *Inorg. Chem.* **2000**, *39*, 3029.

(32) Verhagen, J. A. W.; Lutz, M.; Spek, A. L.; Bouwman, E. "Synthesis and Characterisation of New Nickel-Iron Complexes with an S'4 Coordination Environment around the Nickel Centre." *Eur. J. Inorg. Chem.* **2003**, *2003*, 3968.

(33) Jiang, J.; Koch, S. A. "*fac*-$[Fe^{II}(CN)_3(CO)_3]^-$ and *cis*-$[Fe^{II}(CN)_4(CO)_2]^{2-}$: New Members of the Class of $[Fe^{II}(CN)_x(CO)_y]$ Compounds." *Inorg. Chem.* **2002**, *41*, 158.

(34) Jiang, J.; Lo, W.; Müller, P.; Fine, N. D.; Maruani, M.; Raytman, A. "Synthesis, structure and stability of fac-$[FeII(CO)_3X_3]^{1-}$ (X=Br, I)." *Inorg. Chem. Commun.* **2009**, *12*, 527.

(35) Turrell, P. J.; Wright, J. A.; Peck, J. N. T.; Oganesyan, V. S.; Pickett, C. J. "The Third Hydrogenase: A Ferracyclic Carbamoyl with Close Structural Analogy to the Active Site of Hmd." *Angew. Chem., Int. Ed.* **2010**, *49*, 7508.

(36) Benito-Garagorri, D.; Lagoja, I.; Veiros, L. F.; Kirchner, K. A. "Reactivity of coordinatively unsaturated iron complexes towards carbon monoxide: to bind or not to bind?" *Dalton Trans.* **2011**, *40*, 4778.

(37) Canaguier, S.; Field, M.; Oudart, Y.; Pecaut, J.; Fontecave, M.; Artero, V. "A structural and functional mimic of the active site of NiFe hydrogenases." *Chem. Commun.* **2010**, *46*, 5876.

(38) Canaguier, S.; Artero, V.; Fontecave, M. "Modelling NiFe hydrogenases: nickel-based electrocatalysts for hydrogen production." *Dalton Trans.* **2008**, 315.

(39) Perra, A.; Davies, E. S.; Hyde, J. R.; Wang, Q.; McMaster, J.; Schröder, M. "Electrocatalytic production of hydrogen by a synthetic model of [NiFe] hydrogenases." *Chem. Commun.* **2006**, 1103.

(40) Vaccaro, L.; Artero, V.; Canaguier, S.; Fontecave, M.; Field, M. J. "Mechanism of hydrogen evolution catalyzed by NiFe hydrogenases: insights from a Ni-Ru model compound." *Dalton Trans.* **2010**, *39*, 3043.

(41) Canaguier, S.; Fontecave, M.; Artero, V. "Cp*–-Ruthenium–Nickel-Based H2-Evolving Electrocatalysts as Bio-inspired Models of NiFe Hydrogenases." *Eur. J. Inorg. Chem.* **2010**, *2011*, 1094.

(42) Grapperhaus, C. A.; Darensbourg, M. Y. "Oxygen Capture by Sulfur in Nickel Thiolates." *Acc. Chem. Res.* **1998**, *31*, 451.

(43) Ogo, S. "Electrons from hydrogen." *Chem. Commun.* **2009**, 3317.

(44) Trinquier, G.; Hoffmann, R. "Dinuclear reductive eliminations." *Organometallics* **1984**, *3*, 370.

(45) Ezzaher, S.; Capon, J.-F.; Dumontet, N.; Gloaguen, F.; Pétillon, F. Y.; Schollhammer, P.; Talarmin, J. "Electrochemical study of the role of a H-bridged, unsymmetrically disubstituted diiron complex in proton reduction catalysis." *J. Electroanal. Chem.* **2009**, *626*, 161.

(46) Wu, H.; Hall, M. B. "Density functional theory on the larger active site models for [NiFe] hydrogenases: Two-state reactivity?" *C. R. Chim.* **2008**, *11*, 790.

(47) Siegbahn, P. E. M.; Tye, J. W.; Hall, M. B. "Computational Studies of [NiFe] and [FeFe] Hydrogenases." *Chem. Rev.* **2007**, *107*, 4414.

(48) Gloaguen, F.; Rauchfuss, T. B. "Small Molecule Mimics of Hydrogenase: Hydrides and Redox." *Chem. Soc. Rev.* **2009**, *38*, 100.

(49) Schmidt, M.; Hoffmann, G. G. "Zur Kenntnis Einiger Phosphinkomplexierter Platin-und Nickel-Schwefelverbindungen." *J. Organomet. Chem.* **1977**, *124*, C5.

(50) Hayter, R. G.; Humiec, F. S. "Some mercaptides and mercaptide complexes of nickel and palladium." *J. Inorg. Nucl. Chem.* **1964**, *26*, 807.

(51) Levason, W.; McAuliffe, C. A. "Bidentate ligands containing very soft donor atoms. Nickel(II) complexes of arylarsines and arystibines." *Inorg. Chim. Acta* **1974**, *11*, 33.

(52) Angulo, I. M.; Bouwman, E.; van Gorkum, R.; Lok, S. M.; Lutz, M.; Spek, A. L. "New nickel-containing homogeneous hydrogenation catalysts. Structures of [Ni(o-MeO-dpppol)Cl_2] and [Ni(dcpe)Cl_2]." *J. Mol. Catal. A* **2003**, *202*, 97.

(53) Corain, B.; Longato, B.; Favero, G.; Ajò, D.; Pilloni, G.; Russo, U.; Kreiss, F. R. "Heteropolymetallic complexes of 1,1′-Bis(diphenylphosphino)ferrocene (dppf). III. Comparative physicochemical properties of (dppf)MCl_2 (M = Co, Ni, Pd, Pt, Zn, Cd, Hg)." *Inorg. Chim. Acta* **1989**, *157*, 259.

(54) Bomfim, J. A. S.; de Souza, F. P.; Filgueiras, C. A. L.; de Sousa, A. G.; Gambardella, M. T. P. *Polyhedron* **2003**, *22*, 1567.

(55) Van Hecke, G. R.; Horrocks, W. D., Jr. "Ditertiary Phosphine Complexes of Nickel. Spectral, Magnetic, and Proton Resonance Studies. A Planar-Tetrahedral Equilibrium." *Inorg. Chem.* **1966**, *5*, 1968.
(

56) Kuhn, N.; Göhner, M.; Steimann, M. "[$Ph_2P(O)CH_2Im$][$F_3B(\mu$-OH)BF_3]. Erste strukturanalytische Charakterisierung des Hexafluoro(μ-hydroxo)diborat-Ions." *Z. anorg. allg. Chem.* **2003**, *629*, 595.

(57) Spek, A. L.; van der Sluis, P. "PLATON." *Acta Crystallogr.* **1990**, *A46*, 194.

Chapter 5.

Development of New Building Block Methods for the Synthesis of Diiron and Manganese-Iron Complexes

5.1 Introduction

Compounds of the type $Fe_2(SR)_2(CO)_{6-x}L_x$ are topical because of their relationship to the active sites of the [FeFe]-hydrogenases.[1] Many such compounds have been prepared, motivated by the goal of understanding the biological mechanism and, more generally, designing catalysts for hydrogen production. In this paper, we describe a new route to such compounds, using a new class of ferrous carbonyl dithiolato diphosphine complexes, and show that the method can be extended to related heterometallic derivatives.

As discussed in Chapter 2, compounds of the type $Fe_2(SR)_2(CO)_{6-x}L_x$ are traditionally prepared by the reaction of thiols with $Fe_3(CO)_{12}$.[2] The method is very efficient,[2] but the hexacarbonyls then require substitution to enhance their basicity and redox properties. Complementarily, $Fe_2(S_2)(CO)_6$[3,4] is well suited for producing diiron complexes containing elaborate organosulfur ligands,[5,6] but the precursor disulfido complex remains tedious to prepare.[7] We have also described reductive carbonylation of ferrous halides in the presence of dithiolates (Scheme 5.1).[8] The method, which proceeds in 20-40% yield depending on the dithiolate, is suited for generating ^{57}Fe-labelled derivatives, which are of interest for NRVS and Mossbauer measurements.[9]

Scheme 5.1 Synthesis of $Fe_2(xdt)(CO)_6$ from $FeCl_2$

In seeking new convergent routes to substituted diiron dithiolato complexes we found that ferrous carbonyl dithiolato diphosphine complexes serve as useful starting materials. The related ferrous carbonyl complexes, $FeX_2(CO)_2(PR_3)_2$ (X= halide), were prepared by reaction of Fe(II) carbonyl halides with phosphines.[10,11] A second more convenient route entails carbonylation of suitable ferrous halide complexes (Scheme 5.2). The ferrous halides themselves

are unreactive towards CO, but simple adducts of the type $FeX_2(PR_3)_2$,[12-15] carbonylate to form $FeX_2(CO)_2(PR_3)_2$.[11,13,16] The reductive carbonylation of ferrous halides occurs in the presence of phosphine ligands but the resulting adducts are unreactive toward thiols, unlike $Fe(CO)_{12}$.[17] The latter route is appealing in that it does not require an iron carbonyl source, but instead starts with ferrous halides, thus making it amenable to labeling with ^{57}Fe.

Scheme 5.2 Synthesis of $FeX_2(CO)_2(PR_3)_2$.

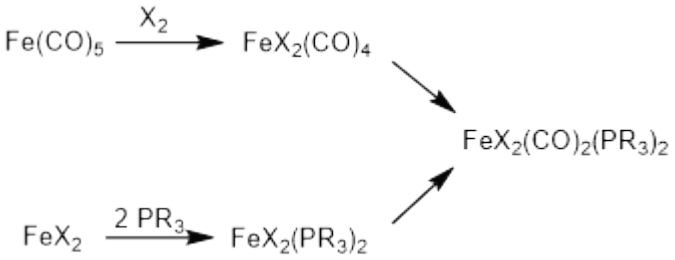

Márko *et al*. reported the synthesis of a variety of ferrous dithiolato complexes of the type $Fe(SR)_2(CO)_2L_2$. His procedure calls for reaction of ferrous sulfate with bidentate ligands and two equivalents of NaSR in the presence of CO[18,19] (Scheme 5.3). The complex $Fe(SPh)_2(CO)_2(dppe)$ (dppe= $Ph_2C_2H_4Ph_2$) was found to form an adduct with $HgCl_2$, but otherwise, reactivity of these ferrous carbonyl complexes with other metals has not been reported.[18]

Scheme 5.3 Synthesis of $Fe(SR)_2(CO)_2$(chelate) complexes developed by Márko.

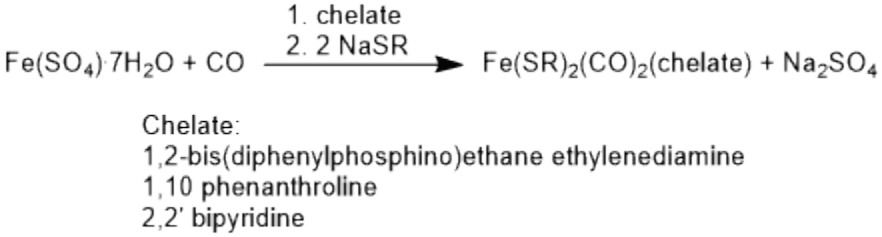

Models of the active site of [FeFe]-hydrogenase ideally contain more biologically relevant bridging dithiolato ligands. We previously reported the synthesis of $Fe(edt)(CO)_2(PMe_3)_2$ (edt= 1,2-ethandithiolate), by a modified version of Márko's method.[20] (Scheme 5.4) Additionally, Ott and coworkers reported the synthesis of monoferrous carbonyls $Fe(S_2C_6H_2X_2)(CO)_2(PMe_3)_2$ (X= H, Cl) with benzenedithiolate ligands. These complexes are

prepared from *di*iron dithiolato hexacarbonyls,[21] which undergo cleavage upon treatment with PMe_3 (Scheme 5.5a). Similar complexes containing bidentate phosphine ligands were prepared, but in this case, pentacoordinate Fe centers are favored, resulting in square pyramidal monocarbonyl complexes (Scheme 5.5b).[22]

Scheme 5.4 Synthesis of $Fe(edt)(CO)_2(PMe_3)_2$

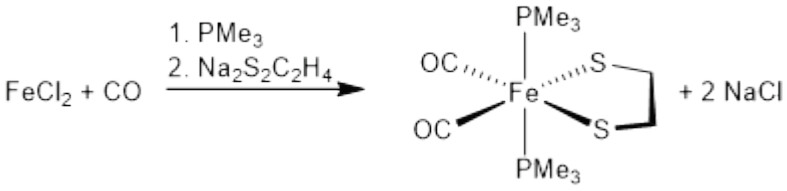

Scheme 5.5 Synthesis of monomeric ferrous carbonyl bis-phosphine dithiolato complexes by Ott.

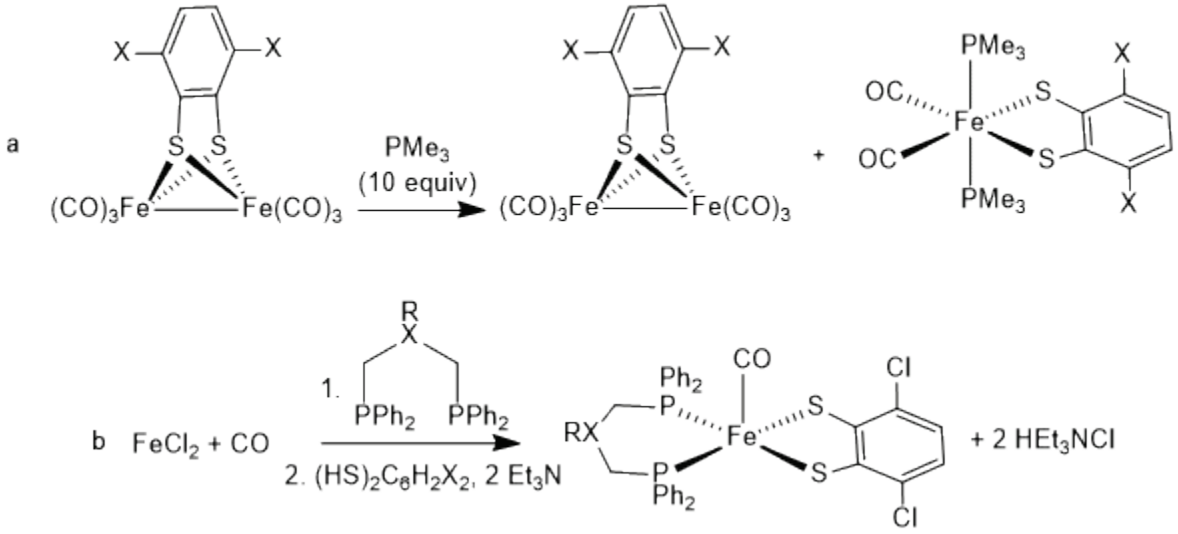

Herein, we report the synthesis of ferrous dicarbonyl dithiolato diphosphine complexes containing chelating diphosphine and dithiolate ligands. We have developed a new building block method for the synthesis of substituted diiron complexes of the type $Fe_2(dithiolate)(CO)_4L_2$, by reaction of $Fe(dithiolate)(CO)_2L_2$ complexes with an Fe(0) tricarbonyl source. Additionally, we extend this building block approach to the synthesis of Mn-Fe analogues of the FeFe complexes. The d^6-d^6 complex $FeMn(\mu\text{-}SPh)_3(CO)_6$ has been described,[23]

but with three bridging thiolates it is not suited for conversion to hydrogen-relevant derivatives. Several reports describe the use of metal dithiolates as precursors to dithiolato-bridged bimetallic complexes.[24,25] We also explored the redox chemistry and reactivity with hydridic ligands of these novel Mn-Fe complexes.

5.2 Ferrous Dithiolato Carbonyls.

New diphosphine-substituted ferrous carbonyl thiolates were prepared by carbonylation of a slurry of anhydrous $FeCl_2$ and the diphosphine ligand, followed by the addition of disodium salts of the appropriate dithiolate. (Scheme 5.6) The reaction afforded a mixture of the two isomers that are possible for an octahedral complex of the type $M(chel)(chel')L_2$.

Scheme 5.6. Synthesis of $Fe(xdt)(CO)_2$(diphosphine) complexes, 1a-1f.

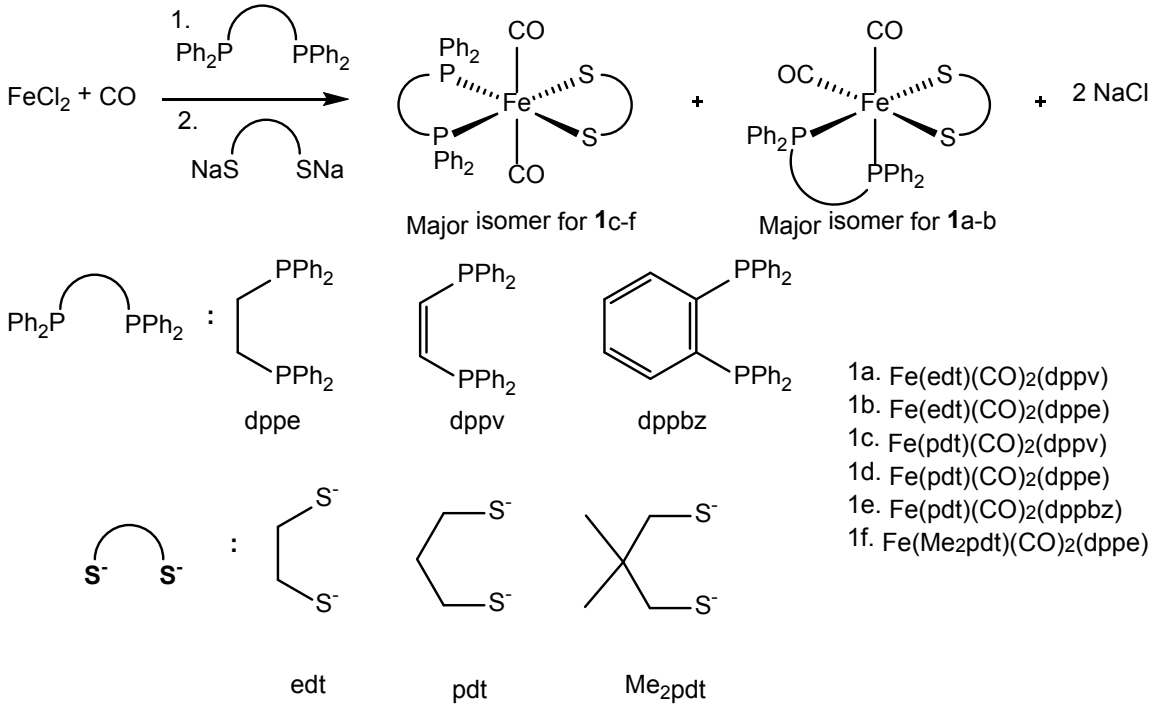

The pathway for the synthesis was not examined, but we note that a likely intermediate $FeCl_2$(diphosphine)$(CO)_2$ is known[16] but is less robust than the corresponding dithiolates. We found that the intermediate in these reactions, $FeCl_2$(diphosphine)$(CO)_2$ could be reduced with

zinc under an atmosphere of CO to give $Fe(CO)_3(dppe)$. This Fe(0) complex however proved unreactive toward 1,3-propanedithiol in refluxing toluene.

The ^{31}P NMR and IR spectra of the new compounds indicate of the presence of two isomers. The ^{31}P NMR spectra exhibit three signals, a singlet corresponding to the symmetrical isomer and a pair of doublets corresponding to the unsymmetrical isomer (Table 5.1, Figure 5.1). For the edt complexes, **1a** and **1b**, the unsymmetrical isomer is the major species, whereas for the 1,3-propanedithiolate (pdt) and 2-dimethyl-1,3-propanedithiolate (Me_2pdt) complexes, **1c-f**, the symmetrical isomer is the major species. (Table 5.1, Figure 5.1) This difference is attributed to differences in steric bulk of the two dithiolate ligands.

Table 5.1. Spectroscopic Data for ferrous carbonyl complexes 1a-f and 2.

Complex	Isomer Ratio Unsym:Sym (20 °C, CH_2Cl_2)	ν_{co} (cm^{-1}) (THF)	^{31}P NMR (δ) Unsym Isomer	^{31}P NMR (δ) Sym Isomer
$Fe(edt)(CO)_2(dppv)$ **1a**	2:1	2013 (s), 1978 (s), 1960 (s)	89.4 (d) 59.9 (d)	87.7 (s)
$Fe(edt)(CO)_2(dppe)$ **1b**	3:1	2009 (s) 1973 (s), 1959 (s)	78.3 (d) 48.1 (d)	77.5 (s)
$Fe(pdt)(CO)_2(dppv)$ **1c**	1:4	2010 (w), 1975 (s)	87.3 (d) 60.4 (d)	81.2 (s)
$Fe(pdt)(CO)_2(dppe)$ **1d**	2:3	2004 (w), 1969 (s), 1958 (sh)	78.0 (d) 51.2 (d)	73.7 (s)
$Fe(pdt)(CO)_2(dppbz)$ **1e**	1:7	2012 (w) 1970 (s)	78.5 (d) 68.2 (d)	80.8 (s)
$Fe(Me_2pdt)(CO)_2(dppe)$ **1f**	1:3	2006 (w) 1969 (s)	78.3 (d) 52.6 (d)	73.8 (s)
$Fe(edt)(CO)_2(PMe_3)_2$ **2**	-	1988 (s), 1939 (s)	-	10.87 (s)

For the edt complexes **1a-b**, the IR spectra exhibit three strong bands at ν_{CO} = ~2000, 1970, and 1960 cm^{-1}. The IR spectrum of $Fe(pdt)(CO)_2(dppe)$, **1d**, exhibits a strong band atν_{CO} = 1969 cm^{-1} and weak bands at ν_{CO} = 2006 and 1958 cm^{-1}. In contrast, the related pdt and Me_2pdt complexes, **1c,e,f**, exhibit a strong band at ν_{CO} = 1970 cm^{-1} and a weak band at ~2000 cm^{-1}. Complexes of the type $FeX_2(CO)_2L_2$ (X = halide or thiolate, L= PR_3) have been synthesized previously, and in most cases, they are present as a single isomer. Typically,

complexes with cis-CO ligands exhibit two intense CO bands at 2007-2024 and 1955-1983 cm^{-1}, whereas, a single CO band at ~1970 cm^{-1} is present in the IR spectra of complexes with trans-CO ligands.[18,26] As judged from prior results, the bands at ~2000 and 1960 cm^{-1} are assigned to the unsymmetrical isomer, and that at 1970 cm^{-1} is assigned to the symmetrical isomer. In the pdt complexes, the second band due to the unsymmetrical isomer is likely obscured by the band for the symmetrical isomer.

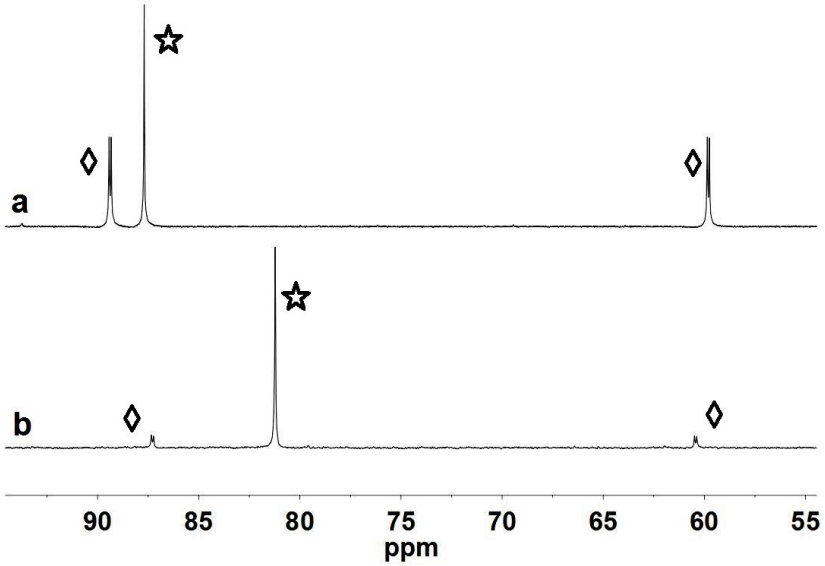

Figure 5.1. ^{31}P NMR spectra of (a) Fe(edt)$(CO)_2$(dppv), 1a, (diamond = unsym isomer, star = sym isomer) and (b) Fe(pdt)$(CO)_2$(dppv), 1c, (diamond = unsym isomer, star = sym isomer) in CD_2Cl_2.

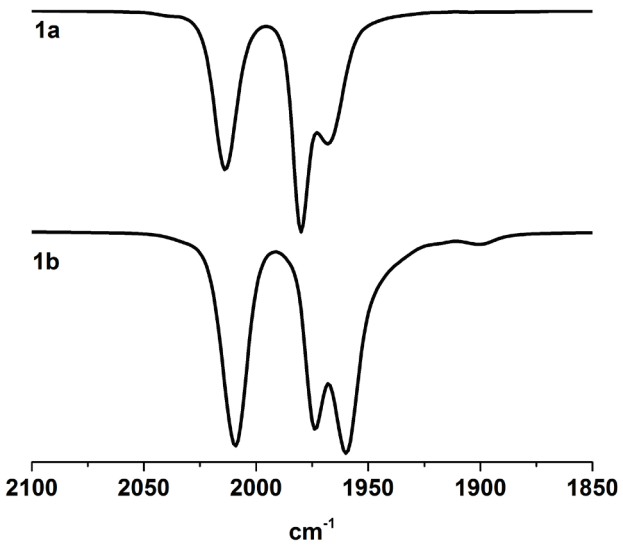

Figure 5.2. IR spectra of Fe(edt)$(CO)_2$(dppv), 1a, and Fe(edt)$(CO)_2$(dppe), 1b, in THF.

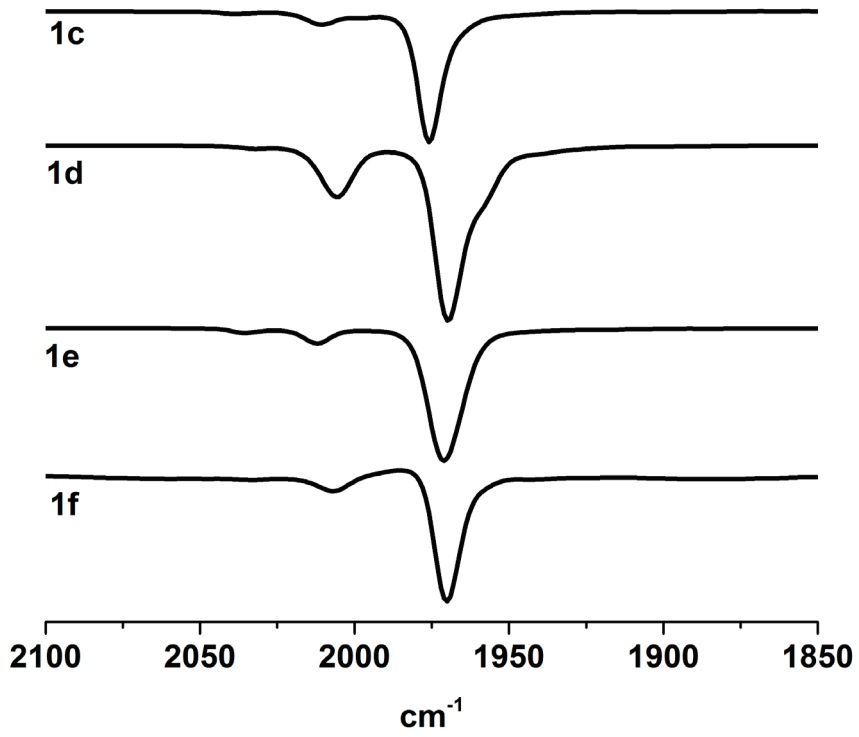

Figure 5.3. IR spectra of Fe(pdt)$(CO)_2$(dppv), 1c, Fe(pdt)$(CO)_2$(dppe), 1d, Fe(pdt)$(CO)_2$(dppbz), 1e, and Fe(Me_2pdt)$(CO)_2$(dppe), 1f in THF.

A former co-worker, Dr. Phillip Volkers, obtained diffraction quality crystals of **1a** and **1c**, and the molecular structures were determined by X-ray crystallography. In both cases, the major solution isomer crystallized.[27] The complex $Fe(edt)(CO)_2(dppv)$, **1a**, crystallized as the unsymmetrical isomer, with all cis ligands. Márko reported the structure of a similar complex with monothiolate ligands, $Fe(SPh)_2(CO)_2(dppe)$, which all crystallizes as the all cis isomer.[18] The complex $Fe(pdt)(CO)_2(dppv)$, **1c**, crystallized as the symmetrical isomer. The structure of the related complex, $FeCl_2(CO)_2(dppe)$, varies based on the solvent in which it is prepared. In benzene, only the trans-chloride, cis-CO isomer (trans,cis-$FeCl_2(CO)_2(dppe)$) is present, and in THF, the cis-chloride,trans-CO isomer is (cis,trans-$FeCl_2(CO)_2(dppe)$) present. In refluxing acetone, trans,cis-$FeCl_2(CO)_2(dppe)$ isomerizes to cis,trans-$FeCl_2(CO)_2(dppe)$.[28] $FeI_2(CO)_2(PR_3)_2$ (R=Me, Et) forms the cis-CO isomer, but isomerizes to the all trans isomer under photolysis.[29]

We previously reported the synthesis and characterization of a related complex containing trimethylphosphine ligands, rather than a diphosphine, $Fe(edt)(CO)_2(PMe_3)_2$, **2**. Unlike complexes **1a-d,** in solution **2** is present as a single isomer, in which the phosphine ligands are in a trans configuration, and the CO ligands are in a cis configuration. The structure was confirmed by X-ray crystallography, ^1H and ^{31}P NMR, and IR spectroscopy (Table 5.1).[20]

5.3 Diiron Dithiolato Carbonyl Complexes via Comproportionation.

We sought to develop a new route to substituted diiron dithiolato carbonyl complexes, utilizing the monomeric ferrous carbonyl complexes discussed in Section 5.2. Dr. Phillip Volkers had previously examined the reaction of **2** with an Fe^0 carbonyl source, $(bda)Fe(CO)_3$ (bda = benzylideneacetone) to afford $Fe_2(edt)(CO)_4(PMe_3)_2$ (Scheme 5.7).[27]

Scheme 5.7 Comproportionation and symmetrization reaction of 2 and $(bda)Fe(CO)_3$.[27]

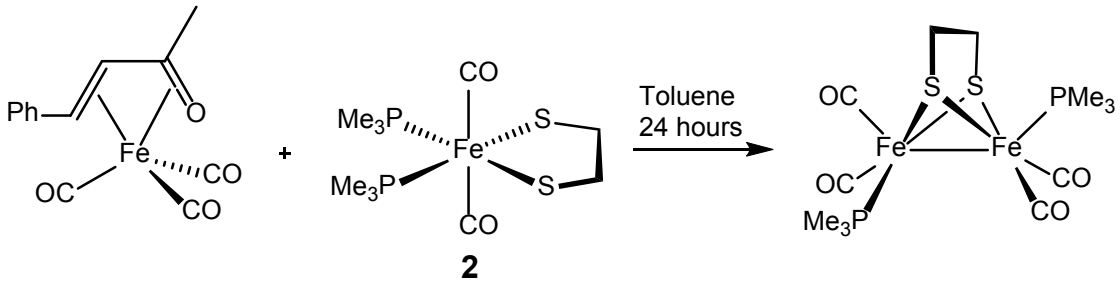

The comproportionation reaction was applied to the synthesis of unsymmetrically disubstituted subferrous diiron dithiolates containing chelating diphosphine ligands. Volkers showed that treatment of **1a** with (bda)$Fe(CO)_3$ forms the known complex $Fe_2(edt)(CO)_4(dppv)$ (Scheme 5.8).[27,30] The reaction occurred over the course of several hours at room temperature, producing a 100% spectroscopic yield by IR spectroscopy (83% isolated yield), which is comparable to the previously reported synthesis from $Fe_2(edt)(CO)_6$ and dppv (Scheme 5.8).[30]

Scheme 5.8. Synthetic pathways to $Fe_2(edt)(CO)_4(dppv)$.

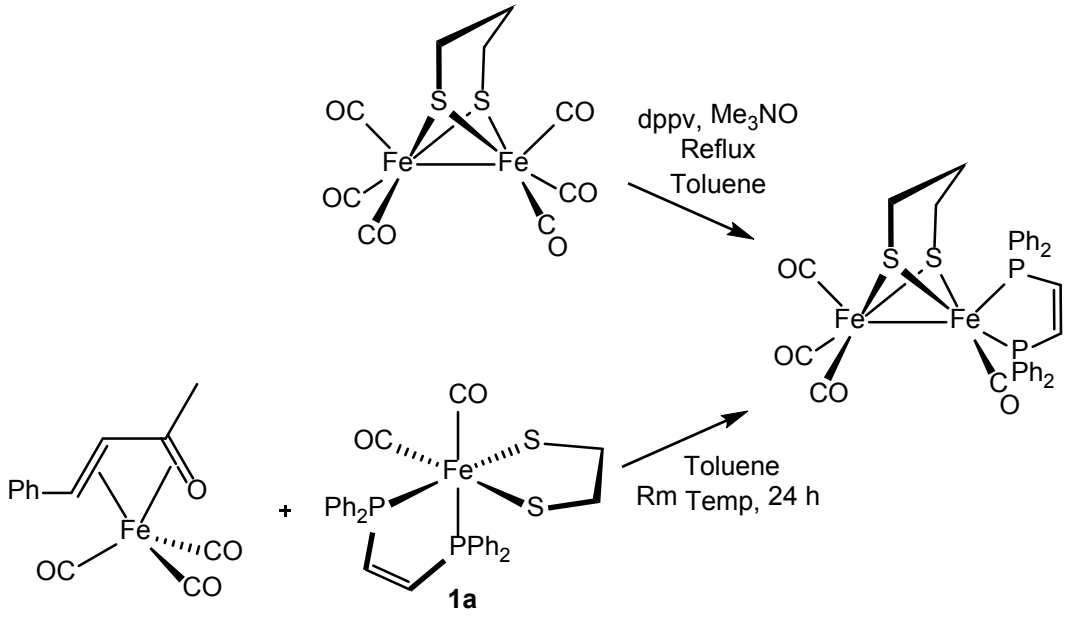

Using the comproportionation method, we also prepared the unsymmetrically substituted complex $Fe_2(pdt)(CO)_4(\kappa\text{-dppe})$, **3**. This species had previously only been obtainable in low yields under very specific conditions via substitution of $Fe_2(pdt)(CO)_6$.[31,32] The low yields reflects complications arising from the flexibility of the dppe ligand, which allows other intra- and intermolecular processes (Scheme 5.9).[31,32] Using the comproportionation method, the unsymmetrically substituted complex **3** can be isolated in yields up to 50%. As has been reported previously, two isomers of **3** form; that with both phosphorus centers in basal positions (dibas) and that with one phosphorus center in an apical position and one in a basal position (ap-bas), present in a ratio of 1:6.[31]

Scheme 5.9. Products of reaction of $Fe_2(pdt)(CO)_6$ with dppe under various conditions (left) and synthesis of $Fe_2(pdt)(CO)_4(\kappa$-dppe) (right).

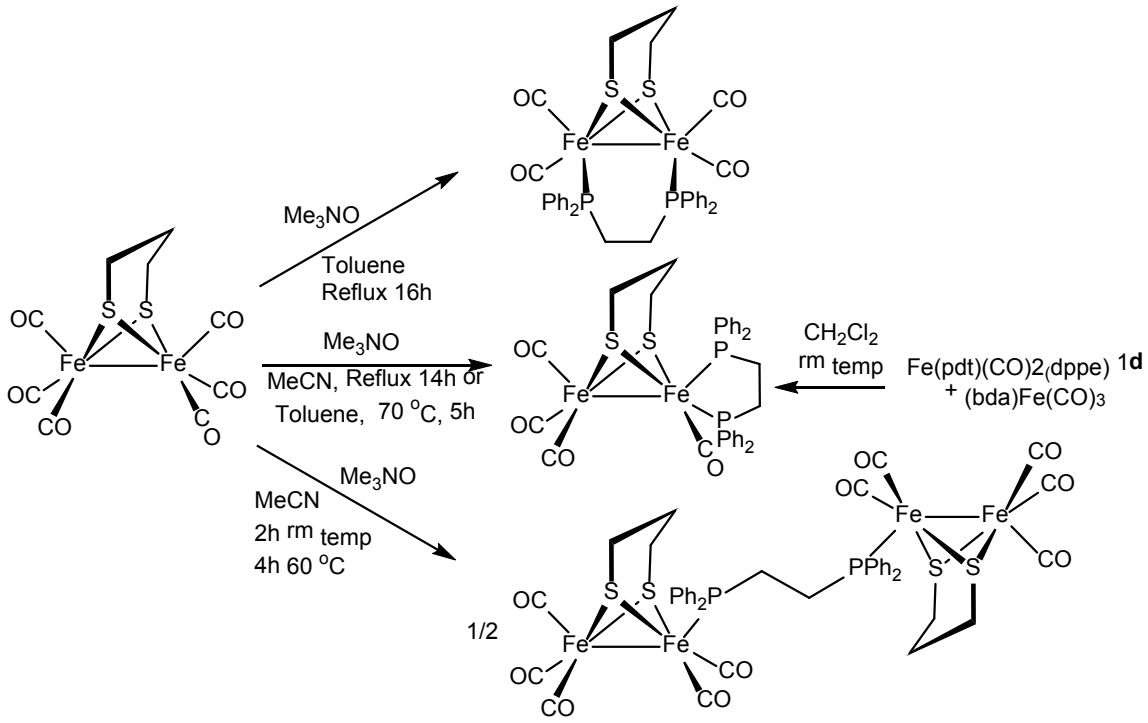

The progress of the reaction may be monitored by both ^{31}P NMR and IR spectroscopy, as shown in Figures 5.4 and 5.5. As judged from the IR spectrum, **1d** and $(bda)Fe(CO)_3$ are converted cleanly into **3**, in ~15 hours. Weak bands are present at 1952 and 1923 cm^{-1}, which are tentatively assigned to $Fe_2(pdt)(\mu$-dppe$)(CO)_4$ (ν_{CO} = 1990, 1953, 1920, and 1902 cm^{-1}).[31] However, when the progress of the reaction is monitored by ^{31}P NMR spectroscopy, the main side product has a signal at δ 96, which does not correspond to that reported for $Fe_2(pdt)(\mu$-dppe$)(CO)_4$ (δ 60) (A weak signal is present at δ 65 that could be due to a small amount of this species). The chemical shift of the main impurity matches that reported for $Fe(CO)_3(dppe)$[33], which could form by reaction of $(bda)Fe(CO)_3$ with dppe.

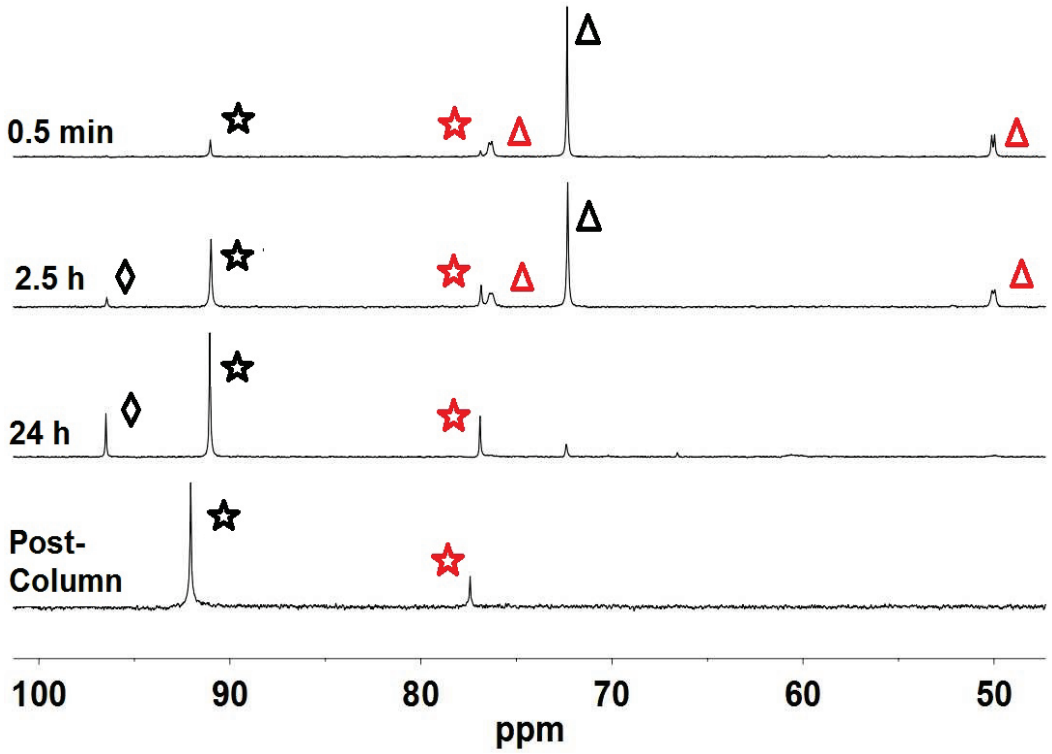

Figure 5.4. ^{31}P NMR spectra of the reaction of (bda)Fe(CO)$_3$ + Fe(pdt)(CO)$_2$(dppe) (1d) (black triangle =sym isomer, red triangle= unsym isomer) in toluene-d$_8$ at 20 °C, forming 3 (black star= ap-bas isomer, red star= dibas isomer, diamond= Fe(CO)$_3$(dppe)).

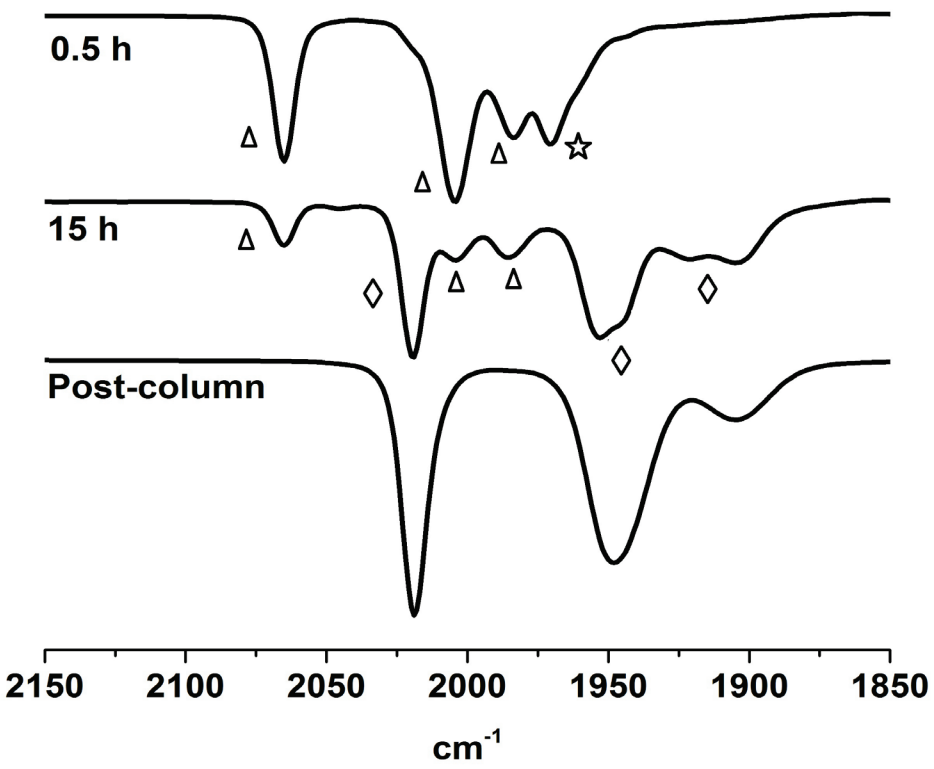

Figure 5.5. IR spectra of (bda)Fe(CO)$_3$ (triangle) + Fe(pdt)(CO)$_2$(dppe) (1d) (star), forming 3 (diamond).

5.4 Synthesis of $Mn^{I}Fe^{II}$ Complexes.

To establish the usefulness of the new building block approach, we examined the reactivity of the ferrous carbonyl thiolates with a source of manganese tricarbonyl. The salt [Mn(CO)$_3$(pdt)Fe(CO)$_2$(dppe)]BF$_4$ ([**4**]BF$_4$) forms by reaction of [(acenaphthene)Mn(CO)$_3$]BF$_4$ with a CH_2Cl_2 solution of **1d** at room temperature (Scheme 5.8). The IR spectrum of [**4**]BF$_4$ is characterized by ν_{CO} = 2053(w), 2027(s), 1992(s), 1974(s), 1905(br) cm^{-1}. (Figure 5.6) When the reaction progress is monitored by ^{31}P NMR spectroscopy, the spectrum initially shows doublets at δ48 and 76, corresponding to the isomer in which the diphosphine spans the apical and basal positions, as well as a singlet at δ58, corresponding to the isomer with dibasal phosphines (Scheme 5.10). Over the course of 24 h, the unsymmetrical isomer converts to the symmetrical isomer with dibasal phosphines, as indicated by the ^{31}P NMR spectrum (Figure 5.7). The presence of a single isomer is also verified by the ^{1}H NMR spectrum (Figure 5.8).

Scheme 5.10. Reaction of [(acenapthene)Mn(CO)$_3$]BF$_4$ with Fe(pdt)(CO)$_2$(dppe) (1d).

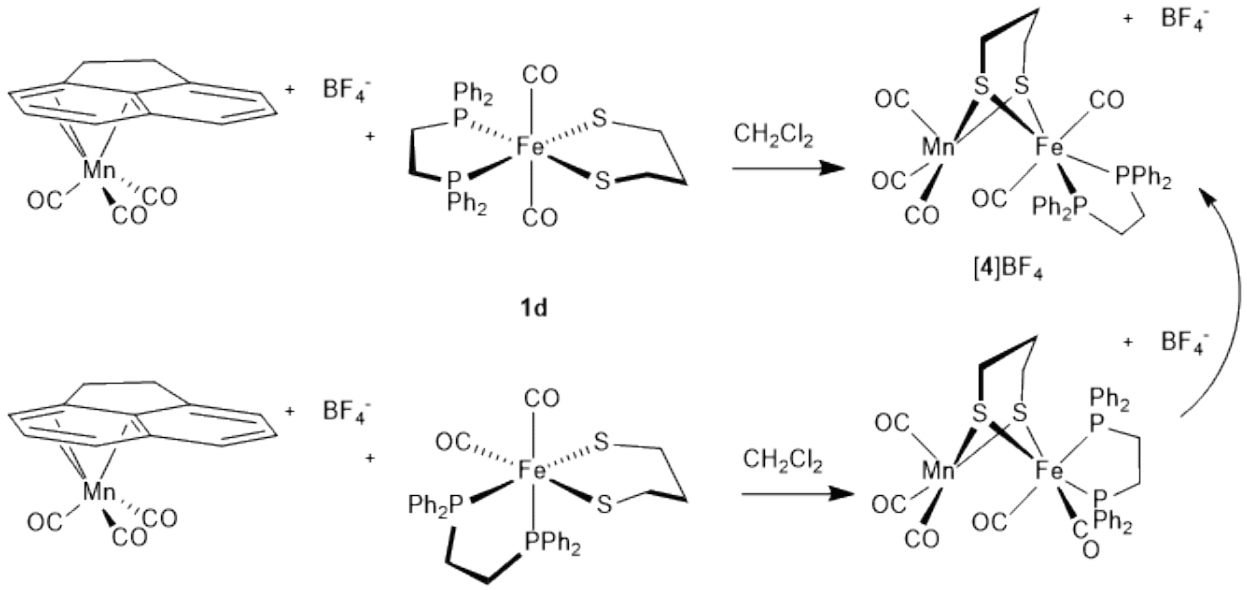

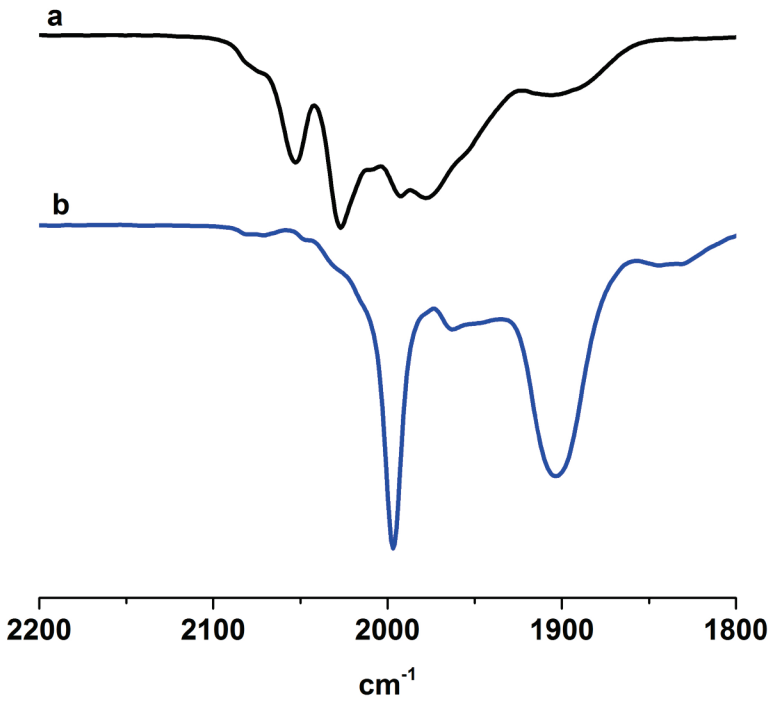

Figure 5.6. IR spectra of CH_2Cl_2 solutions of (a) [Mn(CO)$_3$(pdt)Fe(CO)$_2$(dppe)]BF$_4$ ([4]BF$_4$) and (b) Mn(CO)$_3$(pdt)Fe(CO)(dppe) (4).

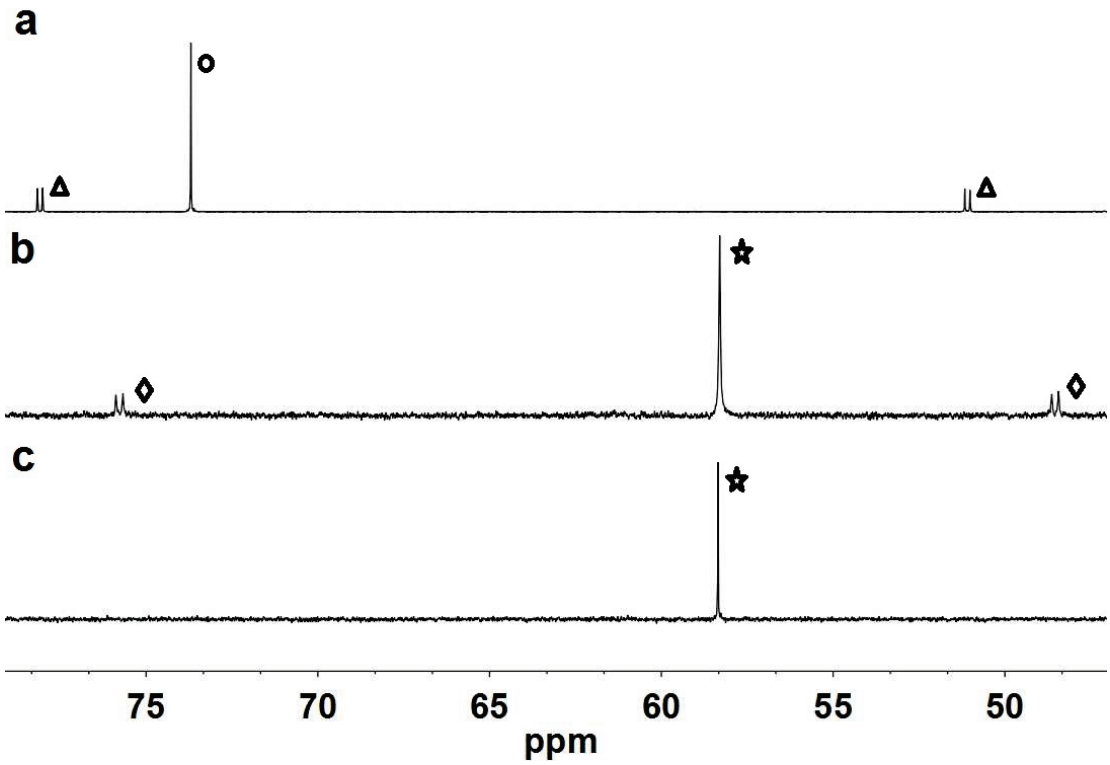

Figure 5.7. ^{31}P NMR spectra of a CD_2Cl_2 solution of (a) Fe(pdt)$(CO)_2$(dppe), 1d, (triangle = unsym isomer, circle = sym isomer) (b) Fe(pdt)$(CO)_2$(dppe) (1d) + [(acenaphthene)Mn$(CO)_3$]BF_4 after 30 minutes (diamond = unsym isomer, star = sym isomer), and (c) Fe(pdt)$(CO)_2$(dppe) + [(acenaphthene)Mn$(CO)_3$]BF_4 ($4BF_4$) after 12 h.

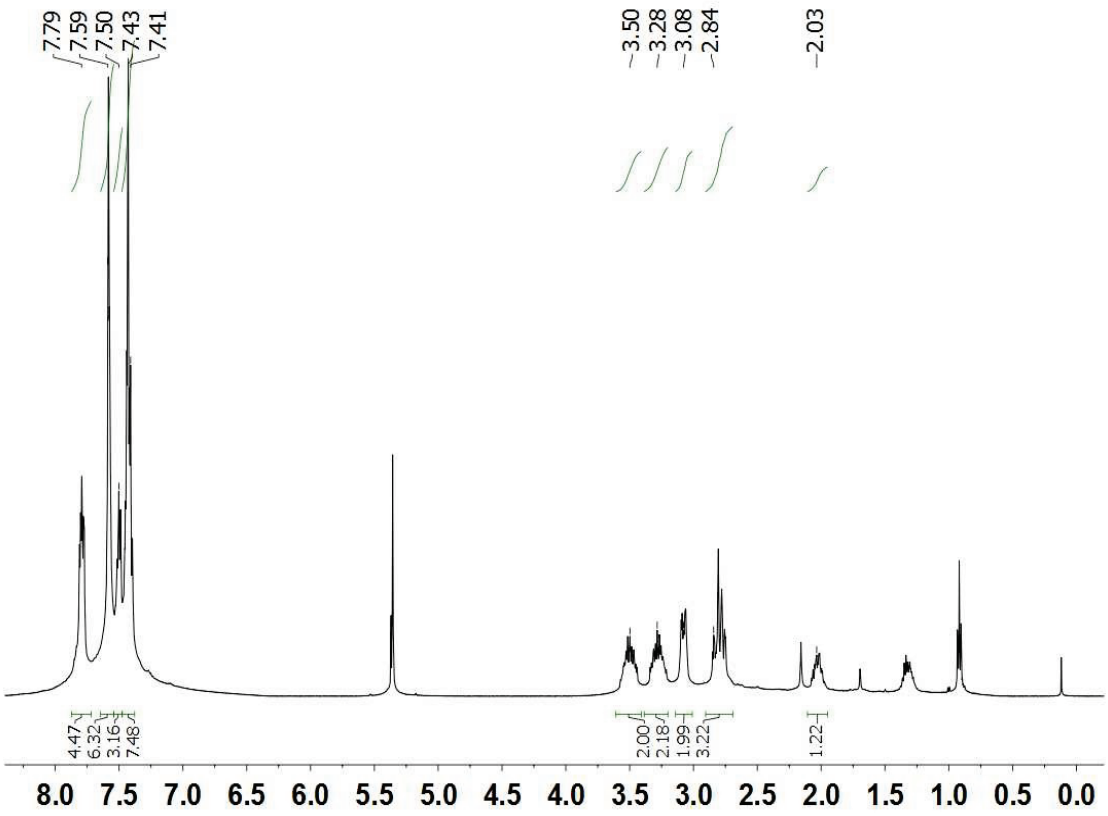

Figure 5.8. ^{1}H NMR spectrum of [4]BF_4 in CD_2Cl_2.

The syntheses of analogous complexes containing variations in the dithiolate and diphosphine ligands were also examined. The reaction of [(acenaphthene)$Mn(CO)_3$]BF_4 with $Fe(pdt)(CO)_2$(dppbz), **1e**, proceeded in a manner similar to the analogous reaction of **1d**, discussed above. Again, a mixture of isomers forms initially and eventually converts to a single isomer, with dibasal phosphorus centers (Figure 5.9). Although the MnFe complex forms, it could not be purified; two signals, at δ 73.1 and 70.2, were present in the ^{31}P NMR spectrum even after multiple recrystallizations (~15% of sample). However, ESI-mass spectrometry verifies that the major species present is $[Mn(CO)_3(pdt)Fe(CO)_2(dppbz)]^+$, with m/z= 802.8) (Figure 5.10).

The reaction of [(acenaphthene)$Mn(CO)_3$]BF_4 with $Fe_2(Me_2pdt)(CO)_2$(dppe), **1f**, does not proceed cleanly, and based on comparison with the ^{31}P NMR spectrum of [**4**]BF_4, only ~10% of the products is the desired MnFe cation.

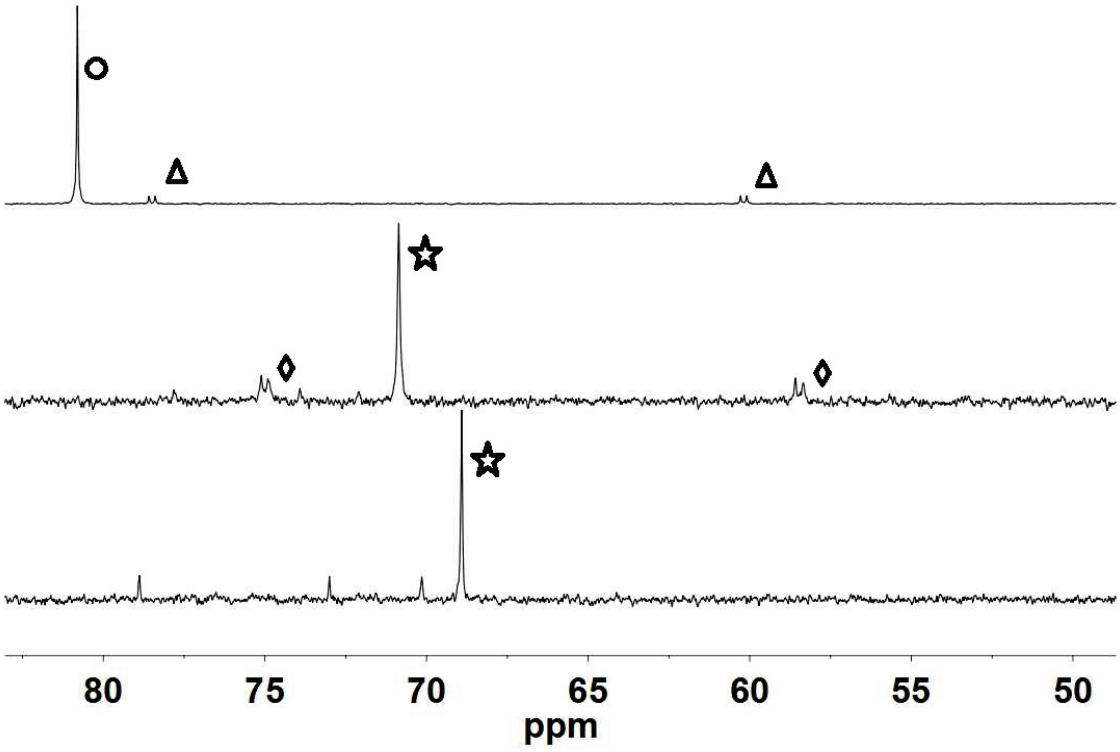

Figure 5.9. ^{31}P NMR spectra of a CD_2Cl_2 solution of (a) Fe(pdt)$(CO)_2$(dppbz), 1e, (triangle = unsym isomer, circle = sym isomer) (b) Fe(pdt)$(CO)_2$(dppbz) (1e) + [(acenaphthene)Mn$(CO)_3$]BF_4 after 3 h (diamond = unsym isomer, star = sym isomer), and (c) Fe(pdt)$(CO)_2$(dppbz) + [(acenaphthene)Mn$(CO)_3$]BF_4 after 12 h and recrystallization from CH_2Cl_2/hexanes (Signals at δ 73.1 and 70.2 ppm are unknown impurities).

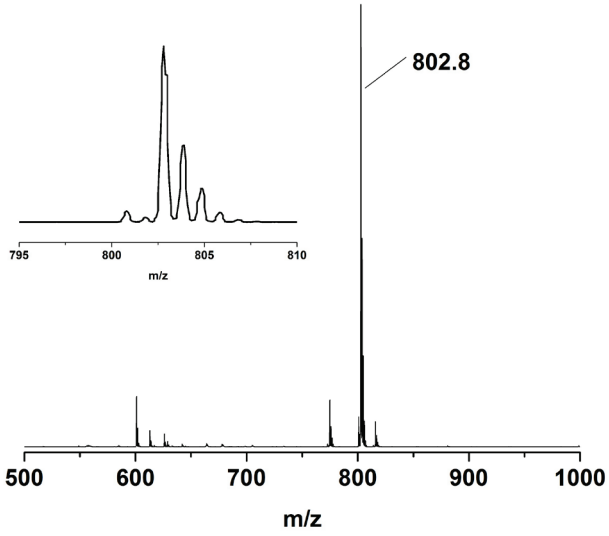

Figure 5.10. ESI-MS of $[Mn(CO)_3(pdt)Fe(CO)_2(dppbz)]^+$ in CH_2Cl_2 (Inset: Mass range for MnFe complex).

Reaction of [(acenaphthene)Mn(CO)$_3$]BF$_4$ with Fe(edt)(CO)$_2$(dppe), **1b**, affords a mixture of isomers, which over the course of weeks does not convert to a single isomer (Scheme 5.11, Figure 5.8). As with the formation of [**6**]BF$_4$, two isomers form initially, a dibasal isomer (**A**) and an apical-basal isomer (**B**). Over time, isomer **B** converts to a mixture of **A**, similar to [**6**]BF$_4$, and a second unsymmetrical isomer **C**, with a structure in which one of the phosphorus centers is located between the Mn and Fe centers. Over the course of weeks, the ratio of **A**:**C**, ~1:2, does not change (Figure 5.11).

Scheme 5.11. Reaction of [(acenapthene)Mn(CO)$_3$]BF$_4$ with Fe(edt)(CO)$_2$(dppe) (1b).

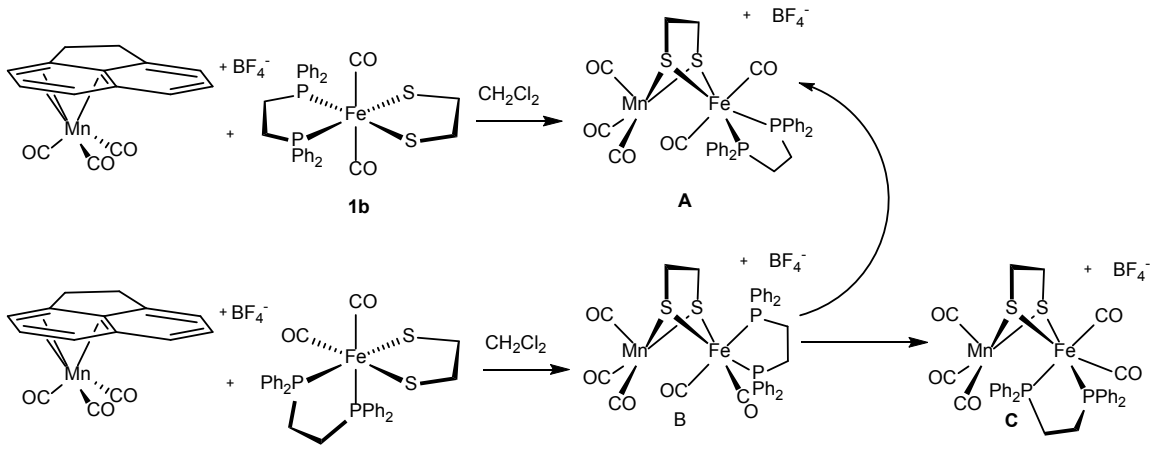

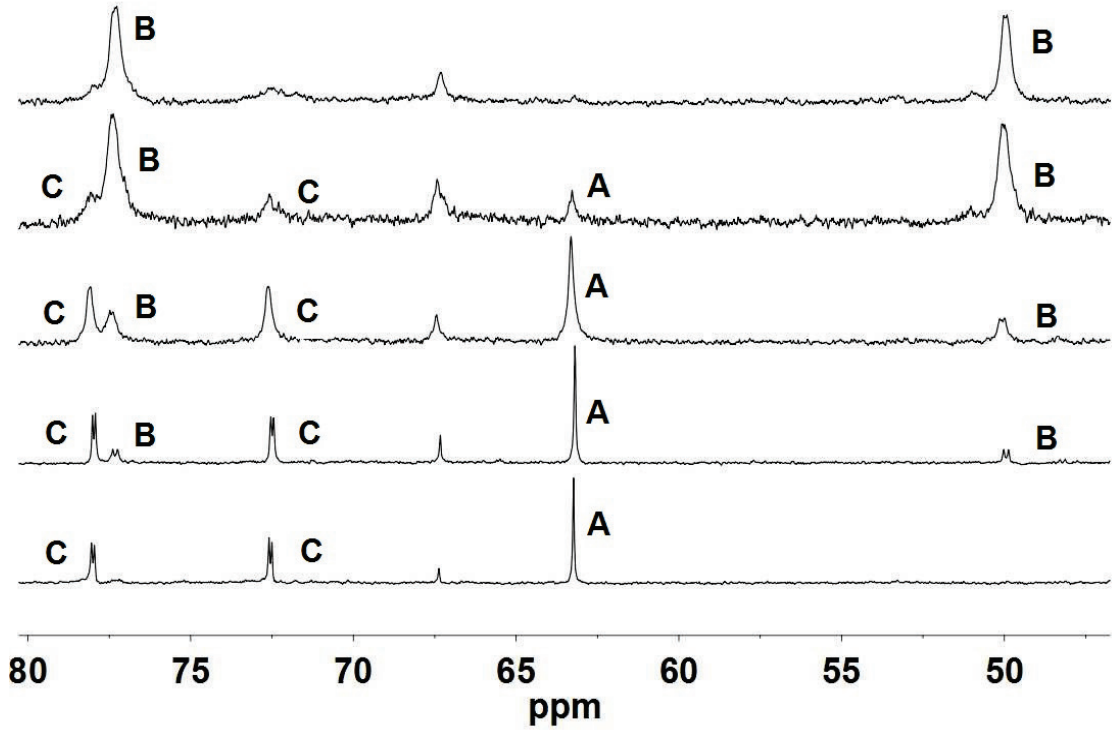

Figure 5.11 Reaction of a 1:1 mixture of [(acenapthene)Mn(CO)$_3$]BF$_4$ with Fe(edt)(CO)$_2$(dppe) (1b) in CD_2Cl_2 at 20 °C, monitored by ^{31}P NMR spectroscopy. (From top to bottom, time= 15 min, 3.5 h, 30 h, 48 h, 3 weeks).

5.5 Redox Properties of [Mn(CO)$_3$(pdt)Fe(CO)$_2$(dppe)]BF$_4$.

The cyclic voltammogram of [**4**]BF$_4$ consists of an irreversible reduction event at -0.98 V vs $Fc^{+/0}$, followed by a reversible reduction at -1.27 V. On the reverse scan, an irreversible oxidation event occurs at -0.26 V (Figure 5.12). When multiple segments were collected, the species responsible for the irreversible event disappeared, whereas the current for the reversible event remained relatively unchanged (Figure 5.13). We propose that the first one-electron reduction labilizes CO, forming (CO)$_3$Mn(pdt)Fe(CO)(dppe), **5**, which is then reversibly reduced to [Mn(CO)$_3$(pdt)Fe(CO)(dppe)]$^-$, [**5**]$^-$ (Scheme 5.12).

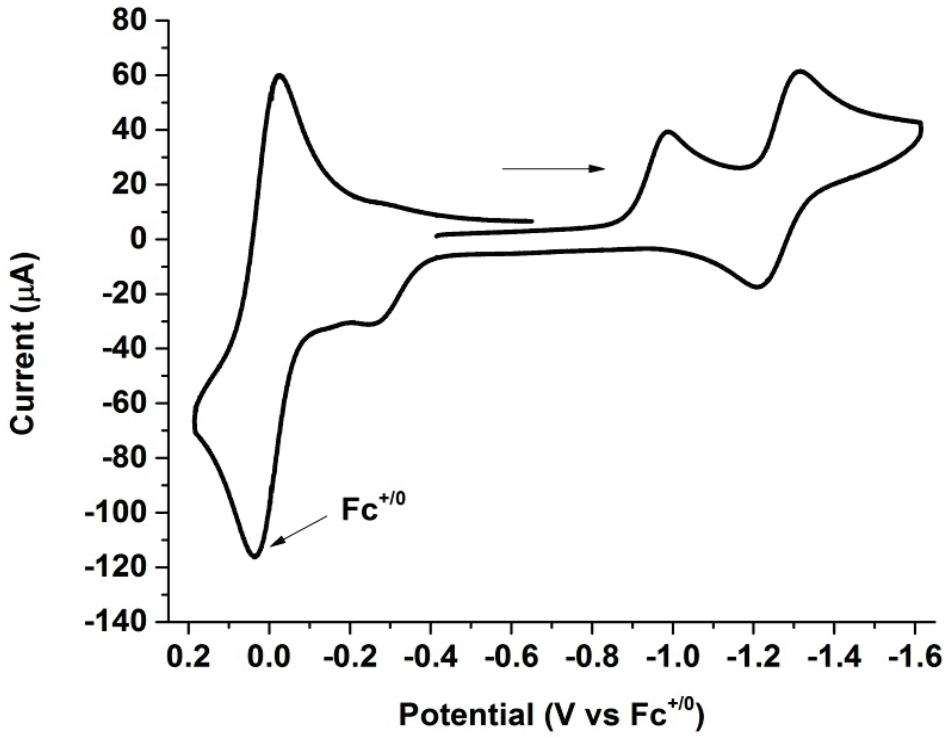

Figure 5.12. Cyclic volatammogram of $[Mn(CO)_3(pdt)Fe(CO)_2(dppe)]BF_4$ ($[4]BF_4$) in CH_2Cl_2. (Conditions: 1.0 mM $1BF_4$, 0.1 M $[Bu_4N]PF_6$, glassy carbon working electrode, Pt counter electrode, Ag pseudoreference electrode, Scan rate= 0.5 V/s).

Scheme 5.12. Proposed reactions induced by reduction of $[4]BF_4$.

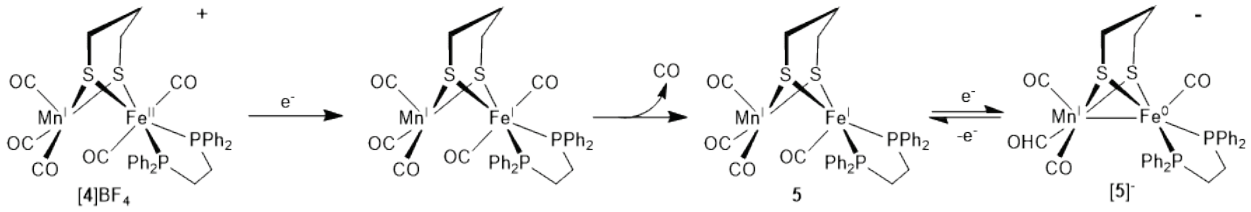

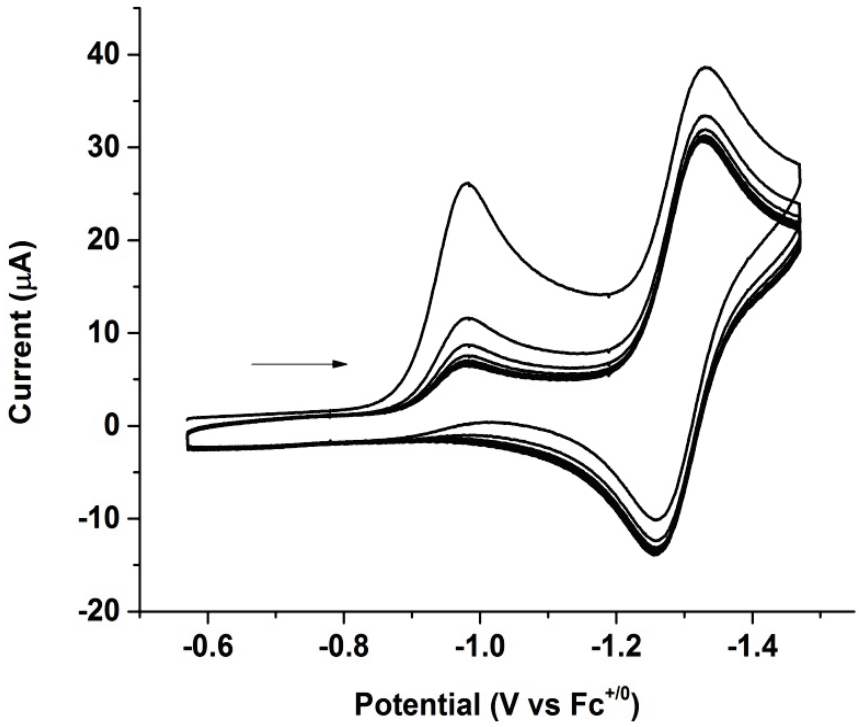

Figure 5.13. Cyclic voltammogram of $[Mn(CO)_3(pdt)Fe(CO)_2(dppe)]BF_4$ ($[4]BF_4$) in CH_2Cl_2, 10 segments scanned, with no intermediate stirring between segments. (Conditions: 1.0 mM $[1]BF_4$, 0.1 M $[Bu_4N]PF_6$, glassy carbon working electrode, Pt counter electrode, Ag pseudoreference electrode, Scan rate= 1.0 V/s).

We investigated the reductive decarbonylation of [**4**]BF_4 to **5** on a preparative scale. Treatment of [**4**]BF_4 with one equiv of Cp_2Co resulted in an immediate color change from brown to red. IR measurements show that reduction was accompanied by a shift in ν_{CO} to lower energy (Figure 5.6b). However, **5** is not particularly stable, and even at reduced temperatures, the IR spectrum indicates decomposition.

Compound **5** was examined by EPR spectroscopy. As can be seen in Figure 5.14, the frozen spectrum (3:1 toluene:CH_2Cl_2) consists of a high field triplet, likely due to coupling with phosphorus, and six lines corresponding to hydperfine coupling with Mn. When the solution is warmed to 0 °C, the Mn coupling disappears, and upon recooling the sample, this Mn coupling is significantly diminished. We propose that two species are present in the frozen sample; **5**, in which the unpaired spin is localized on Fe, accounting for coupling to phosphorus, and the pentacarbonyl, **4**, in which the unpaired spin is delocalized between the two metal centers. When the sample is warmed, **4** decarbonylates, resulting only in **5**. Due to the instability of **5**, other

species are present, and so the data could not be simulated, unless four separate components were ultilized.

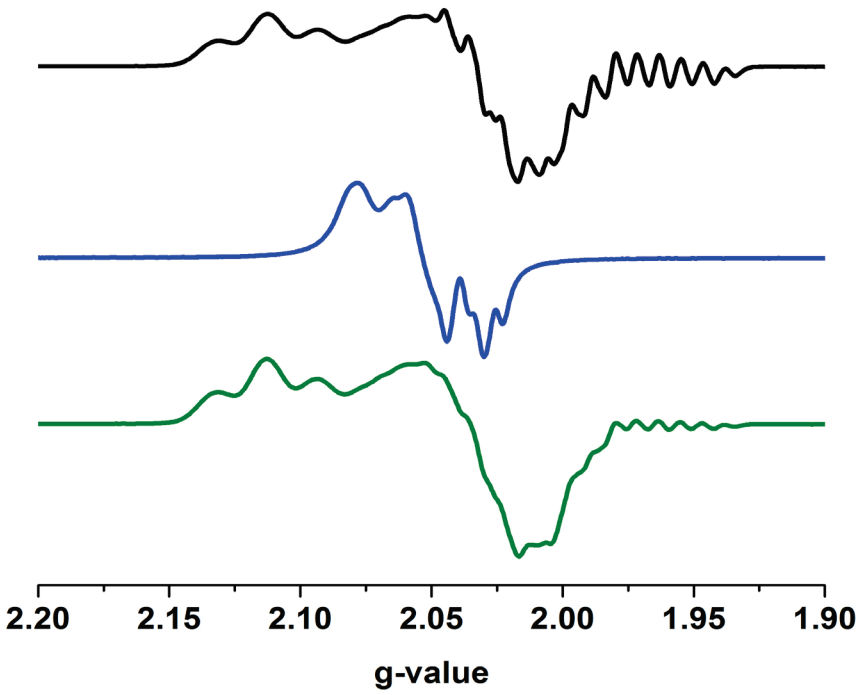

Figure 5.14. X-band EPR spectra of a mixture of [4]BF_4 and Cp_2Co in 3:1 mixture of toluene and CH_2Cl_2. Frozen sample at 110 K (black, top); thawed sample at 273 K (blue, middle); refrozen sample at 110 K (green, bottom).

5.6 Synthesis and Characterization of an $Mn^{I}Fe^{II}$ Hydride.

Reaction of [**4**]BF_4 with $[Bu_4N]BH_4$ results in loss of a CO ligand and formation of the neutral hydride species, $(CO)_3Mn(pdt)(\mu\text{-}H)Fe(CO)(dppe)$, **6**. (Scheme 5.13) The ^1H NMR spectrum of **6** consists of a triplet at δ-12.3, the upfield shift being characteristic of metal hydrides and the triplet indicating coupling to two equivalent phosphorus centers (Figure 5.15). The ^{31}P NMR spectrum exhibits a singlet at δ 80.8, which confirms that the two phosphorus centers are equivalent, both occupying basal positions (Figure 5.16). The IR spectrum in CH_2Cl_2 exhibits ν_{CO} = 2002 (s), 1935 (br), and 1905 (br) cm^{-1} (Figure 5.17). In toluene, the broad band at 1905 cm^{-1} is split into two bands, with ν_{CO}= 1915 and 1905 cm^{-1}.

Scheme 5.13. Reaction of $[Mn(CO)_3(pdt)Fe(CO)_2(dppe)]BF_4$, [4]$BF_4$, with $[Bu_4N]BH_4$, to form $Mn(CO)_3(pdt)(\mu$-H)Fe(CO)(dppe), 6.

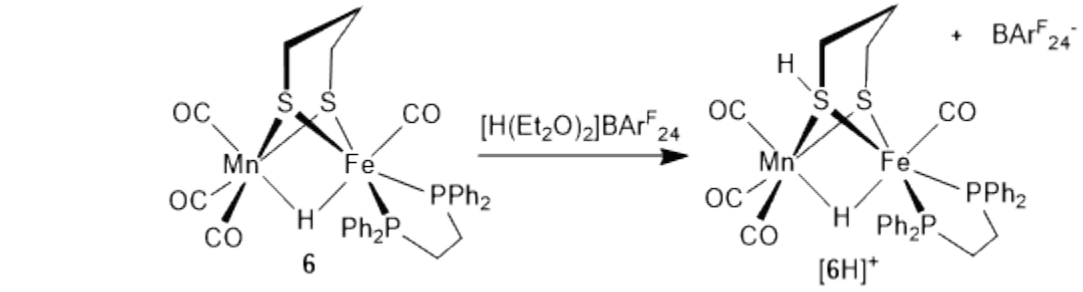

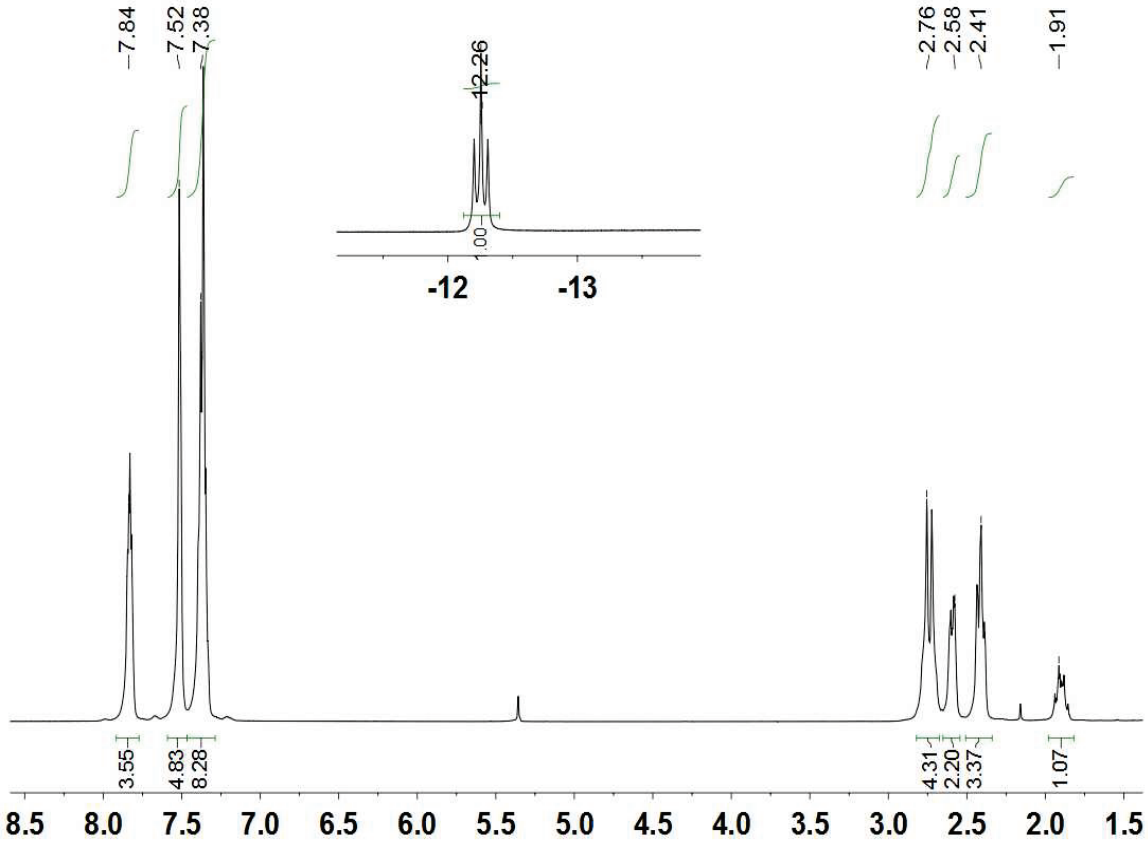

Figure 5.15. ^{1}H NMR spectrum of $Mn(CO)_3(pdt)(\mu$-H)Fe(CO)(dppe), 6, in CD_2Cl_2 (Inset: High field region of spectrum, showing signal for the hydride ligand).

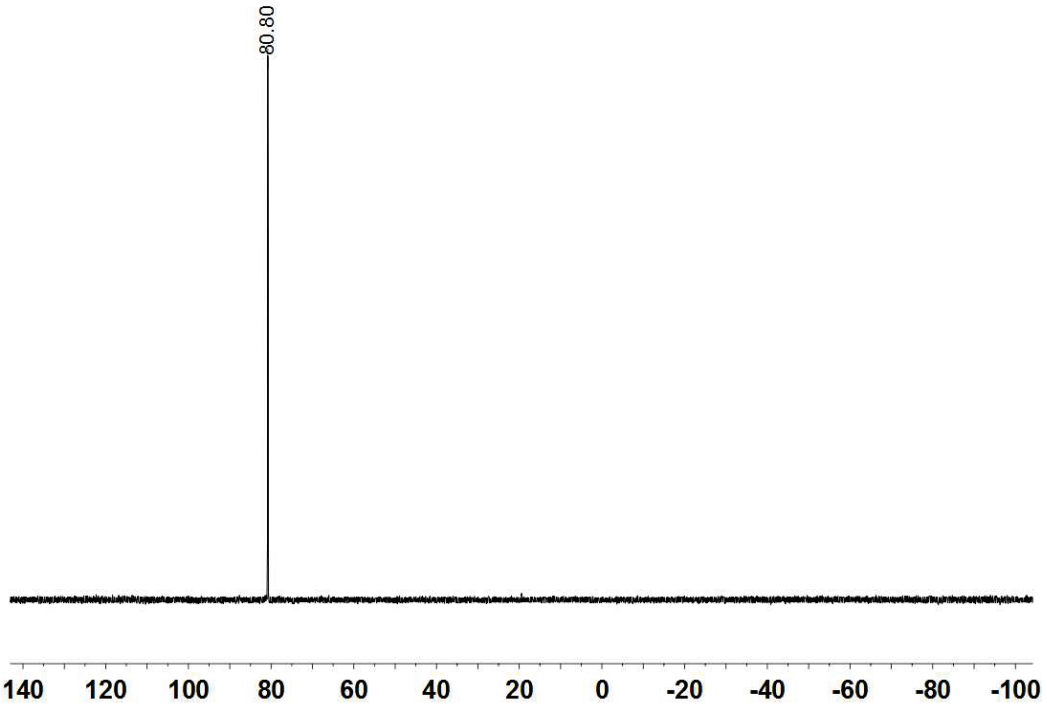

Figure 5.16. ^{31}**P NMR spectrum of Mn(CO)$_3$(pdt)(μ-H)Fe(CO)(dppe), 6, in CD$_2$Cl$_2$.**

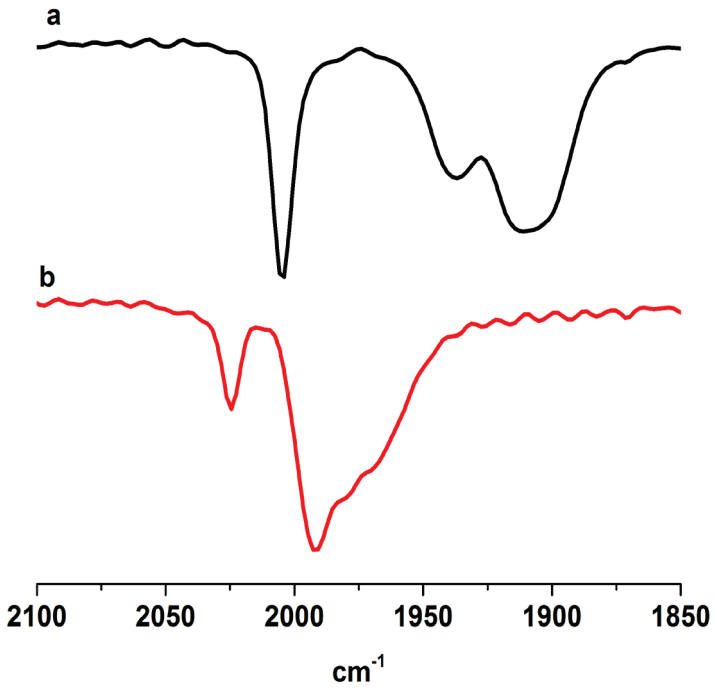

Figure 5.17. IR spectrum of (a) Mn(CO)$_3$(pdt)(μ-H)Fe(CO)(dppe), 6, and (b) 6 + [AcFc]BF$_4$ in CH$_2$Cl$_2$.

The structure of **6** was confirmed by X-ray crystallography, and the details are consistent with the NMR data (Figure 5.18). The phosphorus centers on the dppe ligand both occupy basal positions. The hydride ligand, which was located and refined, bridges the two metals, with a slightly shorter Fe-H distance (1.62(2) Å) than Mn-H distance (1.75(2) Å).

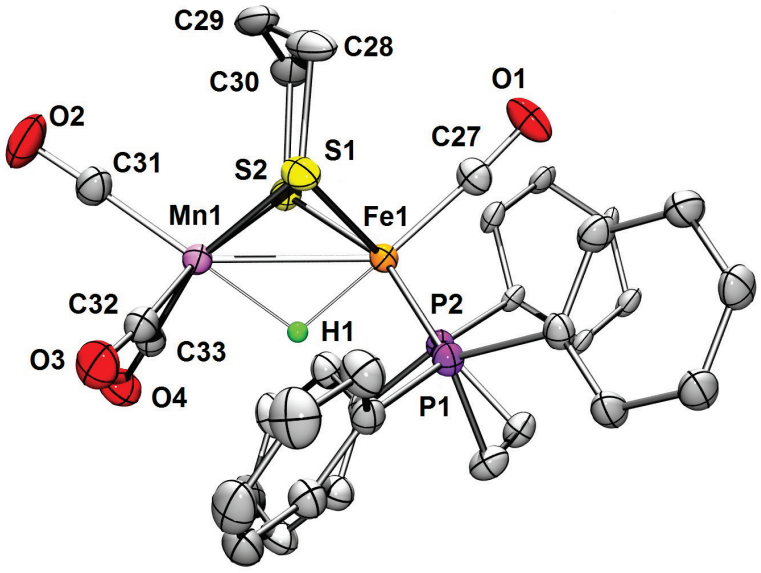

Figure 5.18. Structure of $Mn(CO)_3(pdt)(\mu\text{-}H)Fe(CO)(dppe)$, 6, with thermal ellipsoids drawn at the 50 % Selected distances (Å): Fe1-Mn1, 2.6433(4); Fe1-C27, 1.753(2); Fe1-P1, 2.2139(5); Fe1-P2, 2.2086(5); Fe1-S1, 2.2759(5); Fe1-S2, 2.2648(5); Fe1-H1, 1.62(2); Mn1-C31, 1.789(2); Mn1-C32, 1.813(2); Mn1-C33, 1.799(2); Mn1-S1, 2.3361(6); Mn1-S2, 2.3042(5); Mn1-H1, 1.75(2). (red = O, yellow = S, orange = Fe, pink= Mn, violet = P).

5.7 Redox Properties of the MnFe Hydride Complex, 6.

The cyclic voltammogram of **6** consists of a reversible oxidation event at 0.125 V vs $Fc^{+/0}$ (Figure 5.19). The linear dependence of i_p on (scan rate)$^{1/2}$ for the shows that the $\mathbf{6}^{+/0}$ couple is a diffusion controlled (Figure 5.20). Treatment of a CH_2Cl_2 solution of **6** with one equivalent of [acetylFc]BF_4 resulted in an immediate color change from orange to red brown, and the ν_{CO} bands shifted to higher energy by ~ 50 cm^{-1} (Figure 5.17).

The product of one electron oxidation of **6** was analyzed by EPR spectroscopy. The frozen spectrum shows a six line signal, indicative of coupling of the unpaired spin with the Mn center, suggesting that the unpaired spin is localized on Mn. However, the signal is very broad, and the spectrum could not be accurately simulated.

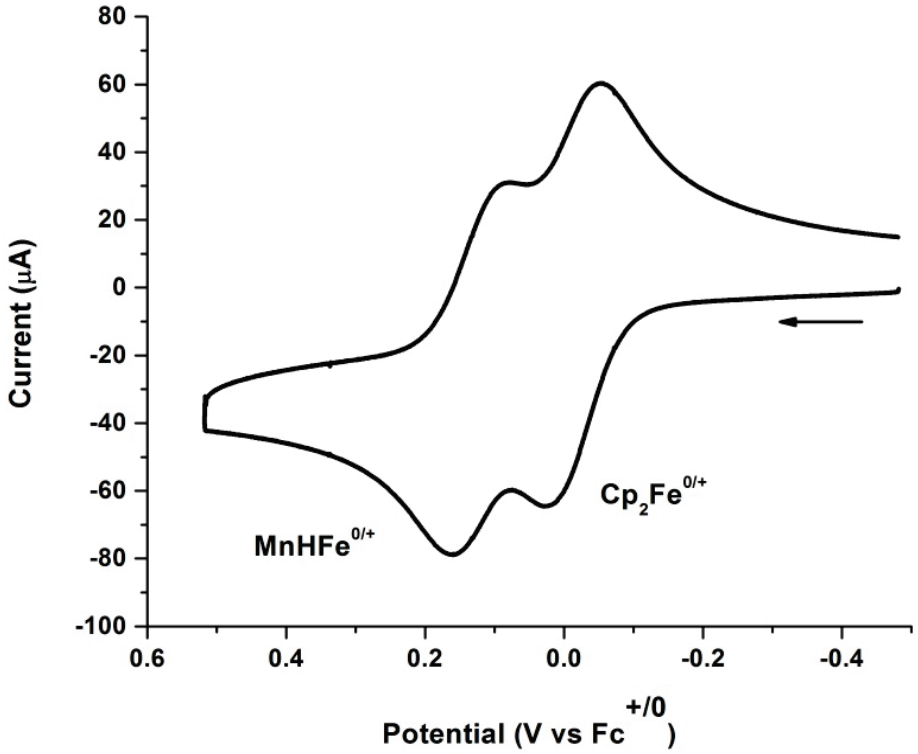

Figure 5.19. Cyclic voltammogram of $Mn(CO)_3(pdt)(\mu\text{-}H)Fe(CO)(dppe)$, 6 in CH_2Cl_2. (Conditions: 1.0 mM $Mn(CO)_3(pdt)(\mu\text{-}H)Fe(CO)(dppe)$, 0.1 M $[Bu_4N]PF_6$, glassy carbon working electrode, Pt counter electrode, Ag pseudo reference electrode, Scan rate= 0.5 V/s).

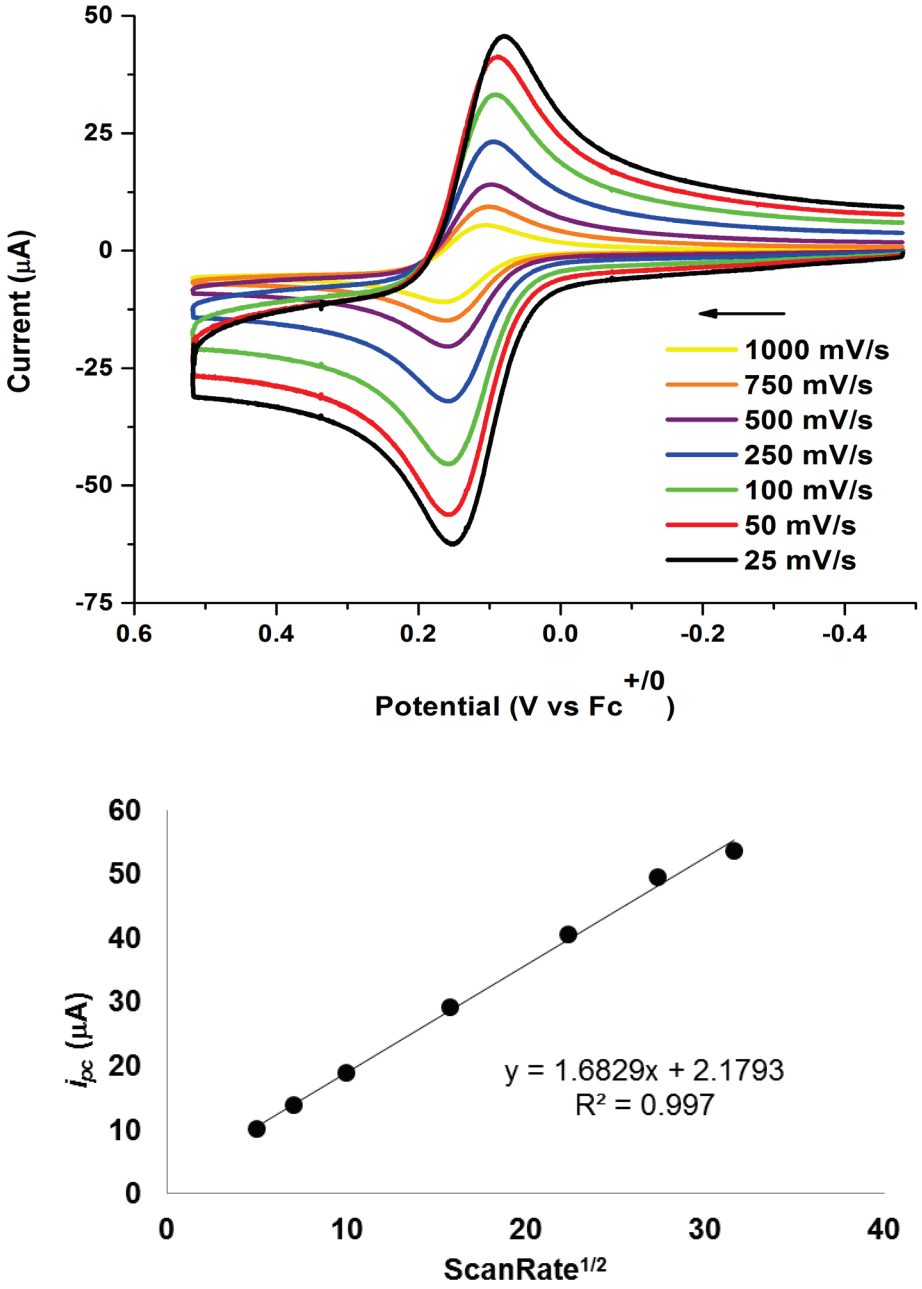

Figure 5.20. Cyclic voltammograms of 6 at various scan rates (top) and plot of i_{pc}/(scanrate)$^{1/2}$ (bottom) (Conditions: See Figure 5.16)

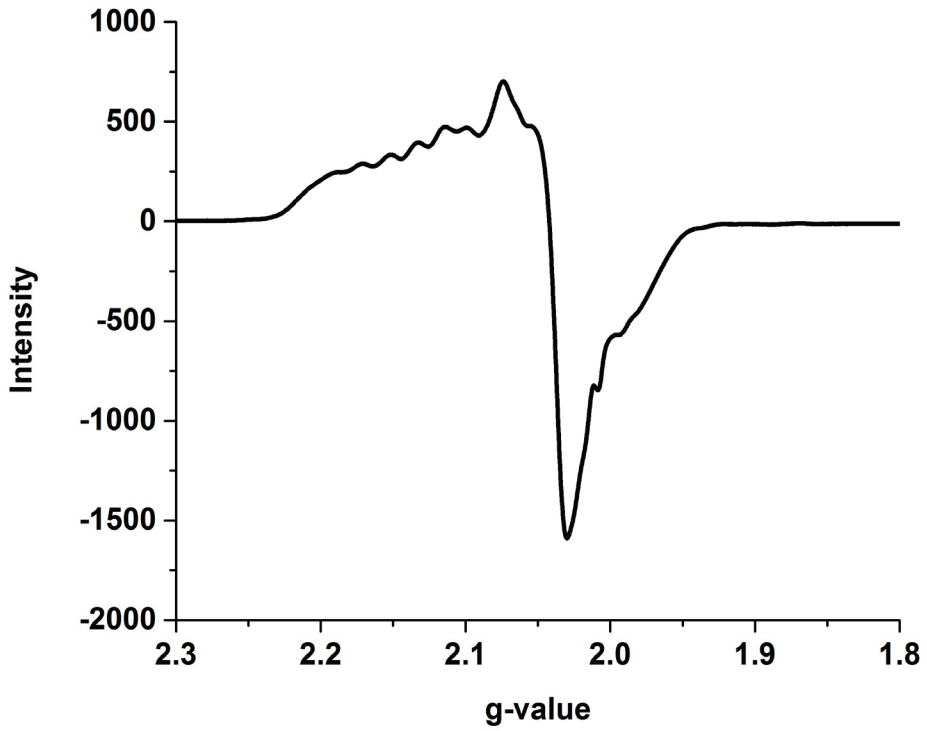

Figure 5.21. X-band EPR spectra of a frozen (110 K) mixture of 6 and [acetylFc]BAr^F_{24} in a 3:1 mixture of toluene and CH_2Cl_2.

5.8 Reactivity of the Mn^IFe^{II} Hydride with Acid.

The acid-base reactivity of **6** was investigated. Upon treatment of its solutions with the strong acid $[H(Et_2O)_2]BAr^F_{24}$ (BAr^F_{24}= tetrakis(3,5-bis(trifluoromethyl)phenyl)borate), the ν_{CO} bands shifted by 20-50 cm^{-1} to higher energy (Figure 5.18). The related complex, $HMn(CO)_3(dppe)$, has been shown to release H_2 upon treatment with strong acid (Scheme 5.14).[34] Therefore, we initially proposed that the reaction of **6** with acid would result in formation a dihydrogen complex or release of H_2.

Scheme 5.14. Reaction of $HMn(CO)_3(dppe)$ with HBF_4.

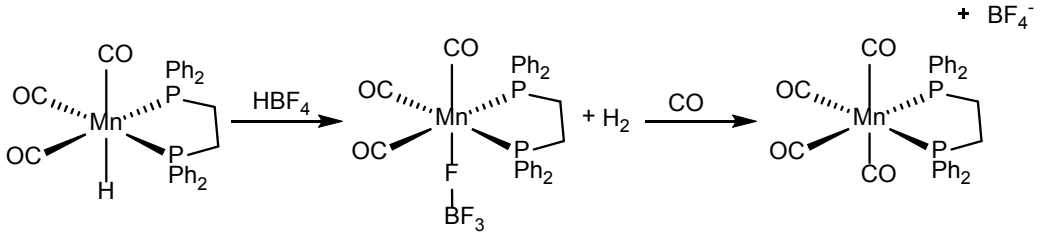

When the acidification was conducted under an atmosphere of CO, however, the IR spectrum of the reaction mixture did not indicate formation of [**4**]BAr^F_{24}. Treatment of the acidified reaction mixture with Et_3N gave back **6** (Figure 5.22). From these results, we tentatively conclude that **6** undergoes protonation at a sulfur of the dithiolate (Scheme 5.15). However, as judged from the IR spectrum, one equivalent of acid does not result in complete conversion to the protonated form. Similar S-protonation has been reported for very electron rich diiron complexes of the type Fe_2(dithiolate)$(CO)_2(PMe_3)_4$,[35] $Fe_2[(SCH_2)_2SiMe_2](CO)_6$,[36] $Fe_2[(SCH_2)_2N(C_6H_4$-*p*-$NO_2](CO)_4(PMe_3)_2$,[37] and $Fe_2[S_2C_6H_2Cl_2](CO)_4$(dppp).[38]

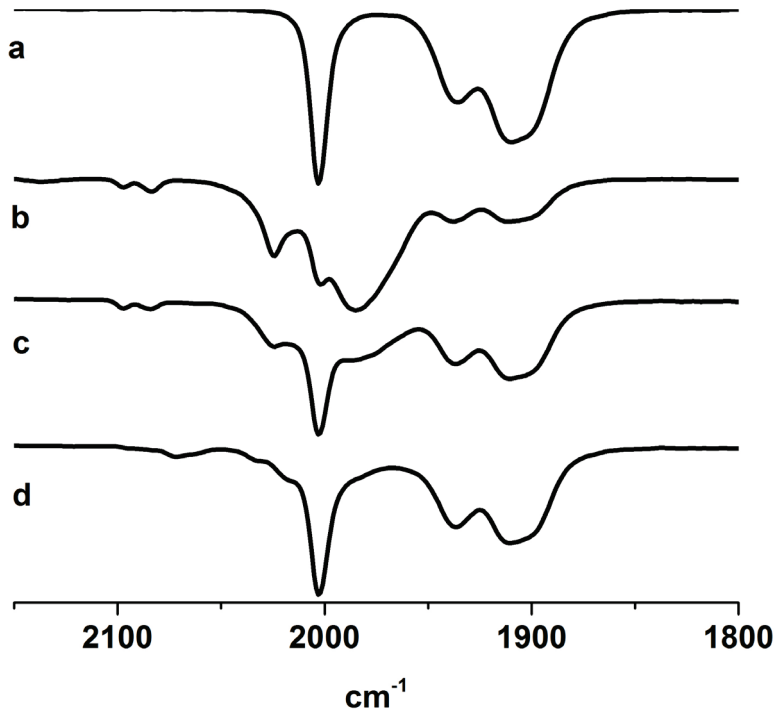

Figure 5.22. IR spectra in CH_2Cl_2 of (a) $Mn(CO)_3$(pdt)(μ-H)Fe(CO)(dppe), 6, (b) after addition of 1 equiv of $HBAr^F_{24}\cdot(Et_2O)_2$, (c) after addition of ½ equiv Et_3N, and (d) after addition of 1 equiv of Et_3N.

Scheme 5.15. Reaction of 6 with $[H(Et_2O)_2]BAr^F{}_{24}$.

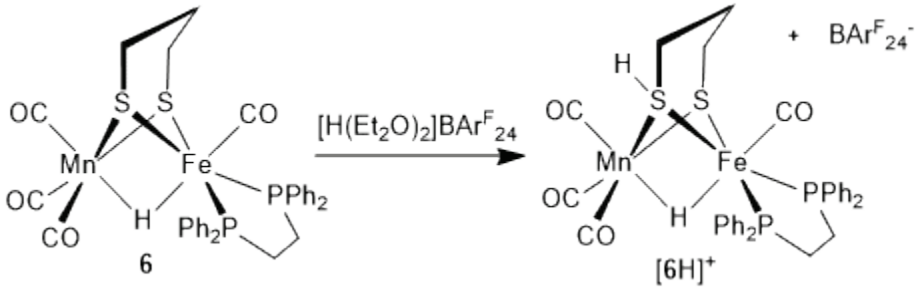

We further verified that protonation occurs at a sulfur atom on a thiolate ligand. The neutral complex, **6**, exhibits a triplet in the ^{1}H NMR spectrum at δ-12 and a singlet in the ^{31}P NMR spectrum at δ 80. Addition of $[H(Et_2O)_2]BAr^F{}_{24}$ to a solution of **6**, causes both of the signals to broaden, and the ^{1}H NMR signal shifts to ~ 0.5 ppm higher field (Figures 5.23, 5,24). The lack of a new hydride signal suggests that a new hydride complex has not formed. The broadening of the signals is likely due to intermolecular exchange of the proton. IR spectroscopy indicates that complete conversion to [**6**H]$^+$ does not occur upon treatment of **6** with one equivalent of acid. Therefore, exchange of a proton between **6** and [**6**H]$^+$ may occur, resulting in broadening of signals in ^{1}H and ^{31}P NMR spectra.

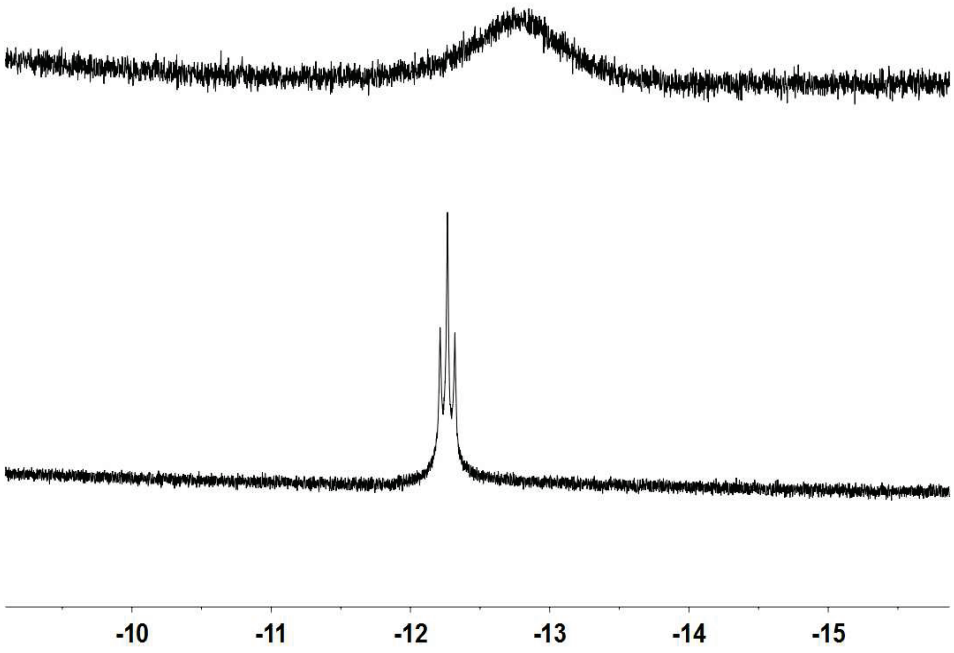

Figure 5.23 High field region of the ^{1}H NMR spectra of 6 (bottom) and a mixture of 8 and $[H(Et_2O)_2]BAr^F{}_{24}$ (top).

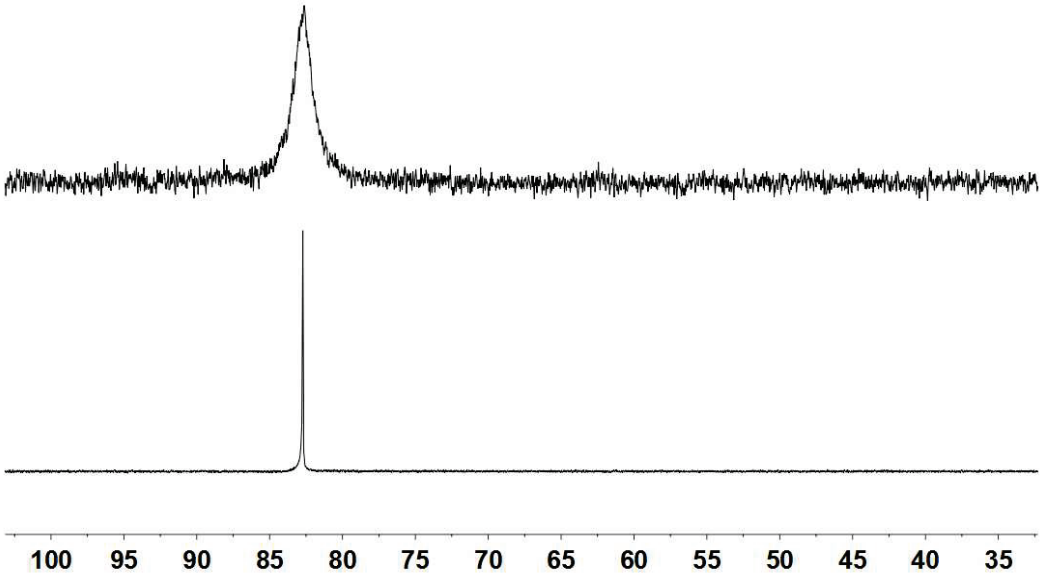

Figure 5.24 ^{31}H NMR spectra of 6 (bottom) and a mixture of 6 and $[H(Et_2O)_2]BAr^F{}_{24}$ (top).

We also investigated the electrocatatytic properties of [**6**H]$^+$, with the expectation that the protonated derivative would undergo reduction at mild potentials. Once the complex was reduced, the hydride ligand could couple with the proton on the thiolate, to ultimately form H_2. Addition of acid leads to the appearance of reductive current (-1.45 V vs $Fc^{+/0}$ for $HBF_4{\cdot}Et_2O$ and -1.95 V vs $Fc^{+/0}$ f or CF_3COOH). However, control experiments indicate that the current is due solely to reduction of protons directly on the glassy carbon working electrode, and is not due to catalysis by **[6**H]$^+$.

5.9 Conclusions

The diiron and manganese-iron complexes described herein are all synthesized from novel ferrous dicarbonyl dithiolato diphosphine complexes. The complexes, **1a-f**, form as a mixture of isomers, and this isomer ratio varies depending on the identity of the dithiolate ligand. The effect appears to be based on the steric bulk of the dithiolate ligand. Complexes containing the less bulky edt ligand exist primarily as the unsymmetrical isomer, in which all ligands are situated cis to each other. Complexes of the more bulky pdt ligand favor the symmetrical isomer, containing trans CO ligands. The CO ligands in analogous complexes of the type $FeX_2(CO)_2(chel)$ and $FeX_2(CO)_2(PR_3)$, where X=halide or thiolate and chel= diphosphine or diamine, are typically mutually cis, and in general, trans CO ligands in ferrous carbonyl complexes are rare.[26] In other words, the strong π-accepting CO ligands tend to be trans to the strong donor ligands (phosphines or amines).

The isomeric form of $FeCl_2(CO)_2(dppe)$ varies according to the identity of the solvent. In benzene, it exists as the cis-CO isomer, whereas in THF and acetone, it exists as the trans-CO isomer.[16] There are some other examples of ferrous complexes with trans CO ligands in the literature, which include Fe(octaethylporphyrin)$(CO)_2$[39], $[Fe(CN)_4(CO)_2]^{2-}$[40], $Fe(CO)_4XX'$ (X=I, X'=Br, Cl)[41], and $Fe(CO)_3I_2(PR_3)$ (R=Ph, Cy).[42] The pdt and Me_2pdt complexes, **1c-f**, are novel examples of trans-CO ferrous complexes, which exist primarily as symmetrical isomers. Unlike $FeCl_2(CO)_2(dppe)$, the ratio of symmetrical: unsymmetrical isomers is unaffected by solvent.

With these new ferrous dicarbonyl dithiolato diphosphine complexes in hand, we were able to devise new building block syntheses of phosphine substituted diiron complexes. These new routes are particularly appealing because they enable to partial labeling of the complexes with ^{57}Fe. The new synthesis of $Fe_2(pdt)(CO)_4(dppe)$, **3**, gives higher yields than previously

reported methods, and it avoids formation of side products in which the flexible dppe ligand bridges two Fe centers.[31,32]

We are able to extend this building block approach to the synthesis of dithiolato bridged iron manganese complexes. The cationic complex, $[Mn(CO)_3(pdt)Fe(CO)_2(dppe)]^+$ (**4**$^+$), forms readily by reaction of $[(acenaphthene)Mn(CO)_3]BF_4$ with $Fe(pdt)(CO)_2(dppe)$. The analogous dimanganese complexes $Mn_2(SMe)_2(\mu\text{-}CO)(CO)_4(PMe_3)_2$[43], $Mn_2(edt)(\mu\text{-}CO)(CO)_4(PMe_2Ph)_2$[44], and $Mn_2(SPh)_2(\mu\text{-}CO)(CO)_4(PR_3)_2$[45] have been reported previously. Based on comparison of electrochemical properties, the dimanganese complexes are significantly more electron rich than the MnFe cation, with the later undergoing two one electron oxidations at ~ 0.1-0.3 V vs $Fc^{+/0}$ [43], whereas the latter cannot be oxidized, but is reduced at ~-1 V vs $Fc^{+/0}$.

Upon reduction of [**4**]BF_4 by one electron, decarbonylation occurs to form complex **5**, which is proposed to be a Mn(I)Fe(I) species. This complex would consist of d^6d^7 metal centers, which is isoelectronic with the H_{ox} state of the [FeFe]-hydrogenase enzyme[46] (Scheme 5.16). Our group has previously synthesized models for H_{ox}[47], and IR spectroscopic data in Table 5.2 shows that the MnFe complex **5** is a good spectroscopic model.[48]

Scheme 5.16. H_{ox} state of [FeFe]-hydrogenase (left) and previous diiron models for H_{ox} (right, A & B).

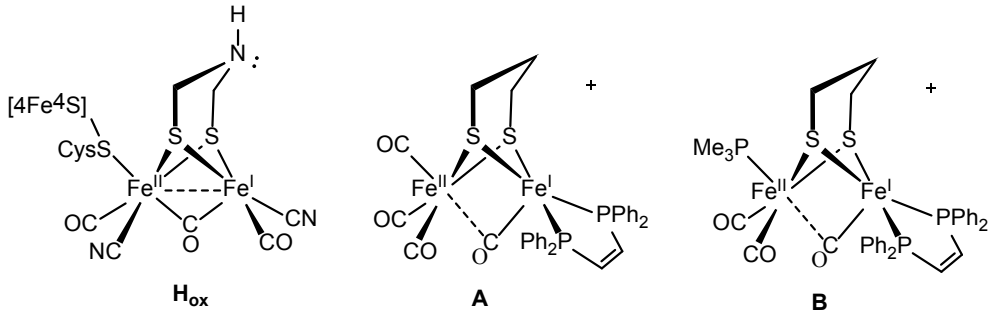

Table 5.2 IR spectroscopic data for H_{ox} and synthetic models.

Complex	ν_{CO} (cm^{-1})
$Mn(CO)_3(pdt)Fe(CO)(dppe)$, **5**	2002 (s), 1905 (s)
$Fe_2(pdt)(CO)_4(dppv)$, **A**	2076 (s), 2019 (s), 1943 (br)[47]
$Fe_2(pdt)(CO)_3(PMe_3)(dppv)$, **B**	2021 (s), 1970 (s), 1883 (br) [47]
H_{ox}	1965, 1940, 1802[48]

Whereas reactivity of the dimanganese complexes with hydrogenic ligands has not been explored, $\mathbf{4}^+$ was found to react with hydride sources to form the bridging hydride complex, **6**, which was characterized crystallographically. The hydride complex is sufficiently electron rich that it undergoes one electron oxidation at fairly mild potential (~0.1 V vs $Fc^{+/0}$). The hydride complex **6** reacts with strong acid via protonation of one of the sulfur centers of the thiolate ligand. This unexpected reactivity underscores the low hydridicity of the bridging hydride ligand. The terminal hydride ligand in the related complex $HMn(CO)_3(dppe)$ is significantly more hydridic as evidenced by the fact the upon reaction with acid, the hydride is protonated to form H_2.[34] Similar low hydridicity for bridging hydrides is also exhibited in related diiron bridging hydride complexes, in which the hydride is again unreactive towards acid.[49]

5.10 Experimental

Reactions were typically conducted using Schlenk techniques at room temperature. Most reagents were purchased from Aldrich and Strem. Solvents were HPLC-grade and dried by filtration through activated alumina or distilled under nitrogen over an appropriate drying agent. $HBF_4{\cdot}Et_2O$ (Sigma-Aldrich) was supplied as 51-57% HBF_4 in Et_2O (6.91 – 7.71 M). $[H(OEt_2)_2]BAr^F{}_4$ was prepared by literature methods.[50] $[Bu_4N]PF_6$ was purchased from GFS Chemicals and was recrystallized multiple times by extraction into acetone followed by precipitation by ethanol. ^1H NMR spectra (500 and 400 MHz) are referenced to residual solvent referenced to TMS. ^{31}P NMR spectra (202 or 161 MHz) were referenced to external 85% H_3PO_4. FT-IR spectra were recorded on a Perkin Elmer Spectrum 100 FT-IR spectrometer.

Fe(edt)(CO)$_2$(dppv), 1a. Under a CO atmosphere, a solution of 190 mg of $FeCl_2$ (1.50 mmol) in 50 mL of acetone was treated with a solution of 595 mg (1.50 mmol) of *cis*-1,2-bis(diphenylphosphino)ethylene (dppv) in 8 mL of THF. The solution changed from pale orange to dark red, signaling formation of $FeCl_2(dppv)(CO)_2$. Separately, $Na_2S_2C_2H_4$ was prepared by combining 143 μL (1.70 mmol) of $C_2H_4(SH)_2$ and 72 mg (3.0 mmol) of NaH in 10 mL of THF). After 1 h, the solution of the $Na_2S_2C_2H_4$ was added to the solution of $FeCl_2(dppv)(CO)_2$. After being allowed to react for 16 h, the mixture was filtered through Celite, and the solvent was evaporated from the filtrate. The residue was purified by flash silica gel column chromatography. After eluting yellow and green bands with CH_2Cl_2, the red band containing product was eluted with 5:1 CH_2Cl_2/Et_2O. Removal of solvent under vacuum afforded $Fe(edt)(CO)_2(dppv)$ as a red

solid. Yield: 455 mg (50%). ^{1}H NMR (CD_2Cl_2, 500 MHz): δ 8.14 - 7.32 (m, 20 H, C_6H_5), 2.53 (s, 2H, CH_2), 2.46 and 2.02 (d each, 1:1 H, CH_2), 2.18 and 0.21 (t each, 1:1 H, CH). ^{31}P NMR (CD_2Cl_2, 23 °C): δ 89.4 (d), 87.7 (s), 59.9 (d). IR (THF): ν_{CO} 2013 (s), 1978 (s), 1960 (s) cm^{-1}.

Fe(edt)(CO)$_2$(dppe), 1b. Under a CO atmosphere, a slurry of 0.950 g of $FeCl_2$ (7.50 mmol) in 120 mL of acetone was treated with a solution of 2.99 g (7.50 mmol) of 1,2-bis(diphenylphosphino)ethane (dppe) in 40 mL of THF. The solution changed from pale orange to green, then to dark red. After 1.0 h, $Na_2S_2C_2H_4$ (prepared from 700 μL (8.30 mmol) of $C_2H_4(SH)_2$ (edtH_2) and 0.359 g (15.0 mmol) of NaH in 15 mL of THF) was added. After 16 h, the solution was filtered through Celite™, and the red filtrate was concentrated in vacuum to dryness. The residue was separated by flash silica gel column chromatography, eluting yellow and green bands with CH_2Cl_2, then a red band with CH_2Cl_2/Et_2O, v/v = 5:1. Removal of solvent under vacuum affords Fe($S_2C_2H_4$)(CO)$_2$(dppe) as a red solid. Yield: 455 mg (50%). ^{1}H NMR (CD_2Cl_2, 500 MHz): δ 7.87 - 7.27 (m, C_6H_5), 2.62 (s, 4H, S CH_2, Sym), 2.50 (s, 4 H, PCH_2, Sym), 2.78 (d 2 H PCH_2, Unsym), 2.16 (d 2 H PCH_2, Unsym), 1.22 (s, 3H, SCH_2, Unsym) 0.34 (s, 1H, SCH_2, Unsym). ^{31}P NMR (CD_2Cl_2, 23 °C): δ 78.3 (d), 77.5 (s), 48.1 (d). IR (THF): ν_{CO} 2009 (s), 1973 (s), 1959 (s) cm^{-1}. Anal. Calcd: $C_{30}H_{28}FeO_2P_2S_2$ (found): C, 59.81 (59.78); H, 4.68 (5.0).

Fe(pdt)(CO)$_2$(dppv), 1c. Under a CO atmosphere, a solution of 190 mg of $FeCl_2$ (1.50 mmol) in 40 mL of acetone was treated with a solution of 595 mg (1.50 mmol) of *cis*-1,2-bis(diphenylphosphino)ethylene (dppv) in 8 mL of THF. The solution changed from pale green to a clear red after about 30 min. After 1.0 h, $Na_2S_2C_3H_6$ (prepared from 171 μL (1.70 mmol) of $C_3H_6(SH)_2$ and 72 mg (3.0 mmol) of NaH in 3 mL of THF) was added dropwise. After 16 h, the solution was filtered and the red filtrate was concentrated in vacuum to dryness. The residue was separated by flash silica gel column chromatography (CH_2Cl_2/Et_2O, v/v = 3:1) to afford Fe($S_2C_3H_6$)(CO)$_2$(dppv) as a dark red solid. Yield 719 mg (78%) ^{1}H NMR (CD_2Cl_2, 23 °C, 500 MHz): δ 7.96 - 7.33 (m, 20 H, C_6H_5), 2.45 (m, 6 H, S $CH_2CH_2CH_2$S), 1.96 (m, 2 H, PCH). ^{31}P NMR (CD_2Cl_2, 23 °C): δ 87.3 (d), 81.2 (s), 60.4 (d). IR (THF) ν_{CO} 2010 (w), 1975 (s) cm^{-1}.

Fe(pdt)(CO)$_2$(dppe), 1d. Under a CO atmosphere, a solution of 190 mg of $FeCl_2$ (1.50 mmol) in 40 mL of acetone was treated with a solution of 598 mg (1.50 mmol) of 1,2-bis(diphenylphosphino)ethane (dppe) in 8 mL of THF. The solution changed from pale green to a clear red after about 30 min. After 1.0 h, $Na_2S_2C_3H_6$ (prepared from 171 μL (1.70 mmol) of

$C_3H_6(SH)_2$ and 72 mg (3.0 mmol) of NaH in 3 mL of THF) was added dropwise. The resulting red solution stirred for 16 h and showed no further reaction. The IR spectrum at this stage revealed bands at 2002, 1983, 1968, 1915, and 1895 cm^{-1}. The solution was filtered and the red filtrate was concentrated in vacuum to dryness. The residue was separated by flash silica gel column chromatography (CH_2Cl_2/Et_2O, v/v = 10:1) to afford $Fe(S_2C_3H_6)(CO)_2$(dppe) as a red solid. Yield 398 mg (43%) ^1H NMR (CD_2Cl_2, 23 °C, 500 MHz): δ 7.89 - 7.32 (m, 20 H, C_6H_5), 2.63 (d, 4 H, SCH_2), 2.50 (d, 4 H, PCH_2), 1.97 (m, 2 H, SCH_2CH_2). ^{31}P NMR (CD_2Cl_2, 23 °C): δ 78.0 (d), 73.7 (s), 51.2 (d). IR (THF) ν_{CO} 2006 (w), 1969 (s), 1958 (sh) cm^{-1}.

Fe(pdt)(CO)$_2$(dppbz), 1e. Under a CO atmosphere, a solution of 500 mg of $FeCl_2$ (3.94 mmol) in 100 mL of acetone was treated with a solution of 1.76 g (3.94 mmol) of 1,2-bis(diphenylphosphino)benzene (dppbz) in 40 mL of THF. The solution turned brown, then orange. After stirring for ~ 20 minutes, the solution was treated with a slurry of $Na_2S_2C_3H_6$ (prepared from 435 μL (4.33 mmol) of $C_3H_6(SH)_2$ and 188 mg (7.88 mmol) of NaH in 15 mL of THF) was added dropwise, causing the solution to change color to dark brown red. The solution stirred for 18 h and showed no further reaction. A large amount of red precipitate had formed during the course of the reaction. The IR spectrum at this stage revealed bands at 1985, 1970, 1917, and 1900 cm^{-1}. The solution was filtered and the red solid was extracted into CH_2Cl_2. The product was recrystallized from hexanes. Yield 400 mg (20 %) ^1H NMR (CD_2Cl_2, 23 °C, 500 MHz): δ 7.4-7.6 (m, 24 H, C_6H_5, C_6H_4), 2.39 (s, 4 H, SCH_2CH_2), 1.94 (s, 2 H, SCH_2CH_2). ^{31}P NMR (CD_2Cl_2, 23 °C): δ 80.8 (s), 78.5 (d), 68.2 (d). IR (CH_2Cl_2) ν_{CO} 2012 and 1970 cm^{-1}.

Fe(Me$_2$pdt)(CO)$_2$(dppe), 1f. Under a CO atmosphere, a solution of 500 mg of $FeCl_2$ (3.94 mmol) in 100 mL of acetone was treated with a solution of 1.76 g (3.94 mmol) of 1,2-bis(diphenylphosphino)ethane (dppe) in 15 mL of THF. The solution turned green, then orange. After stirring for ~ 20 minutes, the solution was treated with a slurry of $Na_2S_2C_5H_9$ (prepared from 600 μL (4.93 mmol) of $C_5H_9(SH)_2$ and 188 mg (7.88 mmol) of NaH in 20 mL of THF) was added dropwise, causing the solution to change color to dark brown red. The solution stirred for 18 h and showed no further reaction. The IR spectrum at this stage revealed bands at 2004, 1982, 1968, 1955, 1914, and 1895 cm^{-1}. The solution was filtered through Celite™ and the red brown solution was concentrated to dryness under vacuum. The product was extracted into CH_2Cl_2 and chromatographed on silica. A yellow band was eluted with CH_2Cl_2, followed by a red band (product), eluted with 5% Et_2O in CH_2Cl_2. The product was recrystallized from

CH_2Cl_2/ hexanes. Yield 1.03 g (40 %) ^{1}H NMR (CD_2Cl_2, 23 °C, 500 MHz): δ 7.4-7.8 (m, 20 H, C_6H_5), 2.65 (dd, 4 H, $P_2CH_2CH_2$), 2.23 (s, 4 H, SCH_2), 1.01 (s, 6 H, CCH_3). ^{31}P NMR (CD_2Cl_2, 23 °C): δ 73.82 (s), 78.35 (d), 52.65 (d). IR (CH_2Cl_2) ν_{CO} 206 (w), 1969 (s) cm^{-1}.

$Fe_2(pdt)(CO)_4(dppe)$, 3, via Reaction of $Fe(pdt)(CO)_2(dppe)$, 1d, with $(bda)Fe(CO)_3$. An orange mixture of 250 mg (0.40 mmol) of $Fe(pdt(CO)_2(dppe)$ and 115 mg (0.40 mmol) of $(bda)Fe(CO)_3$ in 70 mL of toluene gradually darkened over hours to a deep red solution. The reaction was monitored by IR for loss of ν_{CO}= 2065, 2003, 1982 cm^{-1} ($(bda)Fe(CO)_3$), 2010 and1970 cm^{-1} ($Fe(edt)(CO)_2(dppv)$ and the appearance of ν_{CO}= 2019, 1944, and 1904 cm^{-1} ($Fe_2(pdt)(CO)_4(dppe)$). After 24 hours, the IR spectrum no longer changed, and the major species present was $Fe_2(pdt)(CO)_4(dppe)$. The reaction solution was concentrated *in vacuo* and chromatographed on silica gel in air, eluting with toluene. The first brown-red band was collected and dried *in vacuo*. Yield: 150 mg (52%). The IR, ^{1}H NMR, and ^{31}P NMR spectra match those previously reported.[32]

$[Mn(CO)_3(pdt)Fe(CO)_2(dppe)]BF_4$, $[4]BF_4$. In a 250 mL Schlenk flask, 500 mg (1.32 mmol) of $[(acenaphthene)Mn(CO)_3]BF_4$ was dissolved in 125 mL of CH_2Cl_2, and the solution was treated with a solution of 810 mg (1.32 mmol) of $Fe(pdt)(CO)_2(dppe)$ (**1b**) in 50 mL of CH_2Cl_2. The solution stirred for 20 h, and gradually became dark brown in color. The IR spectrum shows ν_{CO}= 2053(w), 2027(s), 1992(s), 1974(s), 1905(br) cm^{-1}. The solution was concentrated to dryness under vacuum, the resulting brown residue was extracted into ~ 30 mL of CH_2Cl_2, and the solution was filtered through a pad of Celite. The volume of the brown solution was reduced to ~ 10 mL, and 100 mL of hexanes was added to the solution. Upon cooling to 0 °C, brown mircrocrystals formed, which were filtered and dried under vacuum. Yield: 1.00 g (90%). Crystals were obtained by layering a CH_2Cl_2 solution with pentane. ^{1}H NMR (CD_2Cl_2, 500 MHz): δ 7.41-7.80 (m, 20 H, C_6H_5), 3.50 (m, 2 H, PCH_2), 3.28 (m, 2 H, PCH_2), 3.08 (m, 2 H, SCH_2), 2.84 (m, 3 H, SCH_2CH_2), 2.03 (m, 1 H, SCH_2CH_2). ^{31}P NMR (CD_2Cl_2): δ 58 (s). IR (CH_2Cl_2) ν_{CO} 2053(w), 2027(s), 1992(s), 1974(s), 1905(br) cm^{-1}. Anal. Calcd for $C_{34}H_{30}MnFeS_2P_2O_5BF_4$ (found): C, 48.48 (48.66); H, 3.59 (3.81).

Reaction of $[(acenapthene)Mn(CO)_3]BF_4$ with $Fe(pdt)(CO)_2(dppbz)$, 1e. In a100 mL Schlenk flask, 57 mg (0.15 mmol) of $[(acenaphthene)Mn(CO)_3]BF_4$ was dissolved in 25 mL of CH_2Cl_2, and the solution was treated with a solution of 100 mg (0.15 mmol) of $Fe(pdt)(CO)_2(dppbz)$ (**1e**) in 20 mL of CH_2Cl_2. The solution stirred for 20 h, and gradually

became dark brown in color. The IR spectrum shows ν_{CO}= 2105(w), 2080 (w), 2055(s), 2030(s), 2005(br), 1993(br), 1982 (br), 1885 (br) cm^{-1}. The solution was concentrated to dryness under vacuum, the resulting brown residue was extracted into ~ 10 mL of CH_2Cl_2, and the solution was filtered through a pad of Celite. The volume of the brown solution was reduced to ~ 5 mL, and 50 mL of hexanes was added to the solution. Upon cooling to 0 °C, brown mircrocrystals formed, which were filtered and dried under vacuum, however, pure compound could not be obtained by this method. Yield: 80 mg (68%). ^{31}P NMR (CD_2Cl_2): δ 73.1, 70.2, 68.9 (s).

Reaction of [(napthalene)Mn(CO)$_3$]BF$_4$ with Fe(Me$_2$pdt)(CO)$_2$(dppe), 1f. In a 100 mL Schlenk flask, 145 mg (0.4 mmol) of [(napthalene)Mn(CO)$_3$]BF_4 was dissolved in 30 mL, and the solution was treated with a solution of 265 mg (0.4 mmol) of Fe(Me$_2$pdt)(CO)$_2$(dppe) (**1f**) in 20 mL of CH_2Cl_2. The solution stirred for 20 h, and gradually became dark brown in color. The IR spectrum shows ν_{CO}= 2092(s), 2073(s), 2040(s), 2030(s), 2015(s), 2000(sh), 1985 (s), 1915(br), and 1883(br) cm^{-1}. The solution was concentrated to dryness under vacuum, the resulting brown residue was extracted into ~ 10 mL of CH_2Cl_2, and the solution was filtered through a pad of Celite. The volume of the brown solution was reduced to ~ 5 mL, and 100 mL of hexanes was added to the solution, but ^{31}P NMR shows a mixture of products and pure compound could not be obtained. The analogous reaction with [(acenapthene)Mn(CO)$_3$]BF_4 as the manganese source was performed, but the results were identical.

Reaction of [(acenapthene)Mn(CO)$_3$]BF$_4$ with Fe(edt)(CO)$_2$(dppe), 1b. In a J-young NMR tube, 20 mg of Fe(edt)(CO)$_2$(dppe) (**1b**) (0.033 mmol) and 13 mg of [(acenapthene)Mn(CO)$_3$]BF_4 (0.033 mmol) were dissolved in ~ 0.75 mL of CD_2Cl_2. The reaction was monitored by ^{31}P NMR spectroscopy for the disappearance of signals for **1b** and the appearance of new signals corresponding to the MnFe complex. Three isomers form, with d 63.2 (s, Isomer A), 49.9 and 77.3 (d, Isomer B), and 78.0 and 72.5 (d, Isomer C) (See Scheme 5.9).

Formation of Mn(CO)$_3$(pdt)Fe(CO)(dppe), 5, by reduction of [Mn(CO)$_3$(pdt)Fe(CO)$_2$(dppe)]BF$_2$, [4]BF$_4$, with Cp$_2$Co. In a 15 mL Schlenk flask, 25 mg of [Mn(CO)$_3$(pdt)Fe(CO)$_2$(dppe)]BF_2, [**4**]BF_4 (0.03 mmol) was dissolved in 5 mL of CH_2Cl_2 and cooled to 0 °C. The solution was treated with a pre-cooled solution of Cp_2Co (0.03 mmol) in 2 mL of CH_2Cl_2. The solution immediately changed color from brown to red. The IR spectrum contains n_{CO}= 1996, 1904 cm^{-1}, as well as weak bands at 2078, 2049, 2027, 1954 cm^{-1}. Warming the solution to room temperature caused the intensities of the weaker IR bands to increase.

Solvent was removed under vacuum. The red product was extracted into toluene and layered with hexanes for crystallization. However, a brown red precipitate forms, which does not have an IR spectrum matching that for **5**.

***In-situ* formation of $Mn(CO)_3(pdt)Fe(CO)(dppe)$, 5, and analysis by EPR spectroscopy.** A solution of 9 mg of $[Mn(CO)_3(pdt)Fe(CO)_2(dppe)]BF_2$, [**4**]$BF_4$ (0.01 mmol) was dissolved in 0.75 mL of CH_2Cl_2, and 2 mg of Cp_2Co (0.01 mmol) was dissolved in 2.25 mL of toluene. Both solutions were cooled to -35 °C, after which they were mixed, transferred to an EPR tube, and immediately frozen in liquid N_2. The EPR spectrum was recorded at 110K, then the instrument/ sample were gradually warmed to 0 °C.

$Mn(CO)_3(pdt)(\mu$-H)Fe(CO)(dppe), 6. A solution of 590 mg (0.70 mmol) of $[Mn(CO)_3(pdt)Fe(CO)_2(dppe)]BF_4$ ([**4**]BF_4) in 100 mL of CH_2Cl_2 was cooled to -78 °C and treated with a pre-cooled solution of 257 mg (0.70 mmol) $[Bu_4N]BH_4$ in 60 mL of CH_2Cl_2 over the course of 90 min, during which time the solution changed color from brown to dark red. The IR spectrum was monitored for loss of ν_{CO}= 2053(w), 2027(s), 1992(s), 1974(s), 1905(br) cm^{-1} for **6**BF_4 and the appearance of ν_{CO}= 1999 (s), 1939 (br) , and 1907 (br) cm^{-1}. The solution was warmed to room temperature, and after 30 min, the IR shows ν_{CO}= 2002 (s), 1999 (sh), 1939 (br) , and 1907 (br) cm^{-1}. The solution stirred at room temperature for 15 h, at which point the IR spectrum contains ν_{CO}= 2002 (s), 1999 (sh), 1939 (br) , and 1907 (br) cm^{-1}, but the shoulder at 1999 cm^{-1} decreased in intensity. The solution was concentrated to dryness under vacuum. The resulting red residue was extracted into ~20 mL of toluene and chromatographed, eluting with a 3:1 toluene/ hexanes mixture. The product (an orange band) eluted first, followed by a brown band. The orange product was collected, and the solution was concentrated to dryness under vacuum, resulting in an orange residue, which was extracted into ~25 mL of toluene and filtered through Celite™. The solution volume was reduced by ½, and 60 mL of hexanes were added. After storage at 0 °C, orange crystals formed which were filtered and dried under vacuum. Yield: 98 mg (20%) Diffraction quality crystals were grown at 0 °C, by layering a toluene solution with hexanes. ^1H NMR (CD_2Cl_2, 500 MHz): δ 7.38- 7.84 (m, 20 H, C_6H_5), 2.76 (m, 4 H, PCH_2), 2.58 (m, 2 H, SCH_2), 2.41 (m, 3 H, SCH_2CH_2), 1.91 (m, 1 H, SCH_2CH_2), -12.26 (t, 1 H, Mn-H-Fe). ^{31}P NMR (CD_2Cl_2): δ 80.80 (s). IR (CH_2Cl_2) ν_{CO} = 2002 (s), 1935 (br), and 1905 (br) cm^{-1}. Anal. Calcd for $C_{33}H_{31}MnFeS_2P_2O_4$ (found): C, 54.41 (54.35); H, 4.29 (4.49).

Oxidation of $Mn(CO)_3(pdt)(\mu\text{-}H)Fe(CO)(dppe)$, 6, with $[AcetylFc]BF_4$. In a 15 mL Schlenk flask, 5 mg (0.0068 mmol) of $Mn(CO)_3(pdt)(\mu\text{-}H)Fe(CO)(dppe)$, **6**, was dissolved in 1 mL of CH_2Cl_2 and cooled to 0 °C. The solution was treated with $[AcetylFc]BF_4$ (0.0068 mmol) in 1 mL of CH_2Cl_2. The solution remained orange, but the IR contains new CO bands at 2023, 1992, 1980, and 1967 cm^{-1}.

***In-situ* oxidation of $Mn(CO)_3(pdt)(\mu\text{-}H)Fe(CO)(dppe)$, 6, and analysis by EPR spectroscopy.** A solution of 1.0 mg of $Mn(CO)_3(pdt)(\mu\text{-}H)Fe(CO)(dppe)$, **6**, (0.0014 mmol) was dissolved in 0.375 mL of toluene, and 1.5 mg of $[AcetylFc]BAr^F{}_{24}$ (0.0014 mmol) was dissolved in 0.125 mL of CH_2Cl_2. Both solutions were cooled to -35 °C, after which they were mixed, transferred to an EPR tube, and immediately frozen in liquid N_2. The EPR spectrum was recorded at 110K, then the instrument/ sample were gradually warmed to 0 °C.

Protonation of $Mn(CO)_3(pdt)(\mu\text{-}H)Fe(CO)(dppe)$, 6, with $[H(Et_2O)_2]BAr^F{}_{24}$ and Subsequent Deprotonation. In a 15 mL Schlenk flask, 11 mg (0.015 mmol) of $Mn(CO)_3(pdt)(\mu\text{-}H)Fe(CO)(dppe)$, **6**, was dissolved in 10 mL of CH_2Cl_2. CO was bubbled through the solution, and a solution of 16 mg (0.015 mmol) of $[H(Et_2O)_2]BAr^F{}_{24}$ was added. The IR spectrum exhibits n_{CO}= 2039(w), 2024(s), 1986 (br), and 1968 (br) cm^{-1}. After ~ 30 minutes, the IR spectrum was unchanged. The solution was treated with 0.1 mL (0.0075 mmol) of a 0.075 M solution of triethylamine, which caused bands for the neutral hydride, **6**, to reappear, and those for the protonated product to decrease in intensity. Treatment with another 0.0075 mmol of triethylamine led to complete conversion to **6**, based on the IR spectrum. The results are identical when the reaction is performed under an atmosphere of Ar, rather than CO.

NMR Scale Protontion of $Mn(CO)_3(pdt)(\mu\text{-}H)Fe(CO)(dppe)$, 6, with $[H(Et_2O)_2]BAr^F{}_{24}$. In a J-young NMR tube, 10 mg (0.014 mmol) of $Mn(CO)_3(pdt)(\mu\text{-}H)Fe(CO)(dppe)$, **6**, and 14 mg of $[H(Et_2O)_2]BAr^F{}_{24}$ were dissolved in CD_2Cl_2 that had been pre-cooled to -35 °C. The tube was placed in a -40 °C bath and analyzed by NMR spectroscopy at -40 °C.

Electrochemistry. All electrochemical measurements were conducted in CH_2Cl_2 solutions. Cyclic voltammetry experiments were conducted using a 20-mL one-compartment glass cell with a tight-fitting Teflon top using a BAS-100 Electrochemical Analyzer. The working electrode was a glassy carbon (GC) disk (diameter = 3.00 mm). A silver wire was used as a quasireference electrode, and the counter electrode was a Pt wire. The electrolyte was 0.1 M

$[Bu_4N]PF_6$, and the analyte was typically 1.0 mM. Ferrocene (sufficient to give ~1 mM solution) was added as an internal reference, and each cyclic voltammagram was referenced to this $Fc^{0/+}$ couple = 0.00 V. *i*R compensation was applied to all measurements using the BAS software. Cell resistance was determined prior to each scan, and the correction applied to the subsequently collected cyclic voltammogram.

5.11 References

(1) Tard, C.; Pickett, C. J. "Structural and Functional Analogues of the Active Sites of the [Fe]-, [NiFe]-, and [FeFe]-Hydrogenases." *Chem. Rev.* **2009**, *109*, 2245.

(2) Mack, A. E.; Rauchfuss, T. B. "(1,3-Propanedithiolato)hexacarbonyldiiron and Cyanide Derivatives." *Inorg. Synth.* **2011**, *35*, 142.

(3) Seyferth, D.; Henderson, R. S.; Song, L. C. "Chemistry of μ-Dithio-bis(tricarbonyliron), a Mimic of Organic Disulfides. 1. Formation of Di-μ-Thiolate-Bis(tricarbonyliron) Dianion." *Organometallics* **1982**, *1*, 125.

(4) Seyferth, D.; Henderson, R. S.; Song, L.-C.; Womack, G. B. "Chemistry of μ-dithiobis(tricarbonyliron), an inorganic mimic of organic disulfides. II. Nucleophilic sulfur-sulfur bond cleavage by organolithium and organomagnesium reagents." *J. Organomet. Chem.* **1985**, *292*, 9.

(5) Lawrence, J. D.; Li, H.; Rauchfuss, T. B. "Beyond Fe-only Hydrogenases: N-Functionalized 2-Aza-1,3-dithiolates $Fe_2[(SCH_2)_2NR](CO)_x$ (x = 5, 6)." *Chem. Commun.* **2001**, 1482.

(6) Lawrence, J. D.; Li, H.; Rauchfuss, T. B.; Bénard, M.; Rohmer, M.-M. "Diiron Azadithiolates as Models for the Iron-only Hydrogenase Active Site: Synthesis, Structure, and Stereoelectronics." *Angew Chem., Int. Ed.* **2001**, *40*, 1768.

(7) Brandt, P. F.; Lesch, D. A.; Stafford, P. R.; Rauchfuss, T. B. "$Fe_2(S_2)(CO)_6$ and $Fe_3Te_2(CO)_9$,10." *Inorg. Synth.* **1997**, *31*, 112.

(8) Volkers, P. I.; Boyke, C. A.; Chen, J.; Rauchfuss, T. B.; Whaley, C. M.; Wilson, S. R.; Yao, H. "Precursors to [FeFe]-Hydrogenase Models: Syntheses of $Fe_2(SR)_2(CO)_6$ from CO-Free Iron Sources." *Inorg. Chem.* **2008**, *47*, 7002.

(9) Silakov, A.; Olsen, M. T.; Sproules, S.; Reijerse, E. J.; Rauchfuss, T. B.; Lubitz, W. "EPR/ENDOR, Moessbauer, and Quantum-Chemical Investigations of Diiron Complexes Mimicking the Active Oxidized State of [FeFe]Hydrogenase." *Inorg. Chem.* **2012**, *51*, 8617.

(10) Cohen, I. A.; Basolo, F. "Kinetics of substitution reactions of dihalo tetracarbonyliron(II) compounds with different reagents." *J. Inorg. Nucl. Chem.* **1966**, *28*, 511.

(11) Zhang, Z.-Z.; Zhang, J.-K.; Zhang, W.-D.; Xi, H.-P.; Cheng, H.; Wang, H.-G. "Carbonylation of iron(II) halide in the presence of chelate diphosphine ligands. Molecular structure of a novel intermolecular adduct $[FeCl_2(dppe)_2][Fe_2(CO)_2Cl_4]$." *J. Organomet. Chem.* **1996**, *515*, 1.

(12) Pignolet, L. H.; Forster, D.; Horrocks, W. D. "Dihalobis(triarylphosphine)iron(II) complexes. Isotropic proton magnetic resonance shifts and the kinetics of ligand exchange." *Inorg. Chem.* **1968**, *7*, 828.

(13) Booth, G.; Chatt, J. "402. The reactions of carbon monoxide and nitric oxide with tertiary phosphine complexes of iron(II), cobalt(II), and nickel(II)." *J. Chem. Soc.* **1962**, 2099.

(14) Baker Jr, W. A.; Lutz, P. M. "Fe(II) and Cr(III) complexes of 1,2-bis(diphenylphosphino)ethane." *Inorg. Chim. Acta* **1976**, *16*, 5.

(15) Synder, B. S.; Holm, R. H. "Hexanuclear iron-sulfur basket clusters: topological isomers of prismanes. Synthesis, structure, and reactions." *Inorg. Chem.* **1988**, *27*, 2339.

(16) Manuel, T. A. "Some tertiary phosphine-iron carbonyl compds." *Inorg. Chem.* **1963**, *2*, 854.

(17) Battaglia, L. P.; Chiusoli, G. P.; Delledonne, D.; Nardelli, M.; Pelizzi, C.; Predieri, G. "Reductive carbonylation of iron(II) with manganese metal. Preparation of carbonyl diphosphine complexes of iron(0)." *Gazz. Chim. Ital.* **1989**, *119*, 345.

(18) Takács, J.; Markó, L.; Párkányi, L. "Synthesis and some reactions of $Fe(CO)_2(dppe)(SR)_2$ and $Fe_3(CO)_6(SAr)_6$ complexes. The crystal structure of cis,cis,cis-$Fe(CO)_2(dppe)(SPh)_2$." *J. Organomet. Chem.* **1989**, *361*, 109.

(19) Takács, J.; Soós, E.; Nagy-Magos, Z.; Markó, L.; Gervasio, G.; Hoffmann, T. "Synthesis and molecular structure of carbonyl derivatives of iron(II) thiolates containing nitrogen-donor ligands." *Inorg. Chim. Acta* **1989**, *166*, 39.

(20) Guo, Y.; Wang, H.; Xiao, Y.; Vogt, S.; Thauer, R. K.; Shima, S.; Volkers, P. I.; Rauchfuss, T. B.; Pelmenschikov, V.; Case, D. A.; Alp, E. E.; Sturhahn, W.; Yoda, Y.; Cramer, S. P. "Characterization of the Fe Site in Methanothermobacter marburgensis Hydrogenase (mHmd) via Nuclear Resonant Vibrational Spectroscopy (NRVS)." *Inorg. Chem.* **2008**, *47*, 3969.

(21) Schwartz, L.; Singh, P. S.; Eriksson, L.; Lomoth, R.; Ott, S. "Tuning the electronic properties of Fe_2(arenedithiolate)$(CO)_{6-n}(PMe_3)_n$ (n = 0, 2) complexes related to the [Fe-Fe]-hydrogenase active site." *C. R. Chim.* **2008**, *11*, 875.

(22) Beyler, M.; Ezzaher, S.; Karnahl, M.; Santoni, M.-P.; Lomoth, R.; Ott, S. "Pentacoordinate iron complexes as functional models of the distal iron in [FeFe] hydrogenases." *Chem. Commun.* **2011**, *47*, 11662.

(23) Walters, M. A.; Dewan, J. C. "Synthesis and characterization of MnFe[Œº-$(SC_6H_5)]_3(CO)_6$, a heterobimetallic complex formed by self-assembly." *Inorg. Chim. Acta* **1991**, *187*, 123.

(24) Cai, S.; Hou, X.-F.; Chen, Y.-Q.; Jin, G.-X. "Synthesis and structure of heterometallic complexes (RhFe, CoFe) containing bridging 1,2-dicarba-closo-dodecarborane-1,2-dichalcogenolato ligands." *Dalton Trans.* **2006**, *0*, 3736.

(25) Murata, M.; Habe, S.; Araki, S.; Namiki, K.; Yamada, T.; Nakagawa, N.; Nankawa, T.; Nihei, M.; Mizutani, J.; Kurihara, M.; Nishihara, H. "Synthesis of Heterometal Cluster Complexes by the Reaction of Cobaltadichalcogenolato Complexes with Groups 6 and 8 Metal Carbonyls." *Inorg. Chem.* **2006**, *45*, 1108.

(26) Benito-Garagorri, D.; Lagoja, I.; Veiros, L. F.; Kirchner, K. A. "Reactivity of coordinatively unsaturated iron complexes towards carbon monoxide: to bind or not to bind?" *Dalton Trans.* **2011**, *40*, 4778.

(27) Volkers, P. I. *PhD. Thesis University of Illinois at Urbana-Champaign* **2007**.

(28) Manuel, T. A. "Some Tertiary Phosphine-Iron Carbonyl Compounds." *Inorg. Chem.* **1963**, *2*, 854.

(29) Bellachioma, G.; Cardaci, G.; Macchioni, A.; Venturi, C.; Zuccaccia, C. "Reductive elimination of halogens assisted by phosphine ligands in $Fe(CO)_4X_2$ (X=I,Br) complexes." *J. Organomet. Chem.* **2006**, *691*, 3881.

(30) Justice, A. K.; Zampella, G.; De Gioia, L.; Rauchfuss, T. B.; van der Vlugt, J. I.; Wilson, S. R. "Chelate Control of Diiron(I) Dithiolates Relevant to the Fe-only Hydrogenase Active Site." *Inorg. Chem.* **2007**, *46*, 1655.

(31) Adam, F. I.; Hogarth, G.; Kabir, S. E.; Richards, I. "Models of the iron-only hydrogenase: Synthesis and protonation of bridge and chelate complexes $[Fe_2(CO)_4\{Ph_2P(CH_2)_nPPh_2\}(\mu\text{-pdt})]$ (n =2-4) - evidence for a terminal hydride intermediate." *C. R. Chim.* **2008**, *11*, 890.

(32) Ezzaher, S.; Capon, J.-F.; Gloaguen, F.; Pétillon, F. Y.; Schollhammer, P.; Talarmin, J.; Pichon, R.; Kervarec, N. "Evidence for the Formation of Terminal Hydrides by Protonation of an Asymmetric Iron Hydrogenase Active Site Mimic." *Inorg. Chem.* **2007**, *46*, 3426.

(33) Ittel, S. D.; Tolman, C. A.; Krusic, P. J.; English, A. D.; Jesson, J. P. "Bis(diphenylphosphino)ethane complexes of iron." *Inorg. Chem.* **1978**, *17*, 3432.

(34) Orchin, M.; Mandal, S. K.; Feldman, J. "Tricarbonyl(hydrido)[1,2-bis(diphenylphosphino)ethane]manganese as precursor to labile site derivatives." *Inorg. Synth.* **1998**, *32*, 298.

(35) Zaffaroni, R.; Rauchfuss, T. B.; Gray, D. L.; De Gioia, L.; Zampella, G. "Terminal vs Bridging Hydrides of Diiron Dithiolates: Protonation of Fe_2(dithiolate)$(CO)_2(PMe_3)_4$." *J. Am. Chem. Soc.* **2012**, *134*, 19260.

(36) Apfel, U.-P.; Troegel, D.; Halpin, Y.; Tschierlei, S.; Uhlemann, U.; Goerls, H.; Schmitt, M.; Popp, J.; Dunne, P.; Venkatesan, M.; Coey, M.; Rudolph, M.; Vos, J. G.; Tacke, R.; Weigand, W. "Models for the Active Site in [FeFe] Hydrogenase with Iron-Bound Ligands Derived from Bis-, Tris-, and Tetrakis(mercaptomethyl)silanes." *Inorg. Chem.* **2010**, *49*, 10117.

(37) Dong, W.; Wang, M.; Liu, X.; Jin, K.; Li, G.; Wang, F.; Sun, L. "An insight into the protonation property of a diiron azadithiolate complex pertinent to the active site of Fe-only hydrogenases." *Chem. Commun.* **2006**, 305.

(38) Ezzaher, S.; Gogoll, A.; Bruhn, C.; Ott, S. "Directing protonation in [FeFe] hydrogenase active site models by modifications in their second coordination sphere." *Chem. Commun.* **2010**, *46*, 5775.

(39) Silvernail, N. J.; Noll, B. C.; Schulz, C. E.; Scheidt, W. R. "Coordination of Diatomic Ligands to Heme: Simply CO." *Inorg. Chem.* **2006**, *45*, 7050.

(40) Jiang, J.; Koch, S. A. "*trans*-$[Fe(CN)_4(CO)_2]^{2-}$, a 21st Century [Fe(CN)(CO)] Compound." *Angew. Chem. Int. Ed.* **2001**, *40*, 2629.

(41) Robertson, E. W.; Wilkin, O. M.; Young, N. A. "The spectroscopic characterisation of cis-$Fe(CO)_4$IBr and cis-$Fe(CO)_4$ICl and an investigation of their halogen exchange reactions in solution and the vapour." *Polyhedron* **2000**, *19*, 1493.

(42) Li, B.; Liu, T.; Popescu, C. V.; Bilko, A.; Darensbourg, M. Y. "Synthesis and Mossbauer Characterization of Octahedral Iron(II) Carbonyl Complexes $FeI_2(CO)_3L$ and $FeI_2(CO)_2L_2$: Developing Models of the [Fe]-H2ase Active Site." *Inorg. Chem.* **2009**, *48*, 11283.

(43) Lyons, L. J.; Tegen, M. H.; Haller, K. J.; Evans, D. H.; Treichel, P. M. "Electrochemical behavior of thiolate-bridged manganese dimers." *Organometallics* **1988**, *7*, 357.

(44) Adams, R. D.; Kwon, O. S.; Smith, M. D. "New evidence on the factors affecting bridging and semibridging character of carbonyl ligands. The structures of $Mn_2(CO)_7$(μ-SCH_2CH_2S) and its phosphine derivatives $Mn_2(CO)_7$-$X(PMe_2Ph)X$(μ-SCH_2CH2_S), × = 1,2." *Israel Journal of Chemistry* **2001**, *41*, 197.

(45) Reyes-Lezama, M.; Höpfl, H.; Zúñiga-Villarreal, N. "One pot synthesis of dimanganese carbonyl complexes containing sulfur and phosphorus donor ligands using tricarbonylpentadienylmanganese." *J. Organomet. Chem.* **2008**, *693*, 987.

(46) Fontecilla-Camps, J. C.; Volbeda, A.; Cavazza, C.; Nicolet, Y. "Structure/Function Relationships of [NiFe]- and [FeFe]-Hydrogenases." *Chem. Rev.* **2007**, *107*, 4273.

(47) Justice, A. K.; De Gioia, L.; Nilges, M. J.; Rauchfuss, T. B.; Wilson, S. R.; Zampella, G. "Redox and Structural Properties of Mixed-Valence Models for the Active Site of the [FeFe]-Hydrogenase: Progress and Challenges." *Inorg. Chem.* **2008**, *47*, 7405.

(48) De Lacey, A. L.; Fernández, V. M.; Rousset, M.; Cammack, R. "Activation and Inactivation of Hydrogenase Function and the Catalytic Cycle: Spectroelectrochemical Studies." *Chem. Rev.* **2007**, *107*, 4304.

(49) van der Vlugt, J. I.; Rauchfuss, T. B.; Whaley, C. M.; Wilson, S. R. "Characterization of a Diferrous Terminal Hydride Mechanistically Relevant to the Fe-Only Hydrogenases." *J. Am. Chem. Soc.* **2005**, *127*, 16012.

(50) Brookhart, M.; Grant, B.; Volpe, A. F. "$[(3,5\text{-}(CF_3)_2C_6H_3)_4B]\text{-}[H(OEt_2)_2]^+$: a convenient reagent for generation and stabilization of cationic, highly electrophilic organometallic complexes." *Organometallics* **1992**, *11*, 3920.

Chapter 6.

Hydrogenase Active Site Mimics Containing CpCo: Studies on the Effect of Replacing $Fe(CO)_3$ with CpCo

6.1 Introduction

The novelty of the cofactors found in hydrogenase enzyme has inspired intense efforts to replicate their structures and function. In a practical sense, the area is motivated by an interest in discovering new catalysts for the processing of small molecules. Two hydrogenases are of particular interest for catalyzing the redox interconversion of H_2 and protons, the [FeFe]- and the [NiFe]-hydrogenases (Scheme 6.1).

Scheme 6.1. Active sites of the [FeFe]- and [NiFe]-hydrogenases

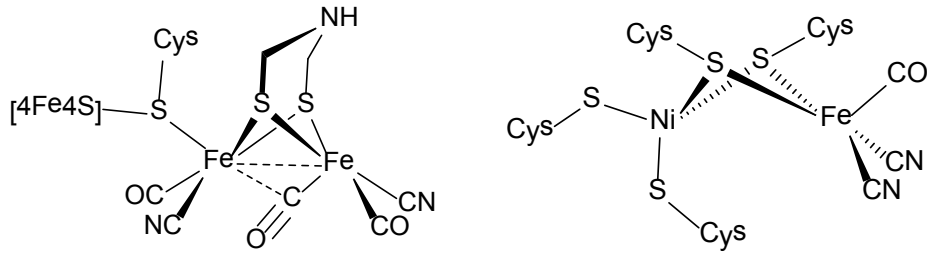

Modeling efforts have primarily focused on the preparation and study of compounds with the cores $Fe_2(\mu\text{-}SR)_2L_x$ and $NiFe(\mu\text{-}SR)_2L_y$, and those that lead to the biologically-relevant hydrides, always begin the assembly of $Fe(CO)_3$ derivatives, such as $(CO)_3Fe(SR)_2Fe(CO)_3$ and $(CO)_3Fe(SR)_2NiL_2$. The hydrogenases, however, do not contain $Fe(CO)_3$ subunits, but $Fe(CO)_2(CN)$, $Fe(CO)(CN)L$, and $Fe(CN)_2(CO)$ subunits, which are significantly more electron-rich than the parent carbonyl. Thus, by virtue of these strong donor ligands, the iron centers can catalyze redox reactions of H_2 and H^+ at low-potential (< 450 mV vs NHE). In order to attain functional models, much effort has been directed toward substitution of the polycarbonylated "pre-models" by electron-donors, such as phosphines and carbenes, and the resulting bimetallic centers are indeed superior models.

Organometallic chemistry is however a powerful art to a significant extent because of the applicability of isoelectronic and isolobal relationships. Such relationships may be relevant in

modeling hydrogenase active sites, specifically, the relationship between the $Fe(CO)_3$, NiL_2, and CpCo units (Cp= $C_5H_5^-$). In order to increase electron density at the metal centers in model complexes, $Fe(CO)_3$ may be replaced with CpCo. Because Cp is a significantly weaker π-acceptor than CO, such a replacement should result in more electron rich metal center.

Previous research has shown that $Fe(CO)_5$ and $CpCo(CO)_2$ exhibt similar reactivity. For example, both complexes react with dienes to form the corresponding adducts, $Fe(CO)_3$(diene) and CpCo(diene) (Scheme 6.2),[1] and analgous adducts of B_4H_8 have also been reported.[2,3] Additionally, $[CpFe(CO)_2]_2$ and $CpCo(CO)_2$ react with dimethyl disulfide to form thiolate bridged dimers (Scheme 6.3).[4]

Scheme 6.2. Isoelectronic diene adducts of CpCo and $Fe(CO)_3$.

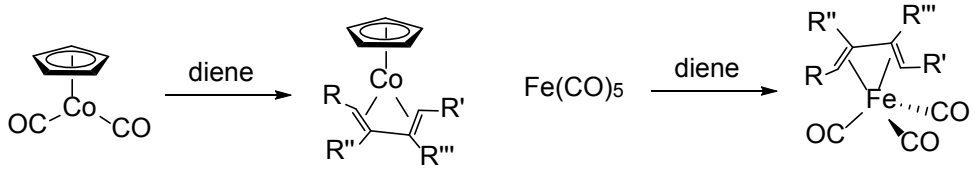

Scheme 6.3. Thiolate bridged CpCo and CpFe(CO) complexes.

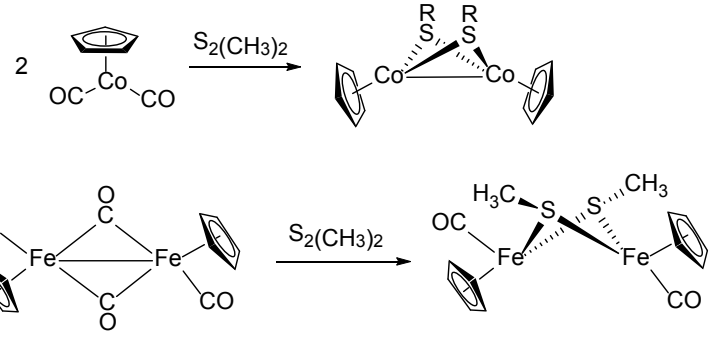

Complexes of CpCo have been found to have interesting and useful reactivity. CpCo complexes also catalyze a number of reactions that are relevant to organic synthesis, including [2+2+2] cyclizations, cyclotrimerization of alkynes, epoxide ring opening, and hydroacylation of alkenes.[5] Additionally, some complexes of the type $CpCo(PR_3)_2$ also catalyze the reduction of protons to form H_2.[6]

The feature of specific interest to this project is our interest in preparing and studying functional analogues of the active sites. The development of thiolato-bridged CpCo compounds is not very well developed. As mentioned above, King reported the synthesis of $Cp_2Co_2(SMe)_2$,

a black sublimable solid, in 1961.[4] This SMe bridged complex, as well as various arylthiolate bridged complexes, may also be synthesized by photolysis of $CpCo(CO)_2$ in the presence of the appropriate disulfide (Scheme 6.4a).[7] The complex $Cp_2Co_2(S^tBu)_2$ has been synthesized by photolysis of $CpCo(CO)_2$ and $Cp_2Ti(S^tBu)_2$ (Scheme 6.4b).[8] There is only one example of an analogous complex, with a dithiolate, rather than a monothiolate, CpCo(edt)CoCp (edt= 1,2-ethanedithiolate). This complex is relevant to synthesis of [FeFe]-hydrogenase mimics, as the active site of the enzyme contains a dithiolate. The complex is synthesized by photolysis of $CpCo(CO)_2$ and thiirane, however, slight variations in the stoichiometry leads to formation of different complexes (Scheme 6.4c).[9]

Scheme 6.4. Syntheses of $Cp_2Co_2(SR)_2$ complexes.

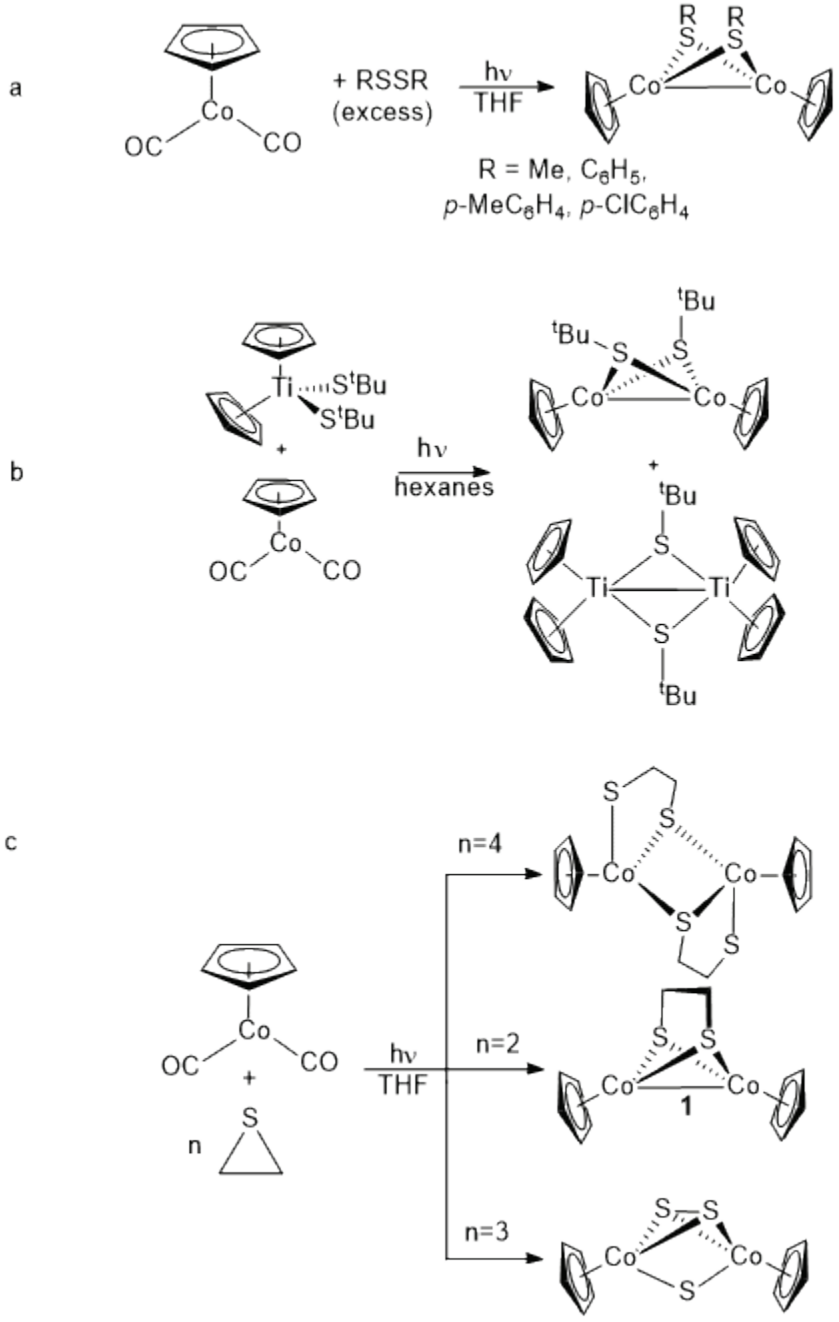

The reactivity of the CpCo dimers with small molecules has not been extensively investigated, and is limited to the reaction of $Cp_2Co_2(SR)_2$ with alkynes[7] and the reaction of CpCo(edt)CoCp with SO_2.[9] The corresponding phosphide complexes, $Cp_2Co_2(PR_2)_2$, have been reported and their reactivity has been studied thoroughly (Scheme 6.5). For example $Cp_2Co_2(PMe_2)_2$ sustains protonation at the Co-Co bond and the resulting bridging hydride

converts to terminal hydrides upon association of tertiary phosphines and phosphites, as well as CO (Scheme 6.6).[10-13]

Scheme 6.5. Syntheses of $Cp_2Co_2(PR_2)_2$ complexes.

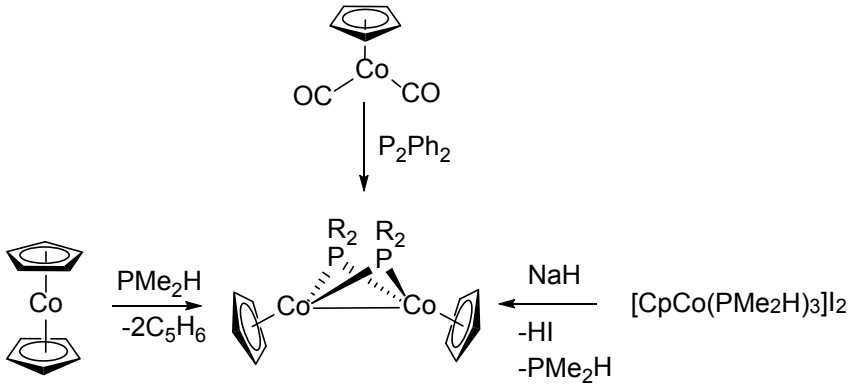

Scheme 6.6. Reactivity of $Cp_2Co_2(PR_2)_2$ complexes.

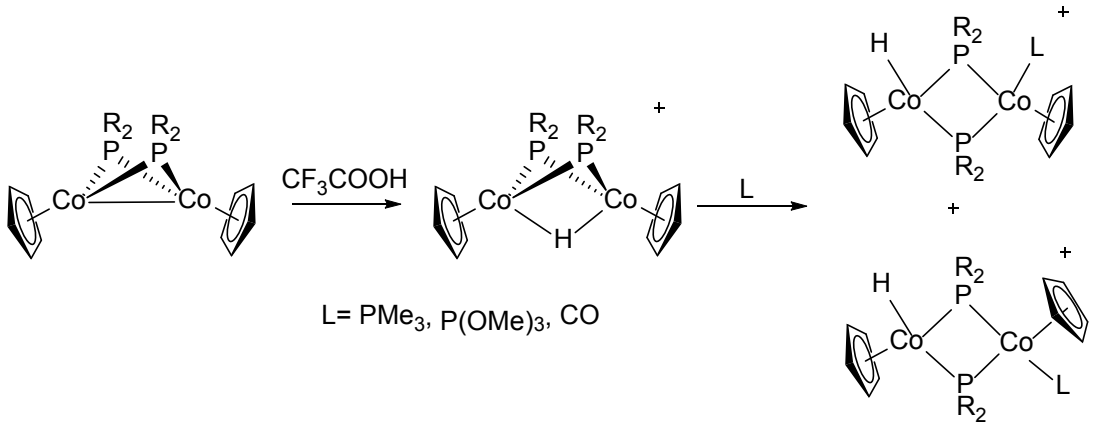

This chapter describes the synthesis and characterization of a series of complexes of the type, CpCo(xdt)CoCp. These compexes undergo protonation to form bridging hydride species. The reactivity of these novel hydride species with a variety of ligands was also investigated, as well as their electrocatalytic properties.

6.2 Synthesis and Characterization of CpCo(xdt)CoCp complexes.

Dicobalt dithiolate complexes have been prepared by the reaction of $CpCo(CO)_2$ with dithiols in refluxing toluene, resulting in $CpCo(xdt)_2CoCp$ (**1-3**) (Scheme 6.7). The complexes range in color from brownish green to purple, and all complexes are highly soluble in CH_2Cl_2

and pentane. Complexes **1-3** can also be prepared by reaction of cobaltocene (Cp_2Co) with the appropriate dithiol, in refluxing toluene, however, higher yields were achieved when $CpCo(CO)_2$ was used as the starting material.

Scheme 6.7. Synthesis of CpCo(xdt)CoCp complexes, 1-3.

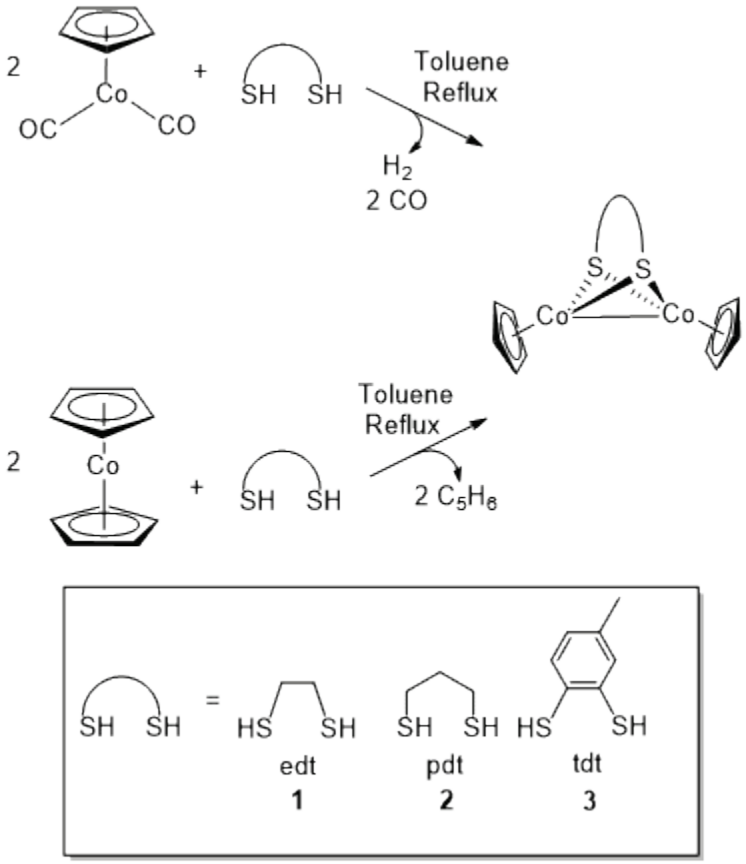

Complexes **1-3** were characterized by ^{1}H NMR spectroscopy. CpCo(edt)CoCp, **1**, had been synthesized previously, and its NMR spectrum matches that reported.[9] All three complexes exhibit singlets at ~5 ppm corresponding to the Cp protons and thiolate backbone protons at ~ δ 1-2 (Figure 6.1). The spectrum of **2** contains two singlets, corresponding to the protons in the pdt backbone. At -70 ^{o}C, the singlet for Cp splits into two signals, and the signals for the protons on the pdt backbone also split into three unresolved multiplets (Figure 6.2). At room temperature, the six membered ring formed by FeS_2C_3 flips, resulting in a single signal for the protons on the two Cp rings and two signals for the pdt backbone protons. At low temperature, the interconversion is frozen on the NMR timescale, so the two Cp rings are inequivalent, as are

the protons on the propanedithiolate strap. The Cp signals coalesce at -60 ^{o}C and the dithiolate signals at -50 ^{o}C. The spectra of **1** and **3** are unchanged at low temperatures because the geometries of the dithiolate ligands in these compounds do not enable the dynamic behavior exhibited by the propanedithiolate ligand to occur**.**

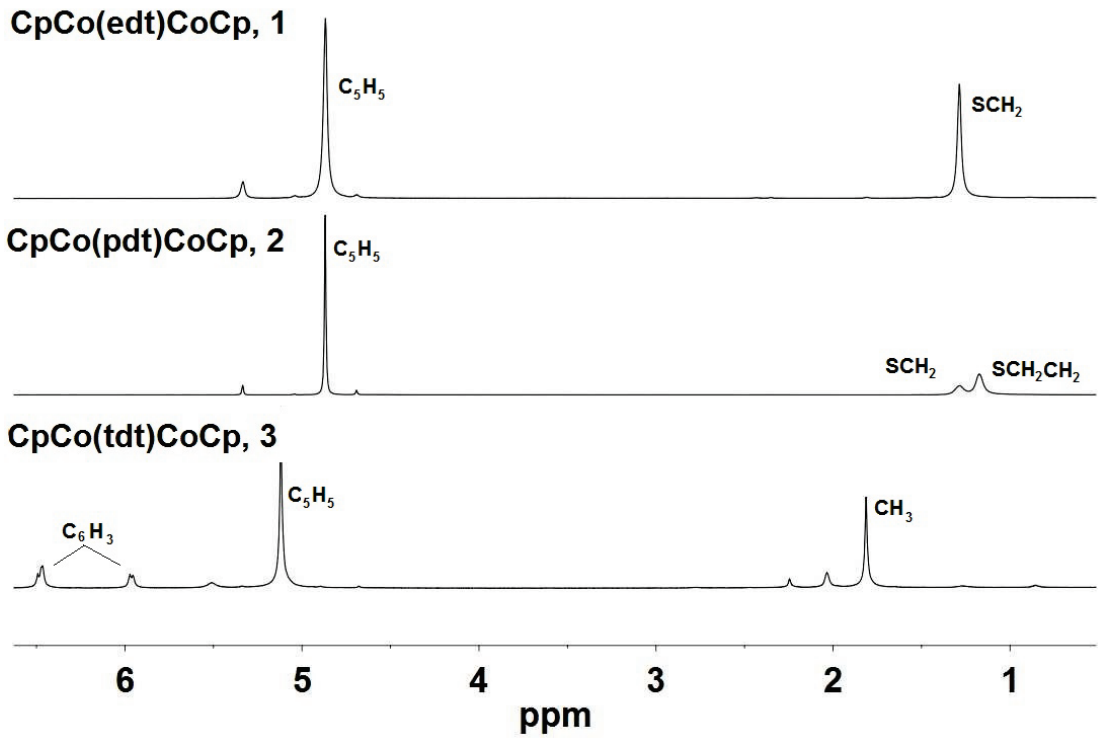

Figure 6.1. ^{1}H NMR spectra of CpCo(xdt)CoCp complexes, 1-3.

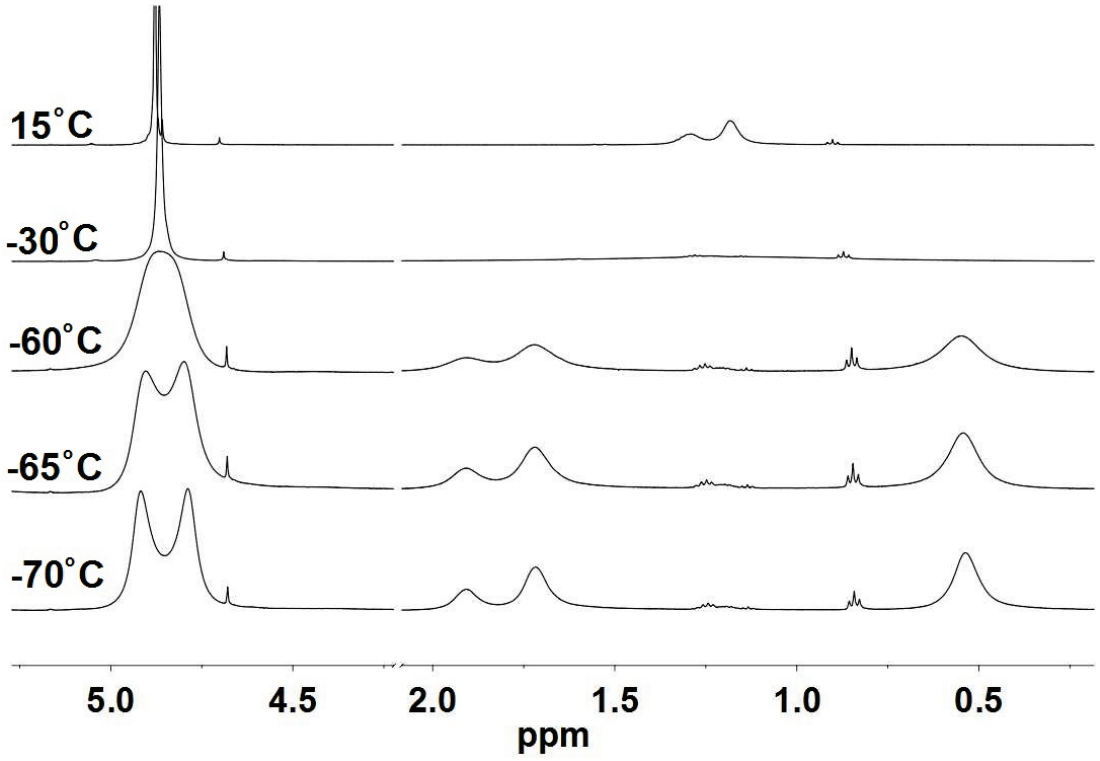

Figure 6.2. Variable temperature ^{1}H NMR spectra of CpCo(pdt)CoCp (2).

6.3 Redox Properties of CpCo(xdt)CoCp

Both dithiolate complexes, **1** and **2**, exhibit reversible one electron oxidations at relatively mild potentials in CH_2Cl_2, whereas complex **3** exhibits a quasi-reversible oxidation (Figures 6.3-6.5, Table 6.1). The new dithiolate complexes are oxidized at less mild potentials than the previously reported methyl thiolate complex, but their oxidation potentials are similar to those reported for the analogous complexes containing terminal aryl thiolates.[14]

The oxidized CpCo species are isoelectronic with the H_{ox} form of the [FeFe]-hydrogenase enzymes, both containing d^7d^6 metal centers.[15] The simplest diiron model complexes that have been studied are diiron dithiolato hexacarbonyls, which are not particularly electron rich. For example, the compounds $Fe_2(xdt)(CO)_6$ are oxidized more positive potentials than the the CpCo complexes (Table 6.2).[16] By replacing $Fe(CO)_3$ units with CpCo, we succeeded in shifting the oxidation potentials negative, by ~ 900 mv.

Many phosphine substituted diiron dithiolato carbonyl complexes have been reported. Compared with the symmetrically substituted diphosphine complexes, $Fe_2(xdt)(CO)_4(PMe_3)_2$ (xdt= edt, pdt), the CpCo complexes are o at milder potentials by ~ 0.1-0.2 V (Table 6.2),

suggesting that the CpCo complexes are more electron rich. When the phosphine substitution is unsymmetrical, as in $Fe_2(xdt)(CO)_4(dppv)$ (Table 6.2), the oxidation potentials are slightly more mild, occurring at potentials similar to those exhibited for the CpCo complexes. This difference is attributed to the presence of two phosphine ligands on an Fe center, thus stabilizing the ferrous center. More highly substituted complexes, such as $Fe_2(xdt)(CO)_3(PMe_3)(dppv)$ and $Fe_2(xdt)(CO)_2(dppv)_2$, where xdt= pdt or edt, are significantly more electron rich than the CpCo complexes, oxidizing at potentials ~ 0.4- 0.6 V more negative (Table 6.2).[17]

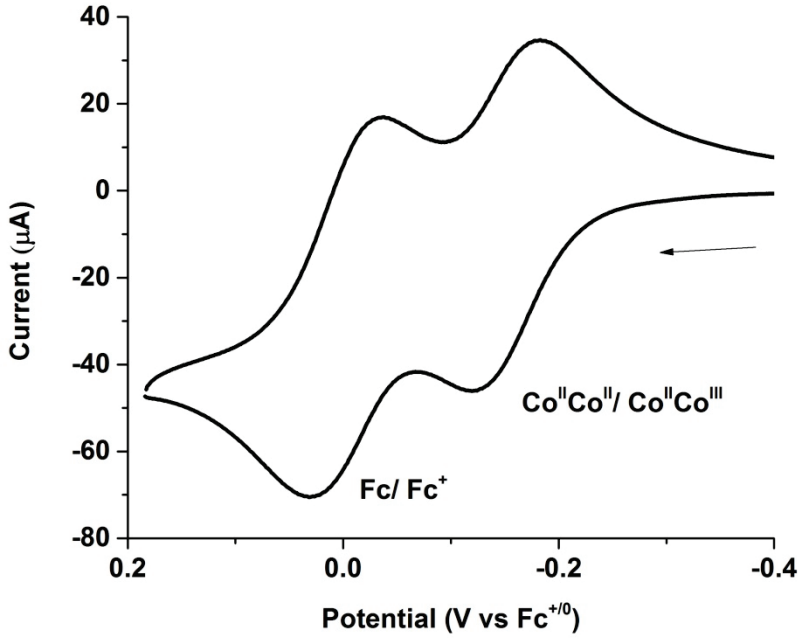

Figure 6.3 Cyclic voltammogram of CpCo(edt)CoCp, 1 in CH_2Cl_2. (Conditions: 0.1 M $[Bu_4N]PF_6$, 1.0 mM 1, glassy carbon working electrode, Ag wire pseudo reference electrode, Cp_2Co internal reference, Pt wire counter electrode)

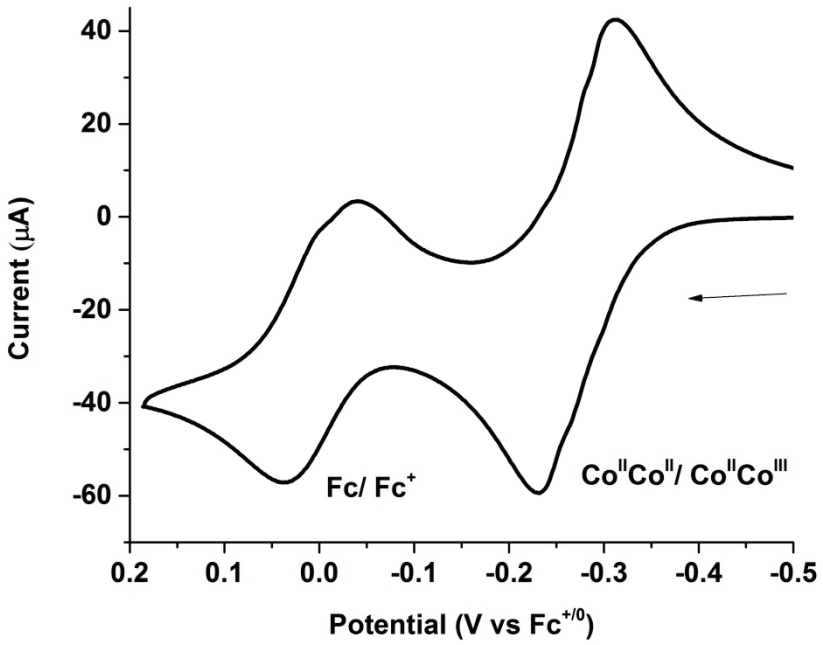

Figure 6.4 Cyclic voltammogram of CpCo(pdt)CoCp, 2 in CH_2Cl_2. (Conditions: See Figure 6.3)

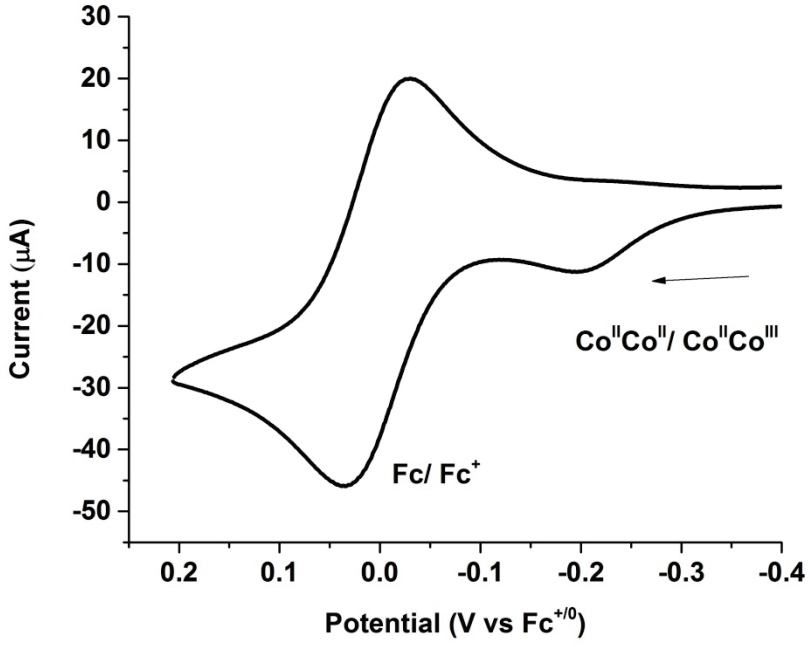

Figure 6.5 Cyclic voltammogram of CpCo(tdt)CoCp, 3 in CH_2Cl_2. (Conditions: Conditions: See Figure 6.3)

Table 6.1 Oxidation potentials of CpCo(xdt)CoCp complexes, 1-3 and $CpCo(SR)_2CoCp$ Complexes

Complex	$E_{1/2}$ (V vs $Fc^{+/0}$)
CpCo(edt)CoCp, **1**	-0.153[a]
CpCo(pdt)CoCp, **2**	-0.275[a]
CpCo(tdt)CoCp, **3**	-0.199[b]
$CpCo(SMe)_2CoCp$	-0.613[a,d]
$CpCo[S(p\text{-}MeC_6H_4)]_2CoCp$	-0.243[c,d]
$CpCo[S(p\text{-}MeC_6H_4)]_2CoCp$	-0.183[a,d]

[a] Reversible; [b] Irreversible; [c] Quasi-reversible; [d]Reference14

[e] Reference Darensbourg 2003 Dalton Trans

Table 6.2 Oxidation potentials of Diiron Model Complexes

Complex	$E_{1/2}$ (V vs $Fc^{+/0}$) xdt = edt	$E_{1/2}$ (V vs $Fc^{+/0}$) xdt = pdt
$Fe_2(xdt)(CO)_6$[c]	0.890[a]	0.740[a]
$Fe_2(xdt)(CO)_4(PMe_3)_2$[c]	-0.06[a]	-0.06[a]
$Fe_2(xdt)(CO)_4(dppv)$[d]	-0.02[b]	-0.21[b]
$Fe_2(xdt)(CO)_3(PMe_3)(dppv)$[d]	-0.45[b]	-0.62[b]
$Fe_2(xdt)(CO)_2(dppv)_2$[d]	-0.65[b]	-0.83[b]

[a] Irreversible; [b] Reversible;
[c] Values obtained from reference 16; [d] Values obtained from reference 17

6.4 Protonation of CpCo(xdt)CoCp Complexes.

The protonation of complexes of the type, $Cp_2Co_2(SR)_2$, where SR is a terminal thiolate ligand, has not previously been investigated. Complexes **1**-**3** are protonated with strong acid, $HBF_4{\cdot}Et_2O$, in dichloromethane, resulting in formation of the corresponding bridging hydrides, $[\mathbf{1}H]^+$, $[\mathbf{2}H]^+$, and $[\mathbf{3}H]^+$. The dark green brown, air sensitive complexes were isolated as their BF_4 salts (Scheme 6.8). The salts are soluble in CH_2Cl_2 and MeCN, but are unstable in MeCN.

Scheme 6.8 Protonation of CpCo(xdt)CoCp complexes, 1-3.

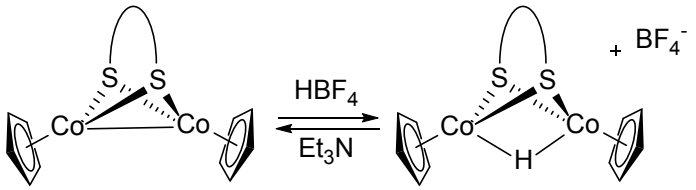

The ^{1}H NMR spectra of the hydride complexes exhibit singlets in the high field region, indicative of metal hydrides (Figure 6.6). Diffraction quality crystals of [**1**H]BF_4 were obtained by vapor diffusion of diethyl ether into a solution of the compound in dichloromethane (Figure 6.7). The hydride ligand, whose position was not refined, symmetrically bridges between the two Co centers, confirming the proposed C_{2V} symmetry of the compound.

Related neutral complexes have been reported previously, including $Cp_2Co_2(S^tBu)_2$[8] and complexes of the type, $Cp^RCo(edt)CoCp^R$, where R= H_4Me, Me_5, and Ph_5.[9] In the structure of [**1**H]BF_4 and previously reported structures, the Cp-Co distances (~ 2.04-2.06 Å), the Co-S distances (~ 2.19 Å) are similar. The S-Co-S and Co-S-Co angles in $Cp_2Co_2(S^tBu)_2$ are larger than those in the edt bridged complexes, likely due to the steric bulk of the ^{t}Bu groups.[8]

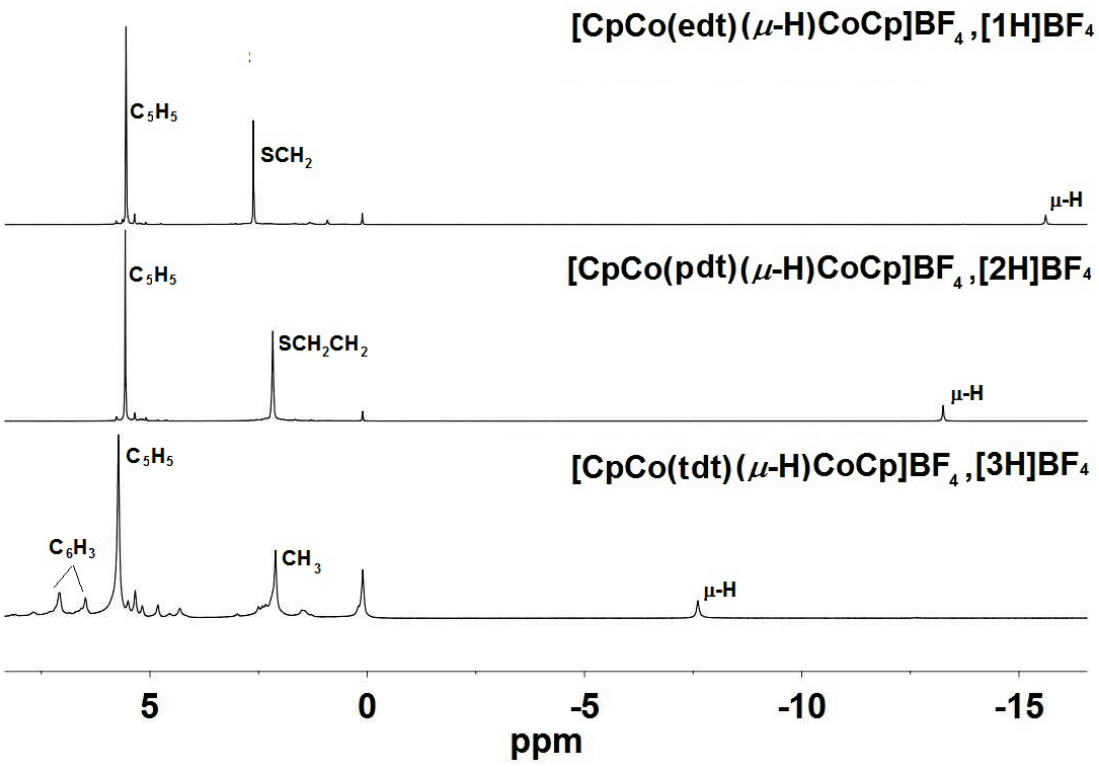

Figure 6.6. ^{1}H NMR spectra of [CpCo(xdt)(μ-H)CoCp]BF_4 complexes, [1H]BF_4- [3H]BF_4.

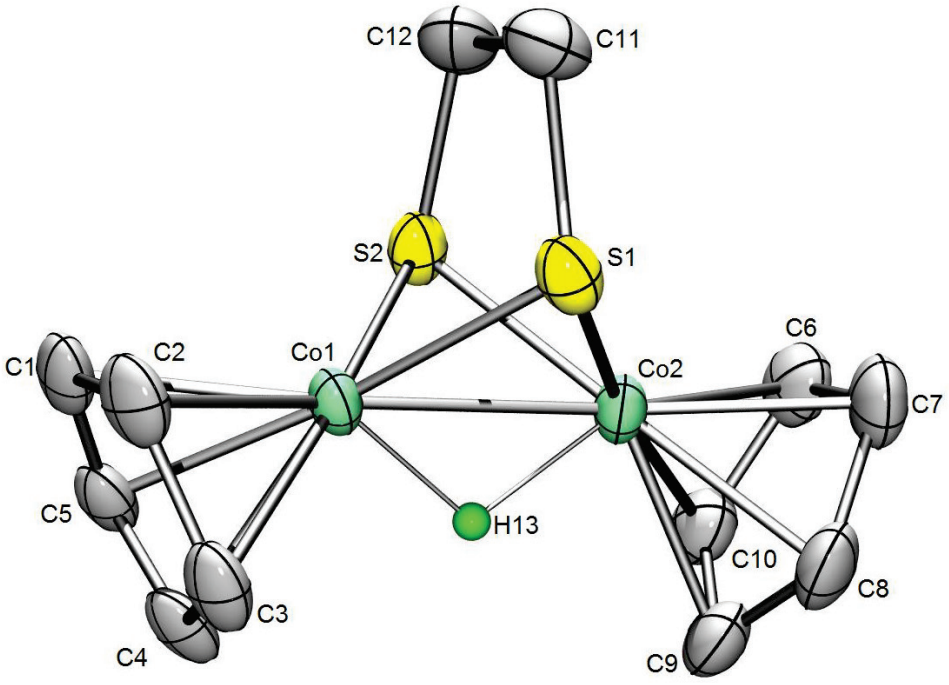

Figure 6.7. Structure of [CpCo(edt)(μ-H)CoCp]BF_4, [1H]BF_4. Counter ions and solvent of crystallization are omitted for clarity. Selected distances (Å): Cp-Co_{avg}, 2.05; Co1-Co2, 2.418; Co1-S1, 2.1977 (11); Co1-S2, 2.1928 (10); Co2-S1, 2.1908 (12); Co2-S1, 2.1891 (10), Co1-H13, Co2-H13, 1.51 (1); Angles (º): S1-Co1-S2, 82.31 (4); S1-Co2-S2, 82.55 (4); Co1-S1-Co2, 67.87 (4); Co1-S2-Co2, 66.98 (3); Co1-H13-Co2, 106.3.

The hydride complexes, [**1**H]$^+$ and [**2**H]$^+$, are deprotonated with triethylamine (pK_a^{MeCN}=18.7)[18] and aniline (pK_a^{MeCN}= 10.7)[18] to cleanly reform the neutral complexes, indicating that the hydride pK_a values are less than 10.7. Deprotonation of [**3**H]$^+$ was not examined. This reactivity differs from that seen for diiron bridging hydride complexes, which cannot be deprotonated. Complexes [**1**H]$^+$- [**3**H]$^+$ are more acidic than NiFe hydride models, which have pK_a values ranging between 11.5- 14.[19] The related bridging phosphide complex $Cp_2Co_2(PMe_2)_2$ has been reported to undergo reversible protonation with CF_3COOH (pK_a^{MeCN} = 12.7)[18] to form a bridging hydride.[11] Complexes **1**- **3** are unreactive towards CF_3COOH, which suggests that the bridging phosphide complex is more basic than the dithiolate complexes.

6.5 Reactivity of CpCo Hydrides with CO and Phosphines.

As mentioned in section 6.1, the dimeric CpCo complex $[Cp_2Co_2(PMe_2)_2(\mu\text{-}H)]^+$, which is related to complexes $[\mathbf{1}H]^+$- $[\mathbf{3}H]^+$, reacts with CO and phosphine ligands. The diphosphide complexes form adducts with CO and phosphines, in which the hydride ligand becomes bound terminally to a Co center.[11-13] This reactivity is of interest because analogous reactivity is not exhibited in diiron complexes. Once diiron complexes are protonated to form bridging hydride complexes, they do not convert to terminally bound hydride complexes, nor do they exhibit Lewis acidity.

When solutions of $[\mathbf{1}H]^+$ and $[\mathbf{2}H]^+$ are saturated with CO, the color changes from dark green to brown after ~ 30 minutes. The IR spectra of the resulting solutions exhibit two strong bands between 1950- 2050 cm^{-1}, indicative of formation of a CO adduct (Table 6.3, Figure 6.8). When the solution is placed under vacuum or an atmosphere of N_2, it changes color from brown to green, and the IR spectrum no longer contains CO bands. The bridging phosphide complex forms a CO adduct that exhibits a single CO band. We propose that the analogous dithiolate complexes, $[\mathbf{1}H]^+$ and $[\mathbf{2}H]^+$ form CO adducts, which could exist as two isomers, depending on the orientation of the CO and hydride ligands with respect to each other, thus resulting in two ν_{CO} bands (Scheme 6.9). The second band in the IR spectra could also be attributed to a Co-H stretch.

Scheme 6.9. Proposed CO adducts of $[1H]^+$ and $[2H]^+$.

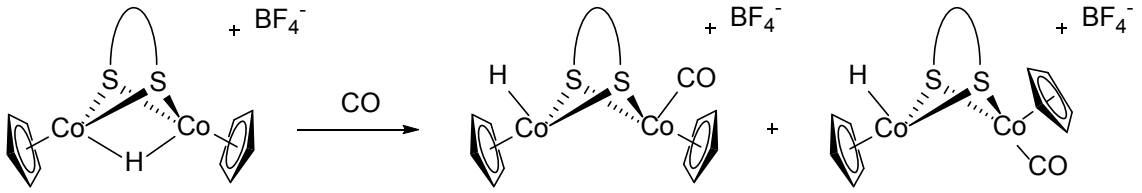

Table 6.3 IR spectroscopic data for CO adducts of CpCo complexes.

Complex	ν_{CO} (cm^{-1})
$[CpCo(edt)(H)(CO)CoCp]BF_4$	2022, 1993 (CH_2Cl_2)
$[CpCo(pdt)(H)(CO)CoCp]BF_4$	2024, 1958 (CH_2Cl_2)
$[Cp_2Co_2(PMe_2)_2(H)(CO)]BF_4$	2010 (KBr)

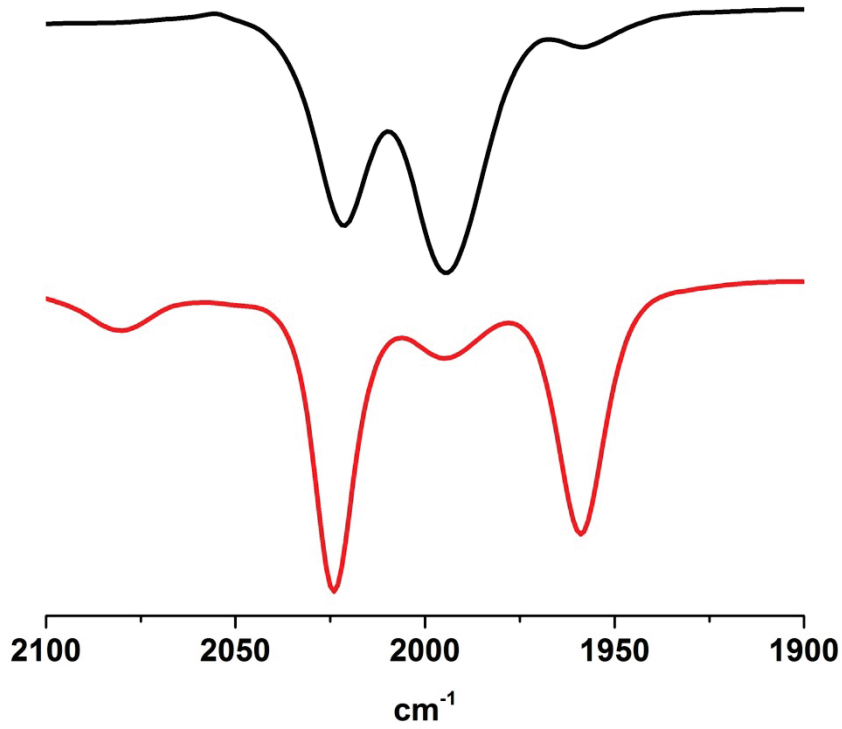

Figure 6.8 IR spectra of [1H]BF_4 + CO (black, top) and [2H]BF_4 + CO (red, bottom) in CH_2Cl_2.

Reaction of [**1**H]$^+$ and [**2**H]$^+$ with PPh_3 does not result in the formation of phosphine bound adduct. Instead, the ^{1}H NMR spectra show the presence of a mixture of hydride and neutral complexes, indicating that PPh_3 (pK_a^{MeCN}= 7.61)[20] partially deprotonates the complexes. Addition of the more electron rich phosphine, PMe_3, to [**1**H]$^+$, results in complete deprotonation to form **1**. These results further emphasize the high acidity of the hydride ligand in [**1**H]$^+$ and [**2**H]$^+$.

6.6 Redox and Electrocatalytic Properties of CpCo Hydrides

The hydride complexes, [**1**H]BF_4 and [**3**H]BF_4 exhibt reversible reduction events at potentials near -1.0 V vs $Fc^{+/0}$ (Table 6.4, Figures 6.9, 6.10). These reduction potentials are 0.5-0.8 V positive of those exhibited for the protonated forms of the diiron complexes $Fe_2(xdt)(CO)_4(PMe_3)_2$ and $Fe_2(xdt)(CO)_2(dppv)_2$ (xdt = adt^{NH}, pdt), suggesting that these phosphine substituted diiron hydride complexes are more electron rich than the new CpCo complexes (Table 6.4).[21,22]

Table 6.4 Electrochemical properties of CpCo hydride complexes and related diiron hydride complexes.

Complex	$E_{1/2}$ (V vs $Fc^{+/0}$)	i_{pc}/i_{pa}
$[CpCo(edt)(\mu\text{-}H)CoCp]BF_4$, $[\mathbf{1}H]BF_4$	-0.980	1.02
$[CpCo(tdt)(\mu\text{-}H)CoCp]BF_4$, $[\mathbf{3}H]BF_4$	-1.1	0.93
$[Fe_2(pdt)(\mu\text{-}H)(CO)_4(PMe_3)_2]BF_4$[a]	-1.5	< 1
$[Fe_2(pdt)(\mu\text{-}H)(CO)_2(dppv)_2]BF_4$[b]	-1.8	1.57

[a] Values obtained from reference 21; [b] Values obtained from reference 22

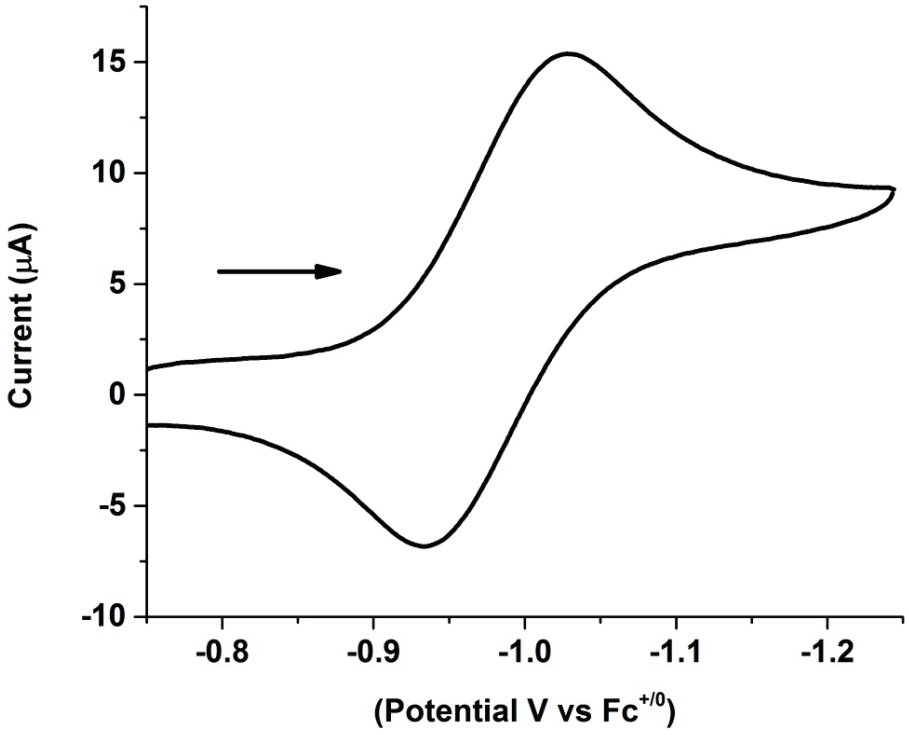

Figure 6.9. Cyclic voltammogram of $[CpCo(edt)(\mu\text{-}H)CoCp]BF_4$, $[1H]BF_4$, in CH_2Cl_2. (Conditions: 0.1 M $[Bu_4N]PF_6$, 1.0 mM $[1H]BF_4$, glassy carbon working electrode, Ag wire pseudo reference electrode, Pt wire counter electrode)

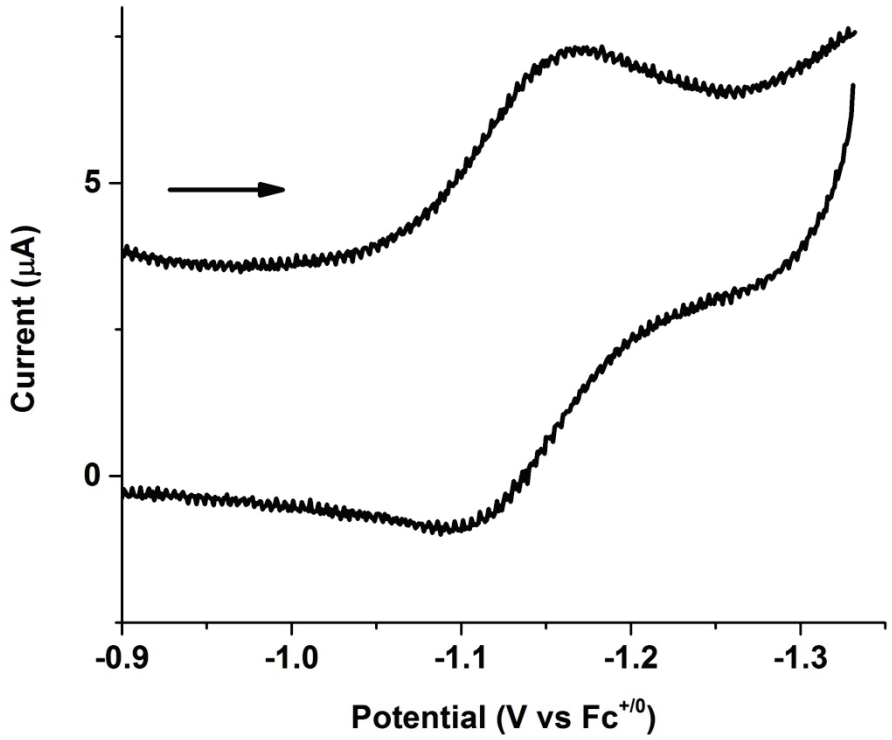

Figure 6.10. Cyclic voltammogram of [CpCo(tdt)(μ-H)CoCp]BF_4, [3H]BF_4, in CH_2Cl_2. (Conditions: See figure 6.9)

The electrocatalytic properties of [**1**H]BF_4 and [**3**H]BF_4 were investigated. In the presence of strong acid, $HBF_4{\cdot}Et_2O$, the reductive current at ~-1.0 V increases and shifts to more positive potentials, indicative of proton reduction catalysis (Figures 6.11, 6,13). For both hydride complexes, the current increases linearly with increased acid concentration (Figures 6.12, 6.14). Even in the presence of up to 25 equivalents of acid, catalysis by $[\mathbf{1}H]^+$ did not reach the acid independent regime. We can therefore conclude that the catalyst operates at a potential of at least 6 s^{-1}, which is comparable with diiron bridging hydride complexes (Table 6.5).[23] In order to obtain a more accurate overpotential value, catalysis by [**1**H]BF_4 was attempted in MeCN. At low acid concentration, the value of i_c/i_p increased, but the sample decomposed during the course of the experiment, likely due to reaction with the solvent.

With increasing amounts of acid, the reductive current for the toluenedithiolate complex, $[\mathbf{3}H]^+$, increases linearly with increasing acid, up to 30 equivalents, at which point it reaches a maximum i_c/i_p of 39 (Table 6.5). The acid independent rate of 294 s^{-1} is comparable with the

rate exhibited for the NiFe model, [(dppe)Ni(edt)(μ-H)Fe(CO)$_3$]BF$_4$, which operates at a rate of ~ 300 s^{-1}.[19]

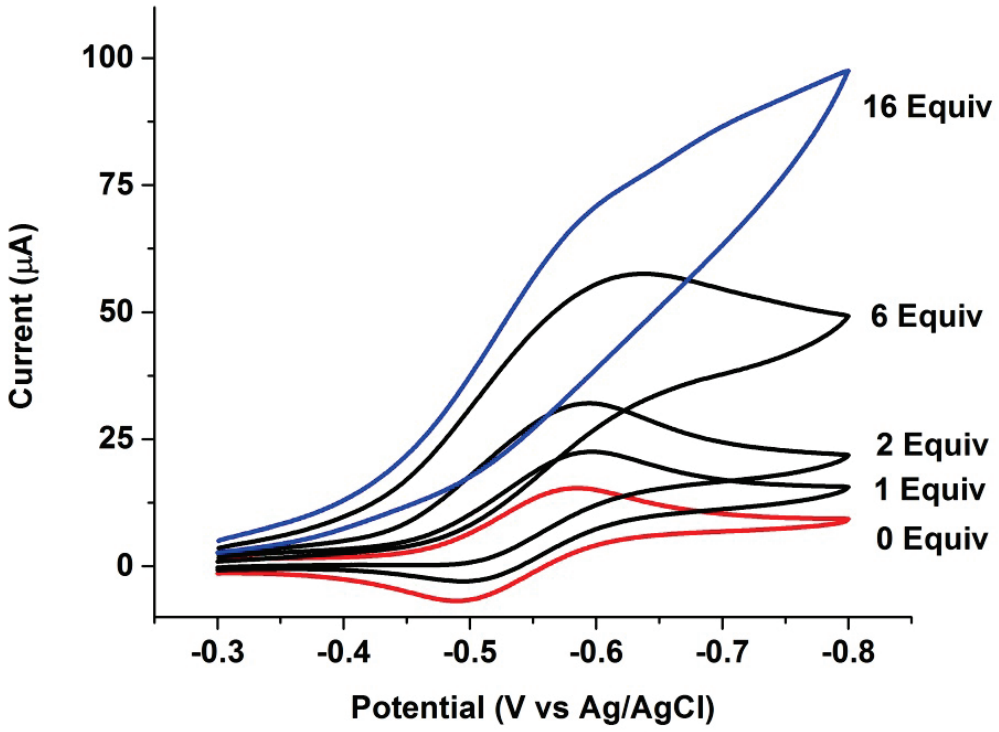

Figure 6.11. Cyclic voltammograms of [CpCo(edt)(μ-H)CoCp]BF$_4$, [1H]BF$_4$, in CH_2Cl_2 with increasing equivalents of $HBF_4.Et_2O$. (Conditions: 0.1 M [Bu$_4$N]PF$_6$, 1.0 mM [1H]BF$_4$, glassy carbon working electrode, Ag wire pseudo reference electrode, Pt wire counter electrode).

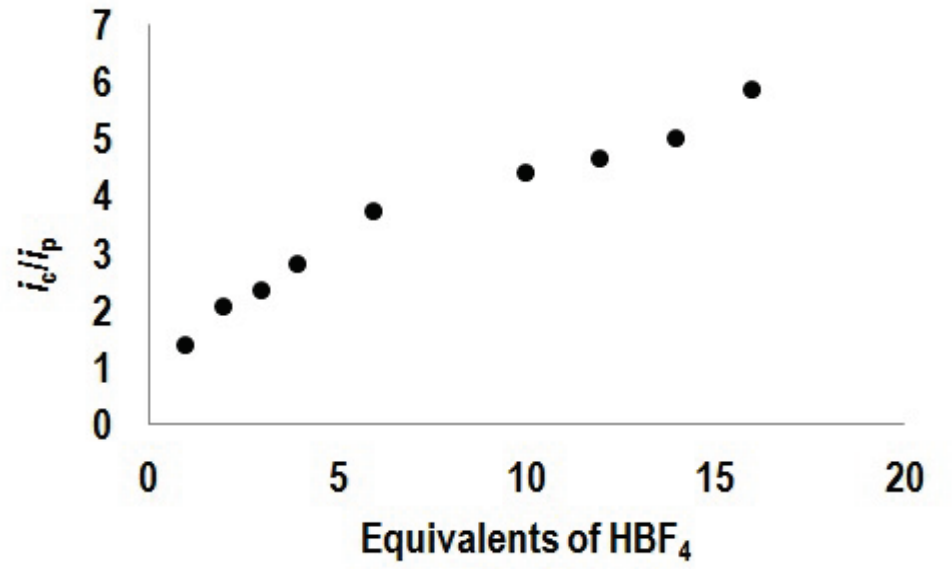

Figure 6.12. Plot of i_c/i_p vs equivalents of $HBF_4 \cdot Et_2O$ added to a solution of $[1H]BF_4$.

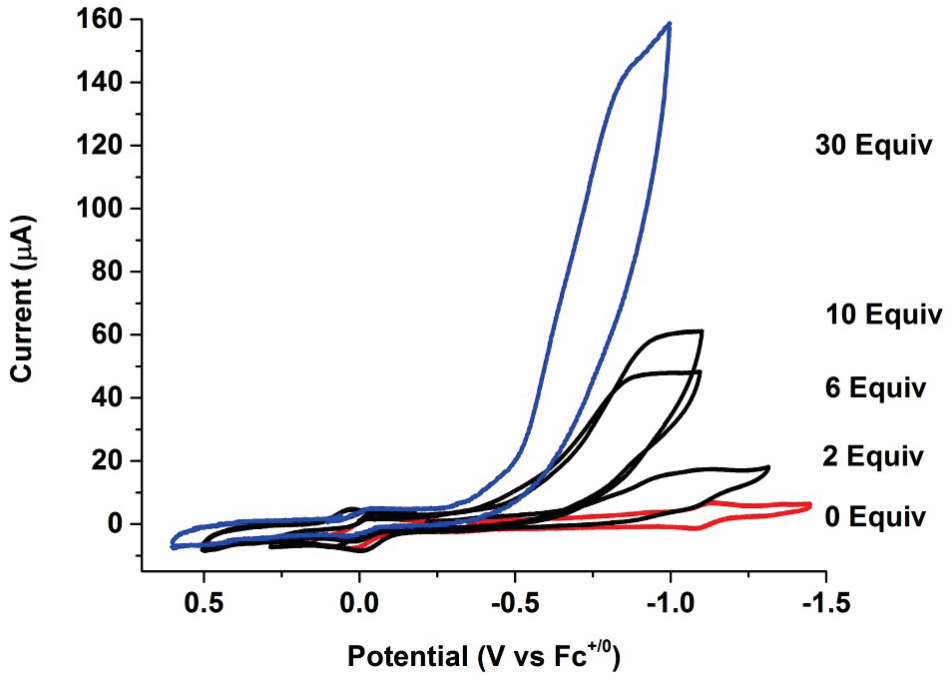

Figure 6.13. Cyclic voltammograms of $[CpCo(tdt)(\mu\text{-}H)CoCp]BF_4$, $[3H]BF_4$, in CH_2Cl_2 with increasing equivalents of $HBF_4 \cdot Et_2O$. (Conditions: 0.1 M $[Bu_4N]PF_6$, 1.0 mM $[3H]BF_4$, glassy carbon working electrode, Ag wire pseudo reference electrode, Pt wire counter electrode)

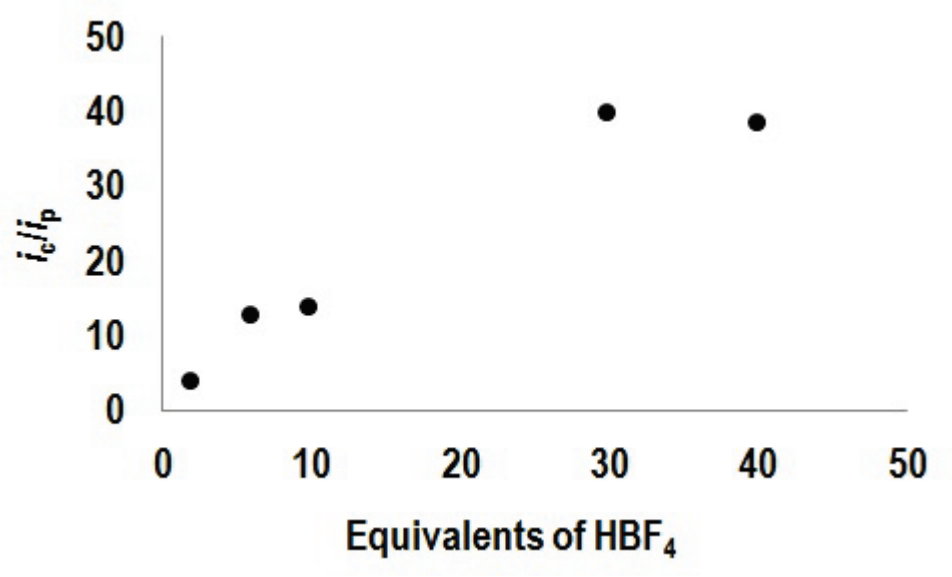

Figure 6.14. Plot of i_c/i_p vs equivalents of $HBF_4 \cdot Et_2O$ added to a solution of $[3H]BF_4$.

Table 6.5 Electrocatalytic properties of CpCo hydride Complexes.

Complex	E_{cat} (V vs $Fc^{+/0}$)	k (s^{-1})	Overpotential (V)
$[CpCo(edt)(\mu\text{-}H)CoCp]BF_4$, $[\mathbf{1}H]BF_4$	-1.073	> 6	0.90
$[CpCo(tdt)(\mu\text{-}H)CoCp]BF_4$, $[\mathbf{3}H]BF_4$	-0.76	294	0.59

Both CpCo hydride complexes require a fairly strong acid, $HBF_4 \cdot Et_2O$, for catalysis to occur. When the weaker acid, CF_3COOH ((pK_a^{MeCN}= 12.6)[18], was employed, there was no catalytic response. The requirement for the use of very strong acid leads to fairly high overpotentials (Table 6.5), compared with the enzymes, which operate at overpotentials of ~ 0.08 V.[24,25] In comparison with other synthetic proton reduction catalysts, the CpCo hydrides operate at overpotentials that are typical.

6.7 Conclusions

A new synthetic route to complexes of the type CpCo(xdt)CoCp has been developed,. The work was motivated by the need for more electron rich bimetallic complexes that mimic the active site of [FeFe]-hydrogenase. Typical diiron models contain $Fe(CO)_{3-n}L_n$ units, and are not

particularly electron rich if the level of substitution is low.[26,27] The CpCo and $Fe(CO)_3$ units are isoelectronic, but CpCo is more electron rich, owing to Cp being a poorer π-acceptor than CO.

Compared to $Fe_2(SR)_2(CO)_6$, the CpCo complexes are more electron rich, based on differences in oxidation potentials.[16] Additionally, the CpCo complexes may be reversibly protonated, whereas complexes of the type $Fe_2(SR)_2(CO)_6$ do not undergo protonation, even with strong acids.[27] The electron density of the CpCo complexes is comparable with diiron tetracarbonyl complexes, but they are less electron rich than the more highly substituted diiron species.[16,17,21,22]

The hydride species, $[\mathbf{1}H]^+$ and $[\mathbf{3}H]^+$ undergo reduction at fairly mild potentials (~ -1 V vs $Fc^{+/0}$), but they only exhibit catalytic behavior in the presence of strong acids. Therefore, although the toluenedithiolate complex, $[\mathbf{3}H]^+$ operates at fairly high rates, by the standards of synthetic catalysts, but it operates at an overpotential that is ~ 0.5 V larger than that reported for the enzyme.[28]

6.8 Experimental.

Reactions were typically conducted using Schlenk techniques at room temperature. Most reagents were purchased from Aldrich and Strem. Solvents were HPLC-grade and dried by filtration through activated alumina or distilled under nitrogen over an appropriate drying agent. $HBF_4{\cdot}Et_2O$ (Sigma-Aldrich) was supplied as 51-57% HBF_4 in Et_2O (6.91 – 7.71 M). $[Bu_4N]PF_6$ was purchased from GFS Chemicals and was recrystallized three times by extraction into a minimal volume of acetone followed by precipitation by an equal volume ethanol. ^1H NMR spectra (500 and 400 MHz) are referenced to residual solvent referenced to TMS. ^{31}P NMR spectra (202 or 161 MHz) were referenced to external 85% H_3PO_4. FT-IR spectra were recorded on a Perkin Elmer Spectrum 100 FT-IR spectrometer.

CpCo(edt)CoCp, 1. A solution of $CpCo(CO)_2$ (1 mL,7.5 mmol) in 100 mL of toluene was treated with 1,2-ethanedithiol (315 μL, 3.75 mmol). The red solution was heated to reflux in a 120°C oil bath, and the progress of the reaction was monitored by IR spectroscopy, for loss of $CpCo(CO)_2$ bands at 2023 cm^{-1} and 1960 cm^{-1}. After 20 h, the solution had changed color from red to brown. The cooled solution was filtered, and the remaining brown residue was washed with toluene to remove any undissolved product. The brown product was concentrated to dryness under vacuum and extracted into pentane. The pentane solution was concentrated and

cooled to -20 °C, resulting in crystallization of the product. ^{1}H NMR (500 MHz, CD_2Cl_2): δ 4.867 (s, 10H, C_5H_5), 1.285 (s, SCH_2CH_2S, 6.47 H). FD-MS m/z: 340.0. Anal calcd for $Co_2S_2C_{12}H_{14}$ (found): C, 42.3 (42.14); H, 4.15 (4.45).

CpCo(pdt)CoCp, 2. A solution of $CpCo(CO)_2$ (1.5 mL , 11.2 mmol) in 100 mL of toluene was treated with 1,3-propanedithiol (560 μL , 5.6 mmol). The red solution was heated to reflux in a 120°C oil bath, and the progress of the reaction was monitored by IR, for loss of $CpCo(CO)_2$ bands at 2023 cm^{-1} and 1960 cm^{-1}. After 16 hours, the solution changed color from red to green. The solution was filtered, and the remaining brown residue was washed with toluene to remove any undissolved product. The green product was concentrated to dryness under vacuum and extracted into pentane. The pentane solution was concentrated and cooled to -20 °C, resulting in crystallization of the product. ^{1}H NMR (500 MHz, CD_2Cl_2): δ 4.868 (*s*, C_5H_5), 1.288 (*s*, SCH_2CH_2,), 1.176 (*s*, SCH_2). When the NMR sample is cooled to -70°C, an additional signal is present at 0.524 ppm, and the signal corresponding to C_5H_5 is split. ^{1}H NMR (500 MHz, CD_2Cl_2) -70°C : δ 4.911, 4.778 (*d*, C_5H_5), 1.897 (*s*), 1.713 (*s*), 0.524(*s*). FD-MS m/z: 354. Anal calcd for $Co_2S_2C_{13}H_{16}$ (found): C, 44.1 (44.02); H, 4.55 (4.48).

CpCo(tdt)CoCp, 3. A solution of $CpCo(CO)_2$ (1 mL,7.5 mmol) in 100 mL of toluene was treated with toluene-3,4-dithiol (.585 g, 3.7 mmol). The red solution was heated to reflux in a 120°C oil bath, and the progress of the reaction was monitored by IR, for loss of $CpCo(CO)_2$ bands at 2023 cm^{-1} and 1960 cm^{-1}. After 20 hours, the solution had changed color from red to dark purple. The solution was filtered, and the remaining brown residue was washed with toluene to remove any undissolved product. The purple product was concentrated to dryness under vacuum and extracted into pentane. The pentane solution was concentrated and cooled to -20 °C, resulting in crystallization of the product. ^{1}H NMR (500 MHz, CD_2Cl_2): δ 6.465 (*s*, Phenyl CH), 5.955 (*s*, Phenyl CH), 5.119 (*s*, C_5H_5), 1.813 (*s*, CH_3). FD-MS m/z: 402.

[CpCo(edt)(*μ*-H)CoCp]BF_4, [1H]BF_4. A solution of **1** (101 mg, 0.3 mmol) in 20 mL of CH_2Cl_2 was treated with one equivalent of $HBF_4 \cdot Et_2O$ (50 μL 54% wt/v, 0.3 mmol). The solution stirred for ten minutes, and then it was concentrated to dryness under vacuum. The resulting brown solid was recrystallized from dichloromethane and hexanes. ^{1}H NMR (CD_2Cl_2): 5.551 (*s*, C_5H_5), 2.621 (*s*, SCH_2CH_2S), -15.641 (*s*, Co-H-Co). ESI-MS: m/z: 341.2. Diffraction quality crystals of [**1**H]BF_4 were obtained by vapor diffusion of diethyl ether into a solution of the compound in CH_2Cl_2.

[CpCo(pdt)(μ-H)CoCp]BF_4, [2H]BF_4. A solution of **2** (227 mg, 0.64 mmol) in 20 mL of CH_2Cl_2 was treated with one equivalent of $HBF_4 \cdot Et_2O$ (105 μL 54% wt/v, 0.64 mmol). The solution stirred for ten minutes, and then it was concentrated to dryness under vacuum. The resulting green solid was recrystallized from dichloromethane and hexanes. ^{1}H NMR: δ 5.571 (s, 10 H, C_5H_5), 2.172 (s, 12.11 H, $SCH_2CH_2CH_2S$), -13.288 (s, 1.52 H, Co-H-Co). ESI-MS: m/z: 355.2.

[CpCo(tdt)(μ-H)CoCp]BF_4, [3H]BF_4. A solution of **3** (115 mg, 0.3 mmol) in 15 mL of CH_2Cl_2 was cooled in an acetone/ dry ice bath and treated with one equivalent of $HBF_4 \cdot Et_2O$ (50 μL 54% wt/v, 0.3 mmol). The solution stirred for ten minutes, after which time it was warmed to room temperature. The solution was then concentrated to dryness under vacuum, resulting in a green solid that was recrystallized from dichloromethane and hexanes. ^{1}H NMR(500 MHz, CD_2Cl_2): 7.091 (*s*, Phenyl CH), 6.483 (*s*, Phenyl CH), 5.728 (*s*, C_5H_5), 2.112 (*s*, CH_3), -7.613 (*s,* Co-H-Co) ESI-MS: m/z: 341.2.

Reaction of [CpCo(μ-H)(μ-edt)CoCp]BF_4 with CO. A solution of [**1**H]BF_4 was saturated with CO, causing the green solution to turn brown. IR spectra show the appearance of bands at 2022 and 1993cm^{-1}. Solvent was removed under vacuum. When the solid is redissolved in CD_2Cl_2, the ^{1}H NMR spectrum matches that for [**1**H]BF_4, and the IR spectrum does not contain CO bands.

Reaction of [CpCo(μ-H)(μ-pdt)CoCp]BF_4 with CO. A solution of [CpCo(μ-H)(μ-pdt)CoCp]BF_4 was saturated with CO, causing the green solution to brown. IR spectra show the appearance of ν_{CO} at 2024 and 1960 cm^{-1}. Solvent was removed under vacuum, and the hydride and Cp signals in the ^{1}H NMR match those for [CpCo(μ-H)(μ-pdt)CoCp]BF_4 . An ESI mass spectrum in CH_2Cl_2 contains m/z=355, indicating that the predominant species is [CpCo(μ-H)(μ-pdt)CoCp]BF_4. An IR spectrum of the CH_2Cl_2 solution does not contain CO bands.

CO was bubbled through a solution of [CpCo(μ-H)(μ-pdt)CoCp]BF_4 in CH_2Cl_2, and the progress of the formation of CO binding was monitored by IR. Over the course of 7 hours, CO bands at 2024 and 1960 cm^{-1} appear. The solution was then bubbled with N_2, and over the course of 18 hours, the intensity of the CO bands decreases; however they do not completely disappear. Additionally, the color of the solution does not change to green, that of [CpCo(μ-H)(μ-pdt)CoCp]BF_4, rather it remains brown, suggesting that CO binding is not completely

reversible. When the solution is once again exposed to CO, the bands at 2024 and 1960 cm^{-1} reappear.

Analysis of the CO adduct by ^1H NMR was attempted. A CD_2Cl_2 solution of $[\mathbf{2}H]^+$ was frozen in a J-young NMR tube, and the tube was evacuated and refilled with CO. However, the ^1H NMR spectrum only shows a signal in the high field region corresponding to $[\mathbf{2}H]^+$. Additionally, the CO adduct was formed as described above and precipitated from a CH_2Cl_2 solution by addition of hexanes. The resulting brown solid was analyzed by ^1H NMR, but the spectrum only contains signals corresponding to $[\mathbf{2}H]^+$.

Reaction of [CpCo(μ-H)(μ-edt)CoCp]BF_4 with PPh_3. A solution of $[\mathbf{1}H]BF_4$ was dissolved in CH_2Cl_2 and treated with a solution of PPh_3. The solution turned slightly brown in color. After stirring for ~12 h, the solution was concentrated to dryness under vacuum. The ^1H NMR spectrum of the proton indicates the presence of both **1** and $[\mathbf{1}H]BF_4$, present in a ratio of ~ 1:2.

Reaction of [CpCo(μ-H)(μ-pdt)CoCp]BF_4 with PPh_3. A solution of $[\mathbf{2}H]BF_4$ was dissolved in CH_2Cl_2 and treated with a solution of PPh_3. The solution turned slightly brown in color. After stirring for ~12 h, the solution was concentrated to dryness under vacuum. The ^1H NMR spectrum of the proton indicates the presence of both **1** and $[\mathbf{1}H]BF_4$, present in a ratio of ~ 2:1.

Electrochemistry. Electrochemical experiments were carried out on CH Instruments Model 600D Series Electrochemical Analyzer or a BAS-100 Electrochemical Analyzer. Cyclic voltammetry experiments were conducted using a 10-mL one-compartment glass cell with a tight-fitting Teflon top. The working electrode was a glassy carbon (GC) disk (diameter = 3.00 mm). A silver wire was used as a quasi-reference electrode, and the counter electrode was a Pt wire. Ferrocene was added as an internal reference, and each cyclic voltammogram was referenced to this $Fc^{0/+}$ couple = 0.00 V. *i*R compensation was applied to all measurements using the CH Instruments or BAS software. Cell resistance was determined prior to each scan, and the correction applied to the subsequently collected cyclic voltammogram. For all experiments, the electrolyte solution was prepared and sparged in the cell, which was fitted with electrodes. A CV of the electrolyte was collected prior to the addition of Fe_2 compound, in order to check the purity of the electrolyte. The dicobalt compound was then dissolved in the electrolyte solution and transferred to the cell.

General Procedure for Proton Reduction Catalysis. A 1 mL solution of 0.1 M $[Bu_4N]PF_6$ and 1.0 mM CpCo hydride was treated with increasing amounts of a 0.365 M $HBF_4 \cdot Et_2O$ stock solution. After each addition of acid, a CV was collected. The working electrode was polished after each acid addition, and the solution was briefly sparged with N_2.

6.9 References

(1) King, R. B.; Treichel, P. M.; Stone, F. G. A. "Chemistry of the metal carbonyls. XII. New complexes derived from cyclopentadienylcobalt dicarbonyl." *J. Am. Chem. Soc.* **1961**, *83*, 3593.

(2) Miller, V. R.; Grimes, R. N. "Preparation of stable closo- and nideo-cobaltaboranes from sodium(+) octahydropentaborate(-). Complexes of the formal octahydrotetraborate(2-) and hexahydrotetraborate(4-) ligands." *J. Am. Chem. Soc.* **1973**, *95*, 5078.

(3) Greenwood, N. N.; Savory, C. G.; Grimes, R. N.; Sneddon, L. G.; Davison, A.; Wreford, S. S. "Preparation of a stable small ferraborane, $B_4H_8Fe(CO)_3$." *J. Chem. Soc., Chem. Commun.* **1974**, 718.

(4) King, R. B.; Treichel, P. M.; Stone, F. G. A. "Chemistry of the Metal Carbonyls. XIV. New Organosulfur Derivatives of Iron and Cobalt." *J. Am. Chem. Soc.* **1961**, *83*, 3600.

(5) Malacria, M.; Aubert, C.; Renaud, J. L. "Product class 4: organometallic complexes of cobalt." *Sci. Synth.* **2002**, *1*, 439.

(6) Koelle, U.; Paul, S. "Electrochemical reduction of protonated cyclopentadienylcobalt phosphine complexes." *Inorg. Chem.* **1986**, *25*, 2689.

(7) Pétillon, F. Y.; Le Quere, J. L.; Le Floch-Perennou, F.; Guerchais, J. E.; L'Haridon, P. "Reaction of dinuclear thiolato-bridged cobalt compounds with activated alkynes. Formation and x-ray structure of an unusual trinuclear cobalt complex, [Co3(.eta.5-C5H5)3(SMe)2(CF3.tplbond.CCF3)2]." *J. Organomet. Chem.* **1985**, *281*, 305.

(8) Shaver, A.; Morris, S.; Turrin, R.; Day, V. W. "The novel redox reaction and thiolato ligand transfer between $Cp_2Ti(SCMe_3)_2$ and $CpCo(CO)_2$. Preparation and structure of [CpCo(m-SCMe3)]2." *Inorg. Chem.* **1990**, *29*, 3622.

(9) Drobnik, S.; Stoll, C.; Noeth, H.; Polborn, K.; Hiller, W.; Lorenz, I.-P. "Photolytically induced reactions of $CpCo(CO)_2$ (Cp = C_5H_5, C_5H_4Me, C_5Me_5, and C_5Ph_5) with thiirane yielding dinuclear 1,2-ethanedithiolato-S,S complexes." *Z. Naturforsch., B: Chem. Sci.* **2006**, *61*, 1365.

(10) Hayter, R. G.; Williams, L. F. "Phosphorus- and arsenic-bridged complexes of metal carbonyls. VIII. Cyclopentadienylcobalt and -manganese complexes." *J. Inorg. Nucl. Chem.* **1964**, *26*, 1977.

(11) Werner, H.; Hofmann, W. "Stepwise Addition of a Lewis Acid and a Lewis Base to a Metal-Metal Bond." *Angew. Chem. Int. Ed.* **1979**, *18*, 158.

(12) Werner, H.; Hofmann, W.; Zolk, R.; Dahl, L. F.; Kocal, J.; Kuehn, A. "Synthesis and reactions of a nucleophilic bis(m-dimethylphosphido)dicobalt complex. The crystal and molecular structure of $[C_5H_5Co(\mu\text{-}PMe_2)]_2$ and $[(C_5H_5Co)_2(\mu\text{-}H)(\mu\text{-}PMe_2)_2]BPh_4$." *J. Organomet. Chem.* **1985**, *289*, 173.

(13) Werner, H.; Zolk, R.; Hofmann, W. "Metal complexes with bridging dimethylphosphido ligands. II. Opening of the hydrido bridges in the $[(C_5H_5Co)_2(\mu\text{-}PMe_2)_2(\mu\text{-}H)]^+$ cation with Lewis bases and formation of μ-formimidoyl complexes across hydrido(isonitrile) and .mu.-aminocarbyne compounds as intermediates." *J. Organomet. Chem.* **1986**, *302*, 65.

(14) Frisch, P. D.; Lloyd, M. K.; McCleverty, J. A.; Seddon, D. "Electrochemical oxidation of thio-bridged binuclear .pi.-cycopentadienyl complexes of molybdenum, iron, cobalt, and nickel." *J. Chem. Soc., Dalton Trans.* **1973**, 2268.

(15) Fontecilla-Camps, J. C.; Volbeda, A.; Cavazza, C.; Nicolet, Y. "Structure/Function Relationships of [NiFe]- and [FeFe]-Hydrogenases." *Chem. Rev.* **2007**, *107*, 4273.

(16) Chong, D.; Georgakaki, I. P.; Mejia-Rodriguez, R.; Sanabria-Chinchilla, J.; Soriaga, M. P.; Darensbourg, M. Y. "Electrocatalysis of Hydrogen Production by Active Site Analogues of the Iron Hydrogenase Enzyme: Structure/Function Relationships." *J. Chem. Soc., Dalton Trans.* **2003**, 4158.

(17) Justice, A. K.; De Gioia, L.; Nilges, M. J.; Rauchfuss, T. B.; Wilson, S. R.; Zampella, G. "Redox and Structural Properties of Mixed-Valence Models for the Active Site of the [FeFe]-Hydrogenase: Progress and Challenges." *Inorg. Chem.* **2008**, *47*, 7405.

(18) Izutsu, K. *Acid-Base Dissociation Constants in Dipolar Aprotic Solvents*; Blackwell Scientific Publications: Oxford, U.K., 1990; Vol. 35.

(19) Carroll, M. E.; Barton, B. E.; Gray, D. L.; Mack, A. E.; Rauchfuss, T. B. "Active-Site Models for the Nickel-ìIron Hydrogenases: Effects of Ligands on Reactivity and Catalytic Properties." *Inorg. Chem.* **2011**, *50*, 9554.

(20) Kaljurand, I.; Kütt, A.; Sooväli, L.; Rodima, T.; Mäemets, V.; Leito, I.; Koppel, I. A. "Extension of the Self-Consistent Spectrophotometric Basicity Scale in Acetonitrile to a Full Span of 28 pKa Units: Unification of Different Basicity Scales." *J. Org. Chem.* **2005**, *70*, 1019.

(21) Gloaguen, F.; Lawrence, J. D.; Rauchfuss, T. B.; Bénard, M.; Rohmer, M.-M. "Bimetallic Carbonyl Thiolates as Functional Models for Fe-Only Hydrogenases." *Inorg. Chem.* **2002**, *41*, 6573.

(22) Barton, B. E.; Rauchfuss, T. B. "Terminal Hydride in [FeFe]-Hydrogenase Model Has Lower Potential for H2 Production Than the Isomeric Bridging Hydride." *Inorg. Chem.* **2008**, *47*, 2261.

(23) Carroll, M. E.; Barton, B. E.; Rauchfuss, T. B.; Carroll, P. J. "Synthetic Models for the Active Site of the [FeFe]-Hydrogenase: Catalytic Proton Reduction and the Structure of the Doubly Protonated Intermediate." *J. Am. Chem. Soc.* **2012**, *134*, 18843.

(24) Jones, A. K.; Sillery, E.; Albracht, S. P. J.; Armstrong, F. A. "Direct Comparison of the Electrocatalytic Oxidation of Hydrogen by an Enzyme and a Platinum Catalyst." *Chem. Commun.* **2002**, 866.

(25) Hambourger, M.; Gervaldo, M.; Svedruzic, D.; King, P. W.; Gust, D.; Ghirardi, M.; Moore, A. L.; Moore, T. A. "[FeFe]-Hydrogenase-Catalyzed H2 Production in a Photoelectrochemical Biofuel Cell." *J. Am. Chem. Soc.* **2008**, *130*, 2015.

(26) Gloaguen, F.; Rauchfuss, T. B. "Small Molecule Mimics of Hydrogenase: Hydrides and Redox." *Chem. Soc. Rev.* **2009**, *38*, 100.

(27) Tard, C.; Pickett, C. J. "Structural and Functional Analogues of the Active Sites of the [Fe]-, [NiFe]-, and [FeFe]-Hydrogenases." *Chem. Rev.* **2009**, *109*, 2245.

(28) Wang, M.; Chen, L.; Sun, L. "Recent progress in electrochemical hydrogen production with earth-abundant metal complexes as catalysts." *Energy Environ. Sci.* **2012**, *5*, 6763.